

Simulation of High-Entropy Materials

Gautam Anand



The
University
Of
Sheffield.

Doctor of Philosophy
The University of Sheffield
January 2018

Abstract

Multicomponent materials containing a comparatively large number of different elemental components, yet exhibiting simple crystal structures have opened up a new era of materials design with the possibility of tuning properties of materials with greater degrees of freedom. This poses a formidable challenge in terms of design as the number of parameters involved in simulating such systems increase significantly with the increasing number of components. This work reports a sampling methodology based on hybrid genetic algorithm-molecular dynamics for sampling positional-disordered materials such as high-entropy systems. This investigation also demonstrates the influence of individual cationic species on the evolution of distortion in single-phase solid solution with the rock-salt structure, when oxides such as CoO, CuO, MgO, NiO and ZnO are mixed together. Additionally, the relationship between the number of atomic species and its effect on the lattice distortion has been presented. The influence of alloying elements on the evolution of lattice friction in substitutional alloys has been studied using Monte Carlo simulations with a continuum elasticity relation for dislocations. The spread in energy-range due to elastic properties and size-misfit of elements provides physical justification for friction stress being low in CoNi alloy, high in CoCrNi (medium entropy alloy), along with intermediate values in CoCrFeNi (High Entropy Alloy). A similar approach justifies strengthening due to dilute addition of Al into CoCrFeMnNi and CoCrFeNi. This approach is a computationally cheap method of screening a range of possible alloys with respect to their

lattice friction stress. Spin-polarised density functional theory (DFT) calculations presented here were carried out to study the charge transfer among elements and evolution of distortion in substitutional alloys. To study the characteristics of the individual element, impurity-in-matrix type calculations were carried out. The charge transfer between impurity and matrix element is presented to determine issues with the electronegativity parameter of Miedema's model for enthalpy calculations. The distortion in substitutional alloys, particularly due to Cr has been found to be related to interaction of electrons with complementary spins in their d-orbitals.

* * * * *

Dedication

Dedicated to my teacher, Professor Partha Protim Chattopadhyay

Acknowledgements

I am thankful to Dr. Colin L. Freeman for his guidance during my PhD programme and helping me to develop as an independent researcher by providing me freedom to set achievable goals. I am also thankful to Dr. Russell Goodall for his suggestions during supervisory meetings and particularly helping me to develop an efficient research methodology.

I am thankful to Faculty of Engineering for awarding me a Faculty scholarship without which I would not have been able to carry out this programme. I would like to acknowledge feedback from the thesis assessment committee, including Professor John Harding and Professor Iain Todd for their constructive comments during internal assessments. I am indebted to Aaron, Zhao, James, Robyn, Kai, Matt, Amanda, Adam, and other members of MESAS group for the helpful discussions. I would particularly like to mention our daily tea-session in the Turner's Museum of Glass, which I thoroughly enjoyed for the last three years. The anecdotal quotes made during these sessions would be in my memory forever. This space is simply not enough for me to acknowledge so many people who have helped me directly or indirectly to get to this point in my life. But my seniors like Subhranshu Chatterjee, Santanu Bhowmick, Arijit Sinha, Sumit Chabri and Himel Chakraborty definitely deserve the special mention. I am thankful to Angesh and Nitanshu for their joyful company and listening my ranting on almost every issue for the last four years. I am thankful to my Mother, Gaurav, Mausam and Mamuji for believing in me. My Father is not around to see this, but I am sure he would have been immensely proud of me. I am grateful for the constant support from my fiancée, Madhu who has been a pillar of strength for me.

Declaration

The present work has been carried out by the author between January-2015 and December-2017 for the partial fulfilment of requirements for the PhD degree from The University of Sheffield and this work has not been submitted elsewhere. Part of this thesis have been published and details of which are as follows:

1. Part of Chapter-5 (Phase Stability in Substitutional Alloys) has been published as an article in Scripta Materialia [G. Anand, R. Goodall, Colin L. Freeman, *Scripta Materialia*, 124 (2016) 90-94].
2. Chapter-6 (Phase stability and distortion in high-entropy oxides) has been published as part of an article in Acta Materialia [G. Anand, Alex P. Wynn, Christopher M. Handley, Colin L. Freeman, *Acta Materialia*, 146 (2018) 119-125]. This investigation is joint work of the author and Dr. Colin L. Freeman.

List of Figures

2.1	Variation in the entropy as reaction progresses, for an isolated system of constant internal energy and constant volume containing both reactants and products. Redrawn from ref. [14].	10
3.1	Calculation of area under curve using MC algorithm, redrawn from source-2.	30
4.1	The modification of the original Coulombic potential (V_{true}) and original wavefunction (ψ_{true}) in the pseudopotential framework. The V_{true} is replaced with V_{pseudo} and ψ_{true} is replaced with ψ_{pseudo}	42
4.2	The first Brillouin zone of the FCC crystal structure, which is a truncated octahedron.	44
4.3	The variation of the Fermi-Dirac function with different value of σ . Redrawn from ref. [28].	45
5.1	Schematic figure illustrating the number of paths of length two, which can be traversed such that they start and end at the atom labelled as 'i'. As it is evident, the number of such paths is twelve.	50

5.2	Variation of energy with time-step during MD simulation for BCC and FCC form of $\text{Al}_{0.5}\text{CoCrFeNi}$ and AlCoCrFeNi	55
5.3	Variation of energy with time-step during MD simulation for for BCC and FCC form of CoCrFeNi and CoCrFeNiTi	56
5.4	(a) Schematic to show the R_1 and R_2 in typical RDF of alloys and (b) Ratio of R_2 and R_1 for elements in pure (P) state, BCC- CoCrFeNi (CCFN(B)), FCC- CoCrFeNi (CCFN(F)), BCC- AlCoCrFeNi (ACCFN(B)), FCC- AlCoCrFeNi (ACCFN(F)), BCC- CoCrFeNiTi (CCFNT(B)) and FCC- CoCrFeNiTi (CCFNT(F)).	57
5.5	Visualisation of structure of different alloys after completion of MD simulation. Note that these calculations were carried out for 16384 and 16000 atoms for FCC and BCC atoms respectively for visualisation purposes.	58
5.6	Simulation of peak of X-ray diffraction (XRD) pattern for BCC and FCC form of different alloys. Cu- $K\alpha$ radiation of wavelength 1.54 Å was used as input to the simulation. Note that finite-size broadening is taking place due to use of clusters in simulating XRD profile.	59
5.7	Radial distribution function (RDF) for CoCr , CoFe , CoCrFe , CoFeNi , CoCrNi and CoCrFeNi using EAM potential published in ref. [49].	61
5.8	The electron density distribution (in arbitrary units) in the case of FCC- CoCrFeNi , obtained after superimposition of electron density from EAM potential of the individual elements on MD simulated structure. This figure shows different sections of three dimensional supercell starting from left to right.	61
5.9	The distribution of electron density on the nodes of a cuboidal mesh superimposed on the simulated MD simulation supercell.	62

5.10	The variation of the electron density from the nucleus for Co, Cr, Fe, Ni, Ti and Al [61].	63
5.11	Radial distribution function of FCC form of Cr, AlCr, CoCr, CrFe, CrNi, CoCrFeNi and AlCoCrFeNi with modified EAM potential for Cr. The y-axis represents the intensity of peak in arbitrary units and x-axis is atomic distance in Å.	64
5.12	The variation of electron density of Cr with original [54] and modified EAM potential (inset shows the variation on log scale) [61].	65
5.13	Configurational entropy for different alloys calculated using 2500 random configurations. The inset in the case of CoCrFeNi and CoCrFeNiTi shows the variation of S_{conf} with temperature for BCC forms to demonstrate its increasing trend.	68
5.14	Specific heat at constant pressure (C_p) for different alloys at range of temperature.	69
5.15	The distribution of configurational energy for different alloys. E_m represents minimum energy among 2500 random configurations, while E_i is energy of i^{th} configuration. Note that energies are for whole supercell. Curves in the figures are fitted Gaussian distributions.	71
5.16	Schematic representation of the aim of the swapping process to ensure that swapping leads to inheritance of information regarding the identity of atom at equivalent positions.	74
5.17	Schematic representation of the swapping in configuration files of parents.	75
5.18	Schematic representation of the swapping process.	76
5.19	Variation of the number of configurations having different energy values with the number of generations in GA sampling [61].	78

5.20	Variation of the first and second term of equation 5.22 with temperature.	82
5.21	Comparison of G_{GA-min} , G_{ideal} and $G_{non-ideal}$ for different alloys with the variation in temperature.	83
5.22	Comparison of probability of the i^{th} child (P_i) to be accepted as parent in the subsequent generation of GA using the approach developed in the present work and calculated from Boltzmann scheme. Note that probability distribution has been calculated for BCC-AlCoCrFeNi and temperature of 300 K was used while calculating the probability for i^{th} child.	85
6.1	Variation of order parameter with configurational energy for various schemes of sampling methodology [101].	95
6.2	Variation of number of cation-cation pairs with their corresponding configurational energy with systematic sampling [101].	96
6.3	Variation of number of cation-cation pairs with their corresponding configurational energy for genetic algorithm based sampling.	97
6.4	Bond-length variation for (a) cation-cation pairs and (b) cation-anion pairs [101].	98
6.5	The radial distribution function ($g(r)$) corresponding to the $Cu^{2+}-O^{2-}$ [101].	98

6.6	Average standard deviation (in Å) for bond-length variation for (a) cation-cation and (b) cation-anion pairs [101]. The average standard deviation was calculated by taking average of the standard deviation of all ionic separation forming a particular oxide-mix. For <i>e.g.</i> , in the case of 5-component mix, <i>i.e.</i> , (Co,Cu,Mg,Ni,Zn)O, average over standard deviation in 15 bond-length including Co ²⁺ -Co ²⁺ , Co ²⁺ -Cu ²⁺ , Co ²⁺ -Mg ²⁺ , Co ²⁺ -Ni ²⁺ , etc are used for calculation of average standard deviation.	99
6.7	Variation in bond-length with increase in number of cations for (a) cation-cation and (b) cation-anion pairs [101].	101
7.1	Schematic representation of the first-order dislocation-solute interaction, redrawn from ref. [113].	106
7.2	(a) Schematic figure of variation of function with $\frac{1}{r}$ and $\frac{1}{r^2}$ and (b) variation of $\ln(r)$ and $-\frac{1}{r}$, which is obtained from integration of $\frac{1}{r}$ and $\frac{1}{r^2}$, respectively. w represents the cut-off parameter defined in the Labusch's theory (equation 7.4).	110
7.3	Schematic representation of dislocation moving in a glide plane, redrawn from ref. [110]. w is the amplitude of the fluctuation of length 2ζ on the dislocation of length L	111
7.4	Schematic representation of energetic barrier associated with dislocation migration and the part of the barrier, which is being considered in the present investigation is marked as ΔE_{1-2} and ΔE_{2-3} , when dislocation moves from 1 to 2 and 2 to 3 respectively.	115

7.5	(a) Edge dislocation inside the face-centred cubic (FCC) lattice in unrelaxed state and (b) Schematic representation of the dislocation inside simulation supercell.	118
7.6	Pressure distribution around dislocation	120
7.7	Determination of number of random configurations need to be sampled.	121
7.8	Representation of random behaviour of random number generator used for MC simulation. The counter in y-axis represents the number of times a particular number is obtained when numbers between 1 to 1000 are generated.	122
7.9	Creation of area (ΔA) on the slip plane due to movement of the dislocation segment.	123
7.10	Constraint imposed to maintain continuity of the dislocation line.	123
7.11	Demonstration of movement of pressure field with movement of dislocation.	123
7.12	Variation in the dislocation velocity with applied stress for different alloy systems. The red line in the case of CoCrFeMnNi shows the value of stress applied for studying dislocation movement.	124
7.13	Energies due to dislocation pressure field and misfit volume of elements for different alloy systems.	126
7.14	(a) Difference between maximum (ΔE_{max}) and minimum (ΔE_{min}) energy for different alloy system and (b) Variation of difference between maximum and minimum energy for binary CoNi and FeNi alloys.	127
7.15	Variation in the rejection fraction for different alloys with temperature.	128

7.16	(a) Comparison of rejection fraction for CoNi, CoFeNi, FeNi, CoCrFeNi and CoCrNi at 77K with intercept of Hall-Petch plot for these alloys from literature [143] and (b) Comparison of rejection fraction for different alloys at 77K with lattice friction stress from literature [138, 144, 145]. .	129
7.17	(a) Variation of rejection fraction with atomic-size mismatch for different alloys (inset shows rejection fraction versus atomic size mismatch with data for FeNi, showing linear dependence) and (b) Variation of difference between maximum and minimum energy possible for different alloys with atomic-size mismatch. The atomic size-mismatch is defined to be the mean of the atomic size-mismatch between different binaries which form the particular multicomponent alloy. Data from Table 7.2 was used. . .	130
7.18	Comparison of lattice friction stress values published in ref. [138, 144, 145] and Hall-Petch plot intercept published in ref. [143] for CoNi, CoFeNi, FeNi, CoCrFeNi and CoCrNi.	131
7.19	Influence of dilute addition of Al into CoCrFeMnNi and CoCrFeNi on rejection fraction.	132
7.20	Snapshots of dislocation line of CoCrNi and CoNi alloys taken at different MC steps.	133
7.21	(a) Variation of velocity of the dislocation in different alloy systems with constant applied stress (σ) and (b) Variation of velocity of the dislocation in different alloy systems with normalised applied stress (σ/G).	135
7.22	(a) Variation of rejection fraction for all alloys and (b) Variation of rejection fraction for all alloys, except CoMnNi and FeNi.	137

7.23	Comparison of rejection fraction of alloys, when calculation is carried with G and ν values taken from ref. [138] (published) and when average values of G and ν are determined from elemental values.	138
7.24	Correlation between rejection fraction and atomic-size mismatch of for all alloys, as shown in Fig. 7.23 with removal of alloy cases of CoMnNi and FeNi.	139
7.25	(a) Variation of roughness of the dislocation line for different alloys with atomic-size mismatch (roughness of the dislocation line is defined to be standard deviation of dislocation from the mid-rib of the dislocation, where the mid-rib is an imaginary straight line from one end to another) and (b) Linear correlation between roughness and atomic-size mismatch for all alloys, when CoMnNi and FeNi are not considered.	140
7.26	The variation of the rejection fraction with the number of random configurations for the CoCrNi alloy.	141
7.27	(a) Variation of rejection fraction for alloys with difference between maximum and minimum energy, when stress is not considered, (b) Correlation between energy difference and the Hall-Petch slope published in ref. [143] for sub-alloy systems forming CoCrFeNi, (c) Variation of rejection fraction with energy difference for different alloys when explicit dislocation movement is considered and stress is applied, and (d) Quadratic variation of rejection fraction with energy difference for sub-alloy systems forming CoCrFeNi.	142
8.1	Schematic representation of alloy formation in Miedema's framework, redrawn from ref. [179].	150

8.2	Mulliken charge on impurity at the centre of the supercell along-with that on first and second nearest-neighbours and on each atom for the CoCrFeNi HEA. The terminology used for naming x-axis is as follows: for <i>e.g.</i> , Cr in Co signifies the case where Cr is added to the supercell of Co.	154
8.3	Comparison of Mulliken charge on impurity, when calculations are being carried out for a matrix with the ground-state structure of the element and with the FCC structure. See text for explanation of the terminology used for naming points on x-axis.	155
8.4	CASTEP energy change associated with introduction of impurity into ground-state structures of various metals plotted with (a) Miedema electronegativity scale and (b) Mulliken charge on impurity.	157
8.5	Comparison of Miedema electronegativity difference and Mulliken charge over impurity.	158
8.6	Comparison of Mulliken charge and Bader charge for different impurity-in-matrix calculations.	158
8.7	Frequency (number of times particular interatomic separations) of different interatomic separation in a BCC matrix. Note that the bin-size for plotting the histogram is 0.02 Å.	160
8.8	Frequency of different bond lengths in FCC and HCP (in the case of Co) matrix. Lower values of frequency in case of HCP-Co in comparison with FCC cases is due to the lower number of atoms in HCP-supercell studied here in comparison with FCC supercell.	161
8.9	Bond length values for the CoCrFeNi with reference to bond-length values of the FCC forms of Co, Cr, Fe and Ni.	162

8.10	Schematic figure of the 2X2X2 supercell with SRO. In this figure red blue and golden spheres represents Co, Cr and Fe atoms, respectively. The atomic radius of atoms represented here not to scale the relative atomic-size difference between atoms.	163
8.11	The frequency of different bond lengths for the FCC-matrix with different combination of atomic species in first nearest neighbour (1NN)	167
8.12	The magnetic moment variation for impurity-in-atom and FCC-CoCrFeNi calculation. Similar terminology as mentioned in Fig. 8.2 is employed here for labelling x-axis.	168
8.13	The influence of magnetism on the force constant at the impurity, first nearest neighbour (First) and second nearest-neighbour (Others) atoms. In this figure, we have compared the force constant on the impurity, first nearest-neighbour and second nearest neighbour atoms calculated with and without spin-polarised calculations.	169
8.14	Magnetic moment distribution in a supercell containing Ni impurity in the FCC-Co matrix.	171
8.15	Distribution of positive and negative magnetic moment for Co in FCC-Cr matrix calculations.	172
8.16	Distribution of positive and negative magnetic moment for Fe in FCC-Cr matrix calculations.	172
8.17	Distribution of positive and negative magnetic moment for Mn in FCC-Cr matrix calculations.	173
8.18	Distribution of positive and negative magnetic moment for Ni in FCC-Cr matrix calculations.	173

8.19	Figure showing (a) electrons with positive spin moment surrounding negative spins and (b) electrons with negative spin moment surrounding positive spins for FCC-CoCrFeNi.	174
8.20	Distribution of electrons with positive moment in a 5X2X2 supercell of FCC-CoCrFeMnNi.	174
8.21	Distribution of electrons with negative moment in a 5X2X2 supercell of FCC-CoCrFeMnNi.	175
8.22	Figure showing (a) electrons with positive spin moment surrounding negative spins and (b) electrons with negative spin moment surrounding positive spins for FCC-CoCrFeMnNi.	175

List of Tables

5.1	Lattice parameter of BCC and FCC forms of alloys used in MD calculations [53].	53
5.2	Lattice parameter of BCC and FCC forms of alloys determined from XRD simulation of start and end of MD simulated structures.	60
5.3	Modified EAM potential parameters for Cr [61]. Other parameters can be found in ref. [54].	64
5.4	Enthalpy of FCC and BCC form of different alloys determined by random sampling of 2500 configurations.	66
5.5	Configurational energy values for elements.	77
5.6	The minimum energy of various alloy cases after sampling using GA-MD scheme and corresponding average energy of the alloy, which is the average of configurational energies of elements, as given in Table 5.5.	78
5.7	Value of $G_{non-ideal}$, G_{GA-min} and G_{ideal} at 0 K, determined by interpolating the variation of $G_{non-ideal}$, G_{GA-min} and G_{ideal} to 0 K.	81
6.1	The values of A , ρ , and C used in equation 6.1 taken from ref. [99,100].	91
6.2	Total number of configurations generated for each solid solution mix [101].	93

6.3	Average standard deviation of the cation-cation separations with different numbers of cations in the configuration [101].	101
7.1	G and ν values for alloys taken from ref. [138] for calculation of energy using equation 7.20.	117
7.2	Atomic radii of elements taken from ref. [41].	117
8.1	The plane-wave cut-off energy and number of k-points obtained after convergence testing	149

Contents

Abstract	ii
Dedication	iv
Acknowledgments	v
Declaration	vi
List of figures	vii
List of tables	xviii
1 Introduction	1
2 Fundamentals of Classical and Statistical Thermodynamics	4
2.1 Introduction to thermodynamics	4
2.1.1 First law of thermodynamics	6
2.1.2 Second law of thermodynamics	8
2.2 Theoretical framework using statistical mechanics	11
2.2.1 Background	11

2.2.2	Boltzmann's distribution	13
2.2.3	Determination of the Boltzmann's factor	15
2.2.4	Partition function and calculation of thermodynamic properties	17
3	Classical Atomistic Simulations	20
3.1	Molecular Dynamics	20
3.1.1	Steps of an MD simulation	24
3.1.2	Ensembles in Molecular Dynamics	26
3.2	Monte Carlo method	28
3.2.1	Need for the Monte Carlo method	29
4	Density Functional Theory	32
4.1	Introduction	32
4.2	The Born-Oppenheimer Approximation	33
4.3	Need for Density Functional Theory (DFT)	33
4.4	Hohenberg-Kohn Theorem [22]	35
4.5	Kohn-Sham Formalism [23]	36
4.6	Exchange-Correlation Functional	38
4.7	Spin polarisation	39
4.8	Bloch Theorem	39
4.9	Pseudopotential	40
4.10	k -point sampling	41
5	Phase Stability in Substitutional Alloys	46
5.1	Introduction	46
5.2	Empirical interatomic potential for Metals	48

5.3	Calculation details	53
5.4	EAM potential validation and modification	54
5.5	MD simulation with random sampling	65
5.6	Development of a hybrid genetic algorithm-MD (GA-MD) method . . .	70
5.7	Gibbs free energy calculation	77
5.8	Extension of GA-MD methodology	81
5.9	Conclusions and future work	86
6	Distortion in high-entropy oxides	88
6.1	Introduction	88
6.2	Simulation details	90
6.3	Sampling methodology	92
6.3.1	Analysis Methods	93
6.4	Results and discussions	94
6.5	Conclusions	102
7	Lattice Friction in Substitutional Alloys	103
7.1	Introduction	103
7.1.1	Solution hardening models	107
7.2	Method	116
7.3	Results and discussions	125
7.3.1	Movement of straight dislocation with no applied stress contribu- tions (approach-1)	125
7.3.2	Explicit dislocation movement with sequential dislocation-segment movement with contributions from applied stress (approach-2) .	133

7.3.3	Comparison between approach-1 and approach-2 for lattice friction determination	136
7.4	Conclusions and future work	141
8	Density Functional Theory calculations on substitutional alloys	144
8.1	Introduction	144
8.2	Charge redistribution and its implications for the enthalpy of mixing calculations	149
8.3	Electron spin distribution and implications to distortion in substitutional alloys	156
8.4	Conclusions and future work	176
9	Concluding remarks	178
	Bibliography	181

Chapter 1

Introduction

In the past decade and half, there has been significant scientific interest in the class of multicomponent alloys with simple crystal structure, also known as ‘*high-entropy alloys (HEAs)*’. Initial efforts in this area were exploratory in nature with an emphasis on discovering alloy compositions which might exhibit a single-phase solid solution. This led to a range of rigorous studies related to finding rules concerning the formation of single-phase solid solutions. In the course of such studies, attractive properties have been achieved in this class of alloys, which were not exhibited by conventional engineering alloys. HEAs have shown simultaneous increase in strength and ductility at low temperatures [1], tunable structural properties [2], resistance against hydrogen embrittlement [3] and even increased in the strength and elongation in the presence of hydrogen [4]. But this claim has been challenged recently [5]. These alloys have also shown irradiation resistance [6, 7]. Apart from this HEAs have exhibited interesting magnetic [8] and functional properties [9]. Such design methodology involving multiple components forming alloys has expanded to oxides [10], nitrides [11], cermats [12], plasticines [13], etc.

In view of the above, the present investigation is concerned with three distinct facets of high-entropy materials. The first facet is phase stability in multicomponent systems, the second aspect studied is related to the distortion in high-entropy systems and lastly, finding computationally a cheap method for the prediction of HEAs with attractive mechanical properties.

The second chapter of this thesis presents the basics of thermodynamics and statistical mechanics, while the third and fourth chapters present the basics of classical and *ab-initio* simulations, respectively. In the third chapter, the fundamentals of both Molecular Dynamics and Monte Carlo are elaborated. In the fourth chapter, the basics of the Density Functional Theory (DFT) have been discussed.

In the fifth chapter, phase stability in HEAs is discussed in detail. In this chapter, a hybrid genetic algorithm-molecular dynamics based approach is discussed, which has been developed in this work for sampling positional-disordered systems. Additionally, the modification of the interatomic potential for components forming multicomponent alloys is presented and ultimately, the influence of the configurational entropy on the phase selection is discussed.

In the sixth chapter, the methodology for sampling HEAs presented in Chapter-5 is extended to multicomponent oxides with a simple rock-salt crystal structure for studying evolution of distortion in the multicomponent system. The variation in the bond-length is presented in terms of the multiplicity of the number of cation species in the high-entropy oxides.

In Chapter-7, a mechanistic understanding of lattice friction using analytical elasticity theory and a Monte Carlo approach is presented for HEAs along with binary and ternary alloys. This chapter also presents a computationally cheap method for throughput screening of alloy compositions with possible attractive mechanical properties.

In Chapter-8, DFT studies with an impurity-in-matrix approach applied to transition metals based systems are reported. The calculated electronic structure is discussed from the perspective of charge-transfer and distortion during alloying. The discussion on charge-transfer aspect centres around the critique of electronegativity scales used for determination of enthalpy of mixing of HEAs, while the second issue concerns the evolution of distortion due to certain elements with emphasis on their magnetism.

* * * * *

Chapter 2

Fundamentals of Classical and Statistical Thermodynamics

2.1 Introduction to thermodynamics

Classical thermodynamics is concerned with the study of the universe as a continuum. This part of the universe, which is being studied is called the '*system*'. Thermodynamics aims to describe the properties of the system in terms of quantities such as the work, that is done by or to the system and heat. The system in the thermodynamical framework can be isolated, closed or open. The isolated system cannot exchange energy or mass with its surroundings. The closed system cannot exchange mass, but it can exchange energy with its surroundings. Open systems can exchange both mass and energy with the surroundings.

The quantification of the situation of the system requires the description of the *state* of the system. The state of the system in the microscopic sense can be defined in terms of the positions, masses, velocities, and degrees of freedom associated with

the particles constituting the system. Knowledge of these parameters would help in determining all the properties of the system. For example, if the system is composed of N spherical particles, where particle α has position r_α and momentum p_α and the interaction among the particles is defined by the pair potential $u(|r_\alpha - r_{\alpha'}|)$, then the hamiltonian of the system (H_Γ) in a particular state may be given as:

$$H_\Gamma = \frac{1}{2} \sum_{\alpha \neq \alpha'} u(|r_\alpha - r_{\alpha'}|) + \sum_{\alpha} \frac{p_\alpha^2}{2m} \quad (2.1)$$

The hamiltonian of all the particles would allow the calculation of all the properties of the system. A more conventional description of the system involves the macroscopic description of the system requiring the description of the macroscopic properties of the system. For a complete description of the system, it is required to define a certain minimum number of variables called *independent* variables. The knowledge of independent variables helps in describing the other dependent properties of the system. The description of the system in terms of these variables provide us with the “*equation of state*”. If we consider the case of constant composition; the knowledge of pressure (P) and temperature (T) in a fixed state would allow us to calculate the volume (V) of the system containing one mole of gas, with the equation of state given by the equation 2.2, as:

$$P \cdot V = R \cdot T \quad (2.2)$$

where, R is the Universal Gas constant. Some of properties of the state are dependent upon the size of the system and are known as “*extensive variables*”, while the properties which are independent of size of the system are termed “*intensive variables*”. Properties such as the volume and entropy represent extensive variables and properties such as

temperature and pressure are examples of intensive variables.

2.1.1 First law of thermodynamics

The first law of thermodynamics originates from the determination of the mechanical equivalence of heat, which involves the understanding of the fact that work done on the system leads to the proportionate increase in the temperature of the system. If the system has no mass and energy exchange with its surroundings, then the total energy of the system is constant. This energy of the system, which is a function of the state of the system is termed the “*internal energy (U)*” of the system. In reality, there is simultaneous involvement of work and heat on the system, which alters the state of the system and it is required to study the effect of heat and work on the internal energy of the system. The convention for assigning a sign to the work and heat being exchanged between a system and its surroundings should be noted. If work is done on the system then the sign is negative and it is positive when work is done by the system. The convention for heat flow involves the assignment of a positive sign if heat is gained (*endothermic process*) and a negative sign if heat flows-out of the system (*exothermic process*). Hence, the inflow of heat leads to an increase in the internal energy, while the work done by the system leads to decrease in the internal energy in the adiabatic process, and simultaneous operation of above-stated processes leads to change in the internal energy, which may be expressed as:

$$\Delta U = q - w \tag{2.3}$$

Equation (2.3) represents the “*First Law of Thermodynamics*”. It should be noted that the internal energy of the system is a state function. State functions are dependent upon

the state, but independent of the path taken to move from one state to another. Another important property of state functions is that the cyclic integral of such properties is zero.

If the system moves from state A with internal energy (U_A) to state B with internal energy (U_B), such that the pressure of the system remains constant (*isobaric process*), then the heat content of the system at constant pressure may be expressed as:

$$q = (U_A + PV_A) - (U_B + PV_B) \quad (2.4)$$

The heat content of the system at a particular state at constant pressure is known as “*enthalpy*”, which is again a state function.

Knowledge of the enthalpy and the internal energy of system allows us to define the “*heat capacity (C)*”. The value of the C is either defined at constant pressure (C_P) or volume (C_V), which may be expressed as:

$$C_P = \left(\frac{\delta q}{dT} \right)_P = \left(\frac{dH}{dT} \right)_P \quad (2.5)$$

$$C_V = \left(\frac{\delta q}{dT} \right)_V = \left(\frac{dU}{dT} \right)_V \quad (2.6)$$

C_P and C_V when divided by the number of moles, provides the “*specific heat capacity*” at constant pressure and volume, respectively. So, the first law of thermodynamics introduces internal energy, enthalpy and specific heat capacity as thermodynamic parameters.

2.1.2 Second law of thermodynamics

The first law of thermodynamics provides us with the understanding of change in the internal energy of the system in the extreme cases when work (w) = 0 and $q = 0$, leading to ΔU being equal to q and $-w$, respectively. But, when $q \neq 0$ or $w \neq 0$ simultaneously occur, it leads to a finite amount of work being done by the system during the change of state of the system. In this scenario, considering a spontaneous process, where a system moves from one state to another, such that heat (q) is produced at the temperature T . Since this process is spontaneous, it is irreversible [14]. The degree of the irreversibility is defined in the terms of q/T , which is called increase in *entropy*, which is the measure of irreversibility of the process. Now, the process of movement of the system from a state to another can be either carried out reversibly or irreversibly.

In the case of an irreversible process, a system passes from one state to another through a continuum of equilibrium states. This process requires an infinitesimally minute amount of driving force, when the system is passing through a continuum of numerous equilibrium states. Attainment of complete reversibility may lead to the infinitesimally slow hopping of the system from one equilibrium state to another, requiring an infinite time for completion of the process. For the irreversible processes, change in the entropy of the system (ΔS_{system}^{re}) may be given as:

$$\Delta S_{system}^{re} = \frac{q_{rev}}{T} \quad (2.7)$$

where q_{rev} is the heat exchanged by system with its surroundings. The positive sign in the above equation signifies heat absorption from surroundings. The total entropy change including entropy change for system and surrounding is equal to zero for reversible processes.

For the irreversible processes, when heat (q) is exchanged between a system and its surrounding, there is inherent degradation of work, which gets converted into the heat ($q_{rev} - q$). So, the change in the entropy of the system undergoing an irreversible process (ΔS_{system}^{irr}), may be expressed as:

$$\Delta S_{system}^{irr} = \frac{q}{T} - \frac{q_{rev} - q}{T} = \frac{q_{rev}}{T} \quad (2.8)$$

The total entropy change for system and surroundings undergoing an irreversible process (ΔS_{total}^{irr}) may be written as:

$$\Delta S_{total}^{irr} = \frac{q_{rev} - q}{T} \quad (2.9)$$

Since, $q_{rev} > q$, as mentioned above, there is the increase in the total entropy. It should also be noted that entropy is a state function and hence change in the entropy when system moves from one state to another is independent of whether process is carried out reversibly or irreversibly. So, an understanding of the above leads to the formulation of the “*second law of thermodynamics*”, as:

1. Change in the entropy for the reversible process can be expressed as $dS = \frac{\delta q}{T}$.
2. In an adiabatic process, the entropy can never decrease and it remains constant for reversible processes and it increases during irreversible processes, as:

$$\sum dS_i = dS_{irr} \quad (2.10)$$

Hence, it can be deduced that spontaneous processes are irreversible and there is increase in the entropy during spontaneous processes. So, in view of these observations,

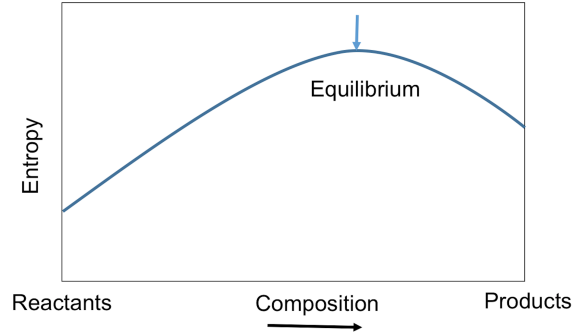


Figure 2.1: Variation in the entropy as reaction progresses, for an isolated system of constant internal energy and constant volume containing both reactants and products. Redrawn from ref. [14].

the equilibrium state of the system can be characterised in term of maximum entropy as shown in Fig. 2.1. Now, combination of the first and the second law of thermodynamics yields the following relation:

$$dU = TdS - PdV \quad (2.11)$$

So, equation 2.11 provides us with the understanding of equilibrium in two scenarios. In the first scenario, when the internal energy and volume are constant, then the entropy is maximised. While in the second scenario, when the entropy and volume are constant, then internal energy is minimised.

As it can be seen from above the variation of S and U as independent variables can help us to study an equilibrium. Controlling S in an experimental set-up is simply impossible. Hence, it is important to rewrite equation 2.11 in terms of intensive variables, which can be controlled easily in an experimental set-up. T and P are chosen as intensive variables, as these parameters can be easily controlled. This lead to the new

function, which is called the “*Gibbs free energy (G)*”, which may be given as:

$$dG = -SdT + VdP \tag{2.12}$$

Thus, the second law of thermodynamics provides the theoretical background of entropy as the main thermodynamic parameter which quantifies the equilibrium of the system. The pragmatic need to express the attributes of equilibrium in terms of experimentally controllable parameters leads to the description of Gibbs free energy.

2.2 Theoretical framework using statistical mechanics

2.2.1 Background

As mentioned above, T and P are convenient independent variables in describing the equilibrium from an experimental point of view. The V and T in constant volume, constant temperature systems are convenient variables in a statistical mechanics framework, as it leads to the quantisation of energy levels (ε), Boltzmann’s factor ($\exp\left(\frac{-\varepsilon}{k_B \cdot T}\right)$) and consequently the partition function of the system [14]. All of these parameters will be discussed in detail below.

The classical thermodynamics discussed in the preceding section provides the description of natural phenomena around us in terms of global variables, which have been derived to quantify the macroscopic properties without any consideration to the microscopic details of the system. Statistical mechanics steps in to find the link between macroscopic properties and the atomic level.

We need to describe the concept of a “*macrostate*” and “*microstate*” before proceeding further. The *macrostate* corresponds to the global state of the system quanti-

fied in terms of state functions such as enthalpy, internal energy, free energy, etc. The particular macrostate can be achieved through numerous microscopic configurations or permutations of particles forming the system. These individual permutations are termed *microstates* of the particular macrostate. Also, there are two basic postulates, which are entombed in the foundations of statistical mechanics:

1. The ergodic hypothesis: It can be stated as “states with equal energy have equal probability of occurrence”.
2. The macrostate with the larger number of microstates will have a larger probability of occurrence.

It is evident that calculation of the number of microstates in each macrostate is the starting point in statistical thermodynamics. Consider a case of arranging n atoms of type A and $(N-n)$ atoms of type B in a total of N lattice sites. The number of microstates (Ω) can be represented by the following permutation formula:

$$\Omega = \frac{N!}{n! \cdot (N-n)!} \quad (2.13)$$

If N is very large, which is the case for materials systems, the calculation of Ω can be a formidable task, .

For large systems, instead of Ω , we choose to deal with $\ln \Omega$ for reasons to be discussed later. The approximate enumeration of the natural logarithm of a number is carried out by *Stirling's approximation* as:

$$\ln n! \simeq n \cdot \ln n - n \quad (2.14)$$

2.2.2 Boltzmann's distribution

Let there be N distinguishable atoms in the system with a total energy, E of the isolated system. Now, this energy will be distributed among all atoms and say n_1 atoms are in energy level ε_1 , n_2 atoms are in energy level ε_2 and so on. Since the system is isolated, then:

$$E = \sum n_i \cdot \varepsilon_i \quad (2.15)$$

$$N = \sum n_i \quad (2.16)$$

So, Ω in this case can be written as:

$$\Omega = \frac{N!}{\prod_i n_i!} \quad (2.17)$$

The most probable macrostate will be the one with the largest number of microstates, *i.e.*, Ω must be maximised. So, taking the natural logarithm of both sides of equation 2.17, we have:

$$\ln \Omega = \ln N! - \sum_i \ln n_i! \quad (2.18)$$

Using Stirling's approximation, we have:

$$\ln \Omega = N \ln N - N - \sum n_i \ln n_i + \sum n_i = N \ln N - \sum n_i \ln n_i \quad (2.19)$$

$$d \ln \Omega = \sum \frac{\partial \ln \Omega}{\partial n_i} dn_i \quad (2.20)$$

Now,

$$\frac{\partial \ln \Omega}{\partial n_i} = -(\ln n_i + 1) \quad (2.21)$$

Then,

$$d(\ln \Omega) = \sum_i -(\ln n_i + 1)dn_i \quad (2.22)$$

Since, the number of atoms are constant, then

$$\sum dn_i = 0 \quad (2.23)$$

$$\sum_i \varepsilon_i \cdot dn_i = 0 \quad (2.24)$$

To maximise $\ln \Omega$, we need to equate $d(\ln \Omega)$ to zero. So,

$$-\sum_i \ln n_i dn_i = 0 \quad (2.25)$$

Simultaneous satisfaction of equations 2.23, 2.24, and 2.25 is required for the maximisation of $d \ln \Omega$. It requires using the Lagrange Method of Undetermined Multipliers. Multiplying α and β with equation 2.23 and 2.24 and adding, we have:

$$\sum_i (\ln n_i + \alpha + \beta \varepsilon_i) dn_i = 0 \quad (2.26)$$

To satisfy the above equation, it is considered that each individual term in the above equation is independent. Hence,

$$(\ln n_i + \alpha + \beta \cdot \varepsilon_i) = 0 \quad (2.27)$$

or,

$$n_i = \exp(-\alpha - \beta \cdot \varepsilon_i) = A \cdot \exp(-\beta \cdot \varepsilon_i) \quad (2.28)$$

The A in the above equation represents $\exp(-\alpha)$ and equation 2.28 represents the equation for Boltzmann's distribution. The main task involves the determination of β , which is the Boltzmann's factor. If we know the value of β , then α can simply be calculated by substituting equation 2.28 in $N = \sum_i n_i$, i.e. A represents the constant for normalisation.

2.2.3 Determination of the Boltzmann's factor

The Boltzmann factor (β) is not a function of the number of particles and energy states in the system, rather it is a function of temperature. Before deriving the value of β , an *unprovable* postulate needs to be considered, i.e., the entropy (S) of the system having a particular number of microstates (Ω) can be expressed as:

$$S = k_B \cdot \ln \Omega \tag{2.29}$$

This is known as the Boltzmann's relation and k_B in this relation is known as Boltzmann's constant and has a value of $1.3807 \times 10^{-23} J \cdot K^{-1}$. The relation between S and Ω can be understood from the fact that S is additive (being an extensive variable), but Ω , which is calculated from probability theory is multiplicative and hence a natural logarithm of Ω needs to be taken so that it may be equated with S .

Now, from the first law of thermodynamics and a reversible process, we know that,

$$dU = dQ - dW \quad \text{and} \quad dQ = TdS \tag{2.30}$$

From the statistical mechanics perspective, the internal energy can be written as:

$$U = \sum_i \varepsilon_i \cdot n_i \quad (2.31)$$

A change in the internal energy (dU) is due to a change in both energy states and the number of particles occupying those states, which can be given as:

$$dU = \sum_i \varepsilon_i dn_i + \sum_i n_i d\varepsilon_i \quad (2.32)$$

The first term in the above equation involves keeping the energy level the same, while changing the number of particles occupying the energy state, which implies that the number of microstates is being changed leading to a change in the entropy (dS). Hence, it can be considered to be equivalent to dQ . The second term corresponds to varying the number of energy states, while keeping the number of particles occupying these states to be constant. This can be understood in terms of application of mechanical work on the system leading to a change in the potential well of the particles, causing the change in the energy state. Hence, the second term in equation 2.30 corresponds to the second term in equation 2.32.

Considering the case, where no work is being done, then we have:

$$dQ = \sum_i \varepsilon_i dn_i = TdS \quad (2.33)$$

Using equation 2.29 in the above equation, we have:

$$Td(k_B \ln \Omega) = \sum_i \varepsilon_i dn_i \quad (2.34)$$

Using equation 2.22, in the above equation, and substituting the value of n_i from equation 2.28, we have:

$$-k_B T \sum_i \ln n_i dn_i = -k_B T \sum_i (-\alpha - \beta \cdot \varepsilon_i) dn_i \quad (2.35)$$

The $-k_B T \cdot \sum_i (-\alpha) dn_i$ terms equate to zero, as $\sum_i dn_i = 0$. Thus,

$$k_B T \sum_i \beta \varepsilon_i dn_i = \sum_i \varepsilon_i dn_i \quad (2.36)$$

or,

$$\beta = \frac{1}{k_B T} \quad (2.37)$$

2.2.4 Partition function and calculation of thermodynamic properties

Since, we know the expression for β , we can introduce it into the expression for U , as given by equation 2.31, we have:

$$U = \sum_i \varepsilon_i \cdot \exp\left(\frac{-\varepsilon_i}{k_B T}\right) \quad (2.38)$$

The i in the above equation, represents the particular microstate. As, can be seen from the above expression, $\sum_i \exp\left(\frac{-\varepsilon_i}{k_B T}\right)$ is one of most important quantities for the determination of other thermodynamic quantities from a statistical mechanics framework. This term is known as the “*partition function*”. So,

$$Q = \sum_i \exp\left(\frac{-\varepsilon_i}{k_B T}\right) \quad (2.39)$$

The value of Q provides all the information about the energy states, which are accessible to the system at a particular temperature. It can be seen from equation 2.39 that the higher the temperature, the larger the number of states accessible and *vice-versa*. The lowest value Q can have is one at absolute zero, implying that the system can only be in its ground state. The value of Q additionally provides the spacing between energy levels, which in turn is defined as a function of β . With the knowledge of Q , enthalpy (H) and the free energy (G) can be expressed as [15]:

$$H = \frac{\sum_i -\varepsilon_i \cdot \exp\left(\frac{-\varepsilon_i}{k_B T}\right)}{Q} \quad (2.40)$$

We can calculate the probability of occurrence (p_i) of state i with energy ε_i as:

$$p_i = \frac{\exp\left(\frac{-\varepsilon_i}{k_B T}\right)}{Q} \quad (2.41)$$

With knowledge of p_i , S can be calculated from the following expression:

$$S = -k_B \sum_i p_i \cdot \ln p_i \quad (2.42)$$

S calculated from equation 2.42 and from $S = \frac{H-G}{T}$ should be the same provided that we know about all possible microstates and their corresponding energies. Often, this is impractical in calculations. Hence, an average over known microstates is performed and convergence with respect to thermodynamic properties are determined. So, the

equation for G can be rewritten as [16,17]:

$$G = k_B T \cdot \ln I - k_B T \cdot \ln \left(\frac{\sum_{i=1}^{I'} \left(\exp \frac{-\varepsilon_i}{k_B T} \right)}{I'} \right) \quad (2.43)$$

while I in the above equation represents the total number of possible microstates and I' is the number of microstates that are sampled in the particular calculations. The first term of equation 2.43 is an ideal term, while the second term provides the information about deviation from ideality. The detailed description of equation 2.43 will be provided in section 5.7.

* * * * *

Chapter 3

Classical Atomistic Simulations

3.1 Molecular Dynamics

Molecular Dynamics (MD) simulation provides the time evolution of the positions of atoms as a result of the solution of the classical equation of motion, where the atoms are considered to be behaving like hard spheres and following Newtonian mechanics. Classical MD has wide applicability for the many-body problem, where neither an analytical solution is possible, nor quantum mechanics based time dependent methods are available. Thermodynamic properties in such simulations are calculated through the Maxwell-Boltzmann scheme.

The description of the motion of an individual particle, when force (F) acts on it can be expressed with Newton's second law of motion:

$$F = ma \tag{3.1}$$

where m is the mass of the particle and a is the acceleration of the particle due to the application of force, F .

The velocity of particle i at time τ can be given as:

$$v_i(\tau) = v_i(0) + \int_0^\tau \frac{dv_i}{dt} dt \quad (3.2)$$

So, if the initial velocity is known then the velocity at any time (τ) can be calculated by integration. The position at time τ can be similarly calculated using the following relation:

$$r_i(\tau) = r_i(0) + \int_0^\tau v_i(t) dt \quad (3.3)$$

As the particle changes its position, the potential experienced by it gets modified leading to a change in the force experienced by it. Hence, the crucial task in MD simulation involves the integration of the equation of motion to obtain the continuous trajectories of the particles.

The integration algorithms use the Taylor series to determine positions and dynamic properties, such as velocities, acceleration, etc., as:

$$r(t + \delta t) = r(t) + \delta t \cdot v(t) + \frac{1}{2} \delta t^2 a(t) + \frac{1}{6} \delta t^3 \cdot b(t) + \frac{1}{24} \delta t^4 \cdot c(t) + \dots \quad (3.4)$$

$$v(t + \delta t) = v(t) + \delta t \cdot a(t) + \frac{1}{2} \delta t^2 \cdot b(t) + \frac{1}{6} \delta t^3 \cdot c(t) + \dots \quad (3.5)$$

$$a(t + \delta t) = a(t) + \delta t \cdot b(t) + \frac{1}{2} \delta t^2 \cdot c(t) + \dots \quad (3.6)$$

where r represents position, while v , a , b , and c are first, second, third and fourth derivative of r respectively. Among various integration schemes, the *Verlet algorithm* is most widely used MD integration algorithm. It uses the position (\mathbf{r}) and acceleration

at time, t and position at the previous step ($r(t - \delta t)$) to calculate the position at time, $t + \delta t$, as:

$$r(t + \delta t) = r(t) + \delta t \cdot v(t) + \frac{1}{2} \delta t^2 \cdot a(t) + \dots \quad (3.7)$$

$$r(t - \delta t) = r(t) - \delta t \cdot v(t) + \frac{1}{2} \delta t^2 \cdot a(t) + \dots \quad (3.8)$$

Adding both of the above equations, we have:

$$r(t + \delta t) = 2r(t) - r(t - \delta t) + \delta t^2 \cdot a(t) \quad (3.9)$$

The velocity at time, $t + \delta t$ can be calculated as:

$$v(t + \delta t) = [r(t + \delta t) - r(t - \delta t)] / 2\delta t \quad (3.10)$$

Additionally, it should be noted that errors in the interpolation of the next point would be fourth order in the time-step, which implies that a trajectory calculated using the Verlet algorithm would be more accurate than by integration of the Taylor series, which has odd order terms in it. Also, this integration is computationally straightforward with limited memory requirements, *i.e.*, only $r(t)$, $r(t - \delta t)$ and $a(t)$ need to be stored. But, it has certain limitations as well:

1. $r + \delta t$ is obtained by adding small term ($\delta t^2 a(t)$) to a large term, *i.e.*, $[2r(t) - r(t - \delta t)]$. So there is loss of precision in determination of position.
2. It is difficult to obtain the velocities and which are only available when the position in the next step has been determined.
3. Since, the position at time, $t + \delta t$ can only be determined if $r(t)$ and $r(t - \delta t)$ is known, at time, $t = 0$, the Taylor series needs to be initially employed.

To overcome the problems in Verlet algorithm, several algorithms have been proposed. The first one of these is the “*leap-frog algorithm*”. In the leap-frog algorithm, the velocity at time, $t+\delta t/2$ is determined from the velocity at time, $t-\delta t/2$ and acceleration at time, t , as:

$$v(t + \delta t/2) = v(t - \delta t/2) + \delta t \cdot a(t) \quad (3.11)$$

From the value of the velocity at time, $t + \delta t/2$, the position at time, t is calculated using following equation:

$$r(t + \delta t) = r(t) + \delta t \cdot v(t + \delta t/2) \quad (3.12)$$

Then, the velocity at time. t is calculated as:

$$v(t) = \frac{1}{2}[v(t + \delta t/2) - v(t - \delta t/2)] \quad (3.13)$$

So, in this algorithm, velocities ‘*leap-frog*’ over position to determine the velocities at time, $t + \delta t/2$, which in turn is used to calculate values of positions at $t + \delta t$, and so on. It has following advantages/disadvantages over Verlet algorithm:

1. The leap-frog algorithm deals with the velocities and hence does not require calculation of differences between large numbers, as required in the Verlet algorithm.
2. It is not possible to calculate the kinetic energy contribution of the total energy, as the positions and velocities of particles are still not calculated simultaneously.

Another algorithm is the “*velocity-verlet algorithm*”, which uses a three stage process.

In the first step, position at time, $t + \delta t$ is calculated as:

$$r(t + \delta t) = r(t) + \delta t \cdot v(t) + \frac{1}{2} \delta t^2 \cdot a(t) \quad (3.14)$$

In a second step, velocities at time, $t + \delta t/2$ are then calculated as:

$$v(t + \delta t/2) = v(t) + \frac{1}{2} \delta t \cdot a(t) \quad (3.15)$$

In the last step, forces are then computed from position at time, $t + \delta t$ to calculate the acceleration at the same time and thus using $a(t)$ and $a(t + \delta t)$, velocity at time, $t + \delta t$ can be calculated by using following equation:

$$v(t + \delta t) = v(t + \delta t/2) + \frac{1}{2} \delta t \cdot a(t + \delta t) \quad (3.16)$$

3.1.1 Steps of an MD simulation

The main steps in a MD simulation are:

1. **Initialisation:** Initial particle configurations are generated either from experimental or theoretical work. Initial velocities of particle are determined using the Maxwell-Boltzmann distribution, which is represented as:

$$p(v_{ix}) = \sqrt{\frac{m_i}{2\pi k_B T}} \cdot \exp\left(\frac{-1}{2} \frac{m_i v_{ix}^2}{k_B T}\right) \quad (3.17)$$

where m_i and v_{ix} are the mass and velocity of i^{th} particle respectively, while T is the temperature of the system.

To ensure zero total momentum of the system, the total linear momentum of the system along the x, y and z directions is calculated, which is subsequently divided

by the total mass of the system. These quantities are then subtracted from the atomic velocities to ensure there is zero overall momentum.

2. **Force calculation:** Calculation of the force on individual atoms by differentiation of the potential field. The detailed discussion on the potential field will be carried out in section 5.2.
3. **Integration of equation of motion:** The third step involves the calculation of atomic motion using the integration algorithms mentioned in the preceding section.

Before going to the final step of the MD calculation, when the thermodynamic properties of the system can be calculated, an ‘*equilibration*’ needs to be carried out. In this phase of the calculation, the velocities are monitored to ensure they are equally distributed along the x, y, and z directions. Another important consideration is that the temperature of the system is the desired temperature (T_{de}), which is fixed by the Maxwell-Boltzmann distribution. It should be noted that the temperature of a MD simulation (T_c) can be expressed as:

$$T_c = \frac{2}{(3N - 3) \cdot k_B} \cdot \langle KE \rangle \quad (3.18)$$

where, $\langle KE \rangle$ is the average kinetic energy per particle, while $(3N - 3)$ represents number of degree of freedoms. Now, to ensure that T_c is equal to T_{de} , kinetic energy is simply removed or added from the system by adding a parameter ‘ s ’ in the expression of kinetic energy as:

$$KE(t) = \frac{1}{2} \sum_i m_i |s \cdot v_i(t)|^2 \quad (3.19)$$

The s in the above equation is $\sqrt{\frac{T_{de}}{T_c}}$. This technique is termed “*velocity rescaling*”. It should be noted that after the equilibration stage, temperature is a variable of the system.

4. The last stage involves the calculation of thermodynamic properties of the system.

Steps (2-4) are repeated for a number of cycles, depending on the convergence criteria for the particular calculations. Another important consideration for MD calculations involves the boundary conditions. Most of the MD simulations are carried out using periodic boundary conditions (PBC), which implies that each end of the system being simulated is connected to the opposite end of the system. Usage of PBC leads to the situation in which a system becomes pseudo-periodic with no surface. Also, correlations in space beyond half of the cell-width become artificial and for this reason, a cut-off in MD simulations need to be less than half of the cell-width.

3.1.2 Ensembles in Molecular Dynamics

Each frame of the MD simulation represents a microstate of the microcanonical ensemble, *i.e.*, NVE ensemble, as the energy (E), volume (V) and number of the particles (N) are constant. Calculations are carried out with the assumption that the time average of the properties over the course of the simulation is equal to the ensemble average, in view of energy conservation. This is the reason that while calculating thermodynamic properties, frames in equilibration stages are not used as energy is exchanged with surroundings to maintain constant temperature.

The MD simulation can be carried out with an NVT or NPT ensemble depending upon the property of interest, which need to be calculated. A constant temperature MD simulation would be required in the scenario, if the effect of temperature on the physical

process needs to be studied and additionally this can be close to real world situation, where phenomena might be taking place at constant temperature. As we have mentioned in equation 3.18, T is related to the kinetic energy of the system, which in turn depends upon the velocities of the particles constituting the system. Hence, the simplest way to control the temperature of the system is to multiply the velocities at each time-step by a λ factor, which may be expressed as:

$$\lambda = \sqrt{\frac{T_{de}}{T_c}} \quad (3.20)$$

where, T_{de} is the desired temperature and T_c is the temperature at end of particular time-step. This process of velocity rescaling may lead to an inhomogeneous energy distribution in the system. This problem can be solved by employing the *extended system method*, which considers the heat reservoir to be an integral part of the system. The thermal reservoir has an additional degree of freedom (' s '). The potential energy of the reservoir is given as $(f + 1)k_B T \ln s$, where f is the degree of freedom associated with the system. The kinetic energy of the reservoir is expressed as $\frac{Q}{2} \cdot \left(\frac{ds}{dt}\right)^2$. Q is a fictitious mass and can be considered an extra degree of freedom. The value of Q determines the coupling of the system and reservoir and it governs the temperature fluctuations. The velocity v_i and time-step (δt) in the 'real' system are related to the velocity $\frac{dr_i}{dt}$ and time-step ($\delta t'$) in the extended system with an additional degree of freedom (s) by $v_i = s \cdot \frac{dr_i}{dt}$ and $\delta t = s \cdot \delta t'$, respectively. The detailed description of this scheme is beyond the scope of present study and can be found elsewhere [18–21].

Constant pressure MD calculations might be carried out to study the pressure-induced physical phenomena or to reproduce the physical phenomena taking place at constant temperature-constant pressure leading to the need for the isothermal-isobaric ensemble.

The pressure of the system can be kept constant by varying its volume and a similar approach is employed in the isothermal-isobaric ensemble. The volume variation is related to the isothermal compressibility (κ) as:

$$\kappa = \frac{1}{V} \cdot \left(\frac{\partial V}{\partial P} \right) \quad (3.21)$$

A larger value of κ for substance implies that the material is easier to compress and *vice-versa*. In NPT MD simulations, volume change can be introduced in either all directions or along one of direction. The pressure control methods are analogous to temperature control methods, as discussed in the earlier section. In extended coupling schemes, an extra degree of freedom is added associated with the volume of the box. The degree of freedom can be understood as a fictitious piston. The kinetic energy associated with this piston is $\frac{1}{2}Q \left(\frac{\partial V}{\partial t} \right)^2$, while its potential energy is PV , where P is the required pressure and V is the volume of the system. Q represents the mass of the fictitious piston, where lower mass allows rapid oscillation of volume and *vice-versa*. The net volume of the system is determined by the internal pressure and desired external pressure of the system.

3.2 Monte Carlo method

The Monte Carlo (MC) simulation methodology involves random sampling of phase space to calculate thermodynamic properties of the system. As we have seen in our discussions in Chapter-2 on fundamentals of classical thermodynamics and statistical

mechanics, the macroscopic property of the system may be expressed as:

$$\langle A \rangle = \frac{\int dp_N dr_N A(p_N, r_N) \exp(-\beta H(p_N, r_N))}{\int dp_N dr_N \exp(-\beta H(p_N, r_N))} \quad (3.22)$$

The β in the above equation is equal to $\frac{1}{k_B T}$ and A is expressed in terms of momentum (p) and position (r). So, calculation of the average of a function, which depends on momenta of particles is comparatively easy and can be done analytically, if hard constraints are not applied (see section 3.1 and 11.2.1 of source-3 for details). While, if the function depends on position, the multidimensional integral over particles is computationally tricky.

3.2.1 Need for the Monte Carlo method

The MC method is employed to determine the value of multidimensional integrals. Consider the curve shown in Fig. 3.1 and the area under the curve, as shown by the hatched region. Random points are generated and recorded as being in the area of curve or outside it. The area under the curve is then determined by multiplying the area of the full box by the ratio of points lying in the hatched region to the number of points lying outside the hatched region. A similar approach can be used to calculate the partition function of the system containing N atoms, which involves the following steps:

1. Generate a random configuration of particles.
2. Calculate the potential energy ($E(r^N)$) of the random configuration generated in step-1.

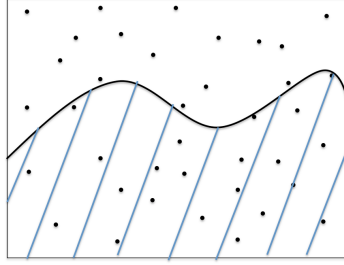


Figure 3.1: Calculation of area under curve using MC algorithm, redrawn from source-2.

3. After a number of iterations (say ‘ x ’), the average value of E is given as:

$$\langle E(r^N) \rangle = \frac{\sum_{i=1}^x E_i(r^N) \exp\left(\frac{-E_i(r^N)}{k_B T}\right)}{\sum_{i=1}^x \exp\left(\frac{-E_i(r^N)}{k_B T}\right)} \quad (3.23)$$

It should be noted that the above strategy is efficient for systems which have clearly delineated energy gaps. Thus, this scheme is not feasible, where a large number of configurations have a negligible contribution to the partition function, due to their high energy. To solve this issue, we must sample only those configurations, which have higher probability of occurrence due to their being low energy states. Such a sampling strategy is known as “*Importance sampling*”. In the importance sampling methodology, the system is biased towards the generation of configurations which have a significant contribution to the integral, most commonly employed in the “*Metropolis method*”. In Metropolis MC scheme, different configurations are generated with a probability equal to $\exp\left(\frac{-E(r^N)}{k_B T}\right)$ and subsequent counting is uniform. Contrastingly, in conventional MC, occupation of each state is given by the same probability and we apply statistical mechanics after all the states are identified. The Metropolis MC assumes the states

follow a Markov chain of events. Another consequence of the Metropolis algorithm is the reversibility of events, where reversibility depends on the difference in the energy of two events (say A and B), *i.e.*,

$$\frac{P_{AB}}{P_{BA}} = \exp\left(-\frac{E(r^N)_B - E(r^N)_A}{k_B T}\right) \quad (3.24)$$

As it is evident from above that the Metropolis MC scheme simulates ‘static’ possibilities of the system and hence it cannot model time evolution.

Now, the application of particular simulation scheme is dependent upon the problem of interest. MD is mostly suitable for problems where time-dependent properties need to be calculated. MC is more suitable for isothermal-isobaric ensemble systems in comparison with the MD method. MD and MC have their own capabilities and limitations for the exploration of phase space. MC is more suitable when global phase space needs to be sampled efficiently. MD is appropriate in the case, when local phase space need to be explored.

Sources

1. Lecture notes of Molecular Simulation Summer School, University of Manchester, 2015.
2. Andrew R. Leach, Molecular Modelling - Principles and Applications, Second edition, Pearson Prentice Hall, 2001.
3. Daan Frenkel and Berend Smit, Understanding Molecular Simulation - From Algorithms to Applications, Second Edition, 2002.

* * * * *

Chapter 4

Density Functional Theory

4.1 Introduction

The aim of first-principles calculations is the determination of the physical properties of a material using only quantum mechanical principles. Considering a system containing multiple electrons and nuclei, the N-body Schrödinger's equation can be written as:

$$\left(-\frac{\hbar^2}{2m}\nabla^2 + \frac{1}{2}\frac{e^2}{4\pi\epsilon_o}\sum_{i\neq j}\frac{1}{|r_i - r_j|} - \frac{e^2}{4\pi\epsilon_o}\sum_{i,I}\frac{Z_I}{|r_i - R_I|} + \frac{1}{2}\frac{e^2}{4\pi\epsilon_o}\sum_{I\neq J}\frac{Z_I Z_J}{|R_I - R_J|} \right) \psi(r_1, r_2, \dots, r_N) = E\psi(r_1, r_2, \dots, r_N) \quad (4.1)$$

The first term in the above equation is the kinetic energy contribution (T_e), the second, third and fourth terms represent electron-electron (V_{ee}), electron-nuclei (V_{en}), and nuclei-nuclei (V_{nn}) Coulombic interactions respectively.

4.2 The Born-Oppenheimer Approximation

One of the first approximations involves the consideration that electronic motion is considerably faster than nuclear motion and hence electronic and nuclear motions can be considered to be decoupled, so the coordinates of the nuclei enter as parameters in Schrödinger equation for electrons. The Schrödinger's equation can also be represented as:

$$H\psi(R_i, r_N) = E\psi(R_i, r_N) \quad (4.2)$$

The above equation implies that the wave function is both a function of electronic and nuclear coordinates. So, Schrödinger's equation is solved for electrons with consideration that nuclear coordinates (R_i) are fixed and hence, $\psi_e(r_N; R_i)$ is the solution of following equation:

$$(T_e + V_{ee} + V_{eN})\psi_e(r_N; R_i) = E_e\psi_e(r_N; R_i) \quad (4.3)$$

and in the last step, Schrödinger equation for the nuclei can be solved, which may be expressed as:

$$(T_N + V_{NN} + E_e)\psi_N(R_i) = E_N\psi_N(R_i) \quad (4.4)$$

So, it can be seen that energy eigenvalue corresponding to a electrons is one of the parameter in Schrödinger equation for nuclei.

4.3 Need for Density Functional Theory (DFT)

The *ab-initio* theories are mainly divided into two categories; wave-function based theories and functional theories. In wave-function based methods, calculations are carried

out using a many-body wave-function. Such calculations can be carried out for arbitrary accuracy with proportionate computational demand and hence these methods are adequate for small molecules.

In view of this, functional methods are appropriate for solving quantum mechanical equations for bulk solids. In functional theories, the total energy of the system is expressed in terms of a certain quantity (which will be discussed shortly) and minimisation of the energy with respect to this quantity is carried out to determine the ground-state of the system. Note that such methods of determination of the ground-state stems from the well known ‘*variational principle*’, which considers that the ground-state energy is a minimum for the true wave-function.

Now the quantity of interest mentioned above with which total energy needs to be minimised can be the probability of finding N electrons at position r_1, r_2, \dots, r_N , which may be expressed as a product of ψ and ψ^* for each electron. Addition of $\psi^*(r_1, r_2, \dots, r_N)\psi(r_1, r_2, \dots, r_N)$ for N electrons yields the electron density, $n(r)$, which may be written as:

$$n(r) = 2 \sum_{i=1}^N \psi^*(r)\psi(r) \quad (4.5)$$

The factor 2 in above equation signifies the fact that Pauli’s Exclusion principle allows two electrons to have a particular spatial wave-function, provided they have different spin. Note that the definition of $n(r)$ only requires knowledge of three coordinates of a point.

4.4 Hohenberg-Kohn Theorem [22]

The DFT approach is based upon the two Hohenberg-Kohn theorems and the Kohn-Sham framework. The first Hohenberg-Kohn theorem can be explained as: “*The minimum or ground-state energy as calculated from Schrödinger equation is an unique functional of the electron density*”. It implies that there is one-to-one correlation between the electron density and the ground-state electronic wavefunction. Hence, the energy of the system can be represented as a functional of electron density, *i.e.*, $E[n(\mathbf{r})]$. The remarkable consequence of the first Hohenberg-Kohn theorem is that the Schrödinger’s equation can be solved in terms of the electron density, which is a function of three spatial coordinates, rather than the electron wavefunction, which is a function of $3N$ variables (where, N is the number of electrons in the system). Though, the first Hohenberg-Kohn theorem shows that the electron density can be used to solve the Schrödinger equation, it does not explain the property or identity of that functional.

The second Hohenberg-Kohn theorem can be stated as: “*The true electron density from the solution of Schrödinger’s equation is same as the electron density, which minimises the energy functional of the system*”. So, the second Hohenberg-Kohn theorem opens up the possibility that if a ‘true’ functional form is known, then using the variational principle, the energy can be minimised with respect to the functional to find the equilibrium electron density. Additionally, it should be noted that the second Hohenberg-Kohn theorem is analogous to the variational principle defined for wavefunction based methods.

Now, the energy functional ($E[n(r)]$) may be written as:

$$E[n(r)] = T[n(r)] + E_{ne}[n(r)] + E_{ee}[n(r)] \quad (4.6)$$

where, $T[n(r)]$ is the kinetic energy, $E_{ne}[n(r)]$ is the energy due to nuclei-electron interaction, while $E_{ee}[n(r)]$ is the electron-electron interaction term, which may be given as:

$$E_{ne}[n(r)] = - \sum_i \int \frac{Z_i n(r)}{|R_i - r|} \quad (4.7)$$

The $E_{ee}[n(r)]$ has two contributions; first is the Coulomb term ($J[n(r)]$) and second is the exchange term ($K[n(r)]$). $J[n(r)]$ is expressed as:

$$J[n(r)] = \frac{1}{2} \int \int \frac{n(r)n(r')}{|r - r'|} dr dr' \quad (4.8)$$

It can be seen that in equation 4.6, $T[n(r)]$ and $K[n(r)]$ are unknown. Modelling these two parameters poses a significant challenge and in view of that the Kohn-Sham formalism is useful in terms of providing a solution.

4.5 Kohn-Sham Formalism [23]

In the Kohn-Sham formalism, the kinetic energy functional is split into terms containing the kinetic energies of non-interacting electron (T_{KS}) and a correction term for the effect of electron interaction. T_{KS} may be expressed as:

$$T_{KS} = -\frac{1}{2} \sum_i \langle \phi_i | \hat{T} | \phi_i \rangle \quad (4.9)$$

where \hat{T} is equal to the $-\frac{\hbar^2}{2m} \nabla^2$. The above equation represents the kinetic energy of a fictitious ensemble of non-interacting electrons, which are mathematically represented

in terms of orbitals (ϕ), which can be used to reconstruct the electron density as:

$$n(r) = \sum_i |\phi_i|^2 \quad (4.10)$$

Note that, replacing the density of a system with interacting particles with the density of a system of non-interacting particles is the essence of DFT. The Kohn-Sham equation can be represented as:

$$\left[-\frac{\hbar^2}{2m} \nabla^2 + V(r) + V_H(r) + V_{XC}(r) \right] \psi_i(r_i) = E_i \psi(r_i) \quad (4.11)$$

Comparison of the above equation with equation 4.1 yields the observation that there are no summations in equation 4.11. This can be understood by the fact that the solution of the Kohn-Sham equation is a single-electron wavefunction, which is only dependent upon three spatial coordinates. In the left hand side of equation 4.11, $V(r)$ is the Coulombic interaction between the electrons and nuclei, $V_H(r)$ is the ‘*Hartree potential*’ and it can be expressed as:

$$V_H(r) = e^2 \int \frac{n(r')}{|r - r'|} d^3r' \quad (4.12)$$

$V_H(r)$ describes the electron-electron interaction in the system or Coulombic repulsion between the electron and the electron density that describes all the electrons in the system. Since the electronic density has a contribution from all electrons constituting the system, $V_H(r)$ includes ‘unphysical’ self-interactions. The correction of self-interaction is included in the V_{XC} term, which is known as the “*exchange-correlation potential*”. V_{XC} is a functional derivative of the exchange-correlation energy (E_{XC}). It is evident from the above that the solution of the Kohn-Sham equation requires knowledge of

$V_H(r)$, which can be determined from $n(r)$. $n(r)$ can be determined from the single-electron wavefunction, which in turn requires solving the Kohn-Sham equation. So, the Kohn-Sham equation must be solved in a self-consistent manner by using the following steps:

1. Guess the trial electron density ($n(r)$).
2. Solve Kohn-Sham equation using $n(r)$ to determine $\psi_i(r)$.
3. Calculate electron density ($n_{KS}(r)$) corresponding to $\psi_i(r)$.
4. Compare $n_{KS}(r)$ and $n(r)$ and if the difference between them is considerably large, update $n(r)$ and go to step-2.

4.6 Exchange-Correlation Functional

As it has been mentioned in the preceding section, the exchange-correlation functional contains information about the correction for the kinetic energy contribution and for self interaction due to electron-electron repulsion. But, an exact form of this functional is unknown. It can be only derived for the limiting case of uniform electron distribution and thus a range of exchange-correlation functionals have been proposed.

The first one of these is the ‘*local density functional (LDA)*’. In this approximation, it is assumed that uniform electron distribution exists locally and the electron-correlation energy per particle is a function of electron density alone. A more advanced approximation than the LDA is the ‘*generalised gradient approximation (GGA)*’. In the GGA, the gradient of electron density is additionally employed. The GGA is mostly employed for metals, as it has been shown to predict properties accurately. There are

further advanced approximations which are described elsewhere and are not relevant for the present work.

4.7 Spin polarisation

So far, we have not discussed the effect of electron spin. Incorporation of spin polarisation in DFT calculations is carried out by defining an exchange-correlation functional for each spin (up and down). So, the presence of spin leads to two separate hamiltonians, which need to be solved simultaneously via the self-consistent framework depicted earlier. Note that two hamiltonians cannot be solved separately as the solution of each hamiltonian should generate a Kohn-Sham orbital corresponding to that particular spin, but that hamiltonian itself depends on the total density ($n(r) = n_{\uparrow}(r) + n_{\downarrow}(r)$), as shown below:

$$\hat{H}_{KS}^{\uparrow} = -\frac{1}{2}\nabla^2 + V(r) + V_H[n](r) + V_{XC}[n_{\uparrow}](r) \quad (4.13)$$

$$\hat{H}_{KS}^{\downarrow} = -\frac{1}{2}\nabla^2 + V(r) + V_H[n](r) + V_{XC}[n_{\downarrow}](r) \quad (4.14)$$

4.8 Bloch Theorem

If nuclei in the system are arranged periodically then their potential and the density also exhibits a similar periodicity. But the wavefunction which is complex in nature shows quasi-periodicity. Bloch's theorem allows the representation of the electron wavefunction ($\psi_k(r)$) as:

$$\psi_k(r) = u_k(r) \exp ik \cdot r \quad (4.15)$$

$u_k(r)$ can be any suitable mathematical function and should have the periodicity of the supercell. Since, the crystal is considered to be periodic, $u_k(r)$ is represented as a three dimensional Fourier series, :

$$u_k(r) = \sum_G c_{GK} \exp i(G + k) \cdot r \quad (4.16)$$

Ideally, the number of k -points and G vectors should be infinite, but since the wavefunction changes very slowly with k , the change in wavefunction is negligible when k -points are close to each other and a finite number of k -points is needed to model the system.

The exact representation of the wavefunction requires an infinite number of G -vectors, which is computationally intractable. But, c_{GK} becomes smaller as $|G|^2$ is larger, hence a finite number of G -vectors is used in plane-wave DFT calculations as defined by a cut-off energy (E_{cut}) as:

$$E_{cut} = \frac{\hbar^2}{2m} |G|^2 \quad (4.17)$$

4.9 Pseudopotential

The electrons near the nucleus (core electrons) do not influence the chemical properties and simply repel valence electrons. So, they can be ignored, owing to their limited role in determining interactions between atoms. Additionally, it should be noted that rapid fluctuations in the wavefunction takes place due to core electrons, which requires large G components to describe, adding computational cost. Hence, the core electrons and nucleus are combined and the Coulomb potential is replaced with a ‘weaker’ potential, this modified potential is termed a *pseudopotential*. This leads to an absence of rapid fluctuations in ψ allowing a smaller value of G and a consequently lower value of E_{cut}

(Fig. 4.1). The charge density from both the wavefunction and pseudo-wavefunction should be same for an accurate determination of exchange-correlation energy (*norm-conserving condition*). This was main idea behind ‘*norm-conserving pseudopotentials*’. This condition may be expressed as:

$$\int_0^{r_c} \psi_{true}^*(r)\psi_{true}(r)dr = \int_0^{r_c} \psi_{pseudo}^*(r)\psi_{pseudo}(r)dr \quad (4.18)$$

But this method is not suitable for valence p -orbitals of electronegative first row elements and for d -orbitals of first row transition metals, where the pseudo-wavefunction is not significantly smoother than the all-electron wavefunction. In view of this, the ultra-soft pseudopotential has been defined, where the norm-conserving condition is relaxed.

4.10 k -point sampling

As mentioned earlier, ideally an infinite number of k -points would be used to describe the wavefunction, but this is computationally intractable. Hence, finite number of k -points are employed. The properties from DFT calculations are often determined using integration over k -space in the Brillouin-zone. The Brillouin zone (BZ) is the Wigner-Seitz cell in the reciprocal lattice of the real crystal. It should be noted that k -points here means the sampling points in first BZ. The coordination of points in reciprocal space are different from their coordination in real space. For example, the reciprocal lattice of the BCC lattice structure exhibits the FCC coordination, while for the FCC lattice structure, the reciprocal lattice has the BCC coordination. Figure 4.2 shows the first BZ for the FCC structure. Integration over this BZ to obtain any ground-state

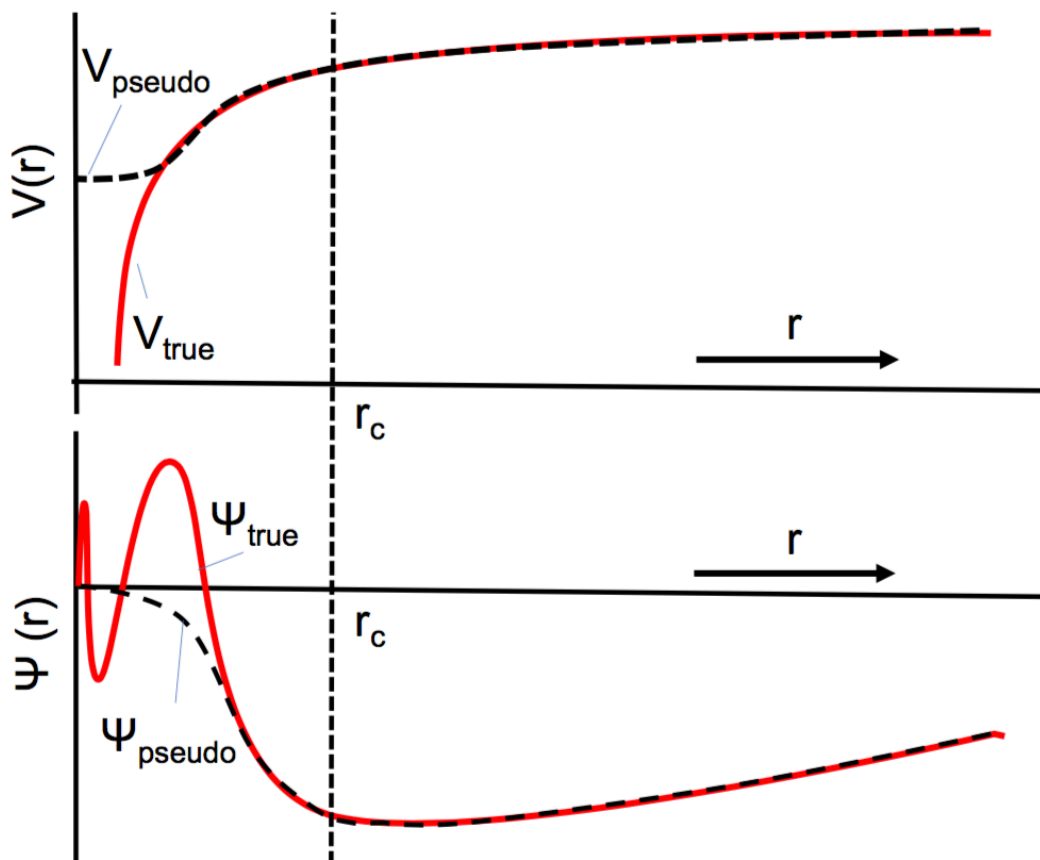


Figure 4.1: The modification of the original Coulombic potential (V_{true}) and original wavefunction (ψ_{true}) in the pseudopotential framework. The V_{true} is replaced with V_{pseudo} and ψ_{true} is replaced with ψ_{pseudo} .

property (X) may be expressed as:

$$X = \frac{1}{V_{BZ}} \int_{BZ} \sum_n X_n(k) f(\epsilon_n(k)) dk \quad (4.19)$$

where, V_{BZ} is the volume of Brillouin zone, n is the number of wave-vectors, and ϵ_n is eigenvalue of wavevector k , and $f(\epsilon_n(k))$ is a factor that controls whether the particular state is occupied. Now, while calculating the value of the integral, as given by equation 4.19, the inherent symmetry of the crystal can be employed to reduce the associated computational cost. In this scheme, instead of considering all the k -points in the BZ, only certain special points in the BZ are considered, which lie in the wedge shaped region as shown in Fig. 4.2; the *irreducible Brillouin zone (IBZ)*. Once the value of the integral has been calculated for the IBZ, the value of the integral for the whole BZ can be determined by introducing certain weighting factors.

Additionally, the distribution of grid of k -points in BZ is mostly carried out using the Monkhorst-Pack scheme involving equally spaced k -points along the each of three orthogonal directions in reciprocal space [24]. It should be noted here that in the original work of Monkhorst and Pack [24], they did not consider Γ -point in the IBZ, while nowadays Γ is considered to be part of the IBZ. The function, which was being integrated in equation 4.19 needs to be continuous for convergence of grid-based schemes as are used in k -space based methods. But, metals have occupied and unoccupied energy states separated by the ‘*Fermi surface*’, i.e., the function in equation 4.19 changes abruptly at the Fermi energy (E_f). This is the reason why we need comparatively larger number of k -points for metals to reproduce the abrupt change in the function. In view of solving the above-stated problem, a range of smearing schemes have been proposed. The physical backing of smearing schemes stems from the consideration that

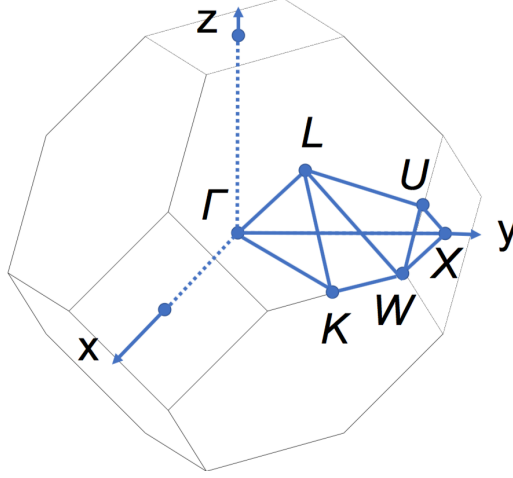


Figure 4.2: The first Brillouin zone of the FCC crystal structure, which is a truncated octahedron.

an abrupt change in the occupancy across the Fermi surface occurs at 0 K, while at finite temperature the abrupt change as expected at 0 K can become diffused leading to occupancy above E_f . So the Fermi-Dirac function is employed to introduce occupancy as a function of temperature, which may be written as:

$$f\left(\frac{x}{\sigma}\right) = \frac{1}{\left[\exp\left(\frac{x}{\sigma}\right) + 1\right]} \quad (4.20)$$

σ in the above equation is equal to $k_B T$ and hence with the increasing values of σ , the abruptness of the function across E_f can be ‘smeared’ as shown in Fig. 4.3. The σ parameter generates the effect of thermally distributed electrons in the system and a correction needs to be carried out in the energies, if such effects are not required. The Fermi-Dirac smearing scheme has a disadvantage due to the large number of partially occupied bands required to describe electron occupation. Numerous other smearing schemes such as Gaussian [25], Methfessel-Paxton [26] and Marzari-Vanderbilt [27] smearing schemes have been proposed. The Gaussian smearing scheme was employed

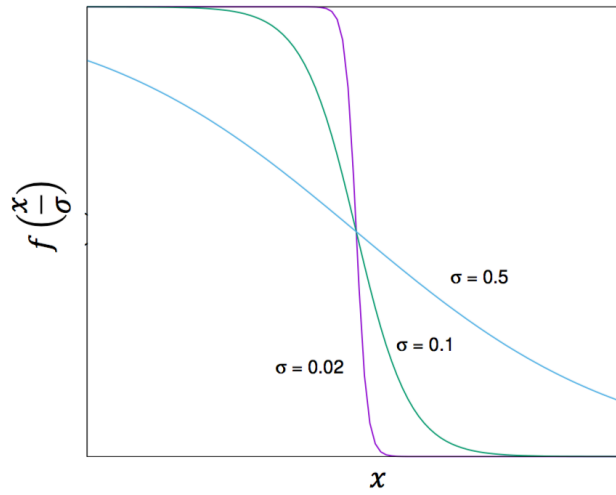


Figure 4.3: The variation of the Fermi-Dirac function with different value of σ . Redrawn from ref. [28].

in the present work, which is the default smearing scheme in CASTEP.

* * * * *

Chapter 5

Phase Stability in Substitutional Alloys[‡]

5.1 Introduction

High entropy alloys (HEAs) are a class of multicomponent metallic alloys [29], which exhibit simple crystal structures such as body-centred cubic (BCC), face-centred cubic (FCC), hexagonal cubic phase (HCP) or orthorhombic crystal structures [30–32]. The stabilisation of a solid solution phase over intermetallic and amorphous alloy formation in such multicomponent systems was initially attributed to the high configurational entropy of mixing [33]. The prediction of the comparative phase stability of BCC and FCC phases for HEAs remains a major debate in the literature. For example, CoCrFeNi shows the FCC structure, but addition of Al causes its transformation to the BCC crystal structure [34]. The phase transformation and existence of HEAs in two main types

[‡]Part of this chapter has been published as an article entitled “*Role of configurational entropy in body-centred cubic or face-centred cubic phase formation in high entropy alloys*” in Scripta Materialia [124 (2016) 90-94.]

of crystal structures was initially rationalised in terms of the conventional metallurgical concept of FCC and BCC stabilising elements [35]. Traditionally, phase stability in alloys has been understood in terms of the number of electrons per atom (e/a) [36], which has been extensively used for Hume-Rothery electron phase stabilisation. In the case of HEAs, which are mostly composed of transition metals, the accurate determination of the e/a ratio is problematic. Hence, the valence electron concentration (VEC) has been employed to rationalise FCC and BCC formation, where higher VEC (≥ 8.0) leads to FCC phases, while lower VEC (≤ 6.87) causes BCC formation, leaving a mixture of BCC and FCC phase for $6.87 \leq VEC \leq 8.0$ [37]. This criterion, however, does not apply to HEAs containing Mn [38], and in certain cases the effect of cooling conditions dominates the phase formation, i.e., alloys with the same composition but subjected to different processing conditions produce different phase occurrence characteristics [39]. Therefore phase selection remains an open debate. Computationally expensive *ab-initio* approaches, such as the coherent potential approximation [40] and special quasi-random structures with density functional theory (DFT) [41] have been used to study HEAs. Given the potential significance of (configurational) entropy in the phase stability in HEAs, there is a need for an extensive sampling of configurations which cannot be achieved easily with *ab-initio* methods which are limited to small cells.

In view of the above, this work explored the feasibility of the available interatomic potentials for studying multicomponent systems. This investigation reports the application of classical atomistic simulation along with a statistical mechanics based framework for calculation of thermodynamic properties. Additionally, a genetic algorithm (GA) based method was employed to find the minimum energy configuration of alloys.

5.2 Empirical interatomic potential for Metals

Determination of the total energy of the system is the most crucial part of studies of the phase stability. One of the simpler approaches to the calculation of total-energy is the pair-potential approach, where the energy (E) of the system of interest may be simply written as [42]:

$$E = \frac{1}{2} \sum_{i,j(i \neq j)}^N V(r_{ij}) \quad (5.1)$$

where r_{ij} is the distance between atom i and j . The pair-potential approach assumes there is no dependence between bonding between any two atoms and other bonds, which leads to the inference that $E \propto -Z$, where Z is the coordination-number of the atom. But, it is well known that $E \propto -Z^{1/2}$ [43]. The pair-wise potential cannot be applied to transition metals or semiconductors for the following reasons:

1. The ratio of elastic constants (C_{12}/C_{44}) or *Cauchy's relationship* must be unity for a central-force pair potential. Note that, there are three unique elastic constants for cubic systems, i.e., (C_{11}, C_{12} and C_{44}). But the experimental ratio for metals deviates from unity.
2. The surface of metals simulated using pair-potentials tends to relax outwards in contrast to the inward relaxation of the surface as is experimentally observed.
3. The ratio of cohesive energy to the melting temperature is underestimated by the pair-potential approach.
4. The ratio of vacancy formation energy to the cohesive energy is predicted to be one by pair-potential simulation (when relaxation effects are ignored), while experimentally such values range from $\frac{1}{3}$ to $\frac{1}{4}$.

The limitation of the pair-potential approach arises from its inability to take into account many-body effects. This approach considers the surface to be stronger than the bulk. In this approach, surfaces have fewer but stronger bonds than the bulk (which has more but weaker bonds) [44]. In view of the problems associated with the pair-potential approach, many-body potentials have been defined, including Finnis-Sinclair [45], Sutton-Chen extension to Finnis-Sinclair model [46] and Embedded-atom method [47] based potentials for metals.

The genesis of many-body potentials is from the density of states (DOS) and the moment theorem. The DOS between an energy interval, E and $E + \Delta E$ is the number of energy states between specified energy levels and the moment of any distribution about a point may be expressed as:

$$\mu^m = \sum_n (E - E_a)^m D(E) \quad (5.2)$$

where, m in the above equation represents the order of the moment of the distribution. The first, second, third and fourth moments of the distribution represent mean, variance, skewness and bimodality of the distribution, respectively. In the context of atomistic simulation, we are interested in the DOS or $D(E)$ distribution. In equation 5.2, E_a is the energy of the atom in its elemental state and the moment of the $D(E)$ is determined with respect to it. The second-moment is important from the perspective of atomic binding, as it represents the difference in energy levels of the atom in the solid state with respect to the energy level of the atom in its elemental state. It has been found that the binding energy of the atom in the solid state is strongly correlated with square-root of the second-moment of the DOS of that particular atom [44] and

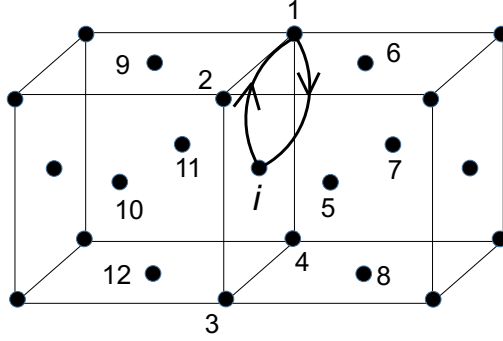


Figure 5.1: Schematic figure illustrating the number of paths of length two, which can be traversed such that they start and end at the atom labelled as ‘ i ’. As it is evident, the number of such paths is twelve.

the binding energy of the i^{th} atom may be expressed as:

$$E_i = \int d_i(E) E dE \quad (5.3)$$

where, $d_i(E)$ is the local density of states of the i^{th} atom. The ‘*moment-theorem*’ relates the characteristics of the neighbours of the atom with the moment of the local DOS. Hence, the moment-theorem provides a way of calculating the binding energy of the atom without explicitly calculating the DOS using electronic structure methods.

The ‘*moment-theorem*’ may be expressed as: “The m^{th} moment of the local DOS of the particular atom is the sum of all paths of length ‘ m ’, which start and end at that particular atom”. As can be seen in Fig. 5.1, the second-moment of the DOS of the i^{th} atom would be proportional to $\sqrt{12}$. So, it is clear that for the second-moment of the local DOS, $E_i \propto \sqrt{Z_i}$, where Z_i is the number of first nearest-neighbours of the i^{th} atom. This is also known as the *second-moment approximation*.

In the Finnis-Sinclair model, the energy of the system (E) may be expressed as the

sum of energy due to pairwise contributions and the energy due to the second-moment approximation. It may be expressed as:

$$E = \sum_{i=1}^N \sum_{j=i+1}^N V(r_{ij}) + \sum_{i=1}^N A\sqrt{\rho} \quad (5.4)$$

where, $V(r_{ij})$ is the pair-potential between atoms i and j . The ρ may be expressed as $\sum_{j=1, j \neq i}^N \phi(r_{ij})$, where $\phi(r_{ij})$ is a function of $|r_{ij} - r_c|$, ' r_c ' is the cut-off of the function and the value of $\phi(r_{ij})$ is zero beyond r_c .

The Embedded-atom method (EAM) [47] is another form of many-body potential, which is similar to the Finnis-Sinclair formalism for elements with differences arising when interatomic potentials are generated for alloys [48]. The energy of the ensemble (E) containing a particular number of atoms, N using the EAM force-field in MD simulations can be expressed as:

$$E = \frac{1}{2} \sum_{i,j,i \neq j}^N \phi_{ij}(r_{ij}) + \sum_i F_i(\rho_i) \quad (5.5)$$

where, ϕ_{ij} is the pair energy between atoms i and j , which are separated by a distance, r_{ij} , while F_i represents the embedding energy. This energy arises from inserting or embedding atom i into the medium having electron density, ρ_i , which may be expressed as:

$$\rho_i = \sum_{i=j, i \neq j}^N f_i(r_{ij}) \quad (5.6)$$

where, $f_{ij}(r_{ij})$ is the electron density at site i from an atom at site j at distance r_{ij} . The electron density in the EAM formalism is derived from electronic structure calculations.

The $\phi(r)$ may be expressed as:

$$\phi(r) = \frac{A \exp(-\alpha(r/r_e - 1))}{1 + (r/r_e - \kappa)^{20}} - \frac{B \exp -\beta(r/r_e - 1)}{1 + (r/r_e - \lambda)^{20}} \quad (5.7)$$

where, α , β , A and B are adjustable parameters in the above equation. r_e is the equilibrium nearest-neighbour distance between atoms, while κ and λ are cut-off parameters. The alloy interatomic potential can be generated from elemental interatomic potentials [48] as:

$$\phi^{ab}(r) = \frac{1}{2} \left[\frac{f^b(r)}{f^a(r)} \phi^a(r) + \frac{f^a(r)}{f^b(r)} \phi^b(r) \right] \quad (5.8)$$

where, the form of f (f^a or f^b) in the above equation is taken to be same as the attractive part of the pair-potential with identical values of λ and β , as given in equation 5.7 [49] and it can be written as:

$$f = \frac{f_e \exp -\alpha(r/r_e - 1)}{1 + (r/r_e - \lambda)^{20}} \quad (5.9)$$

Additionally, Zhou *et. al.* [49] introduced three different equations for the embedding energy to ensure this function was applicable for the range of atomic densities, as shown in equations 5.10, 5.11 and 5.12:

$$F(\rho) = \sum_{i=1}^3 F_{ni} \left(\frac{\rho}{\rho_e \times 0.85} - 1 \right)^i ; \rho < (0.85 \times \rho_e) \quad (5.10)$$

$$F(\rho) = \sum_{i=1}^3 F_i \left(\frac{\rho}{\rho_e} - 1 \right)^i ; (0.85 \times \rho_e) \leq \rho < (1.15 \times \rho_e) \quad (5.11)$$

$$F(\rho) = F_e \left[1 - \ln \left(\frac{\rho}{\rho_e} \right)^\eta \right] \left(\frac{\rho}{\rho_e} \right)^\eta ; \rho \leq (1.15 \times \rho_e) \quad (5.12)$$

Alloy	lattice parameter (Å)
BCC-CoCrFeNi	2.850
FCC-CoCrFeNi	3.570
BCC-AlCoCrFeNi	2.850
FCC-AlCoCrFeNi	3.570
BCC-CoCrFeNiTi	2.935
FCC-CoCrFeNiTi	3.628

Table 5.1: Lattice parameter of BCC and FCC forms of alloys used in MD calculations [53].

5.3 Calculation details

The DL_POLY code was employed to carry out Molecular Dynamics (MD) simulations [50]. Position, velocity and acceleration of the atoms were updated via the velocity-verlet integration algorithm [51]. The GULP code [52] was used to generate 7x7x7 (FCC) and 9x9x9 (BCC) cubic supercells for starting configurations. The disordered structures of the alloys were generated by randomising the elements on the lattice sites. The simulations were performed with a 1 fs time-step. The long-range interaction cut-off was set to be 6 Å. The MD simulations were carried out for 10 ps, where the system was equilibrated for first 5000 time steps. The configurational energy was shown to converge over this time (Fig. 5.2 and 5.3). A Nosé-Hoover NPT ensemble with thermostat and barostat relaxation times of 0.01 ps and 0.1 ps, respectively, was used to keep temperature (300 K) and pressure (1 atmosphere) constant. The initial lattice parameters for the BCC and the FCC variant of AlCoCrFeNi, CoCrFeNi and CoCrFeNiTi were taken from first-principle calculations, while for Al_{0.5}CoCrFeNi, the equilibrium lattice parameter was calculated from finding the minimum of the energy-volume curve in an NVT calculation. The initial lattice parameters used in MD simulations are tabulated in Table 5.1. The EAM potential for elements (Al, Co, Fe, Ni and Ti) were taken from Zhou *et. al.* [49] and the interatomic potentials of Cr was taken from Lin *et.*

al. [54]. Although, Lin *et. al.* used a similar parameter model to Zhou *et. al.*, it was found that the parameterisation followed a different rule-set. Similar parameters have been employed to simulate the deformation in tensile loading condition [55], phonon characteristics [56], irradiation induced defect formation [57], deposition of HEA thin films on Si-Substrate [58], etc.

5.4 EAM potential validation and modification

The structures of the BCC and FCC forms of CoCrFeNi, AlCoCrFeNi and CoCrFeNiTi after MD simulations are shown in Fig. 5.5. As it is clearly evident, the FCC structure for each alloy tended to show an inhomogeneous distortion. Figure 5.4(b) shows a plot of the ratio of the second to the first peak of the radial distribution function (RDF) or $g(r)$ of the alloys, which is indicative of the amorphous-like or liquid-like distribution of the atoms [59]. It can be seen that elements tend to arrange themselves in amorphous or liquid type coordination in the FCC structure. The X-ray diffraction profile of the structures were simulated using the Debyer code [60] to determine the lattice parameter after completion of the MD simulation (Fig. 5.6). The position of the most prominent peak was chosen to calculate the lattice parameter. Table 5.2 shows the lattice parameter before and after the MD simulation. It is important to note that the change in the lattice is taking place due to relaxation during the MD simulation. But in the case of the FCC structures, the change is less than for BCC, even though the structure tends to amorphise. To test potential issues with the interatomic potentials, hypothetical equiatomic FCC alloys, such as CoCr, CoFe, CoCrFe, CoFeNi and CoCrNi, along with CoCrFeNi were simulated to study the effect of Cr potentials on the amorphisation tendency. Figure 5.7 shows the RDF of the alloys.

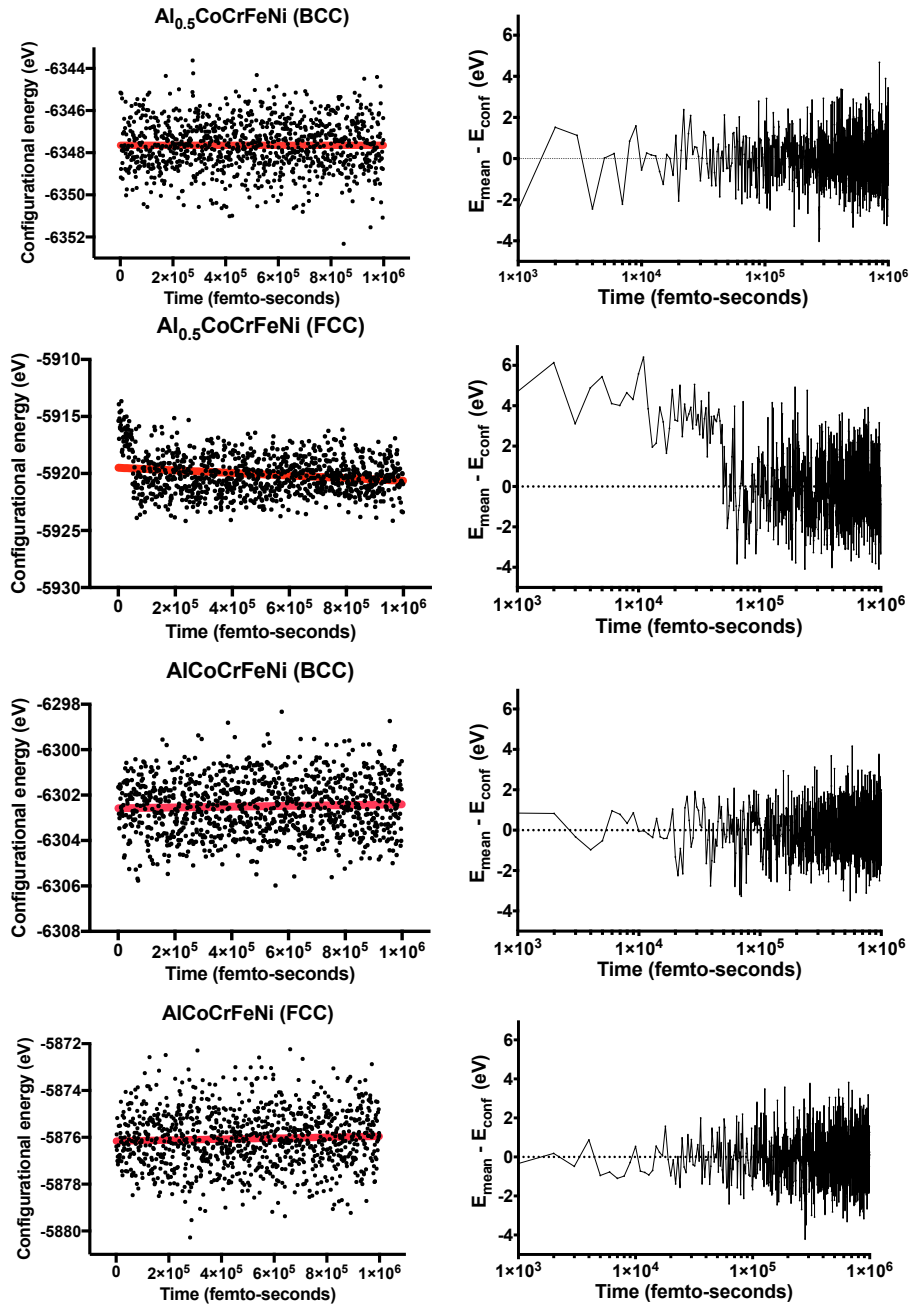


Figure 5.2: Variation of energy with time-step during MD simulation for BCC and FCC form of $\text{Al}_{0.5}\text{CoCrFeNi}$ and AlCoCrFeNi .

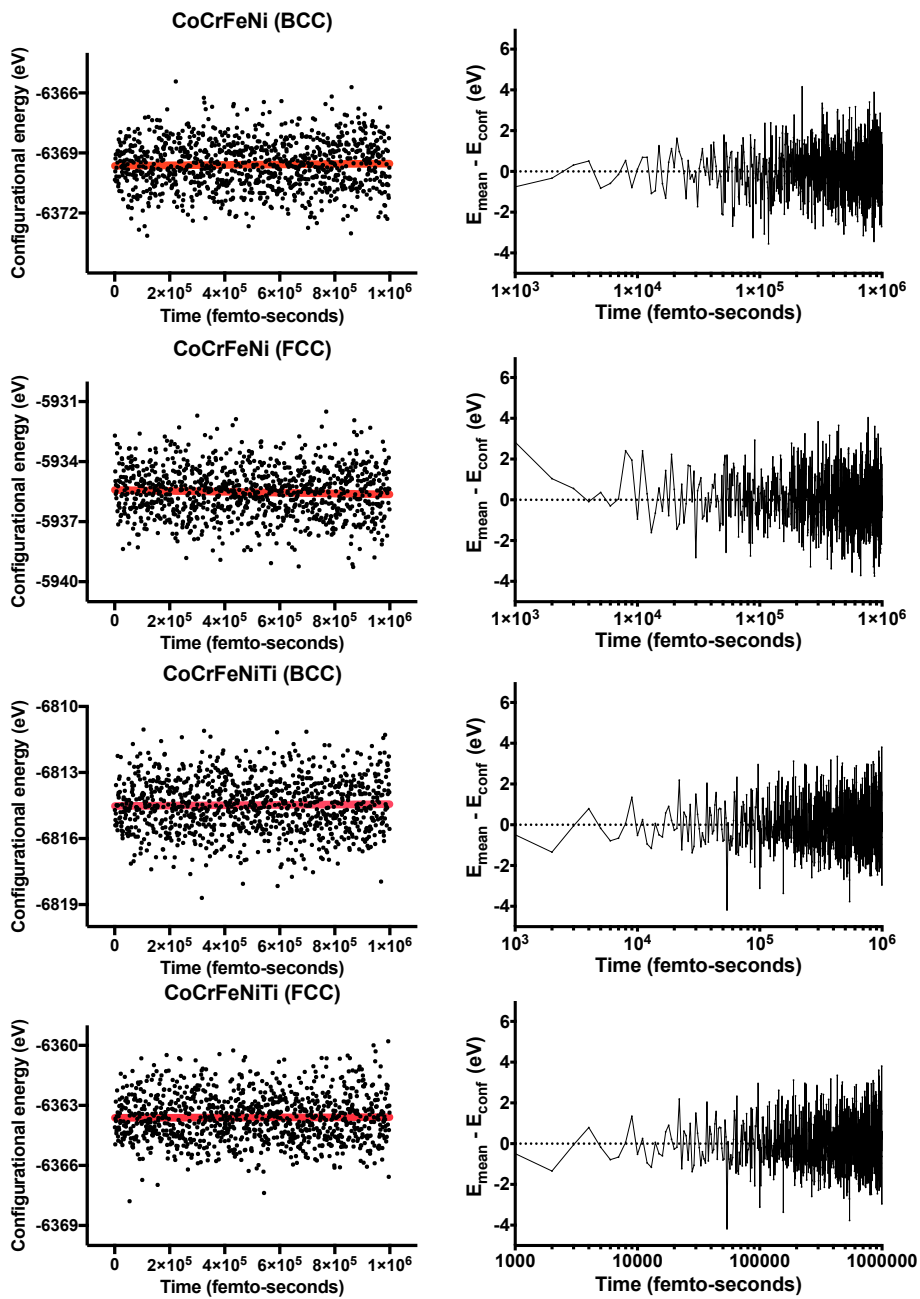
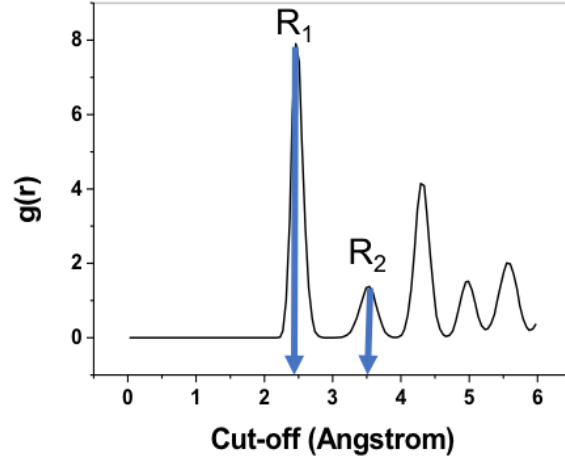
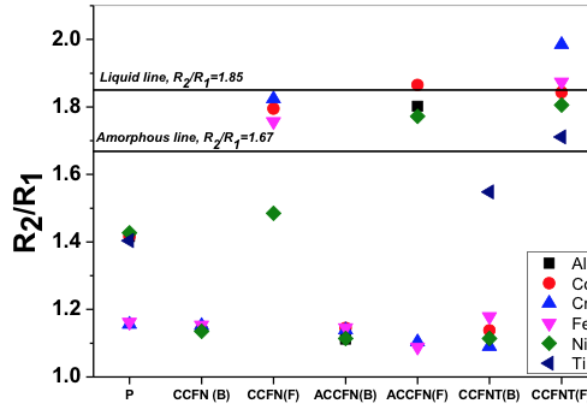


Figure 5.3: Variation of energy with time-step during MD simulation for for BCC and FCC form of CoCrFeNi and CoCrFeNiTi.



(a)



(b)

Figure 5.4: (a) Schematic to show the R_1 and R_2 in typical RDF of alloys and (b) Ratio of R_2 and R_1 for elements in pure (P) state, BCC-CoCrFeNi (CCFN(B)), FCC-CoCrFeNi (CCFN(F)), BCC-AlCoCrFeNi (ACCFN(B)), FCC-AlCoCrFeNi (ACCFN(F)), BCC-CoCrFeNiTi (CCFNT(B)) and FCC-CoCrFeNiTi (CCFNT(F)).

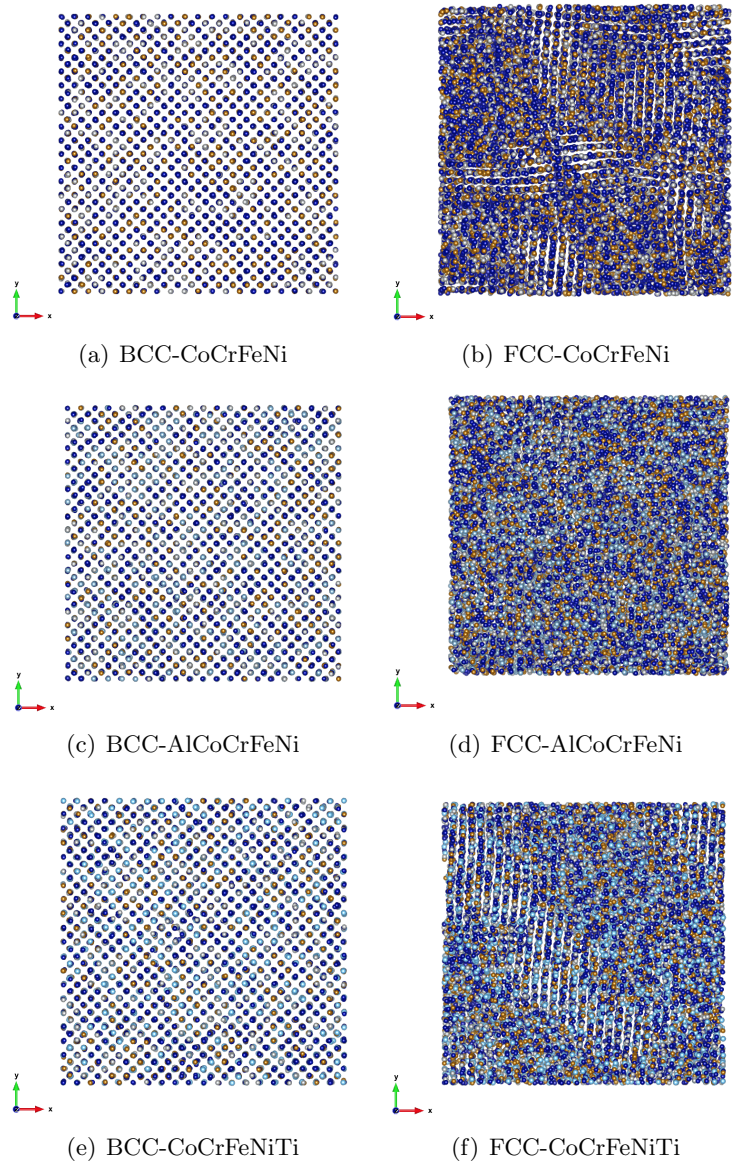


Figure 5.5: Visualisation of structure of different alloys after completion of MD simulation. Note that these calculations were carried out for 16384 and 16000 atoms for FCC and BCC atoms respectively for visualisation purposes.

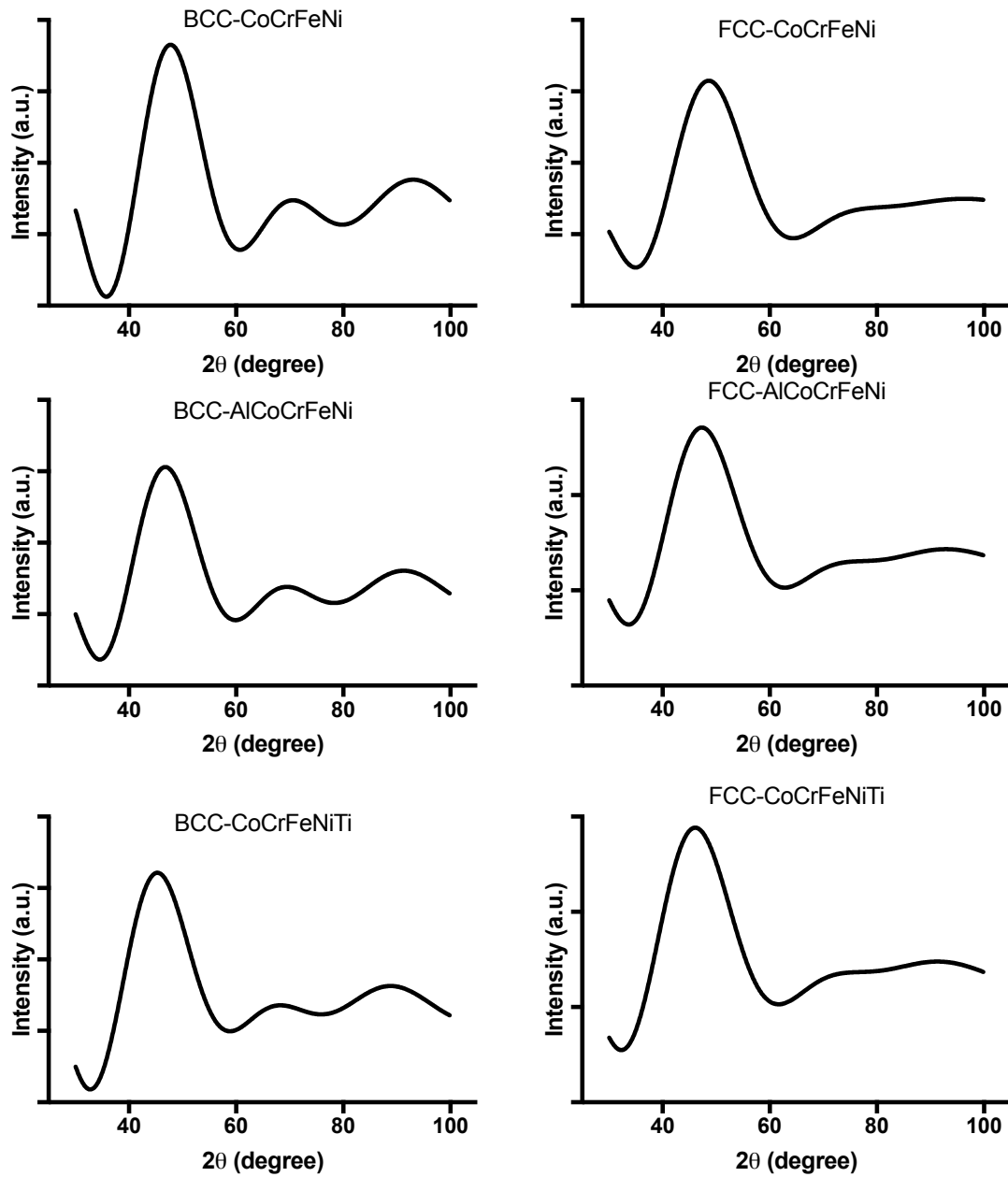


Figure 5.6: Simulation of peak of X-ray diffraction (XRD) pattern for BCC and FCC form of different alloys. Cu-K α radiation of wavelength 1.54 Å was used as input to the simulation. Note that finite-size broadening is taking place due to use of clusters in simulating XRD profile.

Alloy	lattice parameter in start (\AA)	lattice parameter in end (\AA)
BCC-CoCrFeNi	2.850	2.957
FCC-CoCrFeNi	3.570	3.573
BCC-AlCoCrFeNi	2.850	2.882
FCC-AlCoCrFeNi	3.570	3.587
BCC-CoCrFeNiTi	2.935	2.900
FCC-CoCrFeNiTi	3.628	3.620

Table 5.2: Lattice parameter of BCC and FCC forms of alloys determined from XRD simulation of start and end of MD simulated structures.

It is clear that, in the presence of Cr, the simulated structures tend to amorphise, except in the case of CoCrNi. The sharp peak in the RDF signifies the absence of amorphisation in the case of CoFeNi. The amorphisation tendency of FCC alloys can be attributed to the inadequacy of the interatomic potentials of Cr [54], which were taken from a different source to Al, Co, Fe, Ni and Ti [49]. In view of the above, the electron density after the simulation was superimposed on a uniform grid to see, whether a homogenous or inhomogeneous distribution of the electron density is evolving during the relaxation. The electron density was obtained from the TABEAM (tabulated EAM potential) file for each element forming alloy. The coordinates of the atoms were extracted from the REVCON file after completion of the DL_POLY run and a 100X100X100 grid was superimposed over the supercell. The electron density at each node of the superimposed grid is determined by adding the contribution from each atom falling in an imaginary sphere of radius 5.5 \AA around the node. Figure 5.8 shows the electron density distribution for FCC-CoCrFeNi. It is apparent that the system evolves towards an inhomogeneous electron density distribution. Figure 5.8 is condensed into a histogram for better comparison in Fig. 5.9. Figure 5.9 shows the histogram of the number of nodes with respect to the electron density. It can be seen that the BCC and

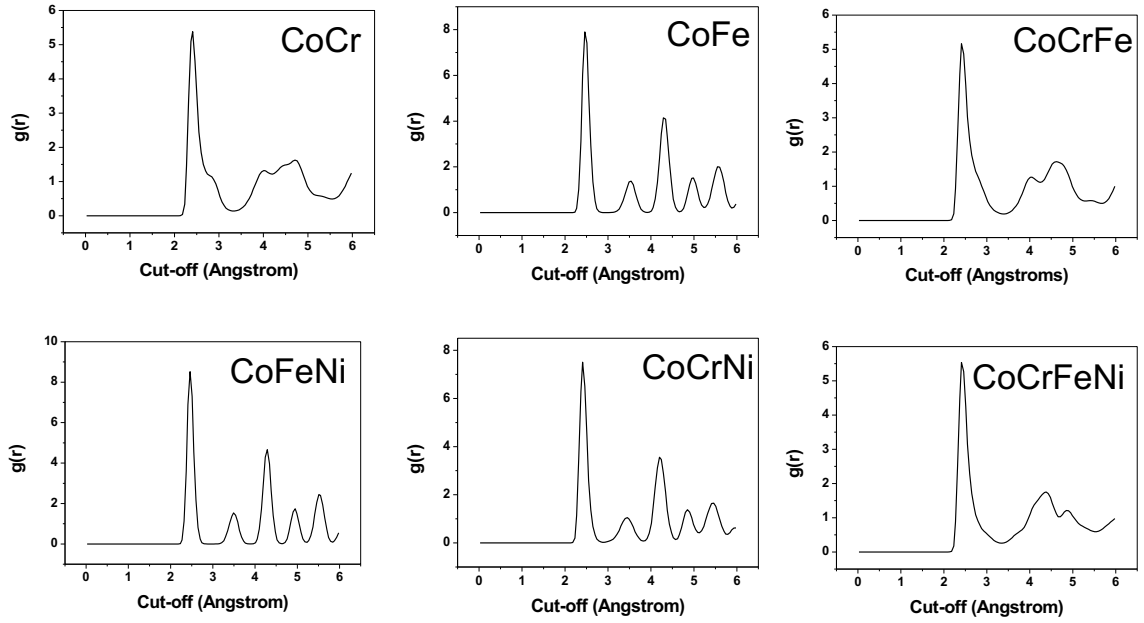


Figure 5.7: Radial distribution function (RDF) for CoCr, CoFe, CoCrFe, CoFeNi, CoCrNi and CoCrFeNi using EAM potential published in ref. [49].

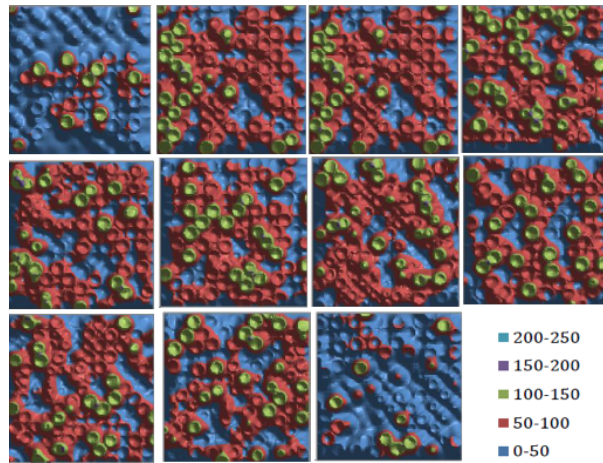


Figure 5.8: The electron density distribution (in arbitrary units) in the case of FCC-CoCrFeNi, obtained after superimposition of electron density from EAM potential of the individual elements on MD simulated structure. This figure shows different sections of three dimensional supercell starting from left to right.

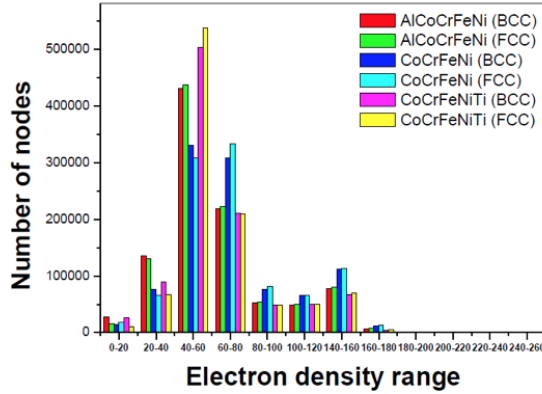


Figure 5.9: The distribution of electron density on the nodes of a cuboidal mesh superimposed on the simulated MD simulation supercell.

FCC structures of the individual alloys show similar variations with slight differences in the number of nodes in a particular electron density range. This implies that, in terms of number density, the electron density is similar in the case of BCC and FCC structures of a particular alloy. The electron density of Fig. 5.10 shows the electron density variation in the individual elements as a function of distance from a nucleus. It should be noted that the electron density around the ionic core is an important parameter for alloy formation. As it is evident from the above, Cr seems to be the only element that is causing an amorphisation tendency in the alloys. It is evident that the electron density for Cr is largest of the elements considered here. The inset of the figure shows the variation of electron density at log scale. It can be seen that Cr shows the maximum decrease with distance in comparison of other elements. So, it can be stated that the Cr exhibits higher electron density in the vicinity of the ionic core with a highest gradient of electron density decrease. The potentials were fitted to match the cohesive energy, lattice parameter and bulk modulus of Cr. In addition, it was ensured that in the FCC structure, Cr maintains its crystal order. We have mentioned that

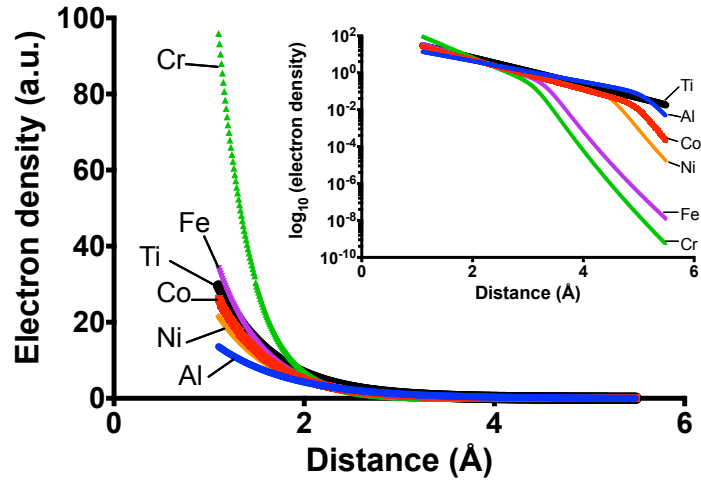


Figure 5.10: The variation of the electron density from the nucleus for Co, Cr, Fe, Ni, Ti and Al [61].

interatomic potentials of Cr were taken from different source [54]. Zhou *et. al.* kept the ratio of α and β to be equal to 1.875, while A and B values for Co, Cr, Fe, Ni and Ti were less than 0.50 and 1.00, respectively [49]. So, an attempt was made to fit the potential of Cr using the same criteria as mentioned elsewhere. This was done to ensure that the potentials of each element for simulating alloy mixes are derived from same rules. Table 5.3 shows the original and modified data set of the interatomic potential of Cr. The potentials were fitted to match the cohesive energy (-4.10 eV), lattice parameter (2.88 Å) and bulk modulus (160 GPa) of the Cr. In addition, it was ensured that in the FCC structure, Cr maintains its crystallinity.

Figure 5.11 shows the FCC structure of the hypothetical solid solutions including Al-Cr, Co-Cr, Cr-Fe, Cr-Ni, Cr-Ti, as well as CoCrFeNi and AlCoCrFeNi with pure Cr. It can be seen that in the binary cases (except for Co-Cr and Cr-Ni), the system maintains the crystalline order. But in the case of CoCrFeNi and AlCoCrFeNi, the absence of a sharp peak can be seen. Figure 5.12 shows the variation in the electron density of Cr. It

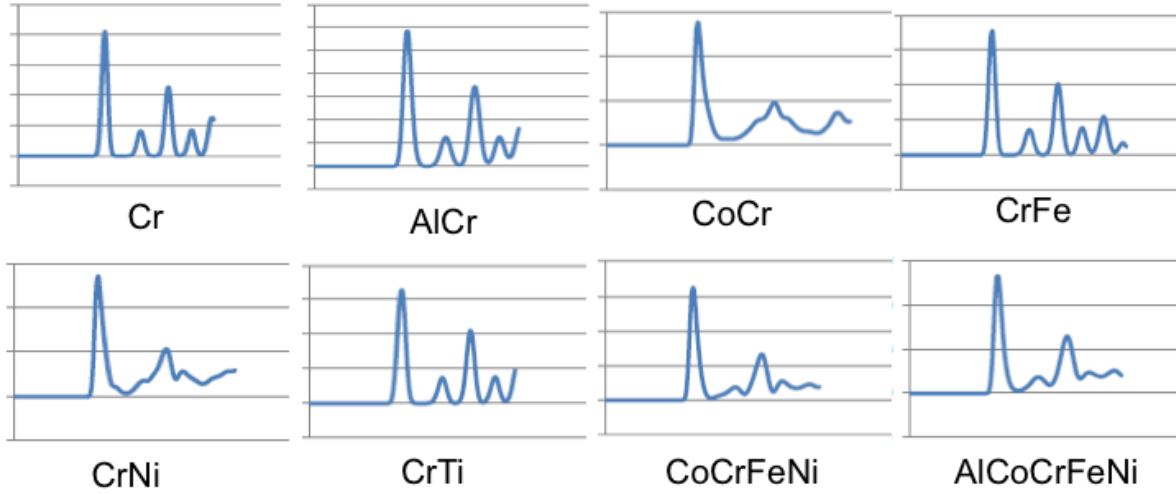


Figure 5.11: Radial distribution function of FCC form of Cr, AlCr, CoCr, CrFe, CrNi, CoCr-FeNi and AlCoCrFeNi with modified EAM potential for Cr. The y-axis represents the intensity of peak in arbitrary units and x-axis is atomic distance in Å.

	Published potential [54]	Fitted potential
β	7.170494	4.589611
A	1.551848	0.480000
B	1.827556	0.800000

Table 5.3: Modified EAM potential parameters for Cr [61]. Other parameters can be found in ref. [54].

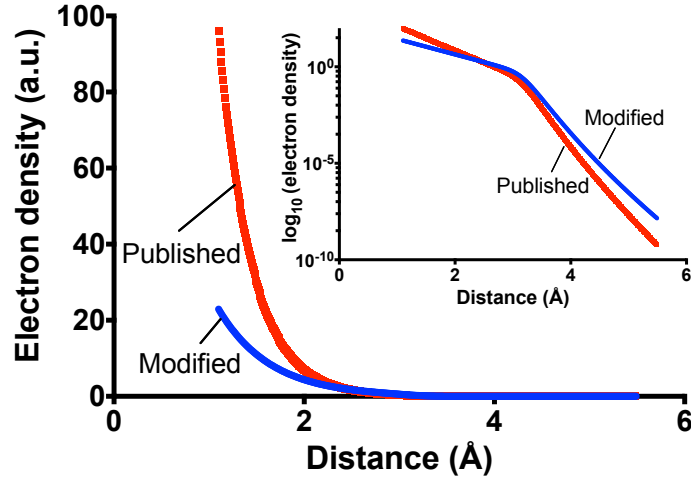


Figure 5.12: The variation of electron density of Cr with original [54] and modified EAM potential (inset shows the variation on log scale) [61].

shows that through fitting the potential the apparent difference in the electron density distribution around the ionic core is decreased, but the decrease in electron density with increase in distance follows roughly the same order of magnitude of electron density, as in the case of the original potential.

5.5 MD simulation with random sampling

2500 random configurations of both the FCC and BCC structures of each of the alloys (CoCrFeNi, Al_{0.5}CoCrFeNi, AlCoCrFeNi and CoCrFeNiTi) were generated. Thermodynamic quantities such as, enthalpy (H) and Gibbs free energy (G) were calculated using the configurational energy (E_i) of the atomic configurations, i . H can be calculated as:

$$H = \frac{\sum_{i=1}^N E_i \exp\left(\frac{-E_i}{k_B T}\right)}{Q} \quad (5.13)$$

Alloy	Enthalpy (eV/atom)
BCC-AlCoCrFeNi	-4.33
FCC-AlCoCrFeNi	-4.28
BCC-CoCrFeNi	-4.37
FCC-CoCrFeNi	-4.33
BCC-CoCrFeNiTi	-4.68
FCC-CoCrFeNiTi	-4.65

Table 5.4: Enthalpy of FCC and BCC form of different alloys determined by random sampling of 2500 configurations.

where N in the above represents the total number of atomic configurations sampled. k_B and T are the Boltzmann's constant and temperature respectively. The Q in the above equation is the partition function, which may be expressed as:

$$Q = \sum_{i=1}^N \exp\left(\frac{-E_i}{k_B T}\right) \quad (5.14)$$

Table 5.4 shows the enthalpy for these alloys. The calculations predict that the BCC structures have a greater enthalpy of mixing than FCC structures. Additionally, the difference between the BCC and FCC structures is greatest for the AlCoCrFeNi. It should be noted that the effect of enthalpy on stabilisation of single phase solid solutions in high entropy alloys has been already reported in the literature [62]. Even though the empirical potentials are not accurate enough to predict the phase stability in high entropy alloys, they do point towards the stabilisation mechanisms. The probability of the occurrence of a particular energy state (P_i) can be calculated from equation 5.15 [63], as:

$$P_i = \frac{\exp\left(\frac{-E_i}{k_B T}\right)}{\sum_{i=1}^N \exp\left(\frac{-E_i}{k_B T}\right)} \quad (5.15)$$

In view of the above, the configurational entropy (S_{conf}) was calculated from the probability of occurrence (P_i) of particular energy state (E_i), using equation 5.16, as:

$$S_{conf} = -k_B \sum_{i=1}^z P_i \ln P_i \quad (5.16)$$

where, z represents the number of energy states having non-zero probability of occurrence. Figure 5.13 shows the variation of S_{conf} with temperature for different alloys. It can be seen that FCC form has always higher S_{conf} in comparison with the BCC form of the alloys. Once, the variation of S_{conf} with temperature is determined, the specific heat at constant pressure (C_p) is determined using following expression [64]:

$$\frac{C_p}{T} = \left(\frac{\delta S}{\delta T} \right)_P \quad (5.17)$$

where, T is the temperature in K and S is the entropy. Note that this expression is valid at constant pressure. We fitted a cubic spline to the curve of S_{conf} versus T and then calculated out first derivative. We then multiplied the derivative with the temperature to obtain the specific heat variation with temperature. Figure 5.14 shows C_p values for the BCC and FCC form of different alloys. It is clear that the magnitude of C_p is considerably lower than expected values. C_p values should be in range of 20-30 J/mol.K, if the rule of mixing is employed for the calculation. We do not expect to obtain precise C_p values. We need to obtain precise values of the configurational entropy and for that we need to have a robust EAM potential for alloys. We have already seen that the EAM potential employed in the present work has limitations. It was noticed that the energy distribution of these randomly generated configurations follows the Normal distribution, suggesting that our distribution did not include many

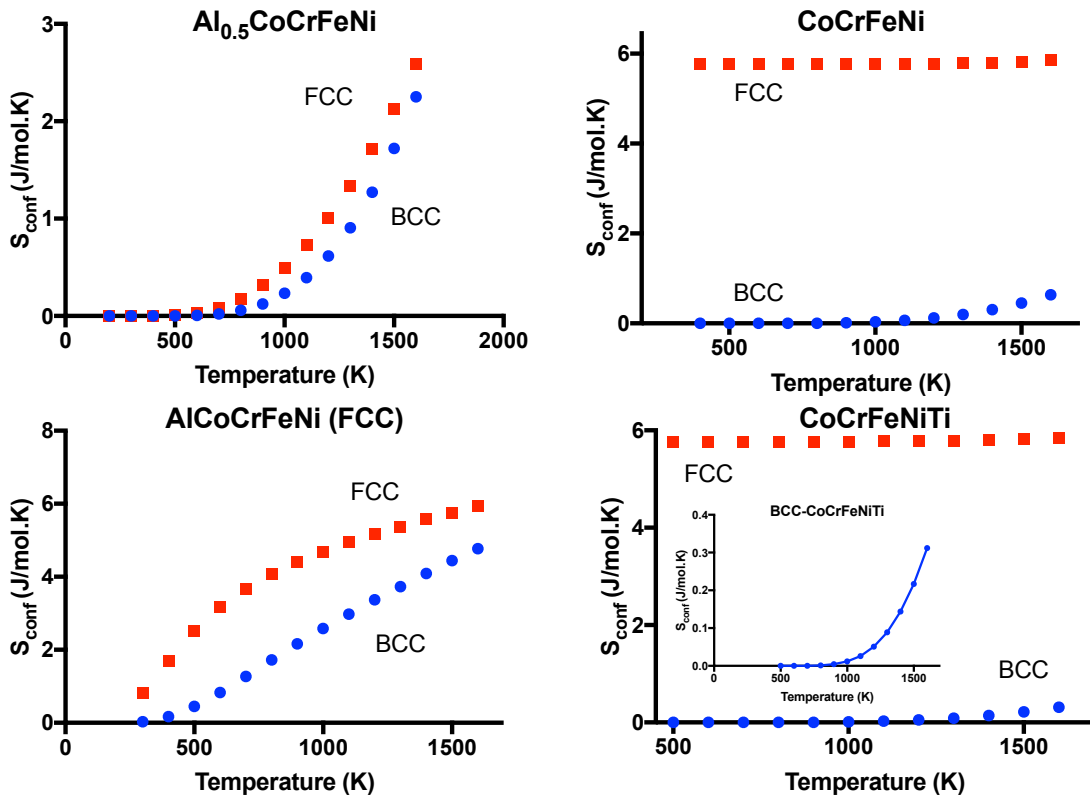


Figure 5.13: Configurational entropy for different alloys calculated using 2500 random configurations. The inset in the case of CoCrFeNi and CoCrFeNiTi shows the variation of S_{conf} with temperature for BCC forms to demonstrate its increasing trend.

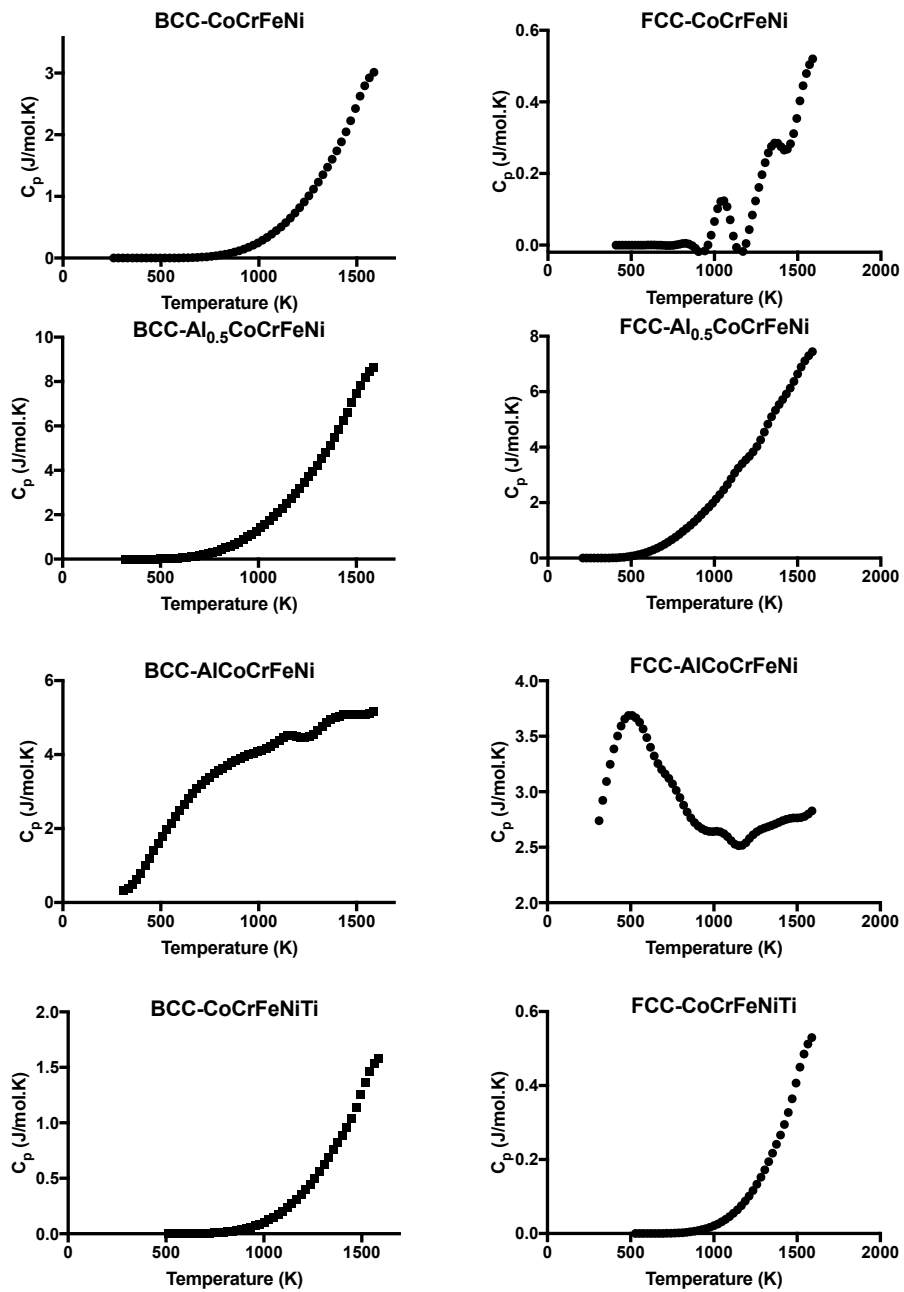


Figure 5.14: Specific heat at constant pressure (C_p) for different alloys at range of temperature.

important lower energy configurations (Fig. 5.15). This provided the motivation for the development of the hybrid GA-MD based methodology to ensure the sampling low energy configurations.

5.6 Development of a hybrid genetic algorithm-MD (GA-MD) method

Genetic algorithm (GA) is one of the evolutionary algorithms used for solving stochastic sampling and optimisation problems. It derives its methodology from evolution theory, where individuals (parents) mate to generate children. Only those individuals survive which meet selection criteria and gradually the system progresses towards a population with fittest individuals. GA was initially employed by Holland [65] for solving computational problems. This technique has been applied to study the range of optimisation [66–69] and sampling [70] problems. The goal of the present work is to develop a sampling methodology for multicomponent positional-disordered materials. Before we delve into details of the sampling procedure, the functional components of GA method need to be understood. As has been mentioned above, the information is shared between two GA individuals (i.e., parents) by the process of mating or crossover. For crossover to take place, information of parents needs to be encoded. There are several encoding schemes, *e.g.*, binary encoding, permutation encoding, value encoding, tree encoding, etc. The selection of encoding scheme is dependent upon the problem of interest and details of such encoding schemes are beyond the scope of present work. In the present work, we have employed permutation encoding as the information which will be swapped between GA individuals is the coordinates of atoms at lattice points

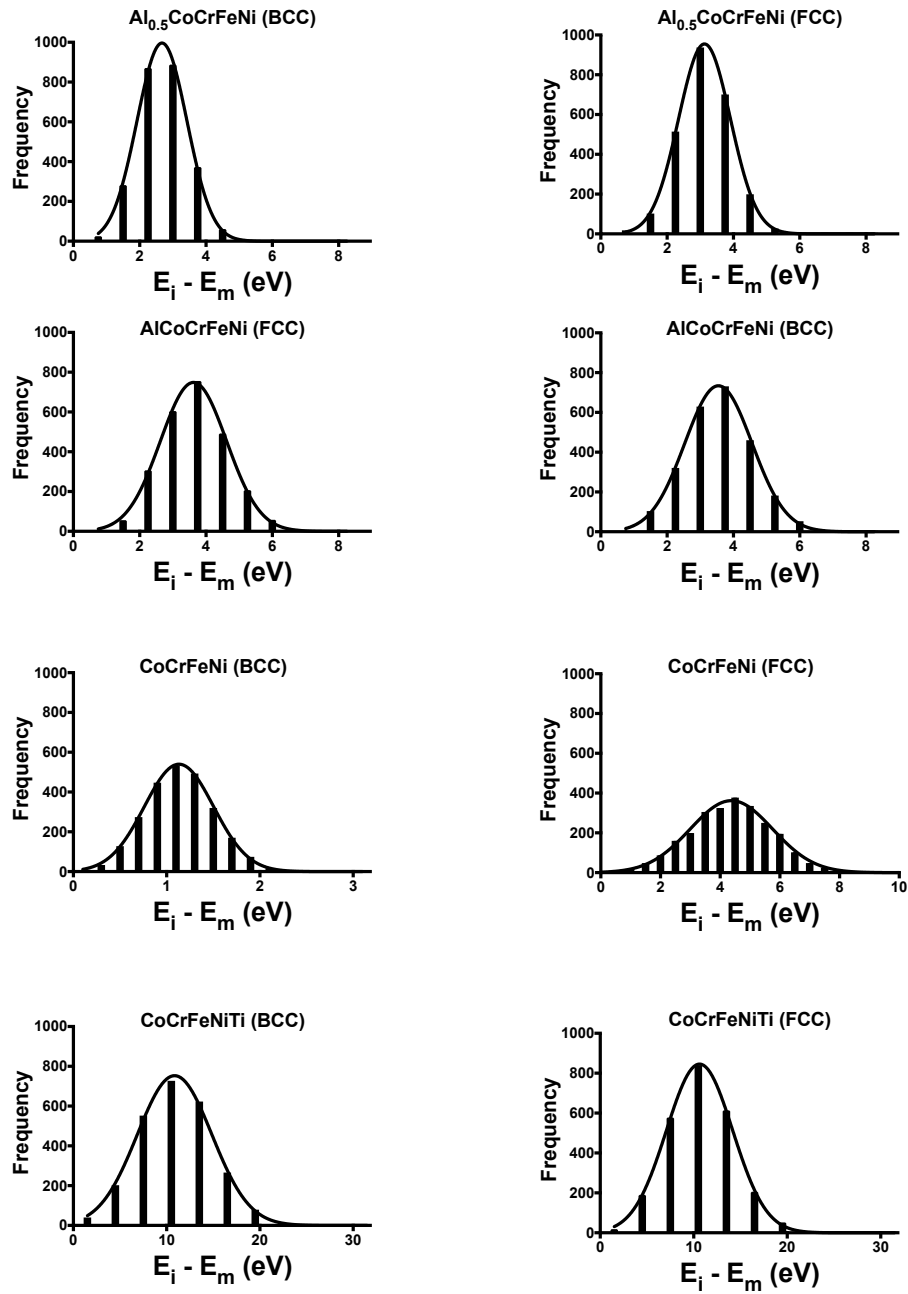


Figure 5.15: The distribution of configurational energy for different alloys. E_m represents minimum energy among 2500 random configurations, while E_i is energy of i^{th} configuration. Note that energies are for whole supercell. Curves in the figures are fitted Gaussian distributions.

and permutation encoding is suitable scheme for problem in hand.

Once, the encoding is done, the selection of parents in GA is carried out. This stage of parent population generation is basically a stochastic selection mechanism, which ensures survival of the fittest by removing less fit individuals from the parent population. After the generation of the parent population, the information between GA individuals is swapped by *cross-over* and in the last stage certain random changes in children are allowed, which is termed *mutation*.

The present sampling approach should ensure that swapping of information between two configurations (i.e., parents) leads to inheritance in new configurations (children), as shown in Fig. 5.16. Another important constraint which needs to be applied while generating new configurations concerns with the maintenance of constant composition of the supercell during sampling. The steps of GA-MD procedure developed can be stated as:

1. Initially, the 100 configurations with the lowest energies are chosen from 2500 randomly generated configurations.
2. Generate a random number (say x) between 1-1024. If $1 \leq x \leq 511$, then choose any configuration number 1 to 10, if $512 \leq x \leq 767$, then choose any configuration number 11 to 20, if $768 \leq x \leq 895$, then choose any configuration number 21 to 30, if $896 \leq x \leq 959$, then choose any configuration number 31 to 40, if $960 \leq x \leq 991$, then choose any configuration number 41 to 50, if $992 \leq x \leq 1007$, then choose any configuration number 51 to 60, if $1008 \leq x \leq 1015$, then choose any configuration number 61 to 70, if $1016 \leq x \leq 1019$, then choose any configuration number 71 to 80, if $1019 \leq x \leq 1023$, then choose any configuration number 81 to 90 and if $x = 1024$, then choose any configuration number from 91 to 100 randomly.

3. Once a list of 100 configurations are chosen, these act as reservoir of parents for particular GA generation. Two parents are chosen sequentially, i.e., configuration number 1 and 2 are chosen to be parent 1 and parent 2 respectively, configuration number 3 and 4 are chosen to be parent 3 and parent 4, respectively and so on. Note that swaps between consecutive parents are carried out, i.e., parent-1 and parent-2, parent-3 and parent-4, etc.

4. Swapping between configuration files is carried out as shown in Fig. 5.17 and steps in such a swap process are shown in Fig. 5.18. Firstly, the number of swaps is decided to be randomly in between 10-30%. In each swap: a random number (i) between 1 and N (number of atoms in the supercell) is generated, which corresponds to the particular atom and its coordinates. It is important to note that configuration files are generated in a way such that list of atomic symbols in both the files are in same order. So, the i^{th} position in both files corresponding to parent-1 and parent-2 corresponds to same atomic species, also shown in Fig. 5.18(a). After finding the coordinate of the i^{th} atom in both parent-1 and parent-2, which are (X_A, Y_A, Z_A) and (X_B, Y_B, Z_B) respectively, the identity of atomic species at (X_B, Y_B, Z_B) in parent-1 and identity of the atomic species at (X_A, Y_A, Z_A) in parent-2 is determined. It is demonstrated for sake of understanding in Fig. 5.17 and also in Fig. 5.18(b), that in parent-1 the atomic species in question is Fe (j^{th} position in configuration file of parent-1) and Co in case in parent-2 (k^{th} position in configuration file of parent-2). In the next stage, swapping between the i^{th} and j^{th} positions in the configuration file of parent-1 and the i^{th} and k^{th} positions in the configuration file of parent-2 is carried out (Fig. 5.18(c)), which leads to a change in the atomic configurations in both parent-1

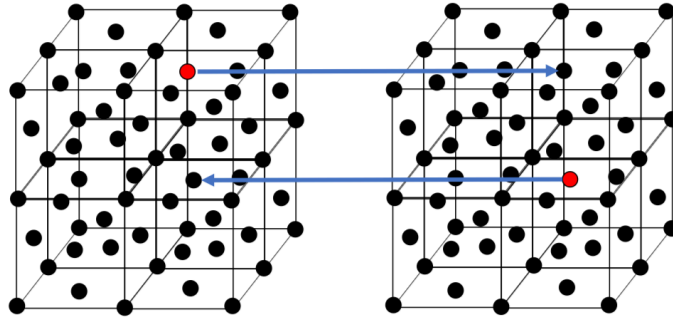


Figure 5.16: Schematic representation of the aim of the swapping process to ensure that swapping leads to inheritance of information regarding the identity of atom at equivalent positions.

and parent-2. Note that in Fig. 5.18(d), the new configuration from parent-1 has inherited Cr atom (red dot) where a Cr atom was present in the case of parent-2, while the same is the case for the new configuration generated from parent-2. Such a swapping process is repeated several times, lying between 10-30% of the total number of atoms in the supercell. Also one swap lead to an associated mutation, i.e., Fe atom (green) is at the position, where Cr was initially present in the case of parent-1, while a Co atom (blue) is present at the position, where Cr was present initially.

5. After the generation of 100 new children configurations, MD relaxation is carried out for each of these configurations and their energy is stored.
6. The reservoir of parents for the next generation is chosen again using the process depicted above in step 2.
7. The process depicted from step 2 to step 5 is repeated until all the energies from 100 configurations exhibit the same value.

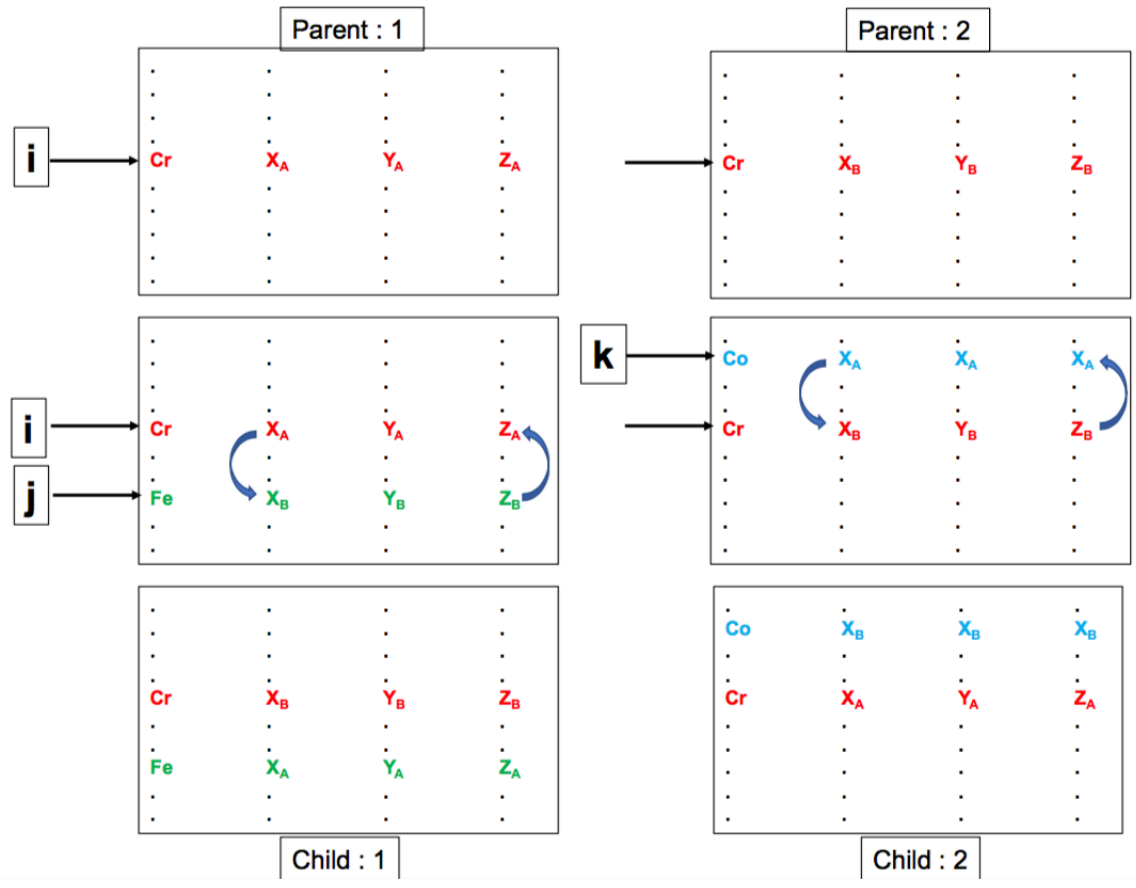
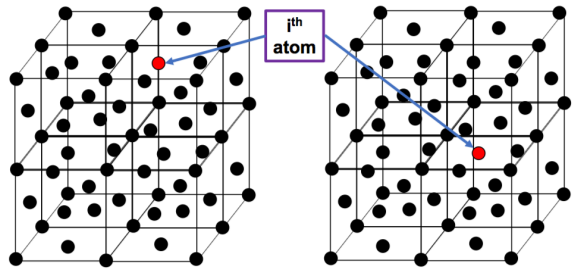
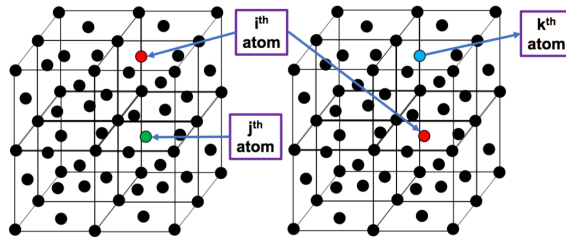


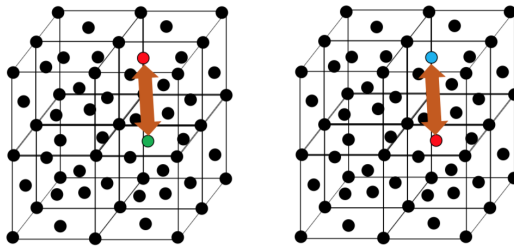
Figure 5.17: Schematic representation of the swapping in configuration files of parents.



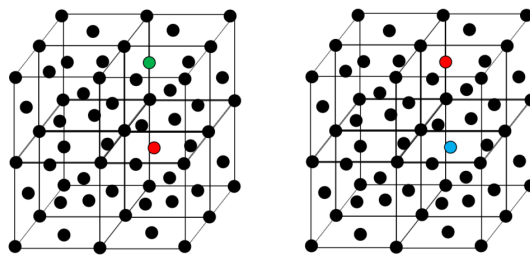
(a)



(b)



(c)



(d)

Figure 5.18: Schematic representation of the swapping process.

Element	Configurational energy (eV/atom)
Al	-3.541326
Co	-4.532784
Cr	-3.982647
Fe	-4.251920
Ni	-4.495262
Ti	-4.889643

Table 5.5: Configurational energy values for elements.

It is important to note that, once the energy variation in the population had reached zero (all configurations had the same energy), then further sampling was unlikely to improve the population in terms of finding lower energy configurations. Therefore, this provided the rationalisation to stop the GA-MD cycle.

Figure 5.19 shows that 61 and 71 generations of a GA-MD cycle are required for the BCC and FCC variants of $\text{Al}_{0.5}\text{CoCrFeNi}$ to reach the state, when all the configurations have equal energy. For AlCoCrFeNi , the BCC and FCC phases both required 77 cycles. For BCC- CoCrFeNi , 71 generations were required, while 82 cycles were required for the FCC variant. 55 and 56 generations were required for BCC and FCC variants of CoCrFeNiTi , respectively. It should be noted that the BCC variant reaches the state when all the configurations have same energy before the FCC variants in all the cases, which is surprising since the number of atoms simulated in the BCC (1458 atoms) was slightly higher than the FCC (1372 atoms).

5.7 Gibbs free energy calculation

The expression for Gibbs free energy (G) employed in the in the present work has been obtained from Allan *et. al.* [16], where it is expressed for an isothermal-isobaric

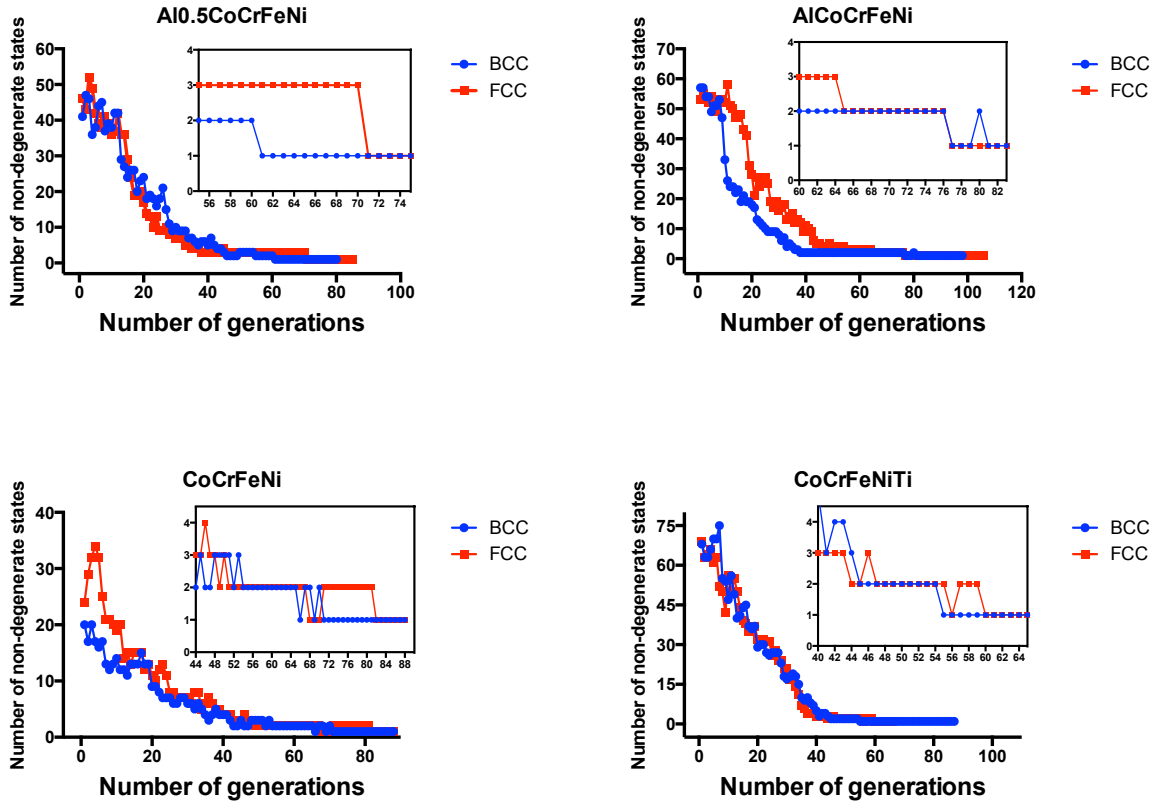


Figure 5.19: Variation of the number of configurations having different energy values with the number of generations in GA sampling [61].

Alloy	Minimum energy (eV/atom)	Average energy (eV/atom)
BCC-AlCoCrFeNi	-4.33	-4.16
FCC-AlCoCrFeNi	-4.30	-4.16
BCC-CoCrFeNi	-4.37	-4.32
FCC-CoCrFeNi	-4.33	-4.32
BCC-CoCrFeNiTi	-4.70	-4.43
FCC-CoCrFeNiTi	-4.66	-4.43
BCC-Al _{0.5} CoCrFeNi	-4.36	-4.24
FCC-Al _{0.5} CoCrFeNi	-4.32	-4.24

Table 5.6: The minimum energy of various alloy cases after sampling using GA-MD scheme and corresponding average energy of the alloy, which is the average of configurational energies of elements, as given in Table 5.5.

ensemble as:

$$G = -k_B T \ln I - k_B T \ln \left(\frac{\sum_{i=1}^I \exp\left(\frac{-G_i}{k_B T}\right)}{I} \right) \quad (5.18)$$

where, G_i is the free energy of the i^{th} configuration. The I in the above equation may be expressed as:

$$I = \frac{y!}{\prod x!} \quad (5.19)$$

where, y in the above equation represents the total number of atoms in the supercell and hence, $y = \sum_{i=1}^k x_i$ and k is the number of elements in the alloy. The x_i is the number i^{th} element. Stirling's approximation can be employed to calculate $\ln I$ instead of I , as I can be a very large number to calculate.

$$\ln I = y \ln y - \sum_{i=1}^k x_i \ln x_i \quad (5.20)$$

Now, since I can be a very large number and this many configurations is impractical to consider for many cases, instead of I , smaller numbers of configurations (I') are used for the calculation of G and equation 5.18 may be modified as:

$$G = -k_B T \ln I - k_B T \ln \left(\frac{\sum_{i=1}^{I'} \exp\left(\frac{-G_i}{k_B T}\right)}{I'} \right) \quad (5.21)$$

In the present calculation, we have employed the configurational energy of the i^{th} configuration instead of G_i used in equation 5.21. The replacement of G_i with E_i is a

difference between the Allan *et. al.* [16] approach and the present approach. As we know that $G = E + PV + TS$ and in present work we are ignoring the vibrational entropy term. Additionally, we are ignoring the PV term. However it is three orders of magnitude lower than E_i . So in the present work, Gibbs free energy may be expressed as:

$$G_{non-ideal} = -k_B T \ln I - k_B T \ln \left(\frac{\sum_{i=1}^{I'} \exp\left(\frac{-E_i}{k_B T}\right)}{I'} \right) \quad (5.22)$$

It should be noted that we are denoting this Gibbs free energy to be non-ideal, as the ideal free energy is denoted to be $G_{ideal} = H_{mean} - TS_{ideal}$, where H_{mean} is the non-Boltzmann weighted configurational energy of 2500 random configurations sampled in the present work and S_{ideal} is equal to $-k_B \sum_{i=1}^k x_i \ln x_i$ with x_i being the atomic fraction of the i^{th} element. Figure 5.20 represents the variation of the first and second term of equation 5.22 along with $G_{non-ideal}$ for all the alloy cases. It is apparent that $G_{non-ideal}$ for the BCC structure is always lower than that of FCC structure, which is not observed experimentally for $Al_{0.5}CoCrFeNi$, $CoCrFeNi$ and $CoCrFeNiTi$ at least at room temperature. We might be getting such results due to inadequacy of the EAM potential employed in the present work. We have also used the energy of the minimum energy configuration (Table 5.6) and calculated the free energy associated with it, considering it has zero configurational entropy associated with it and called it G_{GA-min} . We have plotted G_{GA-min} , G_{ideal} and $G_{non-ideal}$ for different alloys, as shown in Fig. 5.21. Additionally, Table 5.7 presents the intercept of the curves shown in Fig. 5.21 at $T = 0$ K. It is clear that G_{GA-min} is greater than $G_{non-ideal}$ at 0 K (except in the case of BCC-COCrFeNi) and this points towards the limitation of the present

Alloy	$G_{non-ideal}$	G_{GA-min}	G_{ideal}
BCC-CoCrFeNi	-4.372	-4.370	-4.367
FCC-CoCrFeNi	-4.330	-4.330	-4.326
BCC-AlCoCrFeNi	-4.327	-4.330	-4.324
FCC-AlCoCrFeNi	-4.287	-4.300	-4.280
BCC-CoCrFeNiTi	-4.680	-4.700	-4.674
FCC-CoCrFeNiTi	-4.647	-4.660	-4.638
BCC-Al _{0.5} CoCrFeNi	-4.357	-4.360	-4.354
FCC-Al _{0.5} CoCrFeNi	-4.318	-4.320	-4.314

Table 5.7: Value of $G_{non-ideal}$, G_{GA-min} and G_{ideal} at 0 K, determined by interpolating the variation of $G_{non-ideal}$, G_{GA-min} and G_{ideal} to 0 K.

GA sampling approach in finding the lowest energy structure. If both GA and random sampling procedure might have been able to find the lowest energy structure, then at $T = 0$ K, we would have expected $G_{GA-min} = G_{non-ideal}$. So, in the future work GA sampling need to be further modified, so that it might be able to find lowest energy structure.

5.8 Extension of GA-MD methodology

The above-stated GA-Md methodology can be extended to calculate the thermodynamic properties using the statistical mechanics based framework. But, the sampling procedure developed in the present work has fundamentally two crucial issues, which need to be considered to use this approach for carrying out thermodynamic integration for calculation of thermodynamic properties. The first issue is with acceptance of children and the second is selection of children which will be acting as parents in subsequent generations. In the present approach, once the swapping between two parent configurations is complete to generate two children configurations, they are accepted and are considered for the next generation depending upon their energies. Such a proce-

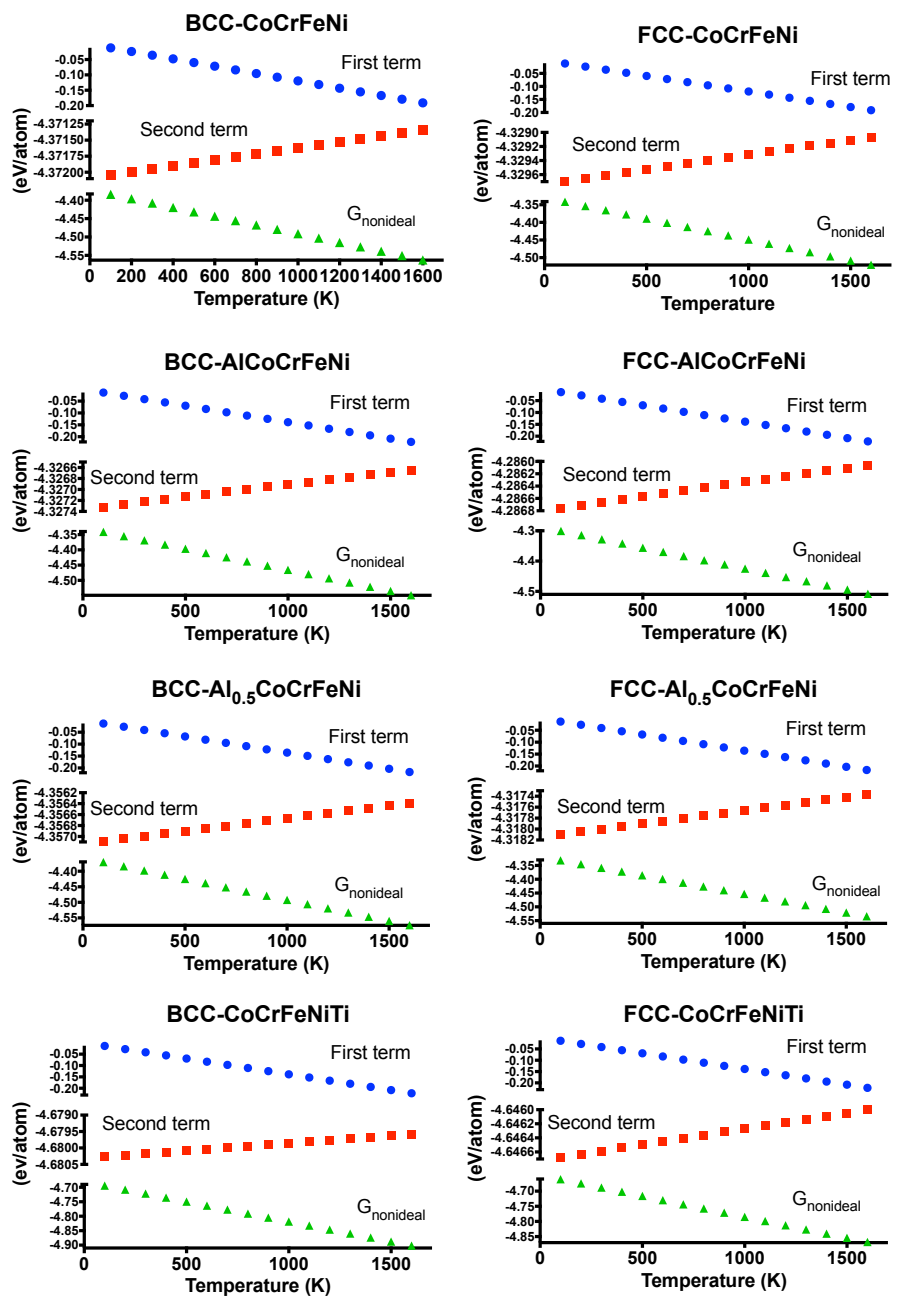


Figure 5.20: Variation of the first and second term of equation 5.22 with temperature.

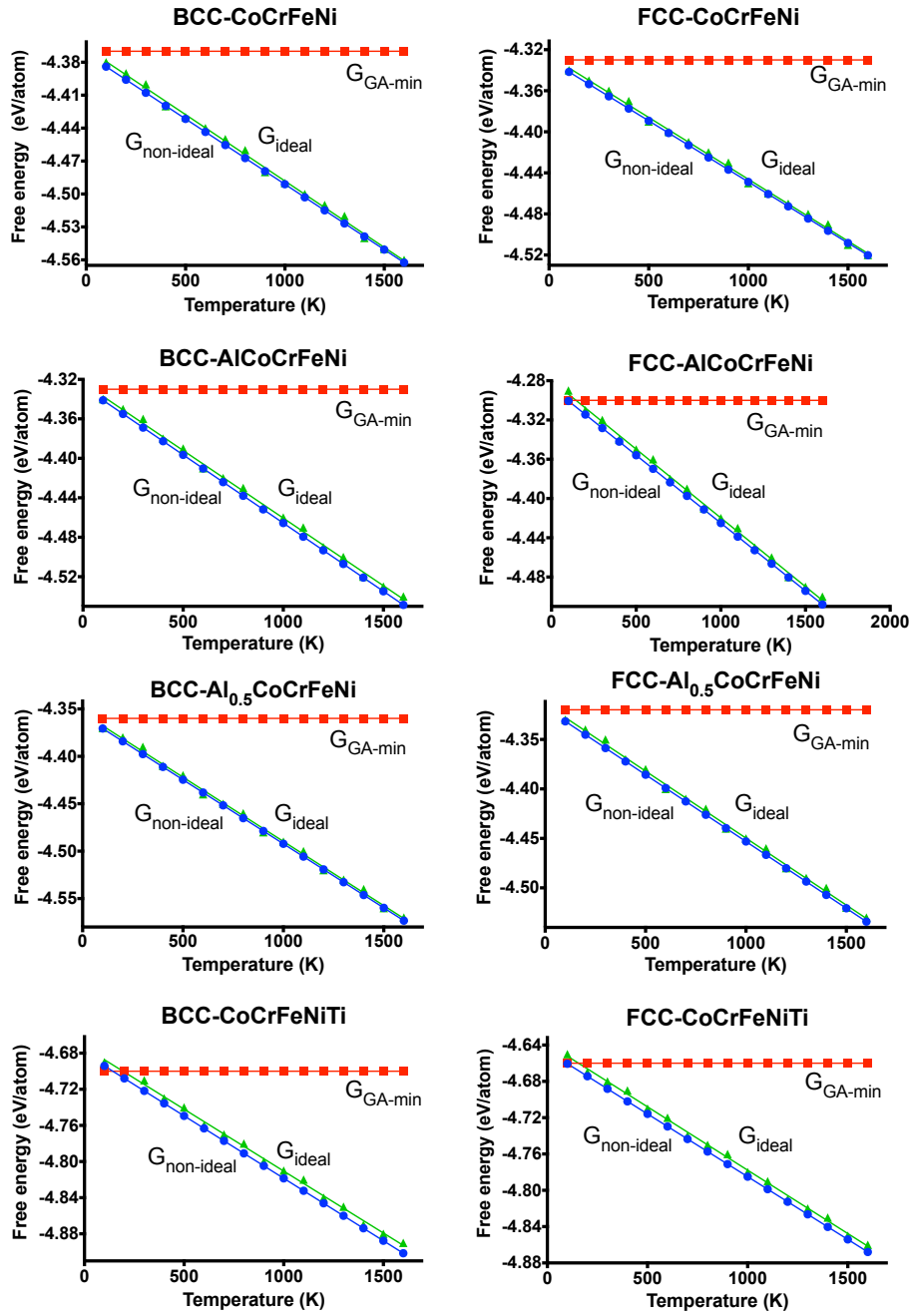


Figure 5.21: Comparison of G_{GA-min} , G_{ideal} and $G_{non-ideal}$ for different alloys with the variation in temperature.

dure might lead to incorrect statistical sampling, since the present approach biases the system to progress towards the low energy region. In the present work, the GA is only trying to find the minimum energy. But for accurate sampling, Metropolis algorithm needs to be employed, which generates the states with the probability appropriate for a Boltzmann distribution. In view of that, the Metropolis-Hastings algorithm aims to move the system towards the desired probability distribution by generating a range of states using a Markov process. In this algorithm correct statistical sampling is ensured by the fulfilment of two conditions [71, 72], which are:

1. The first condition is the existence of a stationary probability distribution, which may be ensured by enforcing the ‘*detailed balance*’ condition. Such a condition may be mathematically expressed as:

$$P(x'|x)P(x) = P(x|x')P(x') \quad (5.23)$$

where, $P(x'|x)$ is the transition probability from state x to x' and $P(x)$ is the value of probability distribution function at x .

2. The second condition is uniqueness of the stationary distribution. This condition requires the system to be aperiodic, *i.e.*, the system does not return to a particular state periodically and the system returns to its original state in finite time.

The detailed balance condition in the present model can possibly be enforced by either keeping parents or by choosing children with the probability calculated using $\left(\exp\left(\frac{-\Delta E}{k_B T}\right)\right)$.

Another important issue concerns the protocol with which parents are chosen. As, it has been mentioned in step 2, the parents for a particular generation are chosen from

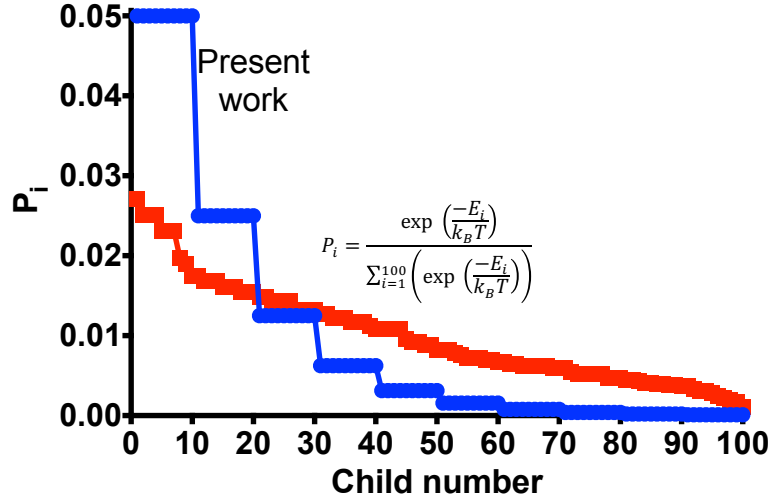


Figure 5.22: Comparison of probability of the i^{th} child (P_i) to be accepted as parent in the subsequent generation of GA using the approach developed in the present work and calculated from Boltzmann scheme. Note that probability distribution has been calculated for BCC-AlCoCrFeNi and temperature of 300 K was used while calculating the probability for i^{th} child.

children of the previous generation and the probability of acceptance of particular configuration is dependent only upon its position in the list of children when they are arranged in ascending order of their configurational energies with no dependence on temperature and their comparative energy differences, as shown in Fig. 5.22. It can be seen that the probability of acceptance of children to act as parents in subsequent generations, if statistical weighting is employed is different from probability distribution employed in the present work. So, in the future work instead of using the distribution of the present work, the probability distribution calculated using the Boltzmann approach need to be used. Additionally, a consistent temperature in selection of parents, for MD relaxation and acceptance of children.

5.9 Conclusions and future work

The present work can be summarised as:

1. An attempt was made to test the EAM force-field developed earlier and modifications were made to eradicate the problems encountered, when published force-fields were used for multicomponent alloys. The application of an elemental EAM potential to generate a multicomponent alloy EAM force-field can be questionable.
2. This study provides a methodology for determining low energy configuration of a particular alloy using a hybrid GA-MD framework.

In view of above future studies in this area may be carried out in following areas:

1. The development of reliable interatomic potential remains an issue. In the absence of EAM potentials for multicomponent alloys, several investigations have employed Lennard-Jones pair potentials [73–75]. More recently, there have been efforts to fit modified EAM (MEAM) force-fields for binaries and ternaries which form the five-component CoCrFeMnNi alloy [76, 77]. Additionally, a Meta-MD approach has been formulated for CoCrFeMnNi recently [78]. The EAM interatomic potential for AlCrFeCuNi HEA was determined using published potential parameters for Cr-Fe-Ni [79], Cu-Cu [80], Al-Al [81], while a Morse potential was employed to model the interactions between Cu-Cr, Cu-Fe, Al-Ni, Cu-Al, Al-Fe, Cu-Ni and Al-Cr [82]. Detailed comparison of these approaches needs to be carried out to determine the trade-off between theoretical rigorousness and finding an appropriate force-field scheme with a manageable number of parameters.
2. With the recent progress in the development of force-fields for multicomponent alloys, a Monte Carlo approach [83] might be used to study the phase stability in

such systems.

3. The hybrid GA-MD model developed in the present work needs to be modified to include the recommendations made in section 5.8 to ensure adequate statistical sampling and thermodynamic integration should be carried out for the accurate calculation of thermodynamic properties.

* * * * *

Chapter 6

Distortion in high-entropy oxides[†]

6.1 Introduction

As we strive to find future materials that have properties beyond those we currently use, there has been an increased interest in a materials design methodology based on multiple components for example in Li batteries [84] and thermoelectrics [85]. By increasing our number of components we massively increase the configurational space for exploration of new materials. Early attention in this field has been on metallic systems, also known as “High-Entropy Alloys” [29, 33, 86]. These systems tend to exhibit single-phase solid solutions with simple crystal structures, mostly as face-centred cubic or body-centred cubic crystal structures. Inspired by the above-stated strategy, multiple component oxides of Mg, Co, Cu, Ni and Zn, exhibiting a rocksalt-type simple crystal structures with uniform distributions of ions in the crystal have recently been synthesised [10, 87]. This was particularly surprising given that none of the constituent binary oxides show solid solubility within each other. Hence, the high configurational entropy of

[†]Part of this chapter has been published as article entitled “*Phase stability and distortion in high-entropy oxides*” for publication in *Acta Materialia* [146 (2018) 119-125].

mixing has been used to explain the formation of the single phase solid solution. This has subsequently been further supported by the formation of a multicomponent rare-earth based oxide (Ce,La,Pr,Sm,Y)O [88] and more recently, a class of high-entropy perovskite oxides has been reported [89]. This raises a clear question of how the entropy within these systems is able to overcome the presumed enthalpic penalty associated with mixing these oxides. Manipulating and controlling this entropy factor may facilitate the production of a whole new class of materials.

Although a simple rock-salt structure has been reported for the binary oxide mixes recent studies have begun to examine the structural displacements. Berardan *et. al.* [90] demonstrated that no severe lattice distortion was present in the case of multiple-component oxide when no CuO was included, i.e., $(\text{MgCoNiZn})_{0.8}(\text{LiGa})_{0.2}$. CuO containing solid solutions are particularly interesting, as Cu^{2+} ions in an octahedral coordination are expected to express a Jahn-Teller type distortion of the O^{2-} sub-lattice around them resulting in four short and two long Cu-O separations. Density functional theory calculations have shown that the Jahn-Teller distortion due to Cu^{2+} ions can be attributed to the splitting of Cu-d bands near the Fermi level [91]. Further Extended X-ray Absorption Fine Structure (EXAFS) studies have supported this distortion around the Cu^{2+} cation [92]. None of the other cations in these multicomponent oxides show such behaviour. The simple crystal structure, however, suggests there cannot be a cooperative distortion of all octahedra in a similar direction [90]. The structural displacement of ions in the unit cell of complex oxide solid solutions will potentially influence the functional properties of such materials [93] and exciting results reported for these ceramics include large dielectric constants over a range of frequencies [94] and room temperature fast ion conductivity [95]. Jahn-Teller effects in transition metal oxides can possibly lead to anisotropic transport properties [96] and it

has been shown that functional properties such as resistivity and dielectric constant can be tuned by varying the degree of distortion [90]. Therefore there is a strong interest in understanding the structural behaviour in these materials. Although informative, DFT studies [91,92] are limited to a few configurations of relatively small sizes which makes it difficult to cover the whole range of structures available to this complex mix. Classical potentials are much less expensive and therefore we can analyse a huge number of configurations and explore the different variation in structural relaxations around the cations.

Thus, in the present investigation we have performed a detailed structural analysis to determine how regular the rock-salt structure is, if any clustering or ordering occurs within the solid solution and whether particular distortions are observed around particular cations.

6.2 Simulation details

Cells were constructed from a rock-salt lattice with 1000 cations and 1000 oxide anions. All cells were fully geometry optimised (relaxing both cell and ionic positions) using the GULP code [97] before collecting any structural or energetic data. The classical Born model is assumed for oxides, where they are considered to be fully ionic and hence formal charge can be assigned to them while developing interatomic potentials for them (i.e. cations and oxides had a charge of $+2e$ and $-2e$, respectively) [98]. The Buckingham interatomic potential depicting ionic interaction between ion i and j may be expressed as [99]:

$$V_{ij}(r_{ij}) = A_{ij} \exp\left(\frac{-r_{ij}}{\rho}\right) - \frac{C_{ij}}{r_{ij}^6} \quad (6.1)$$

Interaction type	A	ρ	C
Cu ²⁺ - O ²⁻	3860.60000	0.242700	0.00
Mg ²⁺ - O ²⁻	821.600000	0.324200	0.00
Ni ²⁺ - O ²⁻	683.500000	0.333200	0.00
Zn ²⁺ - O ²⁻	499.600000	0.359500	0.00
Co ²⁺ - O ²⁻	696.300000	0.336200	0.00
O ²⁻ - O ²⁻	22764.0000	0.149000	43.00000

Table 6.1: The values of A , ρ , and C used in equation 6.1 taken from ref. [99,100].

where, the values of A_{ij} , ρ_{ij} , and C_{ij} are dependent upon the identity of ionic species, while r_{ij} depicts the distance between species i and j . The values of A , ρ , and C were taken from the literature [99,100] using cutoffs of 10 Å (Table 6.1). It should be noted that potentials employed here had been originally fitted for binary systems but were used for ternary systems by Lewis and Catlow themselves to explore variation in coordination [99]. We chose this forcefield due to the consistency with the same O²⁻ anion. All the oxides were fitted using the same short range terms for the O²⁻ anion and therefore the chemistry and physics is the same for this anion in all cases. This means that when we combine the different cations we are unlikely to encounter transferability issues. The quinary [(Co, Cu, Mg, Ni, Zn)O, quaternary [(Cu, Mg, Ni, Zn)O, (Co, Mg, Ni, Zn)O, (Co, Cu, Ni, Zn)O, (Co, Cu, Mg, Zn)O and (Co, Cu, Mg, Ni)O], ternary (Co, Cu, Mg)O, (Co, Cu, Ni)O, (Co, Cu, Zn)O, (Co, Ni, Zn)O, (Co, Mg, Zn)O, (Cu, Mg, Zn)O, (Cu, Ni, Zn)O, (Co, Mg, Ni)O, (Cu, Mg, Ni)O, (Mg, Ni, Zn)O] and binary [(Cu, Co)O, (Co, Mg)O, (Co, Ni)O, (Co, Zn)O, (Cu, Ni)O, (Cu, Mg)O, (Cu, Zn)O, (Mg, Ni)O, (Mg, Zn)O and (Ni, Zn)O] oxide-mixes were simulated in the present investigation.

6.3 Sampling methodology

We have employed several different sampling procedures for the generation of configurations.

1. *Random*: Cations were randomly assigned to the 1000 lattice points in the cells.
2. *Systematic*: Twenty different cation arrangements were initially assigned to the lattice. After each optimisation the cations were moved to the next lattice point in the structure (i.e. a Mg at lattice point 1 was moved to lattice point 2). As the lattice sites were listed randomly this procedure effectively randomly sampled configurations.
3. *Ordered*: Particular arrangements representing ordering of the cations into layers/clusters were specifically sampled to examine potential segregation of the cations.
4. *Genetic Algorithm*: In the genetic algorithm 100 configurations were randomly generated and optimised. These were then ranked based on their lattice energy with the lowest energy configuration at the top of the list. The algorithm systematically counted through the list from the top and had a 5% chance of selecting a configuration as a parent. Once two parents were selected a new configuration (child) was generated by merging the cation arrangements of the two configurations. Therefore configurations higher in the list (with lower lattice energies) were more likely to be selected for breeding. Each cation site was then given a 2% chance of mutation via swapping with another cation. 100 children were generated for each cycle and optimised to become the parents of the next generation. A total of 10 generational loops were carried out for each initial set of 100 configurations.

Mix	Number of configurations
(Mg,Co,Cu,Ni,Zn)O	23536
(Ca,Co,Cu,Ni,Zn)O	351
(Mg,Co,Cu,Ni)O	899
(Mg,Co,Cu,Zn)O	583
(Mg,Co,Ni,Zn)O	1099
(Mg,Cu,Ni,Zn)O	708
(Co,Cu,Ni,Zn)O	899

Table 6.2: Total number of configurations generated for each solid solution mix [101].

5. *Swapping*: From the previous sampling methods it was possible to identify low energy configurations. We generated a range of configurations by performing a small number of swaps between cations in the lattice from these low energy configurations with the aim of generating further low energy configurations.

In total the above-listed sampling procedures generated 23536 unique configurations for the 5-component (Mg,Co,Cu,Ni,Zn)O system. Smaller numbers of configurations were generated for the other mixes described in the paper as indicated in Table 6.2.

6.3.1 Analysis Methods

An order parameter was used to analyse the effect of potential preferential segregation/ordering of the cations within the cells and quantify the potential energy landscape being sampled by various sampling schemes employed in the present work, as explained in the above section. Within the rock-salt lattice, each cation has 12 and 6 first and second nearest neighbour (NN) cations, respectively. Therefore, in a perfectly mixed five component system, it can be expected that each cation would be surrounded by 2.4 first NN of each cation type and 1.2 second NN of each cation type. For our cells of 1000 cations with 5 components, we would therefore expect 480 first NN interactions (m_{ij} where i and j are the different cations present) for each cation type (2.4×1000

$\times 2$ (due to double counting of every pair by counting over all cations)). For each configuration we compare the actual recorded number of cation types around each cation to this ideal value via equation 6.2.

$$\text{order parameter} = \sqrt{\frac{\sum (1 - \frac{\sum m_{ij}}{n_{ij}})^2}{K^2}} \quad (6.2)$$

where, m_{ij} is the number of first NN of cation type i to j , n_{ij} is the expected number of NN of cation i to j (i.e. 480) and K is the number of different cations present. Therefore a perfect mix would produce a value of ~ 0 .

6.4 Results and discussions

Figure 6.1 shows the order parameter variation with the energy of the configurations. This shows that there is no clear link between the ordering or segregation of the materials in general and the energetics of the configuration. This implies that we are forming a disordered solid solution mix and particular low energy configurations are not dominating the population. Note that two regions of order were formed due to the different sampling strategies employed.

We can extend this analysis further by examining the frequency of particular first nearest-neighbour (NN) cation pairs in the lattice during systematic sampling to determine if particular cation types will preferentially segregate. For nearly all the cation pairs we see no energy dependence on the number of pairs and they display similar plots to that of Ni-Ni as shown in Fig. 6.2, where the number of Ni²⁺-Ni²⁺ pairs has no correlation to the energy of the configuration. The only pairs where a correlation is observed is for Cu²⁺-Cu²⁺, where the energy lowers as the number of these pairs

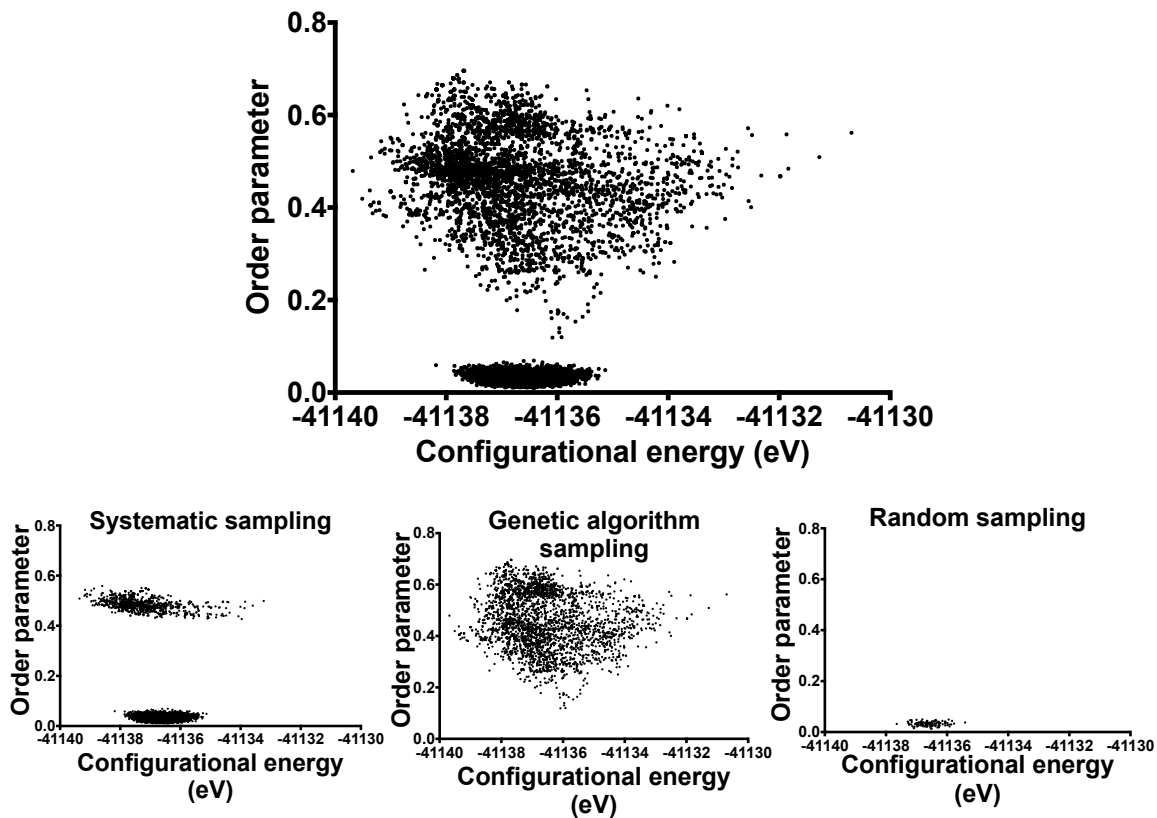


Figure 6.1: Variation of order parameter with configurational energy for various schemes of sampling methodology [101].

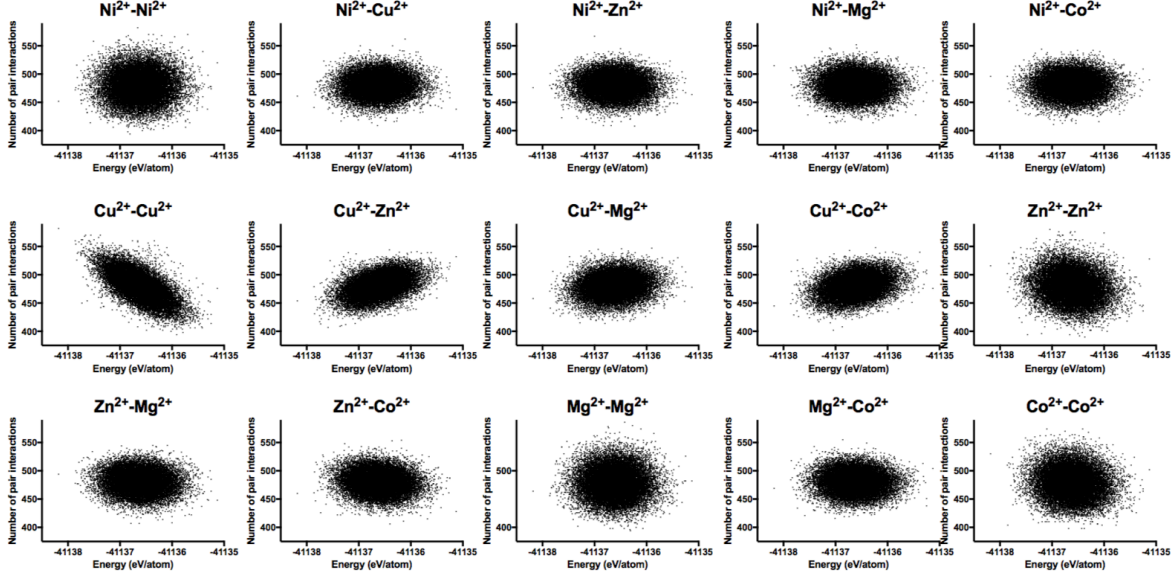


Figure 6.2: Variation of number of cation-cation pairs with their corresponding configurational energy with systematic sampling [101].

increases and $\text{Cu}^{2+}\text{-Zn}^{2+}$, where there is a weak correlation suggesting that more $\text{Cu}^{2+}\text{-Zn}^{2+}$ pairs increases the energy of a configuration. Additionally, we have plotted the frequency of particular first NN cation-pairs in the lattice during GA sampling. We observed the similar nature of distribution of points for $\text{Cu}^{2+}\text{-Zn}^{2+}$ and $\text{Cu}^{2+}\text{-Co}^{2+}$ pairs. But, since the number of sampling points were less in the case of GA sampling (3867) than systematic sampling (19542), the distribution of points seems irregular in case of GA sampling.

Figures 6.4(a) and 6.4(b) show the average cation-cation and cation-oxygen separations in the lattices respectively. For the five-cation ceramic, we get an average separation of 2.08 Å for the cation-oxygen and 2.94 Å for the cation-cation which are both in excellent agreement with the experimentally reported values [92]. As can be seen in Fig. 6.4(a) the cation-cation separations are generally similar for all the cation

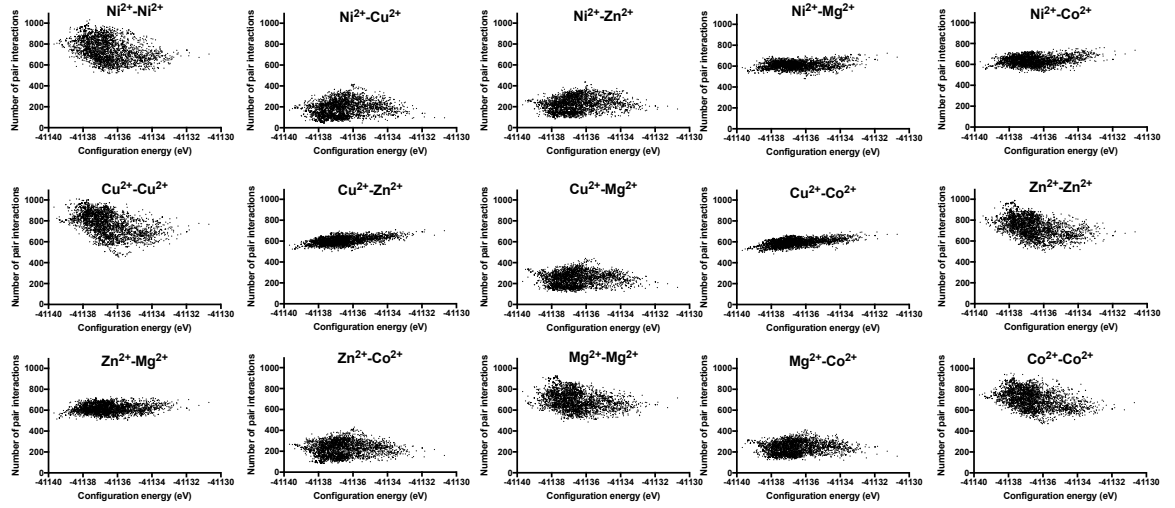


Figure 6.3: Variation of number of cation-cation pairs with their corresponding configurational energy for genetic algorithm based sampling.

pairs with the exception of those involving Cu^{2+} which are significantly shorter. When we examine the separations in the 4-cation systems the values are very similar to the 5-cation case except when Cu^{2+} is absent, *i.e.* $(\text{Co},\text{Mg},\text{Zn},\text{Ni})\text{O}$, where we observe all the separations increase by $\sim 0.02 \text{ \AA}$. A similar effect can be seen for the cation-oxygen separations where the Cu-O separation is much shorter than the other cation-oxygen separations. The cation-anion separation also increases when CuO is removed from the mix to make $(\text{Co},\text{Mg},\text{Zn},\text{Ni})\text{O}$.

Berardan et. al. [90] have reported that a Jahn-Teller effect may be present for the Cu^{2+} cation which leads to the shorter Cu-O separations and causes a bi-modal distribution of separations. More detailed examination of our data in the five cation systems for $\text{Cu}^{2+}-\text{O}^{2-}$ does show a possible two hump distribution with the first peak around 2.02 \AA and the second at 2.07 \AA (Fig. 6.5). The distribution is more concentrated at shorter distance, which again agrees with experiment. The classical nature

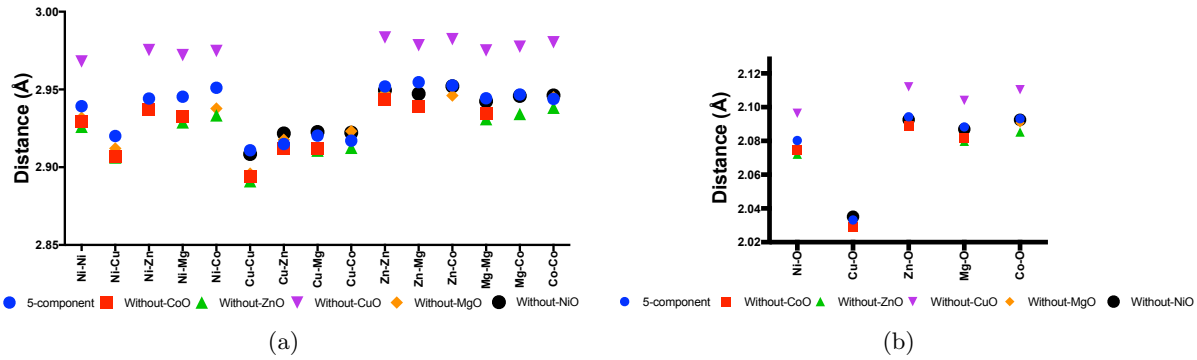


Figure 6.4: Bond-length variation for (a) cation-cation pairs and (b) cation-anion pairs [101].

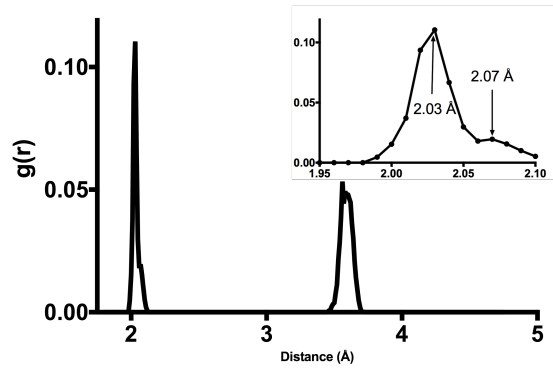


Figure 6.5: The radial distribution function ($g(r)$) corresponding to the Cu^{2+} - O^{2-} [101].

of our simulations where our ions are treated as hard spheres means that no explicit electronic effects are included and thus the Jahn-Teller effect cannot be directly modelled. This means the effect we are observing here is caused by a distortion of the local structure around the Cu^{2+} , simply due to the smaller size of the Cu^{2+} cation compared to the other cations. This implies that the experimentally reported effect may be a combination of both Jahn-Teller and/or simple size arguments.

The standard deviations of the cation-oxygen and cation-cation separations are shown in Figure 6.6(a) and 6.6(b) respectively. It can be clearly seen that, in the case of the oxide mix which does not contain CuO , *i.e.*, $(\text{Co}, \text{Mg}, \text{Ni}, \text{Zn})\text{O}$ the average

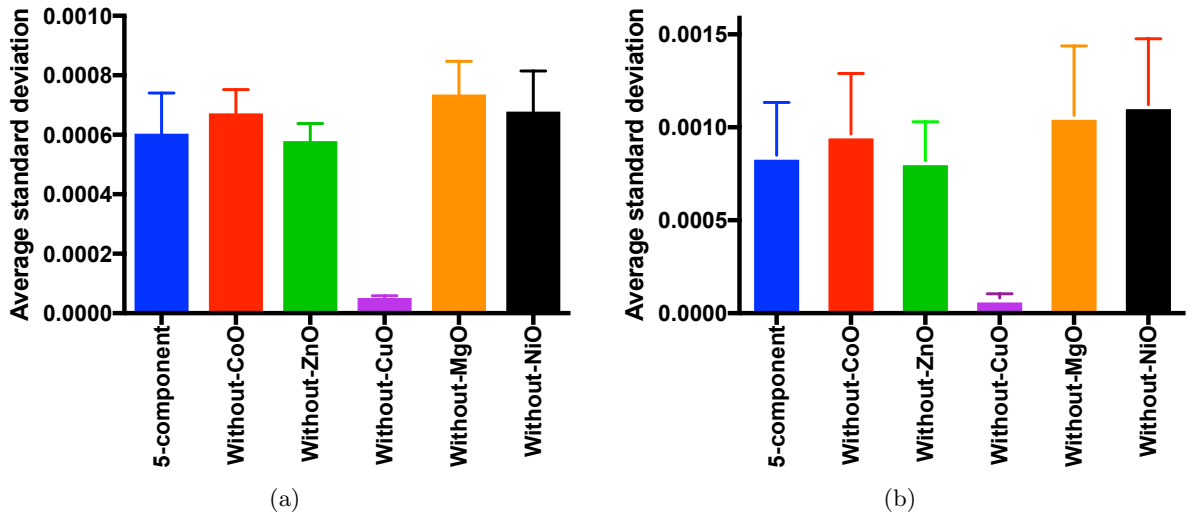


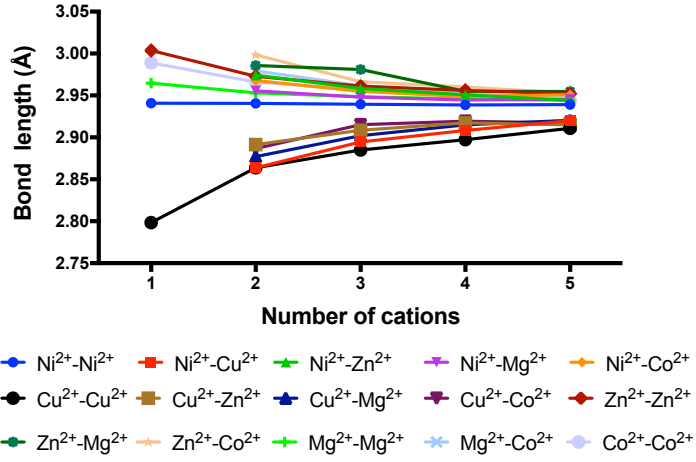
Figure 6.6: Average standard deviation (in Å) for bond-length variation for (a) cation-cation and (b) cation-anion pairs [101]. The average standard deviation was calculated by taking average of the standard deviation of all ionic separation forming a particular oxide-mix. For *e.g.*, in the case of 5-component mix, *i.e.*, (Co,Cu,Mg,Ni,Zn)O, average over standard deviation in 15 bond-length including $\text{Co}^{2+}\text{-Co}^{2+}$, $\text{Co}^{2+}\text{-Cu}^{2+}$, $\text{Co}^{2+}\text{-Mg}^{2+}$, $\text{Co}^{2+}\text{-Ni}^{2+}$, etc are used for calculation of average standard deviation.

standard deviation for the same oxide mix is smallest. The cation-anion and cation-cation separations become longer and far more regular when no Cu^{2+} is present. The presence of Cu^{2+} with its shorter separations clearly causes larger disruptions to the surrounding lattice leading to more variability in other separations. When CuO is removed, all separations become more regular with less local variation.

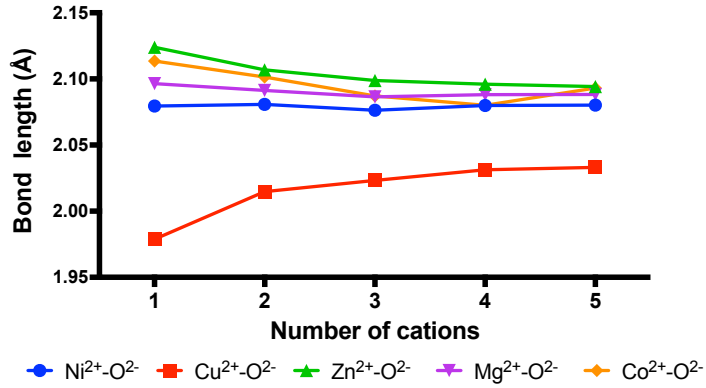
The results for the 4 and 5 component ceramic systems suggest that as the number of cation components in the system is increased we drive the system towards becoming a better solid solution where all the atoms sit in similar environments and therefore the disorder in the system is encouraging further disorder. To pursue this concept further we performed a small set of random sampling on all the 2 and 3 component systems that can be formed from the Mg, Co, Zn, Cu and Ni oxides. These small runs produced

between 50-1000 configurations which were used to produce values.

Figure 6.7(a) shows the average separations between each cation pair in the configurations with the total number of different cations. As might be expected there is a gradual convergence of the separations as the number of different cation types increases. As we add a new cation into a solid solution, that particular cation is forced into the local environment of the solid solution. So in the case of adding NiO to CoO, the Ni²⁺ enters an environment with cation-cation separations of 2.99 Å where it would want 2.94 Å, which leads to substantial disruption to the surrounding lattice. If we add NiO to (Co,Mg)O the separations are now 2.98 Å. NiO inserted into (Co,Mg,Cu)O is entering an environment with separations at 2.92 Å. (Co,Mg,Cu,Zn)O has separations of 2.94 Å. We can see that the mixing creates an average environment that matches better to that of new cations. Coupled to this, the diversity of cation sites increases as more cation types are added as can be evidenced by the increase of the standard deviation of separations as the number of cation types is increased (Table 6.3). Therefore we are generating more different local environments that can accommodate new cation types e.g., the addition of NiO to the (Co,Mg,Cu)O solid solution might seek out sites with more surrounding Cu²⁺ since the Cu²⁺ cation wants shorter cation-oxygen separations and can therefore accommodate the longer Ni-O separations more readily (Fig. 6.7(b)). As we increase the number of components our system becomes more disordered and therefore the penalty of further disorder from further additions is reduced. A similar effect will occur in other multi-component solid solutions as is observed in ceramic systems.



(a)



(b)

Figure 6.7: Variation in bond-length with increase in number of cations for (a) cation-cation and (b) cation-anion pairs [101].

Number of Cations	Standard Deviation
1	0.0
2	0.0003
3	0.0004
4	0.0005
5	0.0006

Table 6.3: Average standard deviation of the cation-cation separations with different numbers of cations in the configuration [101].

6.5 Conclusions

The following conclusions can be drawn from the present investigation:

1. The solid solution does not show any particular ordering or segregation except in the case of $\text{Cu}^{2+}\text{-Cu}^{2+}$ and $\text{Cu}^{2+}\text{-Zn}^{2+}$ pairs. Lower $\text{Cu}^{2+}\text{-Cu}^{2+}$ pairs were seen in higher energy configurations, while larger numbers of $\text{Cu}^{2+}\text{-Zn}^{2+}$ bonds were present in high energy cases.
2. Nearest-neighbour distance analysis showed that lowest cation-cation and cation-anion bond length with minimum variation was seen in the case of $\text{Cu}^{2+}\text{-Cu}^{2+}$ and $\text{Cu}^{2+}\text{-O}^{2-}$, respectively.

The future work in this area should be concentrated on the extension of sampling process as presented in section 5.8 for calculation of thermodynamic properties of high-entropy oxides.

* * * * *

Chapter 7

Lattice Friction in Substitutional Alloys

7.1 Introduction

Dislocation movement in metallic materials is the principal mechanism of permanent or plastic deformation. The disruption of dislocation motion in solid solutions due to the addition of solutes leads to solid solution hardening. Such hardening is caused by the fact that it is more difficult to move dislocations in alloys than it is in pure metals, as lattices of alloys provide an inherent resistance or friction for dislocation movement and lead to alternative deformation modes such as deformation twinning. Such lattice friction is a fundamental parameter, which might act as a starting point for *a priori* prediction of mechanical properties of engineering alloys.

As we have mentioned earlier, there has been significant interest in the development of a newer class of multicomponent alloys known as ‘High-Entropy Alloys (HEA)’ [29,33,102]. These alloys tend to exhibit simple crystal structures, such as face-centred

cubic (FCC), body-centred cubic (BCC), hexagonal closed packed (HCP) in as-cast form. The FCC form has been extensively studied at low temperatures and the CoCrFeMnNi alloy has shown improved fracture toughness, along with improved strength and elongation at cryogenic temperatures in comparison with properties at room temperature [1, 103, 104]. In addition improved fatigue properties have been reported for this alloy [105]. Similar behaviour has been reported in the six-component VCrMnFeCoNi high-entropy alloy [106]. The attractive structural properties of these alloys have been attributed to deformation twinning taking place at cryogenic temperatures, as the critical resolved shear stress (CRSS) for twinning becomes lower than that of dislocation movement [107]. Further improvement in structural properties was reported for a medium-entropy system (CoCrNi), where fracture toughness, yield strength and fracture elongation of $275 \text{ MPa}\cdot\sqrt{m}$, 1.3 GPa and 90%, respectively were found. The CoCrFeMnNi alloy, by contrast showed fracture toughness of $200 \text{ MPa}\cdot\sqrt{m}$, yield strength of 1.28 GPa and fracture elongation of 70 % [1]. The improvement in properties of CoCrNi at cryogenic temperatures in comparison with the CoCrFeMnNi has been attributed to the easier triggering of nano-twinning activity in CoCrNi due to its higher yield strength and work hardening rate, which allows the achievement of twinning stress earlier [108]. There has been significant interest in the determination of the strengthening mechanisms in such multicomponent alloys, with an aim of designing newer alloys with improved structural properties [109–111] requiring elucidation of the mechanisms [86]. Fundamentally, solutes can interact with a dislocation in two ways. The first type of dislocation-solute interaction involves the altering of the topology and structure of the dislocation-core [112] and the second type considers only the interaction, which leaves the structure of dislocation core intact. The study of the first type requires the development of understanding on a case-to-case basis and a generalised rule is not possible.

For the second type an attempt may be made for finding rules for interactions and their consequent effect on the structural properties.

The dislocation-solute interaction without core-reconstruction can be further divided into various categories, namely, first-order interactions, second-order interactions, electrical interactions, chemical interactions, etc. [113]. A first-order interaction is modelled within the continuum framework, where the dislocation-solute interaction is long-ranged. Also the distortion due to volume misfit is assumed to be spherically symmetric. The second-order interaction takes into account the non-linear variation in the elastic properties, possibly due to anharmonic effects. Additionally, such interactions need to be taken into account, when the elastic properties of a solute, such as shear modulus (G) and Poisson's ratio (ν) are significantly different those of from the matrix. The electrical interactions arise due to the dilatational field of the dislocation and the different valency of the solute in comparison to that of the solvent. But, such interactions make limited contributions in metals. The chemical or *Suzuki-interactions* arise from solutes and extended dislocations, where a stacking fault between a partial dislocation has different solubility from the surroundings causing preferential segregation and consequent short-ranged interaction between solute and dislocation.

In this investigation, we wish to explore the alloying effects on dislocation movement using a rapid calculation method that allows us to remove much of the complexity to enable rapid predictions. Therefore, we attempt to model the dislocation-solute interaction and its effect on the dislocation mobility using only first-order interactions. We do not consider dislocation-core effects, a single Volterra dislocation has been considered and the solute is assumed to be an elastic inclusion. Note that the Volterra's description of dislocation considers dislocation to be an elastic discontinuity in a homogenous elastic medium, which is linear response. In this scheme atomistic information is not

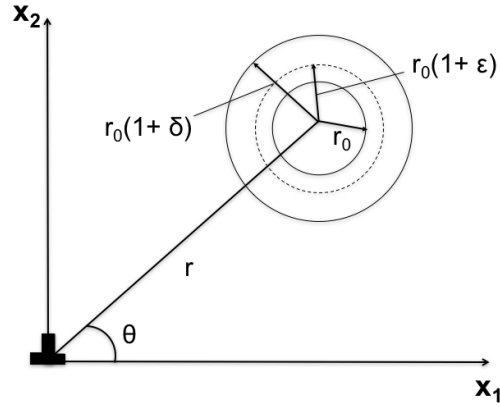


Figure 7.1: Schematic representation of the first-order dislocation-solute interaction, redrawn from ref. [113].

considered. Figure 7.1 shows the schematic representation of a first-order dislocation-solute interaction. In this case, if the solute of radius $r(1 + \delta)$ is introduced into the hole of radius r_0 , which attains radius of $r(1 + \epsilon)$ after relaxation, the interaction energy between the dislocation and the solute (E_{FO}) may be expressed as:

$$E_{FO} = -\delta \int_V p dV \quad (7.1)$$

where, p is the hydrostatic stress due to the dislocation, V represents the volume of the undeformed cavity and δ is related to the ϵ by [113] as:

$$\delta = \frac{3\epsilon(1 - \nu)}{1 + \nu} \quad (7.2)$$

7.1.1 Solution hardening models

Solid strengthening due to dislocation-solute interactions is described by two contrasting theories: First there is the strong-pinning or Friedel and Fleischer's theory [114,115] and second there is the weak-pinning or Labusch's theory [116]. Friedel and Fleischer's theory considers the individual lattice points on glide planes to be the only pinning points. These pinning points are characterised by their resistive force (F), which acts on the dislocation line and causes its bending. The temperature-independent yield strength in Friedel's theory (Y_F) is given as:

$$Y_F = \left(\frac{F}{2\Gamma} \right)^{3/2} \left(\frac{2\Gamma}{b^2} \right) c^{1/2} \quad (7.3)$$

where Γ is the line-tension of the dislocation, which quantifies the tendency of the dislocation to maintain its 'straightness', while b is the Burgers vector of the dislocation. The c in the above equation is the concentration of the solute. It is clear that Friedel and Fleischer's theory does not consider atoms which are not in the glide plane and the collective behaviour of solutes is not considered.

In view of the above, a statistical theory of solid solution strengthening was proposed by Labusch [116], where pinning takes place due to favourable statistical fluctuations of solute compositions around the dislocation line. The temperature-independent yield strength in Labusch's theory (Y_L) may be represented as:

$$Y_L = \left(\frac{F^4 w}{4\Gamma b^7} \right)^{1/3} c^{2/3} \quad (7.4)$$

where, w represents the range of dislocation-solute interaction. Comparing equation 7.3 and 7.4, it can be deduced that yield strength scales to $1/2^{th}$ power of composition

in strong-pinning theory, while in weak-pinning theory strength varies as $2/3^{rd}$ power of composition. The transition from strong-to-weak pinning can be quantified by the parameter ‘ β ’ [116], which may be obtained as a ratio of Y_F and Y_L :

$$\beta = \frac{Fb^2}{4\Gamma cw^2} = \frac{Y_F}{Y_L} \quad (7.5)$$

At the strong-to-weak pinning transition, $\beta = 1$, and hence, a critical composition of the solute (c_{crit}) may be expressed as:

$$c_{crit} = \frac{Fb^2}{4\Gamma w^2} \quad (7.6)$$

The typical value of c_{crit} is ~ 0.01 [117], which leads to the observation that the applicability of these theories depends upon the composition range. At dilute compositions strong-pinning theory is applied, while at higher concentrations Labusch’s theory needs to be used. But, the Friedel model needs to be applied to cases where the solutes significantly alter the dislocation structure and the interaction energy is in the range of 1 eV [118], as this is the scenario of strong-pinning. Note that the energy range for applicability of Labusch’s approach lies in range of $\sim 100 - 200$ meV [117].

It should be noted that both the weak-pinning and the strong-pinning theory have their own shortcomings. The weak-pinning theory only considers the solute atoms in the glide plane and long-ranged interactions are simply not considered. In the Labusch’s weak-pinning model, an arbitrary parameter, *i.e.*, ‘ w ’ needs to be considered (equation 7.4). The need for this arbitrary parameter arises from the fact that dislocation-solute interactions have a $1/r$ dependence, but it should be noted that the interaction between dislocation and solute due to positive or negative Cottrell-interactions (I) [119] is given

as:

$$I = -\frac{(1 + \nu)Gb(\Delta r/r)\Omega z}{\pi(1 - \nu)r^2} \quad (7.7)$$

where, z in the above equation represents one of the Cartesian coordinates. It can be deduced that I has $1/r^2$ dependence. Figure 7.2(a) shows the variation of $1/r$ and $1/r^2$, and Fig. 7.2(b) shows the variation of $\ln(r)$ and $-1/r$, which are the integrals of $1/r$ and $1/r^2$, respectively. It can be seen that the difference between the integral of $\ln(r)$ and $-1/r$ increases with r . Labusch's approach had primarily aimed to resolve this issue by introducing the arbitrary 'cut-off' parameter, w , as mentioned above. The quantification of w remains an issue of concern, as an attempt to determine its value from molecular statics simulations has not yielded reliable methods for its determination [120]. Additionally, the ' F ' parameter of equation 7.4, which quantifies the pinning capability of the solute determined from Labusch's theory is 2-3 times larger than the case, when this parameter is determined by fitting the theoretical expression with experimental results [117, 119]. Hence analytical Labusch's theory has limited applicability in quantitative prediction.

Even with the issues associated with the Labusch's theory, it has traditionally been used for the development of generalised solid solution strengthening models [121, 122] and more explicitly for copper alloys [123, 124], Al alloys [125, 126] and more recently to HEA [109, 127]. In view of the above, a more generalised theory for solid-solution strengthening has been proposed by Curtin *et. al.* [110, 128]. This model extracts its philosophical background from the Embedded-Atom-Method in classical simulation calculations [48], the Coherent potential approximation [129] and the Virtual Crystal Approximation [130] from electronic structure theory. In this theory, first of all an "effective-medium" is defined with properties such as lattice constant, elastic proper-

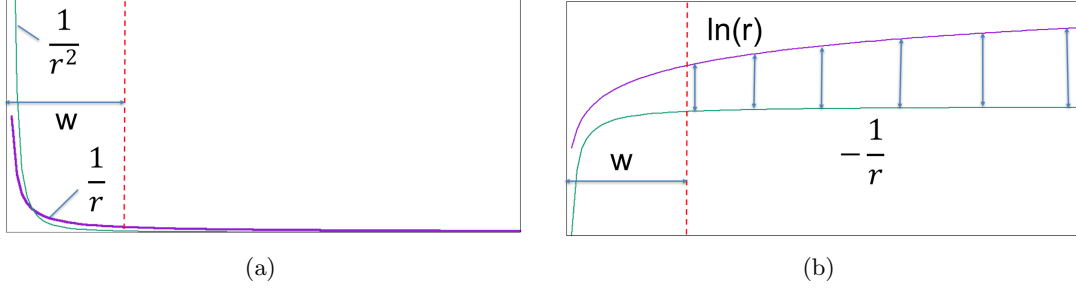


Figure 7.2: (a) Schematic figure of variation of function with $\frac{1}{r}$ and $\frac{1}{r^2}$ and (b) variation of $\ln(r)$ and $-\frac{1}{r}$, which is obtained from integration of $\frac{1}{r}$ and $\frac{1}{r^2}$, respectively. w represents the cut-off parameter defined in the Labusch's theory (equation 7.4).

ties and stacking fault energies, which are an average of the properties of elements forming the alloy. It is considered that the interaction energy of the dislocation with solute arises from elastic interactions between the dislocation and the volume-misfit plus specific interactions between dislocation core and solute. If a dislocation segment of length ' ζ ' is moved by length ' w ' (Fig. 7.3), then the change in the potential energy ΔU_t is given as:

$$\Delta U_t(\zeta, w) = \sum_n \sum_{i,j,k} s_{i,j,k}^n [U^n(x_i - w, y_j, z_k) - U^n(x_i, y_j, z_k)] \quad (7.8)$$

where, $s_{i,j,k}^n$ has a value of 1, if the solute of type n is present at coordinate (x_i, y_j, z_k) and 0, if that is not the case. As the dislocation moves through the random solute field, there is a change in the potential energy which is quantified by standard deviation of $\sigma_{\Delta U_t}$, which may be expressed as:

$$\begin{aligned} \sigma_{\Delta U_t(\zeta, w)} &= [\langle \Delta U_t^2 \rangle - \langle \Delta U_t \rangle^2]^{1/2} \\ \sigma_{\Delta U_t(\zeta, w)} &= \left(\frac{\zeta}{\sqrt{(3)b}} \right)^{1/2} \Delta \tilde{E}_p(w) \end{aligned} \quad (7.9)$$

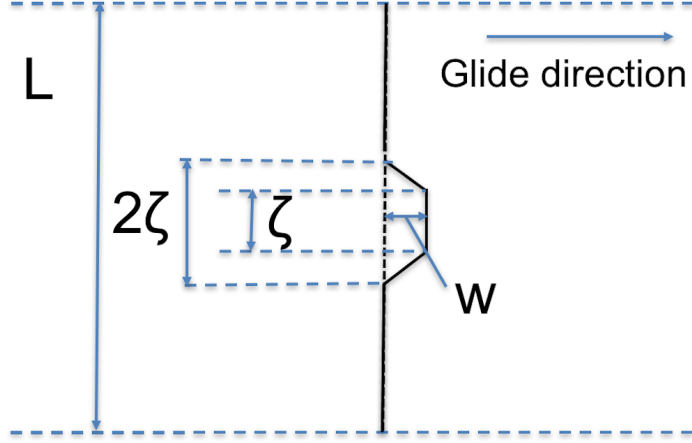


Figure 7.3: Schematic representation of dislocation moving in a glide plane, redrawn from ref. [110]. w is the amplitude of the fluctuation of length 2ζ on the dislocation of length L .

where,

$$\Delta\tilde{E}_p(w) = \left[\sum_n \sum_{i,j} c_n (\bar{U}^n(x_i - w, y_j) - \bar{U}^n(x_i, y_j))^2 + \sigma_{\Delta U_{i,j}^n}^2 \right] \quad (7.10)$$

where, $\bar{U}^n(x_i, y_j)$ is the average value of the dislocation-solute interaction energy, when the average is carried out along the dislocation line and $\sigma_{\Delta U_{i,j}^n}$ is the additional standard deviation of the interaction energy in the effective medium matrix. Note that the standard deviation contains the information about energetic effects of random solute fluctuations as the dislocation moves through a random alloy's lattice. Also, it should be emphasised here that $\sigma_{\Delta U_t}$ contains information about the statistical fluctuation of the interaction energy along the z -direction (when the dislocation is in the x - y plane) due to a random solute field, while $\sigma_{\Delta U_{i,j}^n}^2$ simply provides the information of standard deviation of the interaction energies due to randomness of the alloy. The total energy (E_{tot}) of the dislocation in the lattice has two terms: the first is the energetic contribution due to bowing of the dislocation given as $\frac{\Gamma w^2}{2\zeta} \frac{L}{2\zeta}$ or ΔE_{LT} , where Γ is the line-tension of the dislocation. The second is the contribution of the standard deviation of potential

energy as the dislocation segment of length, ‘ ζ ’ moves by ‘ w ’. So,

$$\Delta E_{tot} = \left[\frac{\Gamma w^2}{2\zeta} - \left(\frac{\zeta}{\sqrt{3}b} \right)^{1/2} \Delta \tilde{E}_p(w) \right] \frac{L}{2\zeta} \quad (7.11)$$

The equilibrium value of w (w_c) and ζ (ζ_c) is determined by minimising the above equation with respect to the particular variable. w_c is determined solely by the potential energy function $\tilde{E}_p(w)$. \tilde{E}_p is not an explicit function of w and hence, w_c needs to be determined numerically. It should be noted that this model does not provide a robust method of determination of w and it should be recalled that similar issues were encountered in Labusch’s model. Additionally, ζ_c is determined by the minimisation of $\Delta \tilde{E}_p$ with respect to ζ and given as:

$$\zeta_c(w) = \left(4\sqrt{3} \frac{\Gamma^2 w^4 b}{\Delta \tilde{E}_p^2(w)} \right)^{1/3} \quad (7.12)$$

Above is then used to get w_c . Now, the total energy barrier of the dislocation movement is given as the difference between the total energy required for moving from one position to another by length ‘ w_c ’ and the energy due to line tension of the dislocation (ΔE_{LT}), which may be written as:

$$\Delta E_b = E'_b - \Delta E_{LT} = 1.22 \left(\frac{w_c^2 \Gamma \Delta \tilde{E}_p^2(w_c)}{b} \right)^{1/3} \quad (7.13)$$

where, E'_b is the amplitude of the sinusoidal variation of potential experienced by the dislocation-segment, ζ_c , as it traverses through the crystal [131]. The value of ΔE_b can be further used to determine the effect of temperature and strain-rate for prediction of yield strength. This model has been extensively used to predict the structural properties

of Al alloys [128, 131] and more recently to high-entropy alloys (HEAs) [110, 132, 133]. Application of such a model to HEAs has proven successful for predicting the yield strength at ambient temperatures, while quantitative disagreement at lower temperatures (*i.e.*, $< 77K$) was seen, which was attributed to neglecting the atomic level fluctuations along the dislocation line. It should be noted that one of the basic assumptions of Curtin’s model is $w_c \ll \zeta_c$ and hence the above-stated issue cannot be resolved by Curtin’s model, as at low temperature possibly, $w_c \simeq \zeta_c$. Also, this model requires the determination of Γ and w , which requires atomistic or DFT simulations, which can be computationally expensive.

In view of the above, to achieve the attractive mechanical properties in multi-component alloys, an understanding of dislocation movement is desired, which in turn requires the thorough understanding of lattice friction in a range of alloys. The theory of dislocation movement in concentrated multicomponent alloys has been discussed in terms of an elasticity model, where the interaction energy of the solute atom at position (x_i, y_i) relative to the dislocation line can be simply expressed as $-P(x_i, y_i) \cdot \Delta V$; where $P(x_i, y_i)$ is a pressure field, due to the dislocation and ΔV is the misfit volume of the solute with reference to the “effective medium matrix” [110]. In such a model, the impedance of dislocation movement arises due to composition fluctuations in the effective medium. We have carried out this work within the first-order approximations, as mentioned in subsection 7.1.1 before without considering the line-tension of the dislocation in order to develop a computationally cheap method of qualitative determination of lattice friction in substitutional alloys. Here, we have carried out Monte Carlo (MC) simulation on the basis of the energy of an edge dislocation in the FCC lattice, calculated from the continuum elasticity relation. An edge dislocation has been considered, as the hydrostatic component of elastic stress of an edge dislocation

interacts strongly with the hydrostatic component of stress due to substitutional atoms introduced in the system, owing to size-mismatch. We have considered that “effective-medium” to be isotropic and the solute maintains its spherical shape to ensure that only edge dislocation-solute interaction takes place [113].

The approach being taken in the present work can be understood in line with the classical theory described to define the motion of the dislocation through crystal lattice. One of the earliest model to describe the dislocation motion is attributed to Peierls and Nabarro [134], which may be expressed as:

$$\frac{W_p}{L} = \frac{Gb^2}{2\pi(1-\nu)} \exp\left(-\frac{4\pi w}{b}\right) = \frac{Gb^2}{2\pi(1-\nu)} \exp\left(-\frac{2\pi d}{b(1-\nu)}\right) \quad (7.14)$$

where G , b , ν , w , and d are shear modulus, Burgers vector, Poisson’s ratio, width of dislocation core and distance between planes on glide planes, respectively. In this model, the dislocation experiences an oscillatory potential as it traverses through the crystal lattice, which is:

$$\frac{W}{L} = \frac{W_p}{L} \sin^2\left(\frac{\pi x}{b}\right) \quad (7.15)$$

where x is the above equation is depicting dislocation displacement. The Peierls stress is defined to be the maximum slope of this oscillatory potential. Physically, Peierls stress is considered to be the stress required for a dislocation to move in a crystal at 0 K and this stress is a measure of the lattice friction.

The phenomenological origin of the Peierls-Nabarro model can be understood in terms of a dislocation in metastable equilibrium, when it lie in one of the valleys of the energy landscape (as shown as region ‘1’ in Fig. 7.4) and stress is required for moving a dislocation from one valley to another. The Peierls-Nabarro explains qualitative trend of decrease in Peierls stress with increase in dislocation-core width (w). Additionally, a

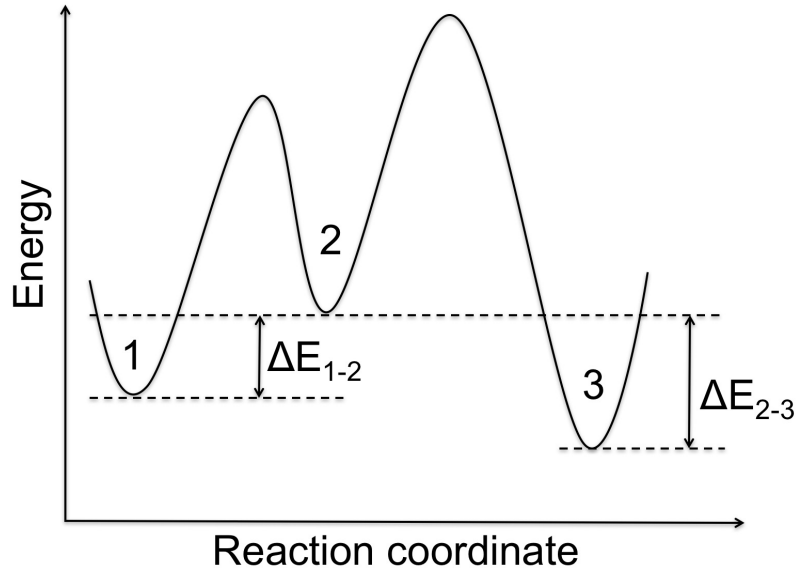


Figure 7.4: Schematic representation of energetic barrier associated with dislocation migration and the part of the barrier, which is being considered in the present investigation is marked as ΔE_{1-2} and ΔE_{2-3} , when dislocation moves from 1 to 2 and 2 to 3 respectively.

lower value of b and a higher value of w corresponds to that of the slip plane, on which dislocation movement would be energetically favourable. The simple form as described in the equation 7.14 is valid for cases where dislocation core is planar and lies on the slip-plane. But if the dislocation core is non-planar, atomistic calculations need to be carried out to determine the Peierls stress [135–137]. In the context of the present work, we have studied the influence of the dislocation-core and we have also not considered the full barrier for dislocation movement as shown in Fig. 7.4. It should be noted that the effect of compositional fluctuation in random alloys is being studied in this work, and therefore we are considering the part of the barrier to movement caused by the misfit volume as indicated in Fig. 7.4 and instrumental in causing pinning [110,117].

7.2 Method

The FCC lattice was generated by the following analytical formula (% in equation 7.16, 7.17, 7.18 is the Modulo operator):

$$x = \begin{cases} \{2 \cdot i + (j\%2)\} \cdot r, & \text{if } (k\%3) = 0 \text{ or } 2 \\ [2 \cdot i + \{1 - (j\%2)\}] \cdot r, & \text{if } (k\%3) = 1 \end{cases} \quad (7.16)$$

$$y = \left[\frac{[j + \{(k\%3)/3\}]}{\sqrt{3}} \right] \quad (7.17)$$

$$z = \left\{ \frac{(2 \cdot k \cdot \sqrt{6})}{\sqrt{3}} \right\} \cdot r \quad (7.18)$$

Figure 7.5(a) shows the FCC lattice with the edge dislocation in the middle of the supercell. The 40 X 20 X 20 supercell was generated along x, y, and z directions respectively. The edge dislocation was introduced in the middle of the supercell, by removing the row of atoms below it and moving the rows of atoms close to each other. Note that no relaxation is carried out in this work. Figure 7.5(b) shows a three-dimensional schematic representation of the dislocation in the supercell and the points correspond to the core of the dislocation. Since, the pressure field (P) around the edge dislocation is the sum of the three principal stresses, it can be expressed by equation 7.19 as:

$$P = -\frac{(\sigma_{11} + \sigma_{22} + \sigma_{33})}{3} = \frac{G \cdot b}{3\pi} \cdot \frac{1 + \nu}{1 - \nu} \cdot \frac{-z}{x^2 + z^2} \quad (7.19)$$

where, G , ν , and b represent the shear modulus, Poisson's ratio and Burgers vector respectively. The values for G and ν for alloys were taken from ref. [138] and presented in Table 7.1. Table 7.2 lists atomic radii of elements used in the present calculations.

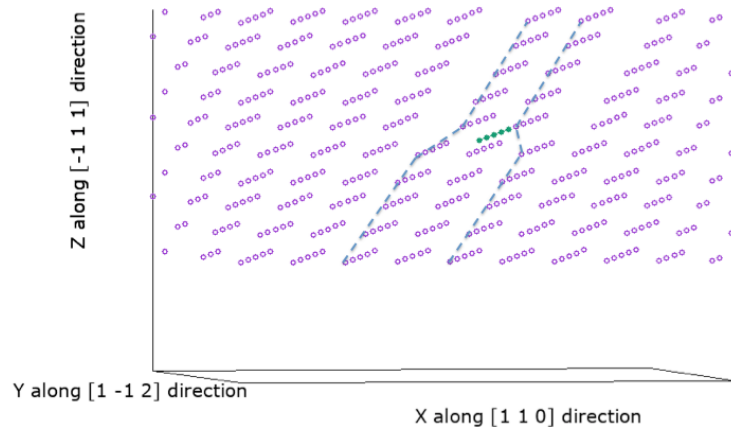
Alloy	Shear modulus (GPa)	Poisson's ratio
CoNi	84	0.29
FeNi	61	0.34
CoFeNi	60	0.35
CoCrNi	87	0.30
CoMnNi	77	0.23
FeMnNi	73	0.24
CoCrMnNi	78	0.25
CoFeMnNi	77	0.22
CoCrFeNi	82	0.28
CoCrFeMnNi	80	0.26

Table 7.1: G and ν values for alloys taken from ref. [138] for calculation of energy using equation 7.20.

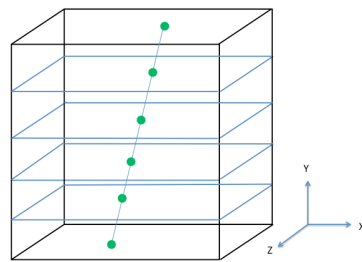
Element	Atomic radius (Å)
Co	1.252
Cr	1.282
Fe	1.274
Mn	1.262
Ni	1.246

Table 7.2: Atomic radii of elements taken from ref. [41].

Figure 7.6 shows the pressure field around the dislocation line, highlighting the compressive field below the dislocation line and tensile field in the region where rows of atoms were removed. The energy of the dislocation inside the supercell is a product of hydrostatic pressure and the change in volume associated with the particular atomic species (i) $\Delta V = V_m - V_i$. The mean volume (V_m) is calculated from the mean radius (r_m), which is in turn calculated in line with Vegard's law as $r_m = \sum c_i \cdot r_i$ (where, c_i is the atomic fraction of the atom i). The energy change at a particular lattice site arises from the size-mismatch introduced by the particular atomic species. The total energy



(a)



(b)

Figure 7.5: (a) Edge dislocation inside the face-centred cubic (FCC) lattice in unrelaxed state and (b) Schematic representation of the dislocation inside simulation supercell.

(E) associated with the supercell is given by equation (7.20) as :

$$E = \sum_{i=1}^k \Delta E_i = \sum_{i=1}^k -P_i \cdot (V_m - V_i) \quad (7.20)$$

where, k represents the total number of atoms in the supercell and P_i is the pressure at a particular lattice site. Note that there is no relaxation is being studied here. 20,000 different configurations were randomly generated for each alloy. A MC process was employed to analyse the dislocation mobility for each alloy. At each MC step a new configuration was randomly chosen from the ensemble of 20,000. If the energy associated with this new configuration was negative it was accepted as a move, but if the energy was positive, then the probability of acceptance (p) was defined by the well-known Boltzmann type expression.

$$p = \exp\left(\frac{-E}{k_B \cdot T}\right) \quad (7.21)$$

where k_B is the Boltzmann constant and T is temperature in Kelvin. A total of 10^5 MC steps were performed for each alloy. 20,000 random configurations were chosen as the number of random configurations whose energies would be used for MC simulations on the basis of a convergence test. In this convergence test, we counted the number of rejected moves out of the total 10^5 MC moves and it can be seen in Fig. 7.7 that the number of rejected moves has converged for 20,000 random configurations of CoCrFeMnNi. By carrying out a MC simulation, we sampled how readily a dislocation might move within the lattice. Note that we do not directly model the dislocation migration here and our method assumes that all 20,000 configurations are available “moves” for the dislocation. Therefore, this method indicates the significance of ener-

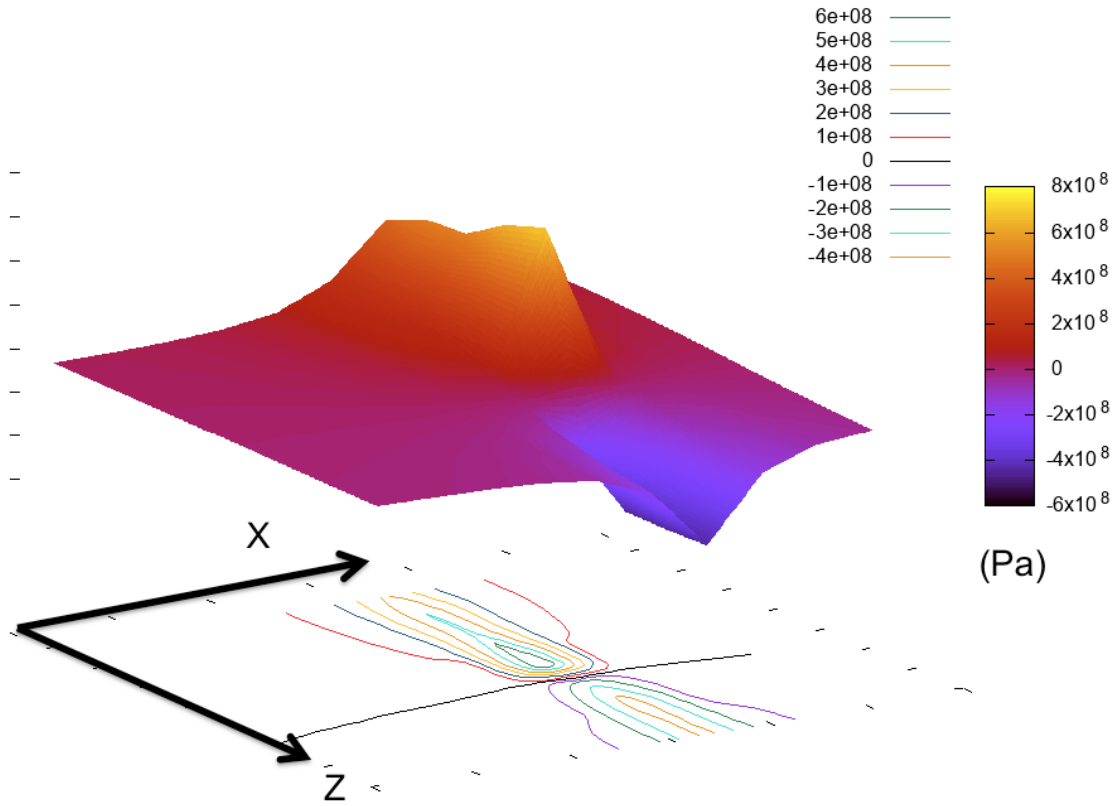


Figure 7.6: Pressure distribution around dislocation

getic differences between dislocation-solute configurations in the lattice and therefore, primarily conveys if a lattice may have more or less pinning sites for a dislocation. We label this method as approach-1 henceforth. It should be noted that random number generation is an important part of this work, as the FCC lattice must be randomly populated and once energies have been calculated and the probability corresponding to the energy is calculated, the acceptance or rejection of move is determined on the basis of a random number. In view of this, we have checked the randomness of our random number generator. Figure 7.8 shows the plot of number of times an integer between 1 to 1000 appears within the random number generator after 500,000 times. It can be seen

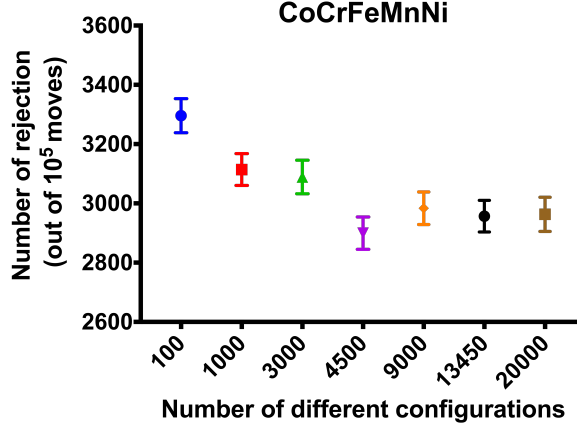


Figure 7.7: Determination of number of random configurations need to be sampled.

that the random numbers do not show any correlation or segregation to any particular value. In order to study the effect of stress on the explicit dislocation movement and the evolution of ‘waviness’ as the dislocation moves through the lattice, which might play a crucial role in strengthening [139], equation 7.21 is modified to include the effect of stress [140] as:

$$p = \exp\left(-\frac{\Delta E - (\sigma b \Delta A)/2}{k_B \cdot T}\right) \quad (7.22)$$

where, σ is the effective stress acting along the slip direction, b is the Burgers vector of the dislocation, and ΔA is the change in the area on the slip plane, caused by movement of the dislocation segment (Fig. 7.9). Additionally, while modelling the explicit dislocation movement, we have introduced a constraint in dislocation movement to ensure the continuity along the dislocation line, as shown in Fig. 7.10. The movement of the dislocation segment from lattice points $DEFG$ to $NMLK$ is only allowed if the dislocation is in configurations $BDEFGI$, $BDEFGJ$, $CDEFGI$ or $CDEFGJ$. The dislocation segment move is forbidden if the dislocation is in configuration $ADEFGI$, $ADEFGJ$, $BDEFGH$ or $CDEFGH$. With the movement of the dislocation segment, the pressure

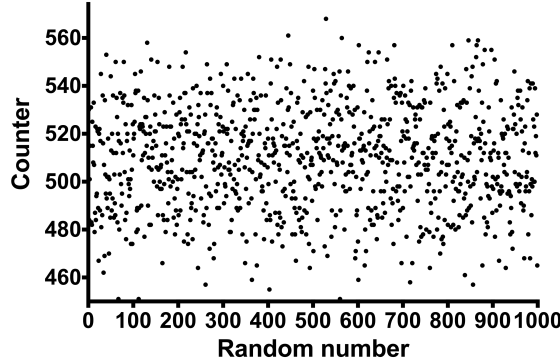


Figure 7.8: Representation of random behaviour of random number generator used for MC simulation. The counter in y-axis represents the number of times a particular number is obtained when numbers between 1 to 1000 are generated.

field is calculated for the supercell, and the rearrangement of the pressure field with dislocation movement is shown in Fig. 7.11.

In order to choose the amount of stress which needs to be applied to study the comparative lattice friction in alloys, we applied a range of stresses and tracked the mid-point of the dislocation during movement. The velocity of the dislocation in arbitrary units was determined as the ratio of the number of lattice points traversed during MC moves to the total number of MC moves. A value of one signifies that every move is accepted. It should be noted that as the stress is increased the velocity generally increases, ultimately achieving a value of one (Fig. 7.12), implying that the energy contribution due to applied stress $((\sigma b \Delta A)/2)$ in equation 7.22 is significantly larger than the energy-change due to size-misfit of the solutes (ΔE) . In view of that, a σ value of $6 \times 10^3 Pa$ was chosen. Note that this value is significantly lower than the reported critical resolved shear stress values for similar alloys systems [141, 142], because we only count energetic contributions due to size-mismatch of the solute (Fig. 7.4). Henceforth, we label this method as approach-2.

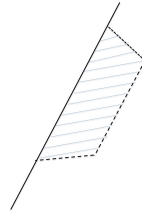


Figure 7.9: Creation of area (ΔA) on the slip plane due to movement of the dislocation segment.

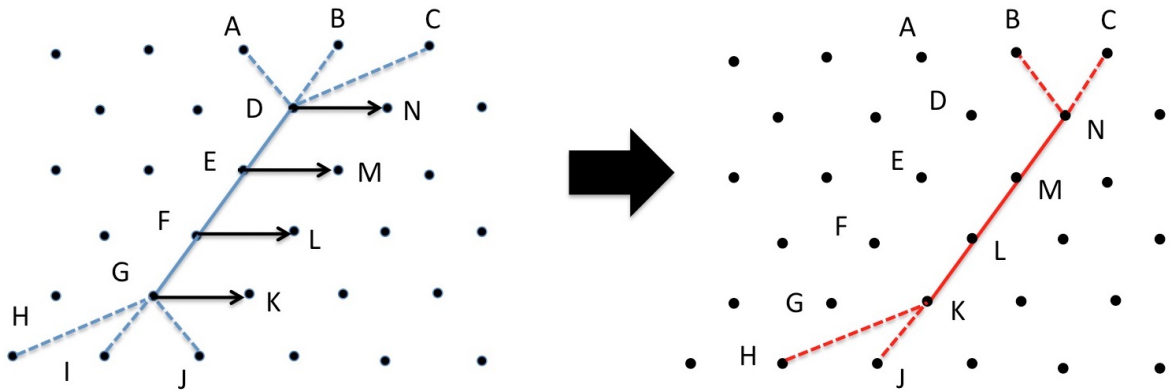


Figure 7.10: Constraint imposed to maintain continuity of the dislocation line.

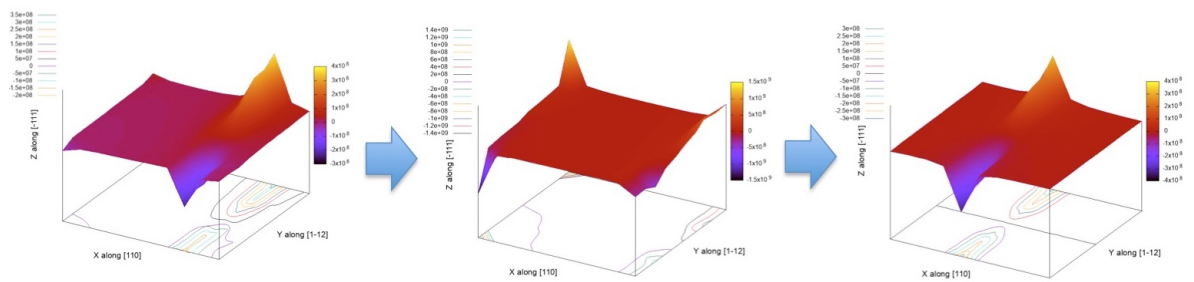


Figure 7.11: Demonstration of movement of pressure field with movement of dislocation.

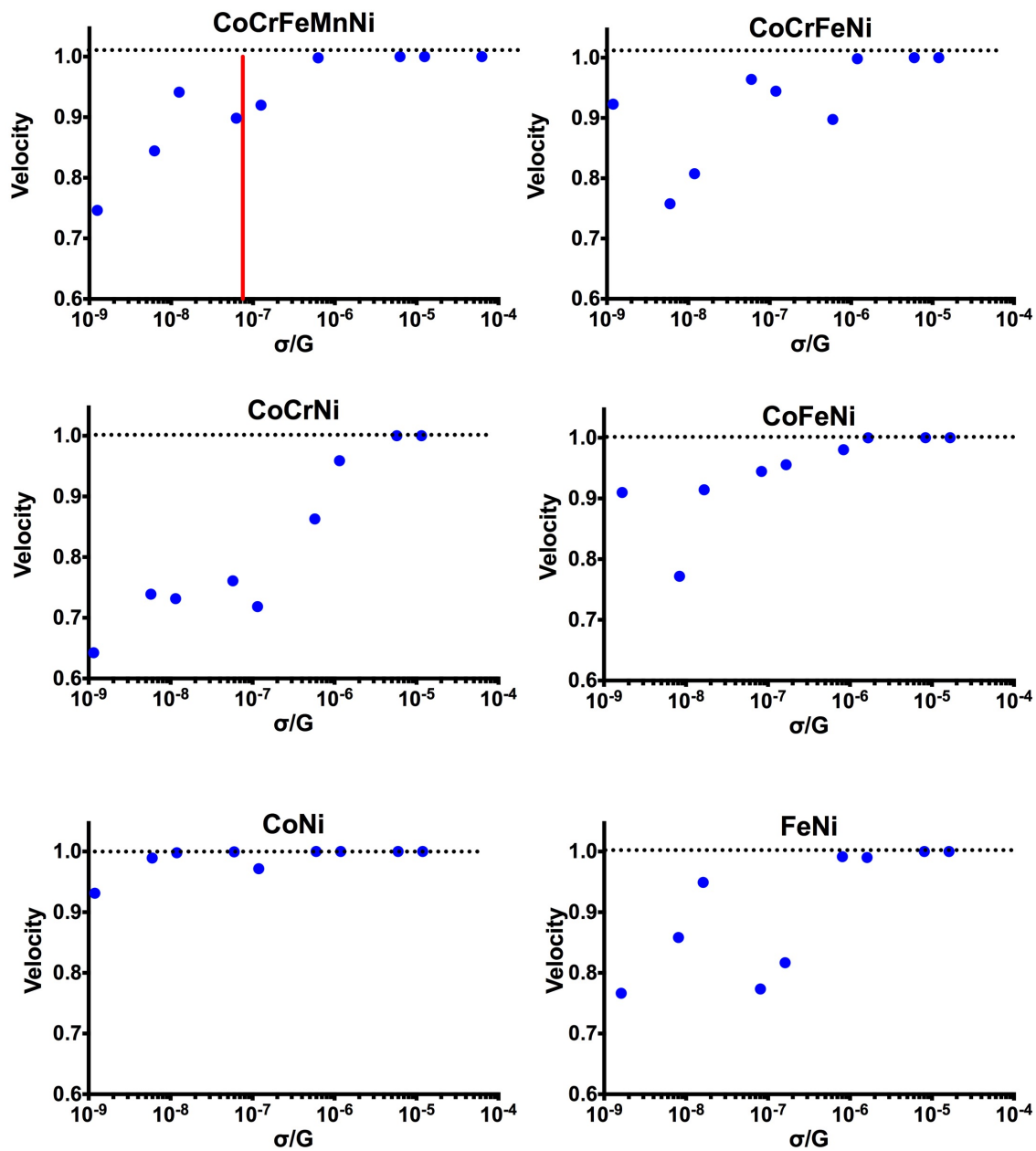


Figure 7.12: Variation in the dislocation velocity with applied stress for different alloy systems. The red line in the case of CoCrFeMnNi shows the value of stress applied for studying dislocation movement.

7.3 Results and discussions

7.3.1 Movement of straight dislocation with no applied stress contributions (approach-1)

Figure 7.13 shows the energy of different configurations for different sub-alloy systems forming the CoCrFeMnNi HEA. It can be seen that each alloy system has a slightly different energy distribution, with almost half of the configurations having negative energy, while the other half exhibit positive energy values. This distribution arises from the fact that almost an equal number of points have negative and positive pressure fields associated with them due to the edge dislocation. The lattice points with a negative pressure field are slightly fewer in number, as one row of atoms is removed when introducing the edge dislocation into the supercell. All these lattice points with particular pressure fields interact with misfit volumes of randomly assigned atomic species, which may be negative or positive, depending upon the value of the atomic radius in comparison to the mean atomic radius of the alloy. The difference between the maximum and minimum energies provides the initial understanding of dislocation mobility, with a larger energy difference signifying greater difficulty in the hopping between different energy states. Figure 7.14(a) shows the energy differences for all the alloys. Figure 7.14(b) shows the compositional variation of the energy difference for CoNi and FeNi alloys. It is clear that the maximum difference arises close to an equiatomic composition. Note that only 100 random configurations at each composition were simulated to show the comparative ability of the solute in varying the energy of the supercell. It can be seen that when Fe is added to a Ni matrix, this causes a larger variation in the energy states in comparison with the Co solute. This is due to the larger size-mismatch introduced by Fe in Ni, than Co in Ni. Figure 7.15 shows the rejection fraction (fraction of rejected moves out of a

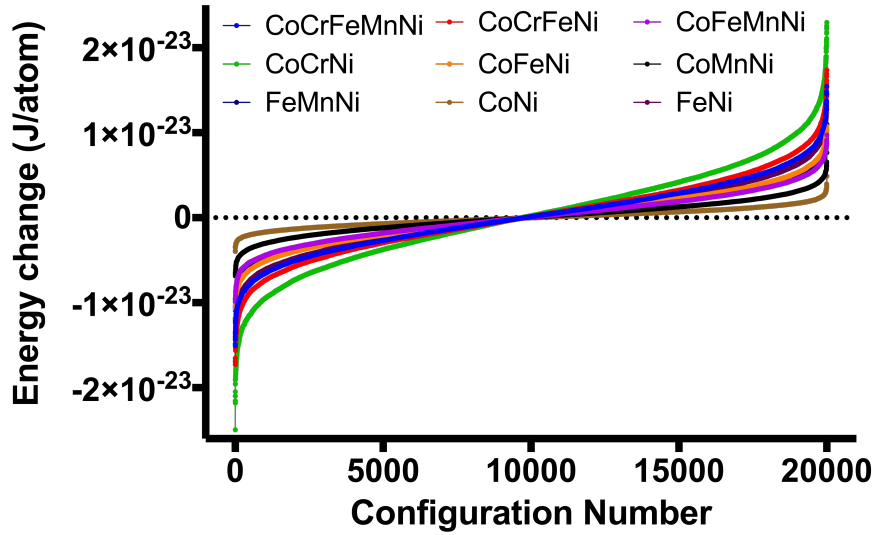
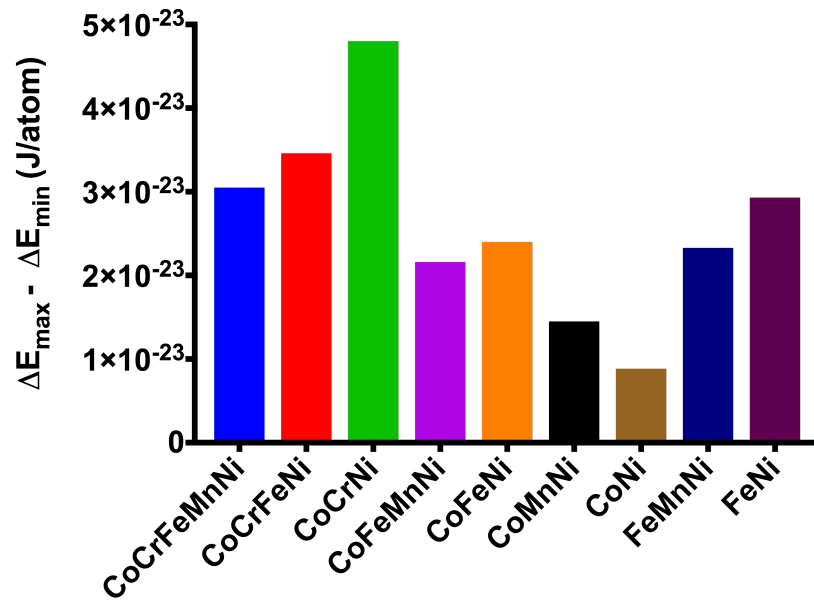
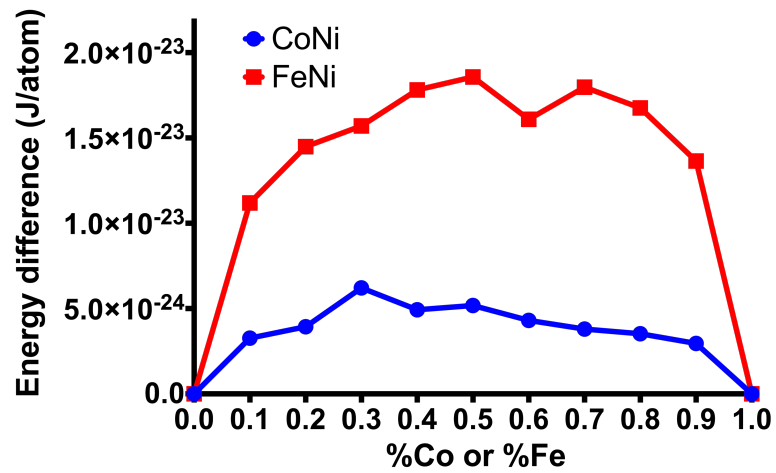


Figure 7.13: Energies due to dislocation pressure field and misfit volume of elements for different alloy systems.

total of 10^5 MC moves) for different alloy systems and its corresponding variation with the temperature. It can be seen that there is an exponential decrease in the rejection fraction with temperature, which physically suggests that as temperature is increased the movement of the dislocation becomes easier. Figure 7.16(a) presents the reported value of the Hall-Petch intercept [143], which essentially represents the lattice friction stress. The friction stress reported for sub alloys of CoCrFeMnNi [138, 144, 145] has been plotted in Fig. 7.16(b). It can be seen that there is excellent agreement between the lattice friction stress of Co, Cr, Fe and Ni containing systems with respect to rejection fraction, while in case for certain Mn containing systems in Fig. 7.16(b), *i.e.*, for CoMnNi or FeMnNi alloys a poor correlation was found. This effect can be understood in terms of a specific effect of Mn in introducing substantial lattice distortion [146]. It should be additionally noted that the above implies that the lattice friction due to



(a)



(b)

Figure 7.14: (a) Difference between maximum (ΔE_{\max}) and minimum (ΔE_{\min}) energy for different alloy system and (b) Variation of difference between maximum and minimum energy for binary CoNi and FeNi alloys.

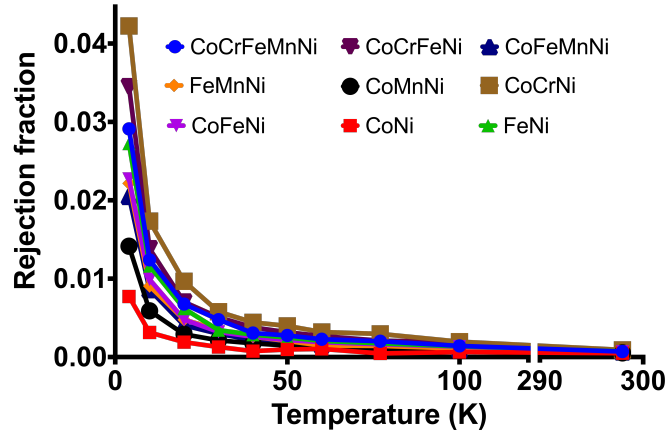
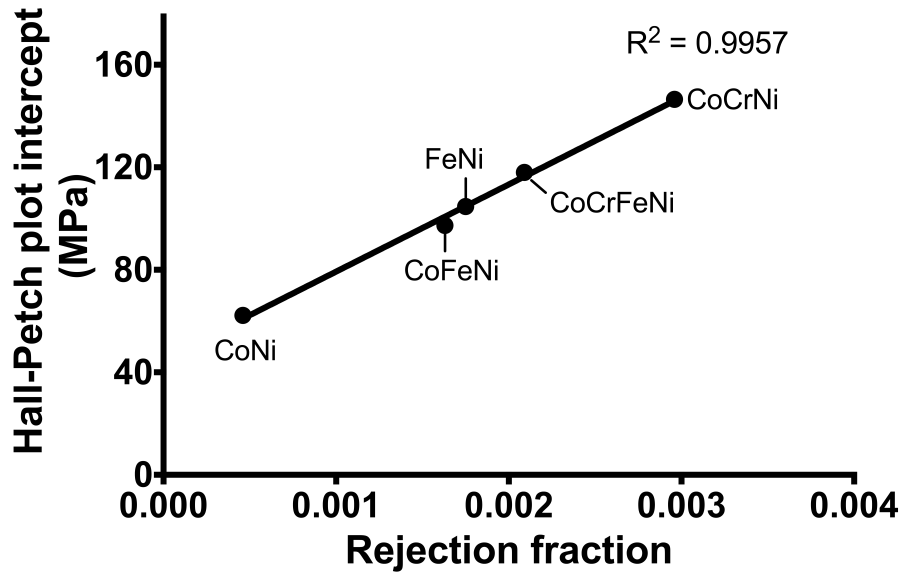
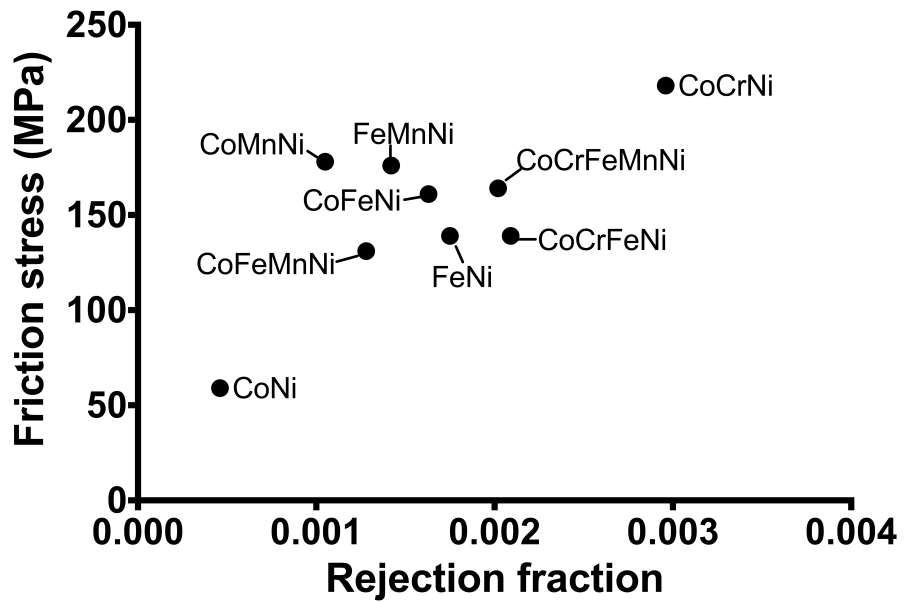


Figure 7.15: Variation in the rejection fraction for different alloys with temperature.

Cr might be due to atomic radius mismatch, while Mn may be causing an increase in lattice friction due to distortion. It should be noted that the rejection fraction acts as an important guide for determining the lattice friction in alloys, which in turn is determined via the magnitude of atomic size-mismatch, as shown in Fig. 7.17(a). It can be seen that atomic-size mismatch and rejection fraction show a linear dependence (inset of Fig. 7.17(a)), except for FeNi. The lower value of the rejection fraction of FeNi, even though it has the largest atomic-size mismatch can be understood in terms of having a smaller value for the energy difference between the maximum and minimum energy states possible (Fig. 7.14(a) and 7.17(b)). So, the energy difference seems to be a much more fundamental parameter for determining lattice friction in alloys than the size mismatch, which is determined from the interaction between the elastic properties of the alloy (G and ν) and atomic-size mismatch of elements forming that particular alloy. Additionally, the lattice friction stresses published in the literature, which were used for benchmarking our calculations have been compared and presented in Fig. 7.18. It can be seen that the values published in ref. [138] show certain anomalies. The fric-

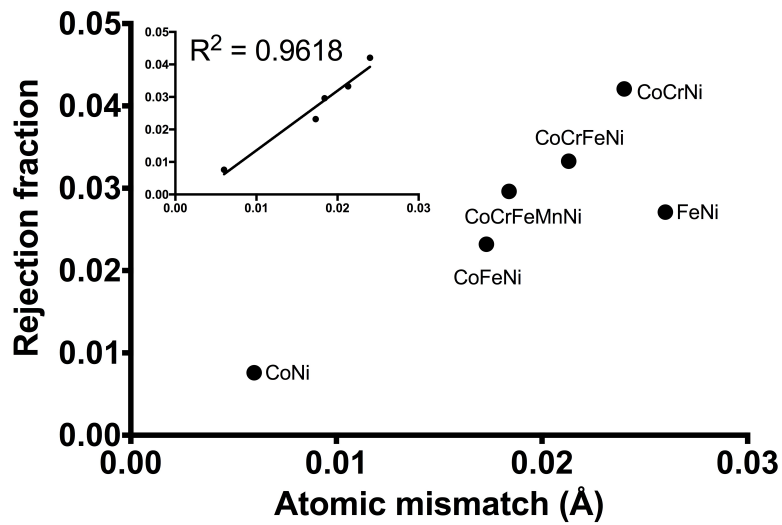


(a)

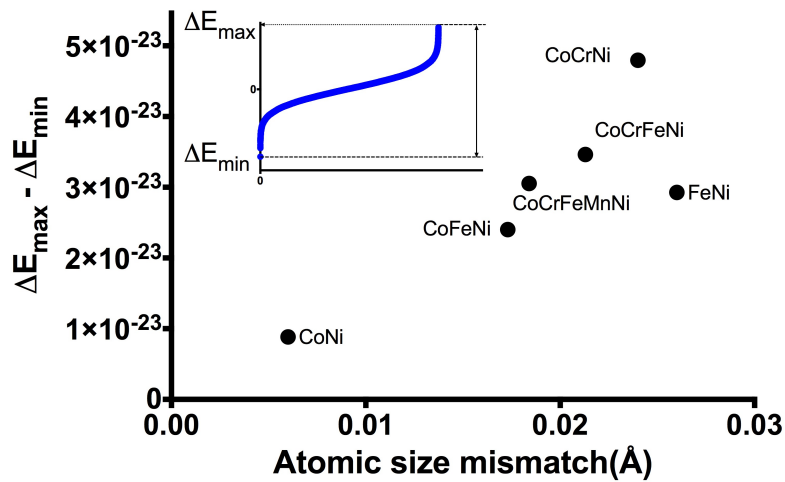


(b)

Figure 7.16: (a) Comparison of rejection fraction for CoNi, CoFeNi, FeNi, CoCrFeNi and CoCrNi at 77K with intercept of Hall-Petch plot for these alloys from literature [143] and (b) Comparison of rejection fraction for different alloys at 77K with lattice friction stress from literature [138, 144, 145].



(a)



(b)

Figure 7.17: (a) Variation of rejection fraction with atomic-size mismatch for different alloys (inset shows rejection fraction versus atomic size mismatch with data for FeNi, showing linear dependence) and (b) Variation of difference between maximum and minimum energy possible for different alloys with atomic-size mismatch. The atomic size-mismatch is defined to be the mean of the atomic size-mismatch between different binaries which form the particular multicomponent alloy. Data from Table 7.2 was used.

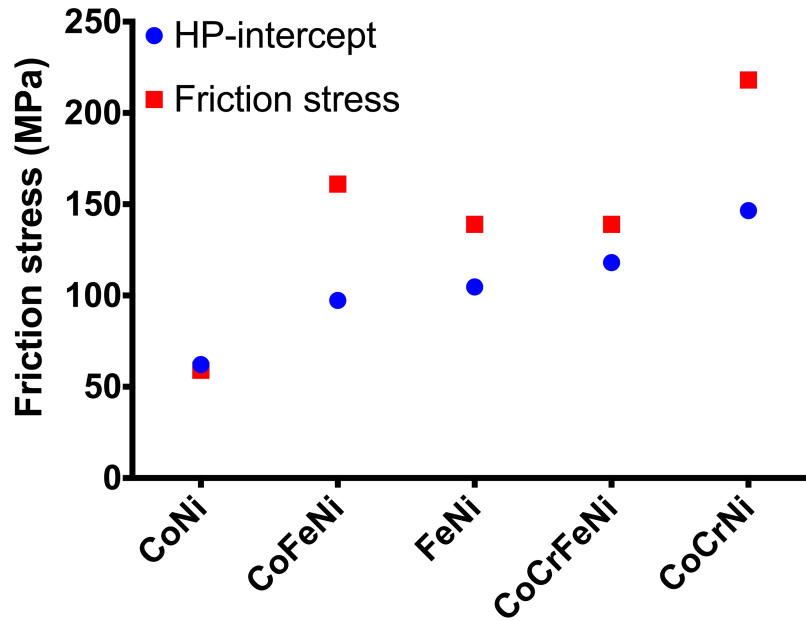


Figure 7.18: Comparison of lattice friction stress values published in ref. [138, 144, 145] and Hall-Petch plot intercept published in ref. [143] for CoNi, CoFeNi, FeNi, CoCrFeNi and CoCrNi.

tion stress for the CoFeNi is higher in comparison with FeNi, even though it has a smaller atomic-size mismatch, while the opposite trend is seen with the Hall-Petch plot intercept in ref. [143]. Additionally, for the CoCrFeMnNi alloy, lattice friction stress values in the range of 130-164 MPa were reported and for CoCrFeNi, the value ranged between 101-139 MPa, as mentioned in ref. [144]. So, there is a substantial variation in reported values depending upon the experimental conditions and hence, it can be deduced that more experimental values are required in this area.

Recently, Varvenne *et. al.* have shown that dilute additions of Al in CoCrFeNi and CoCrFeMnNi lead to significant strengthening in the system, with higher strengthening being observed in the case of addition of Al into CoCrFeNi. We have simulated the compositions in Varvenne *et. al.* i.e., $\text{Al}_{0.071}\text{CoCrFeMnNi}$ and $\text{Al}_{0.071}\text{CoCrFeNi}$ with G

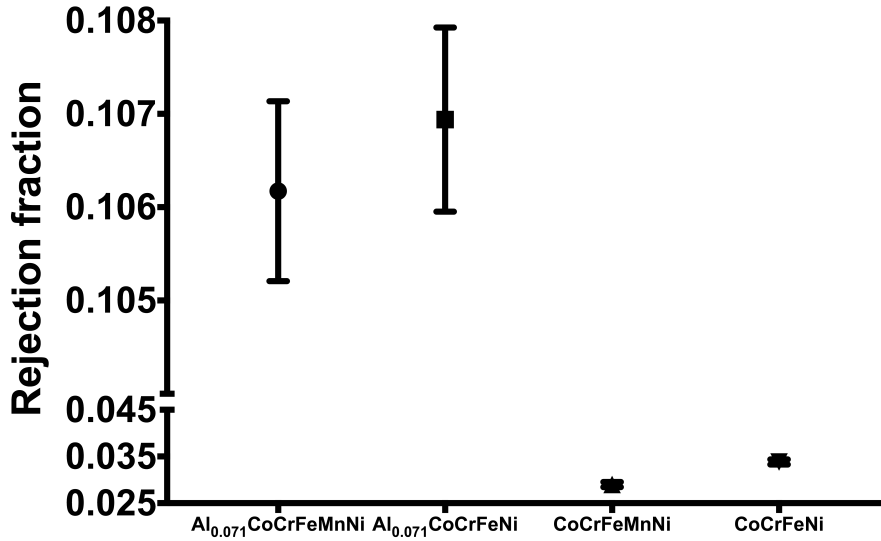


Figure 7.19: Influence of dilute addition of Al into CoCrFeMnNi and CoCrFeNi on rejection fraction.

values of 71.3 GPa and 75 GPa, respectively, while reported values of ν for these alloys were 0.274 and 0.294, respectively [132].

Figure 7.19 shows a significant enhancement in the rejection fraction for both $\text{Al}_{0.071}\text{CoCrFeMnNi}$ and $\text{Al}_{0.071}\text{CoCrFeNi}$ in comparison to CoCrFeMnNi and CoCrFeNi , respectively. It can additionally be seen that the rejection fraction was higher in the case of $\text{Al}_{0.071}\text{CoCrFeNi}$ in comparison to $\text{Al}_{0.071}\text{CoCrFeMnNi}$, which implies that the increased lattice friction in the former case is the mechanism responsible for larger strengthening in the four component matrix in comparison to the five-component matrix. This observation provides further confirmation of the robustness of our approach in the qualitative prediction of the lattice friction stress.

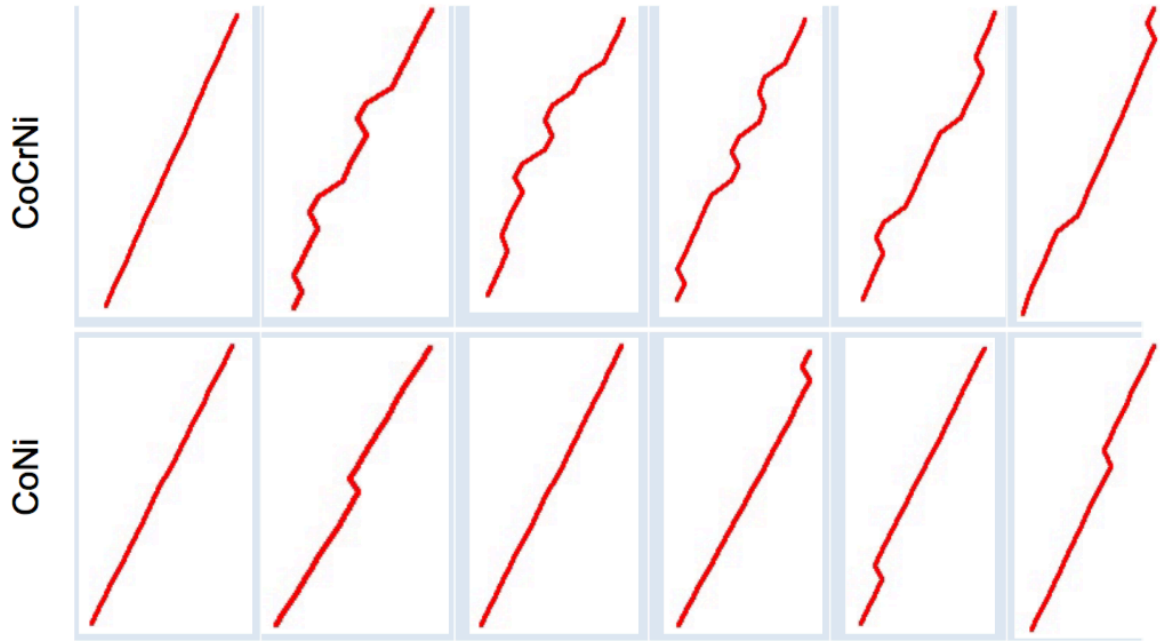
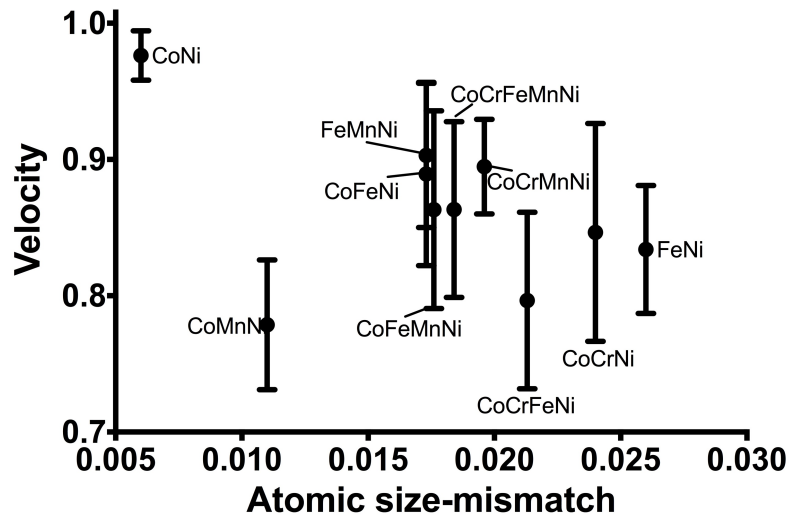


Figure 7.20: Snapshots of dislocation line of CoCrNi and CoNi alloys taken at different MC steps.

7.3.2 Explicit dislocation movement with sequential dislocation-segment movement with contributions from applied stress (approach-2)

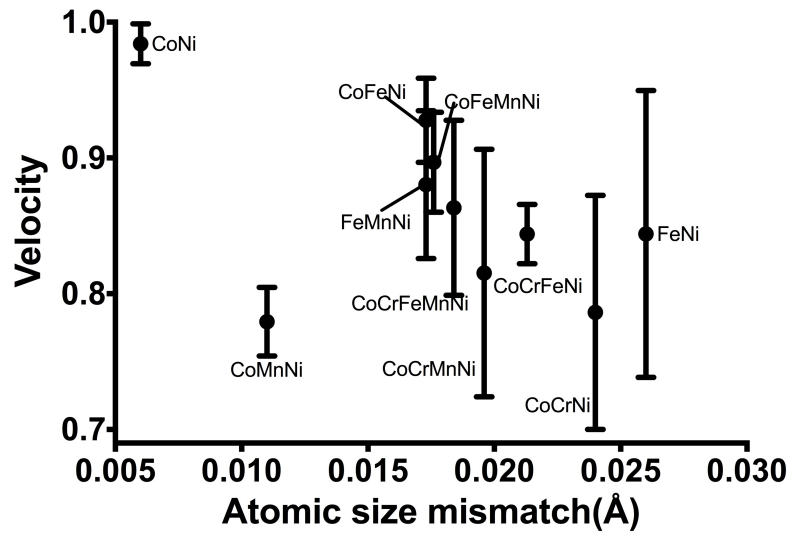
We expanded our model to include the evolution of ‘waviness’ on the dislocation-line caused by localised pinning as mentioned in the Methods section (section 7.2). We also applied the stress to aid the dislocation motion. Note that each MC simulation was carried out for five different random composition fields. Figure 7.20 shows snapshots of the dislocation line for the CoCrNi and the CoNi alloys with increasing number of MC steps. It is evident that CoCrNi exhibits a rougher dislocation-line, while in case for the CoNi alloy, the dislocation line maintains a straight character. Additionally, we tracked the mid-point of the dislocation-line and determined the effective velocity of

the dislocation by dividing the number of lattice points traversed by the mid-point of the dislocation line by the total number of MC steps. The unity value of velocity of the dislocation signifies the fact that each MC-move has been accepted with no-pinning of the dislocation line. Figure 7.21(a) shows the effective velocity of the dislocation line in different alloys, when constant stress is applied. It can be seen that there is a general decrease in the velocity of the dislocation with increasing size-mismatch, but the decreasing trend is not uniform. We applied constant normalised stress to all alloys systems, where normalised stress corresponds to the ratio of applied stress to shear modulus of the alloy (σ/G). It can be seen that no uniform trend is present in this case either (Fig. 7.21(b)). CoMnNi and FeNi alloys particularly show a distinct separation from any trend. Even if CoMnNi and FeNi are not considered, the decrement trend is not uniform, possibly because we have introduced a constraint condition to maintain the continuity of the dislocation line and it might be influencing the mobility of the dislocation. To further quantify the pinning of the dislocation, we enumerated the rejection of dislocation-segment moves out of total 10^4 MC moves for different alloys systems (Fig. 7.22(a)). All the alloy cases except CoMnNi and FeNi showed a quadratic increment with atomic size-mismatch (Fig. 7.22(b)). We carried out similar calculations with G and ν values determined as an average of elemental G and ν values. It should be noted that it has been assumed that elastic properties of alloys vary linearly with the composition [109, 147–149], even though we have not considered the effect of change of composition, but while determining the net G and ν values for equiatomic compositions, we have assumed that the contribution from each element comprising the particular alloy would be same. It can be seen in Fig. 7.23 that CoMnNi and FeNi remain outside the quadratic trend as observed in Fig. 7.24, please note that such disjointness from a particular trend may be attributed to the fact that energy trends exhibited by these



(a)

$$\sigma/G = 7.5e-08$$



(b)

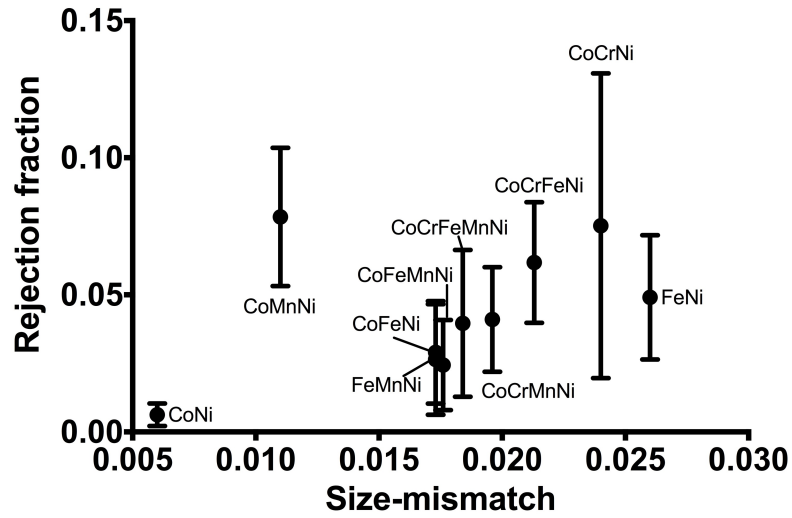
Figure 7.21: (a) Variation of velocity of the dislocation in different alloy systems with constant applied stress (σ) and (b) Variation of velocity of the dislocation in different alloy systems with normalised applied stress (σ/G).

alloys do not follow atomic-size mismatch, as we have already shown for FeNi alloy in the calculation using approach-1. Apart from these exceptions, it can be deduced that the trend of rejection fraction remains the same and our technique can be applied for qualitative comparison to hitherto unknown compositions, whose elastic properties might not be known.

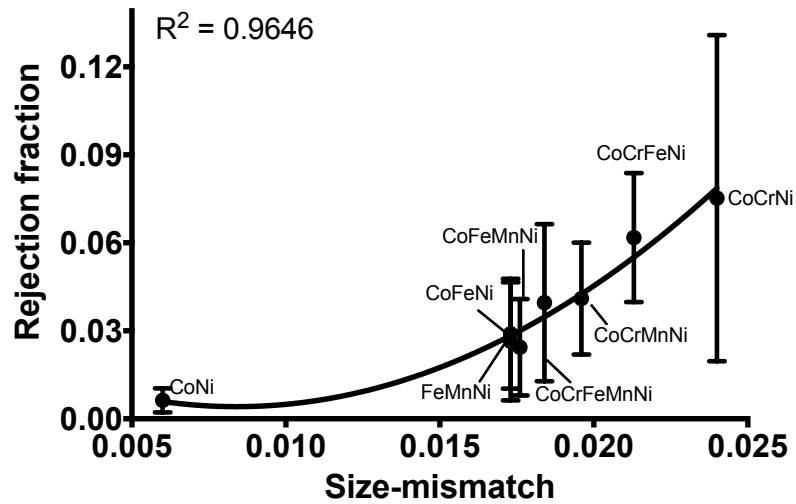
Figure 7.25(a) shows the roughness of the dislocation line, where a value of one signifies a perfectly straight dislocation line. With increasing atomic size-mismatch there is a linear increase in the roughness (Fig. 7.25(a)), except for FeNi and CoMnNi. The linear dependence between size-mismatch and roughness of the dislocation line is shown in Fig. 7.25(b). It is obvious that there is a significant fluctuation in the rejection fraction, i.e. effective velocity and roughness of the dislocation line. To enquire, whether this is an convergence issue, we have simulated different number of random configurations and plotted the rejection fraction with 5, 10, 15, 20, 25 and 30 random configurations, as shown in Fig. 7.26. It is evident that fluctuations in rejection fraction does not seem to be a convergence issue.

7.3.3 Comparison between approach-1 and approach-2 for lattice friction determination

As has been mentioned earlier, the rejection fraction for dislocation movement in MC simulations, which is determined by the energy difference between the maximum and minimum possible energy for a particular alloy, is a much more fundamental parameter for quantifying the lattice friction of alloy than atomic-size mismatch. The variation of rejection fraction with energy difference is plotted in Fig. 7.27(a). It is evident that the rejection fraction shows a perfectly linear dependence on the energy difference. Similarly, the reported values of the Hall-Petch intercept [143], which essentially is the



(a)



(b)

Figure 7.22: (a) Variation of rejection fraction for all alloys and (b) Variation of rejection fraction for all alloys, except CoMnNi and FeNi.

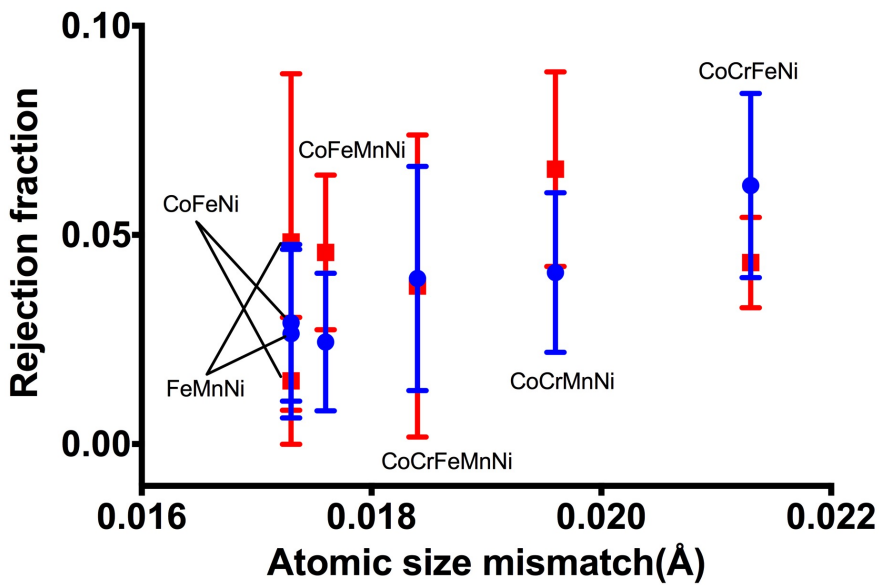
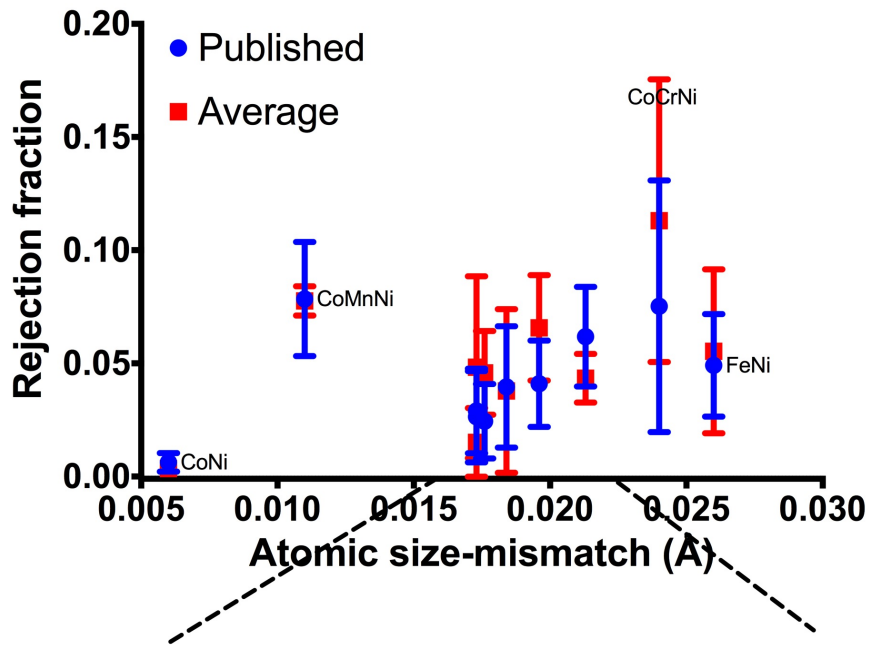


Figure 7.23: Comparison of rejection fraction of alloys, when calculation is carried with G and ν values taken from ref. [138] (published) and when average values of G and ν are determined from elemental values.

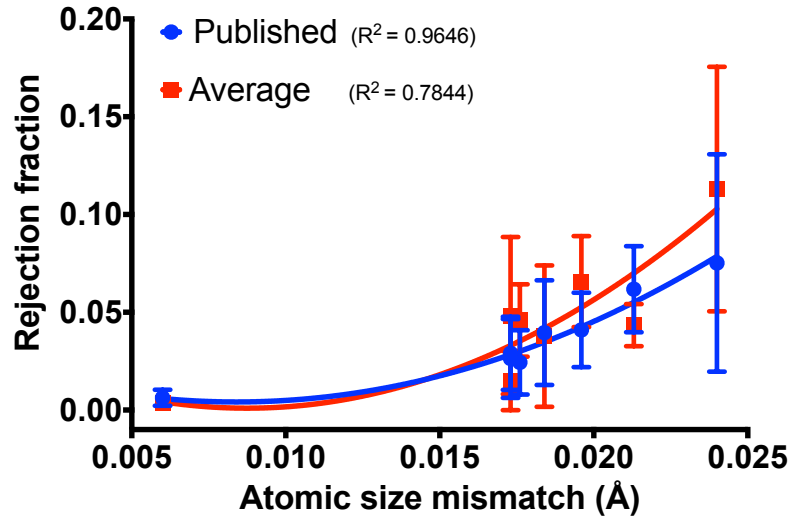
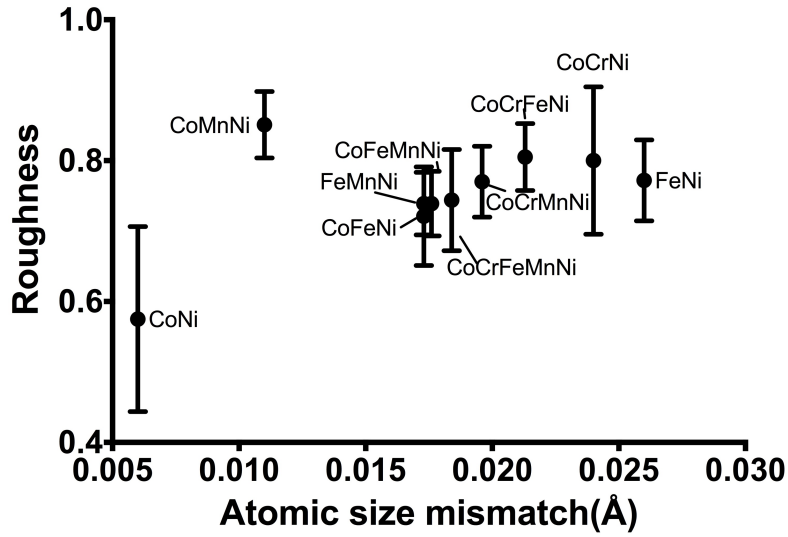


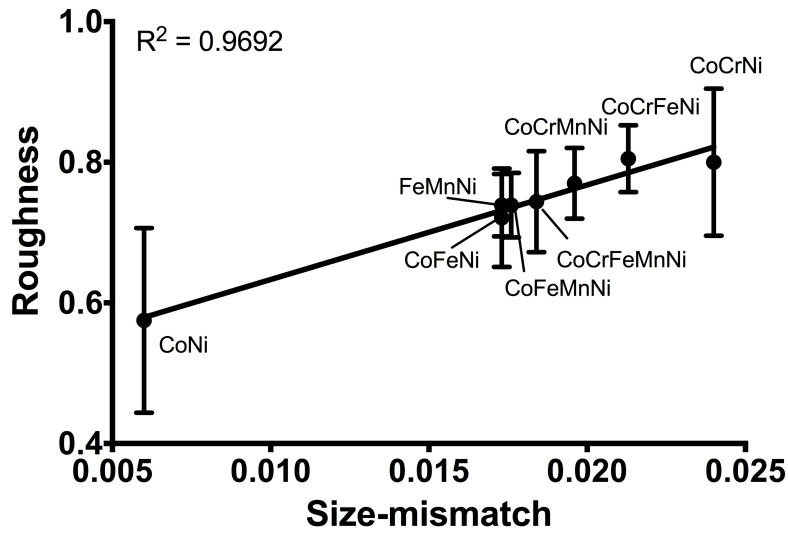
Figure 7.24: Correlation between rejection fraction and atomic-size mismatch of for all alloys, as shown in Fig. 7.23 with removal of alloy cases of CoMnNi and FeNi.

lattice friction stress in the absence of defects such as grain boundaries, shows linear dependence on energy difference. It can be seen that there is excellent agreement between the lattice friction stress of Co, Cr, Fe and Ni containing alloys and the rejection fraction. Thus, it shows that simply increasing the number of components might not be enough for a corresponding increase in lattice friction, in contradiction to earlier understanding [102]. Rather it is the energy-range which governs the magnitude of lattice friction. This observation is in line with the reported observation that Cr containing alloys are strongest [86,138], possibly due to their large spread in the energy-range (Fig. 7.14(a)).

Figure 7.27(c) shows the variation of rejection fraction with energy difference for alloys, when stress is applied and ‘waviness’ of the dislocation line is allowed to evolve by moving segments of the dislocation line. It can be seen that linear dependence is lost. The quadratic dependence of rejection fraction with energy difference was seen for



(a)



(b)

Figure 7.25: (a) Variation of roughness of the dislocation line for different alloys with atomic-size mismatch (roughness of the dislocation line is defined to be standard deviation of dislocation from the mid-rib of the dislocation, where the mid-rib is an imaginary straight line from one end to another) and (b) Linear correlation between roughness and atomic-size mismatch for all alloys, when CoMnNi and FeNi are not considered.

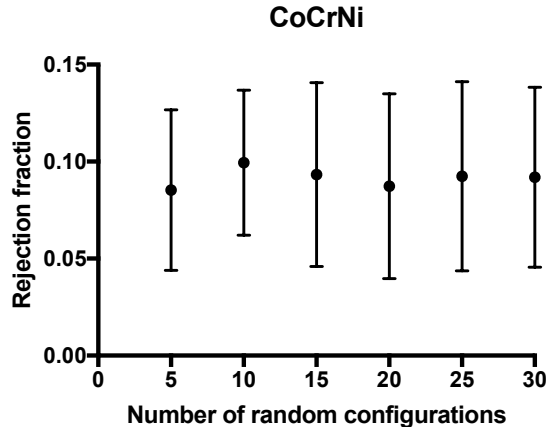


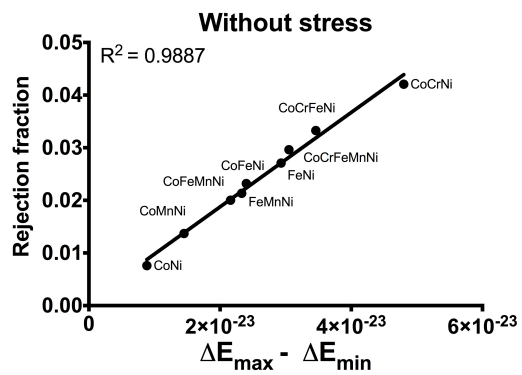
Figure 7.26: The variation of the rejection fraction with the number of random configurations for the CoCrNi alloy.

alloys which do not contain Mn.

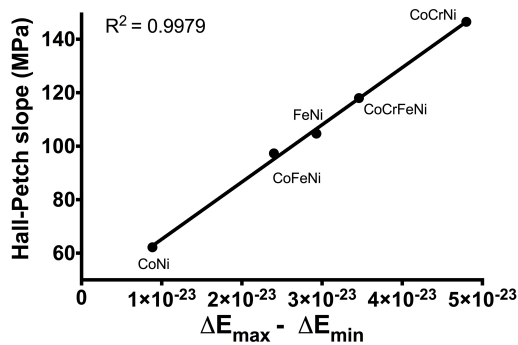
7.4 Conclusions and future work

The present investigation aimed to understand the mechanism behind the evolution of lattice friction for dislocation movement in substitutional alloys, as the number of element forming alloys varies, with particular emphasis on HEA systems. The following conclusions can be drawn from this work:

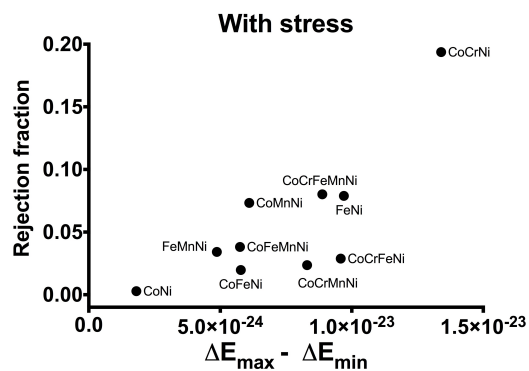
1. The lattice friction is not simply a function of the number of elements forming the alloys, rather it is a function of energy-states permissible in the particular system.
2. The elastic interaction model, which derives its theoretical basis from first-order strengthening models [113], Labusch's approach [116] and a simplification of Curtin's approach [110] can be applied for qualitative screening of substitutional alloys with respect to their lattice friction.



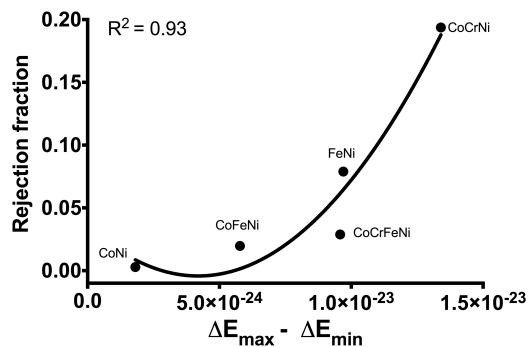
(a)



(b)



(c)



(d)

Figure 7.27: (a) Variation of rejection fraction for alloys with difference between maximum and minimum energy, when stress is not considered, (b) Correlation between energy difference and the Hall-Petch slope published in ref. [143] for sub-alloy systems forming CoCrFeNi, (c) Variation of rejection fraction with energy difference for different alloys when explicit dislocation movement is considered and stress is applied, and (d) Quadratic variation of rejection fraction with energy difference for sub-alloy systems forming CoCrFeNi.

3. The limitation of the present approach for Mn containing concentrated alloys can be understood in terms of markedly different elastic properties of Mn [150] with respect to other transition-metal elements studied in this work.

In view of the above, future work in this area should be done in the following directions:

1. This approach can be further developed to provide a quantitative understanding of barriers for dislocation movement, which would be helpful in the prediction of structural properties of alloys.
2. We have limited our investigation to FCC alloys with only substitutional alloying, but this approach could be generalised to interstitial alloying elements, where a tetrahedral distortion might lead to much more pronounced pinning of dislocations.
3. In this investigation, only edge dislocation-solute interactions have been considered. Screw dislocation-solute interactions need to be studied as well, particularly for interstitial solutes as mentioned above.

* * * * *

Chapter 8

Density Functional Theory calculations on substitutional alloys

8.1 Introduction

Alloy formation is fundamentally guided by electronic redistribution in the system and *ab-initio* density functional theory (DFT) can be used for studying electronic and consequent structural properties of alloys. Most DFT studies in alloys design or more recently in High-Entropy alloys (HEA) have been concentrated in two distinct schemes. The first scheme is based on the Coherent-Potential Approximation (CPA), while another scheme is known as the Special Quasi-Random Structure (SQRS) generation.

The CPA scheme was originally formulated by Soven [151], Taylor [152] and later by Gyorffy [129] for studying electronic properties of random substitutional alloys. This approach has an inherent assumption of an effective medium, where the alloy is considered to have effective properties. This method considers a single-site approximation, where knowledge concerning the potential and charge density beyond a polyhedral or

spherical region around a particular impurity is not considered. The characteristics of the CPA medium is dependent upon the formalism used to describe it. The Korringa-Kohn-Rostocker (KKR) [153, 154] and exact muffin-tin orbital (EMTO) implementations have been widely employed. In the KKR-CPA approach with the muffin-tin approximation, the spherical one-electron potential (i.e. potential of a single electron in a many-body electronic system) centred on a atom lies within a muffin-tin sphere with no overlap and there is a constant potential in the interstitial region, while in the EMTO-CPA framework, the overlapping between muffin-tin potentials is allowed to ensure a spherical representation of the one-electron potential [155]. The detailed formal description including derivation of both these frameworks is beyond the scope of present work.

The KKR-CPA framework has been employed for studying phase stability in $\text{Al}_x\text{CoCrFeNi}$ systems, where this approach predicted that a fcc-to-bcc transformation takes place due to the reduction of the local energy of the transition metals by Al due to p-d hybridisation [156]. Zhang *et. al.* employed the KKR-CPA approach to quantify the mechanism behind slow damage accumulation with increasing chemical disorder [157]. In this work, a reduction in the electron mean free path and thermal conductivity was reported as the number of alloying elements was increased from elemental Ni to multicomponent CoCrFeNi HEA. The slow energy dissipation mechanisms in the early stages of defect formation was found to be the reason behind slow damage accumulation during irradiation. Sharma *et. al.* employed the KKR-CPA to fit the interatomic potential of $\text{Al}_{0.1}\text{CoCrFeNi}$ HEA. Singh *et. al.* used this technique in collaboration with the electronic structure based thermodynamic theory to predict short-range order in HEA [158, 159]. Jassiewicz *et. al.* have used this approach for studying electronic characteristics related to the superconducting $\text{Ta}_{34}\text{Nb}_{33}\text{Hf}_8\text{Zr}_{14}\text{Ti}_{11}$

HEA [160].

The EMTO-CPA scheme has been employed for predicting the fcc-bcc phase transition in an Al alloyed 3d-transition metal based HEA and the elastic properties of such HEA [40]. Additionally, the onset of ductility of HEA with the B/G ratio (where, B and G are bulk and shear modulus, respectively) was predicted using Pugh's criteria. Pugh's criteria predicts ductile behaviour when, $B/G > 1.75$ [161]. Tian *et. al.* also employed the EMTO-CPA scheme along with the supercell approach to determine the Wigner-Seitz radius of CuNiCoFeCrTi, CuNiCoFeCr and CoCrFeNi HEA and good agreement was reported. But a large deviation between predicted and experimental Young's modulus was observed as well [162].

The CPA approach is fundamentally inadequate for dealing with the short-range order [163] and anisotropic distortion in the system. But, it should be noted that the EMTO-CPA method has been able to account for energetic effects associated with the local distortion [164]. The incorporation of short-range order effects in the KKR-CPA formalism was attempted by Rowlands *et. al.* [165–167] using the KKR-Non local CPA (KKR-NLCPA) formalism, which has been recently applied to binary random alloys [168]. But, we have not come across non-local CPA calculations for HEA systems.

The SQRS method involves the generation of cells with a limited number of atoms, which mimics the true random solid solutions in terms of correlation function, defined for certain nearest-neighbours only [169]. This approach assumes that interaction beyond a pre-defined nearest-neighbours have negligible effect. Also, this approach was defined for binary random alloys. SQRS has been employed for studying mechanical properties and calculation of stacking fault energies of CoCrFeMnNi [41], phonon broadening in refractory HEA [170], for quantifying the atomic displacement of constituent elements forming CoCrFeMnNi HEA [171], for determining distortion associated with

Mn [146], etc. But, there are certain considerations associated with the SQR structure generation. Firstly an appropriate cell size must be chosen which is large enough to sample configurational space, while computationally within the capability of DFT calculations. Secondly, the determination of stopping criteria for SQRS generation is not clear, as ideally the SQRS calculation should provide a true random solid solution with the correlation function of a random system. This might not happen due to inadequate configurational sampling from a small cell size and, lastly, the cluster or number of nearest neighbours, which would be considered for SQRS generation needs to be specified. Hence, application of this technique requires certain theoretical expertise with heuristic decision-making, which is not an ideal scenario. Additionally, the SQRS technique has difficulty in dealing with magnetic or, particularly, paramagnetic systems [172].

Another scheme which might be used for simulating disorder in alloys is the ‘Virtual Crystal Approximation (VCA)’ [173], which involves assigning fractional occupancy of an atom at a particular lattice site. But this scheme cannot be applied to system containing elements with competing magnetic ground-states and additionally, local distortion cannot be modelled using this technique.

It is apparent that most of the DFT studies on HEAs reported so far have emphasised the effect of disorder on the properties of such alloys with little emphasis on the influence of the characteristics of an individual metal on another. In the view of this, we have aimed to develop more fundamental understanding of the electronic redistribution in transition metal based systems with simple supercell calculations with spin-polarised DFT. In this work, we have tried to develop the above-stated understanding keeping in mind two main issues in line with the ongoing debate in the area of HEAs: The first issue to be presented in this chapter is related to the enthalpy calculation for such alloys and the second issue is related to the evolution of distortion in such alloys.

Calculation details

DFT calculations were performed using the CASTEP code [174], which uses a plane-wave expansion of one-electron wave functions. The ultrasoft pseudopotential was used to define the electron-ion interaction [175]. The electron exchange-correlation was defined using the generalised gradient approximation [176] with a Perdew-Burke-Ernzerhof functional [177]. Spin-polarised calculations were carried out to introduce magnetism. The geometric optimisation was carried out in all the cases to obtain the statically relaxed structure with tolerance values for ionic displacement, force on ions, stress on ions set to 0.001 Å, 0.05 Å, and 0.1 GPa, respectively. The DFT calculations with the supercell approach were carried out with the impurity-in-matrix methodology for elements forming a CoCrFeMnNi alloy. By impurity-in-matrix calculation, we mean that a different element is added in the centre of the supercell of another element. The FCC structure was modelled for Co, Cr, Fe, Mn and Ni, while a BCC structure for Cr, Fe and Mn was generated. The HCP structure for Mn was generated as well. A 2X2X2 supercell was generated for BCC, FCC and HCP cases, containing 16, 32 and 16 atoms respectively. In each of these cases, the remaining elements are added as a perturbation substitutionally to determine their individual effect on the bond-lengths to characterise the influence of individual elements on distortion in alloys. The 2X2X2 supercell of the FCC form of CoCrFeNi and CoCrFeMnNi (containing 6 atoms each of Co, Cr, Fe, Ni and 8 atoms of Mn) was generated as well for reference along with a 5X2X2 supercell for FCC-CoCrFeMnNi. It should be noted that geometry optimisation parameters were slightly relaxed with tolerance values for ionic displacement, force on ions, stress on ions set to be 0.005 Å, 0.08 Å, and 0.8 GPa, respectively. The plane wave cut-off energy and number of k -points were determined using convergence testing.

Atomic species	E_{cut} (eV)	k-points
Co	500	10^3
Cr	700	12^3
Fe	500	10^3
Mn	700	10^3
Ni	500	12^3

Table 8.1: The plane-wave cut-off energy and number of k-points obtained after convergence testing

The plane wave cut-off energy and k-point required for Brillouin-zone integration was determined for each individual with a tolerance of 1 meV. Table 8.1 shows the plane wave cut-off energy (E_{cut}) and k-points required for each individual atomic species. In the case of impurity-in-matrix calculations, the higher E_{cut} and k -point numbers among the matrix or impurity were chosen, unless stated otherwise. For CoCrFeNi alloys, an E_{cut} of 600 eV and 10^3 k-points were used.

8.2 Charge redistribution and its implications for the enthalpy of mixing calculations

Previously, the semi-empirical Miedema's model was proposed for the calculation of the enthalpy of mixing of liquid or solid binary alloys [178]. In Miedema's model, it is considered that each atom in the solid can be quantified by its Wigner-Seitz cell, which is the smallest polyhedron formed by planes bisecting the line joining the particular atom to its nearest neighbours. This cellular model considers the alloy formation, which may be expressed schematically as shown in Fig. 8.1. In the most simple case, there is no change in the volume and it simply represents the case where there is no energetic change associated with alloy formation. If, however there is a change in the volume of the constituents, there would be an energetic change associated with it, which will lead

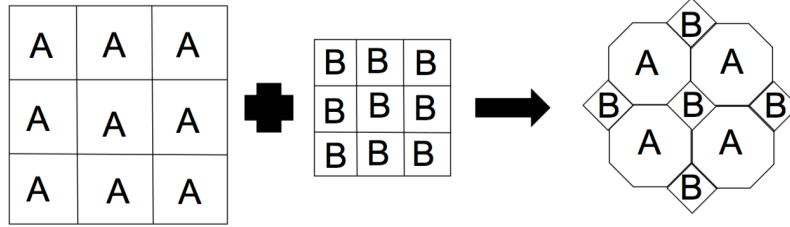


Figure 8.1: Schematic representation of alloy formation in Miedema's framework, redrawn from ref. [179].

to a non-zero enthalpy of mixing.

When atoms A and B are mixed with each other, the non-zero value of the enthalpy of mixing arises due to the interface between the Wigner-Seitz cells of atom A and B (A-B interface). In Miedema's model, this A-B interface is defined by assuming the interface at the atomic scale would have similar characteristics to the interface of bulk metal A and B, i.e., the interaction between atoms at the atomic scale can be approximated to be same as they would behave, when bulk metals are brought together. Additionally, Miedema's model considers the heat of solution of liquids, heat of formation of condensed or solid systems and interfacial enthalpy of bulk metals on similar footing, which can be considered to be a broad generalisation.

In Miedema's scheme, the enthalpy change (ΔH) due to mixing atoms may be represented as:

$$\Delta H = F(c) [-X(\Delta\phi)^2 + Y(\Delta n^{1/3})^2] \quad (8.1)$$

where, $F(c)$ is a term dependent on the concentration of the solute, $\Delta\phi$ is the difference in electronegativity between the elements and Δn is the difference between electron density in the Wigner-Seitz cells of the elements forming the alloy.

The enthalpy of mixing for HEA has been extensively calculated using Miedema’s model [180–183]. But more recently Tsai *et. al.* [184] showed that certain compositions of HEA exhibit intermetallic phases, even though their enthalpy of mixing is predicted to be near zero. This observation deviates from the basic thermodynamic rule of formation of intermetallic phases, which suggests intermetallics only form when the enthalpy of mixing has a large negative value. Miedema’s model is used solely for pragmatic reasons, even though it has some limited theoretical backing [179]. It has been shown that the electronegativity parameter is one of the most important parameters in the determination of phase stability in HEA [185] and electronic redistribution takes place when intermetallic forming elements are added to multicomponent HEA mixes [186].

In view of the above, we have plotted the Mulliken charge (which is the net charge on an atom) calculated from our CASTEP calculations. The Mulliken charge analysis is one of the first schemes for calculating the net charge on an atom [187, 188]. This method employs a basis function to express the orbitals. Considering the case of two non-interacting atoms (X and Y) forming a bond, the orbital ($\psi(r)$) on an atom (say X) may be expressed as:

$$\psi(r) = \sum_X \sum_{\mu \in X} c_\mu \chi_\mu \quad (8.2)$$

where, χ_μ is the basis function around atom X. Now, the total number of electrons (N) in X-Y molecule may be given as [188]:

$$N = \sum_{X,Y} \sum_{\mu \in X, \nu \in Y} \sum_i^{ocp} n_i c_{\mu i} c_{\nu i} \int \chi_\mu * \chi_\nu dr \quad (8.3)$$

where, n_i is the occupancy of the i^{th} orbitals. The $\sum_i^{ocp} n_i c_{\mu i} c_{\nu i}$ term in the above

equation is $D_{\mu,\nu}$, which is the density matrix, while $\int \chi_\mu * \chi_\nu dr$ is the overlap integral ($S_{\mu,\nu}$) between $\chi_\mu(r)$ and $\chi_\nu(r)$. The total Mulliken population (Q_μ) of the χ_μ may be expressed as:

$$Q_\mu = D_{\mu,\mu}S_{\mu,\mu} + \frac{1}{2} (D_{\mu,\nu}S_{\mu,\nu} + D_{\nu,\mu}S_{\nu,\mu}) \quad (8.4)$$

where, $D_{\mu,\mu}S_{\mu,\mu}$ is the Mulliken population acquired by χ_μ in the X-Y molecule. Note that the concept of charge transfer was originally introduced for molecules, hence the discussion here is being carried out in terms of two elements forming a molecule. The Q_X^M or Mulliken charge on atom X may be expressed as the difference between the nuclear charge of atom X (Z_X) and the sum of total Mulliken populations around atom X :

$$Q_X^M = Z_X - \sum_{\mu \neq \nu} Q_\mu \quad (8.5)$$

Though, this approach is extensively applied for quantifying a charge on the atom, it does not converge with increasing basis set size and can provide erroneous charge [188]. But for the purpose of comparison, the Mulliken population analysis can provide the relative value, provided a consistent basis set is employed [189].

In view of the issues with Mulliken population analysis, a range of population analyses have been proposed, which are based on electron density as a function of spatial coordinates. Among them, one of the important schemes is known as the “*atom in molecule*” or Bader population analysis [190]. In this scheme, the topology of the electron distribution around the atom is employed to quantify the bonding. In this method, first of all the bond critical points are determined, which are the points with minimum charge density. These bond critical points are used to determine surfaces with negligible electron density, which ultimately divides the molecule into atoms. The

Bader charge on the atom X (Q_X^B) may be expressed as:

$$Q_X^B = Z_X - \int \rho(r) dr \quad (8.6)$$

where, $\rho(r)$ is the electron density.

It can be seen in Fig. 8.2 that the HCP and FCC Co-matrices show similar behaviour in terms of charge rearrangement, with Cr having net positive charge associated with it, while Ni and Mn have a slight negative net charge on them. In the case of the BCC-Cr matrix, a significant charge fluctuation is taking place at nearest neighbour Cr atoms, with Co, Fe and Mn atom impurities showing negative charge concentration. Similar charge redistributions can be seen in the case of impurities in the FCC-Cr matrix calculations with less fluctuations of charge in the nearest-neighbour. In the case of impurities in BCC-Fe and FCC-Fe, the charge redistribution characteristics are similar with only one exception; the case of BCC-Fe matrix with a Cr impurity. The same can be seen for BCC, FCC-Mn calculations, where charge fluctuations in first nearest-neighbour Mn atoms are present for the BCC-Mn matrix when Cr is introduced as an impurity in the centre of supercell. For the FCC-Ni matrix calculation, all the impurities have a net positive charge on them. It can be clearly seen from observing all the calculations that Cr adopts a comparatively large positive charge in the presence of Co, Fe, Mn and Ni. Additionally, the charge (either negative or positive) on a particular impurity shows similar values, which are independent of the crystal structure of the matrix (Figure 8.3). So, from now on while comparing the charge of a particular atom introduced into a range of matrices, we will discuss the ground-state structure, *i.e.* Co-matrix in HCP form, Cr-matrix in BCC form, Ni-matrix in FCC form and so on.

We also plotted the energy change associated with the introduction of impurity-

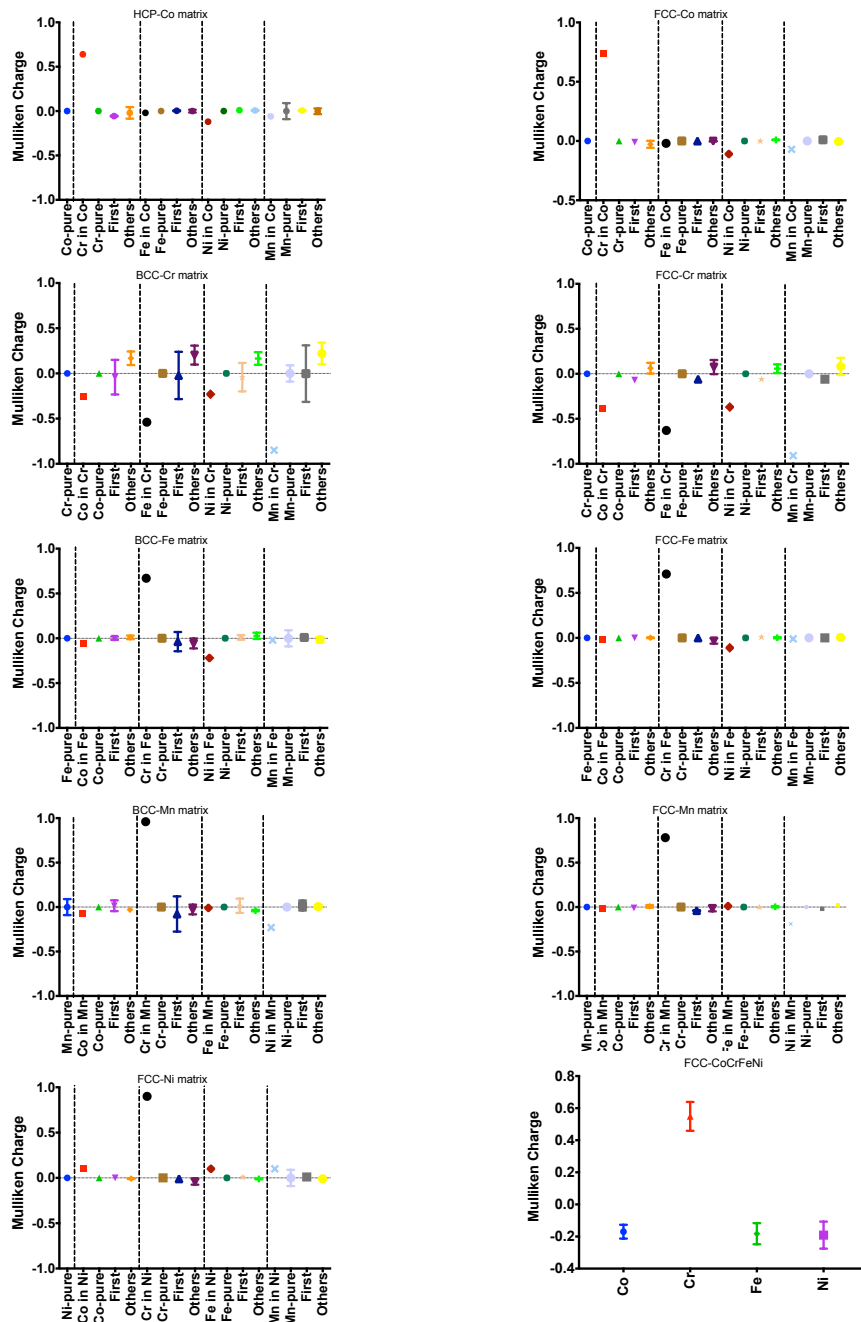


Figure 8.2: Mulliken charge on impurity at the centre of the supercell along-with that on first and second nearest-neighbours and on each atom for the CoCrFeNi HEA. The terminology used for naming x-axis is as follows: for *e.g.*, Cr in Co signifies the case where Cr is added to the supercell of Co.

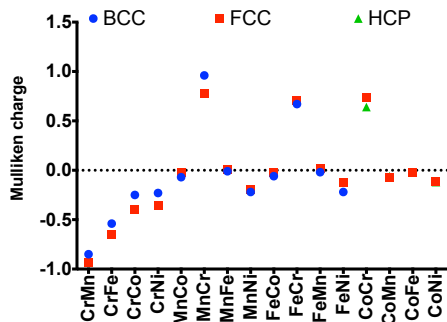


Figure 8.3: Comparison of Mulliken charge on impurity, when calculations are being carried out for a matrix with the ground-state structure of the element and with the FCC structure. See text for explanation of the terminology used for naming points on x-axis.

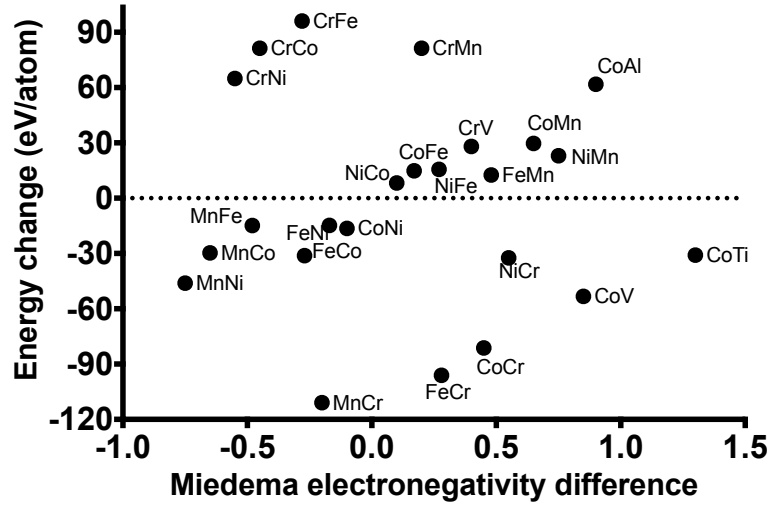
in-matrix against the electronegativity difference of matrix and impurity. Note that we have followed the same nomenclature for marking the points shown in Fig. 8.4(a) and 8.4(b), where the first element name corresponds to that of the matrix and the second denotes the impurity atom. So, FeCr is a Cr impurity in a Fe-matrix. The Miedema electronegativity corresponds to $\Delta\phi$, as used for the enthalpy calculation in Miedema's model (equation 8.1). $\Delta\phi$ is equal to $\phi_m - \phi_i$, where ϕ_m and ϕ_i are Miedema electronegativities for matrix and impurity respectively. A negative value of $\Delta\phi$ signifies that the matrix is more electronegative than the impurity, while a positive value of $\Delta\phi$ implies the opposite. It can be seen in Figure 8.4(a), that $\Delta\phi$ or the Miedema electronegativity has a significant spread in comparison to the observed Mulliken charge, although there is qualitative agreement. For example, if we consider Cr in a Co-matrix, it has a positive Mulliken charge associated with it, which signifies it has lost electrons, and $\Delta\phi$ is positive, which implies that Co is more electronegative than Cr. Quantitative agreement would not be expected, since the Miedema electronegativity values for elements have been determined by a fitting procedure with the little physical meaning, while the Mulliken charges on atoms has been determined using DFT calculations. Clear

qualitative disagreement is evident for Cr in a Mn-matrix, and Mn in a Cr-matrix, Fe in a Co-matrix, etc (Fig. 8.5). So, it can be deduced that the Miedema electronegativity scale has limitations for certain cases and their usage for determining the enthalpy of mixing for multicomponent HEAs could lead to further erroneous predictions. To further confirm the charge disproportion, as observed earlier, we have calculated Bader charges on the atom first using the charge density file of CASTEP reformatted as the CHGCAR file of VASP [191], which is subsequently employed in a post-processing code written by Henkelman *et. al.* [192] for DFT calculations. It can be seen that both Mulliken and Bader formalisms show qualitative agreement as shown in Fig. 8.6.

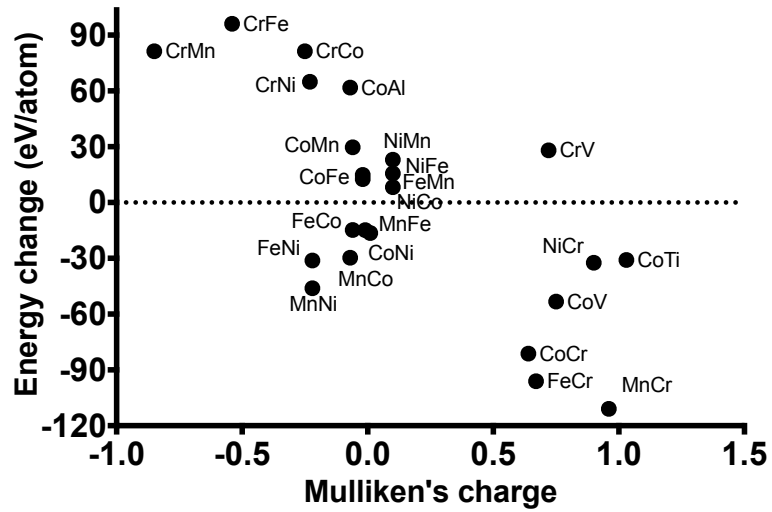
8.3 Electron spin distribution and implications to distortion in substitutional alloys

To explicitly elucidate the evolution of the distortion due to the particular atomic species, we have extracted the interatomic separation values from the CASTEP output files. Figure 8.7 represents the frequency plot of bond length between neighbouring atoms. It can be seen that in the pure BCC form each of Fe, Cr and Mn show two different distinct interatomic separations. We would expect that in BCC, the first nearest neighbour is at $2r$, while the second nearest neighbour is at $2.3r$ (where r is the atomic radius). But, addition of the Ni to BCC-Cr leads to additional variation in the interatomic separation, while for the BCC-Fe matrix, there is negligible variation from impurities, except when Mn was added.

Figure 8.8 shows the interatomic separation variation for impurity-in-matrix calculations for FCC Co, Cr, Fe, Mn and Ni matrices. In case of the FCC-Co matrix, addition of Cr, Fe and Mn impurities leads to similar effects involving the appearance



(a)



(b)

Figure 8.4: CASTEP energy change associated with introduction of impurity into ground-state structures of various metals plotted with (a) Miedema electronegativity scale and (b) Mulliken charge on impurity.

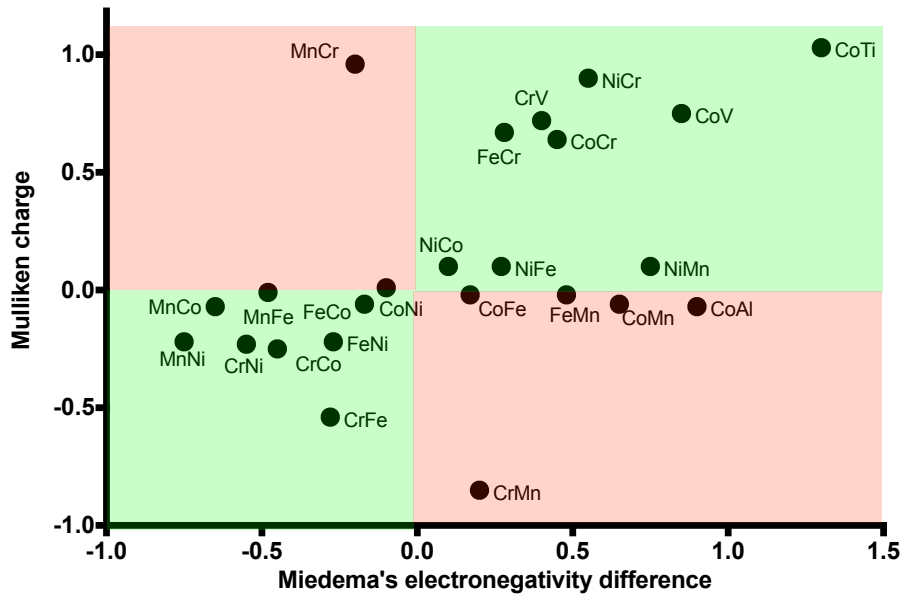


Figure 8.5: Comparison of Miedema electronegativity difference and Mulliken charge over impurity.

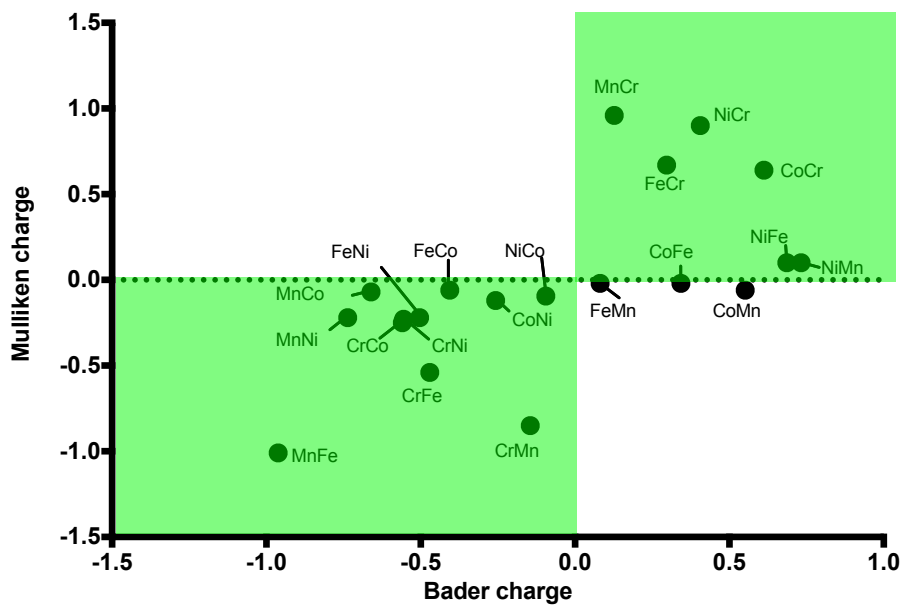


Figure 8.6: Comparison of Mulliken charge and Bader charge for different impurity-in-matrix calculations.

of interatomic separations at lower values of 2.48 Å, along with the originally present bonds having a bond-length (2.50 Å), except in the case of the Ni impurity, which only shows one interatomic separation of 2.50 Å. It implies that addition of Ni in FCC-Co matrix causes negligible fluctuations in bond-length. Addition of Co, Cr and Fe in FCC-Cr leads to the occurrence of five interatomic separation values, i.e., 2.50, 2.52, 2.56, 2.60 and 2.62 Å, respectively. It is evident that there is significant distortion in the FCC-Cr matrix, when an impurity is introduced into the FCC-Cr supercell. So, it can be deduced that Cr tends to get distorted in the presence of another transition metal and this may be the reason that Cr has a significant influence on mechanical and functional properties [193,194]. Negligible distortion can be seen when different impurities are added to FCC-Fe, FCC-Mn and HCP-Co matrix with two exceptions. The first exception is the distortion of 0.10 Å in the case of a Cr impurity in the FCC-Mn matrix, while in the second case, Mn impurity in the HCP-Co matrix causes a distortion of 0.08 Å. So, it can be deduced that FCC-Cr has distinctly different behaviour from the FCC-Co, Fe, Mn and Ni matrices. We will discuss the reason behind this shortly.

Figure 8.9(a) shows the bond-length variation in the case of FCC-CoCrFeNi plotted together with interatomic separation values of FCC-Co, Cr, Fe and Ni. It is evident that the interatomic separation shows a Gaussian distribution, as shown by the curve in Fig. 8.9(b), which is similar to that reported in the literature [195]. The mean interatomic separation for FCC-CoCrFeNi is 2.50 Å. So, possibly the occurrence of different atomic species leads to the range of interatomic separation values with a Gaussian distribution.

The effect of Cr on short range ordering has been reported in the case of CoCrNi and CoCrFeNi [196,197]. The short range order (SRO) can have a significant influence on the structural properties of the metallic alloys. It may increase the yield strength at low temperature, but may cause the yield strength to drop at higher temperatures [198].

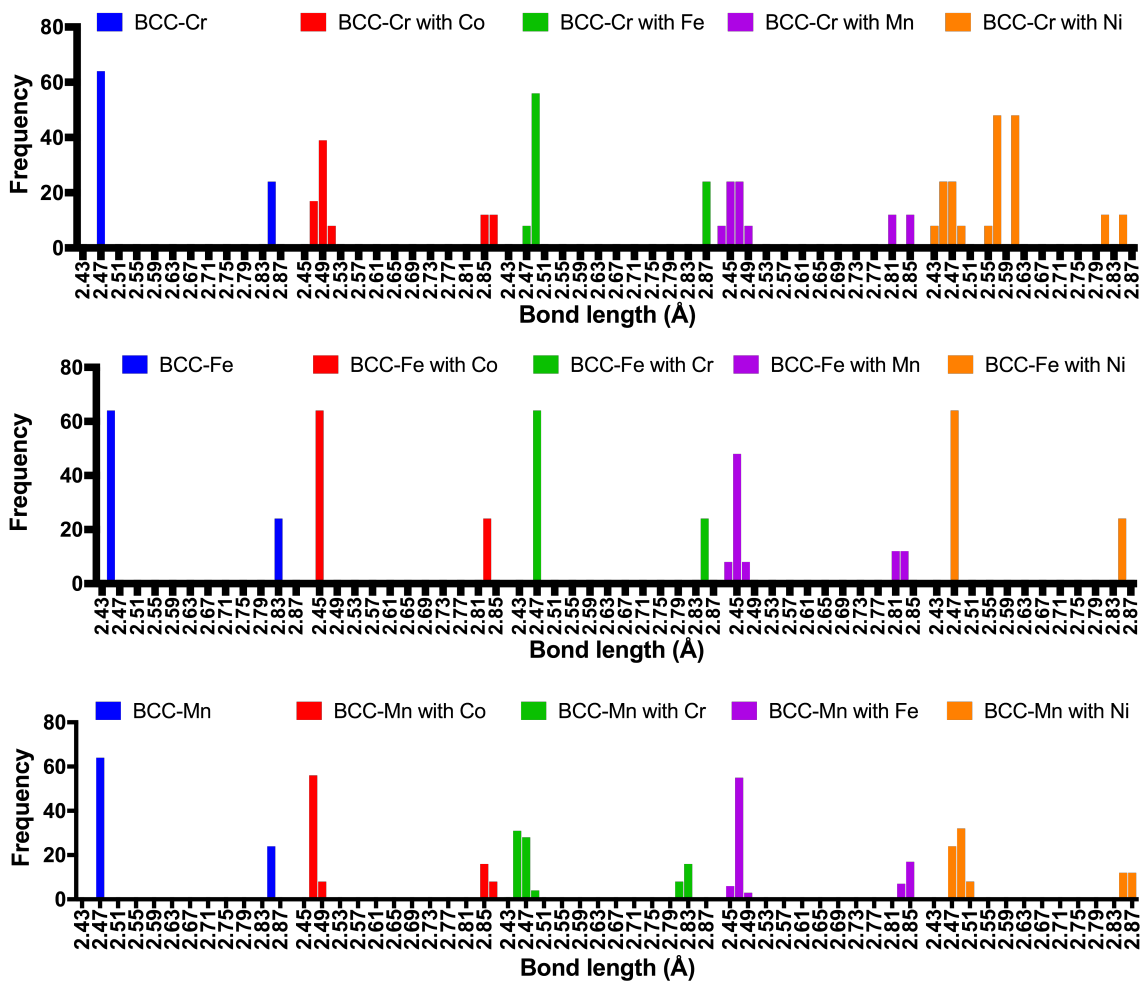


Figure 8.7: Frequency (number of times particular interatomic separations) of different interatomic separation in a BCC matrix. Note that the bin-size for plotting the histogram is 0.02 Å.

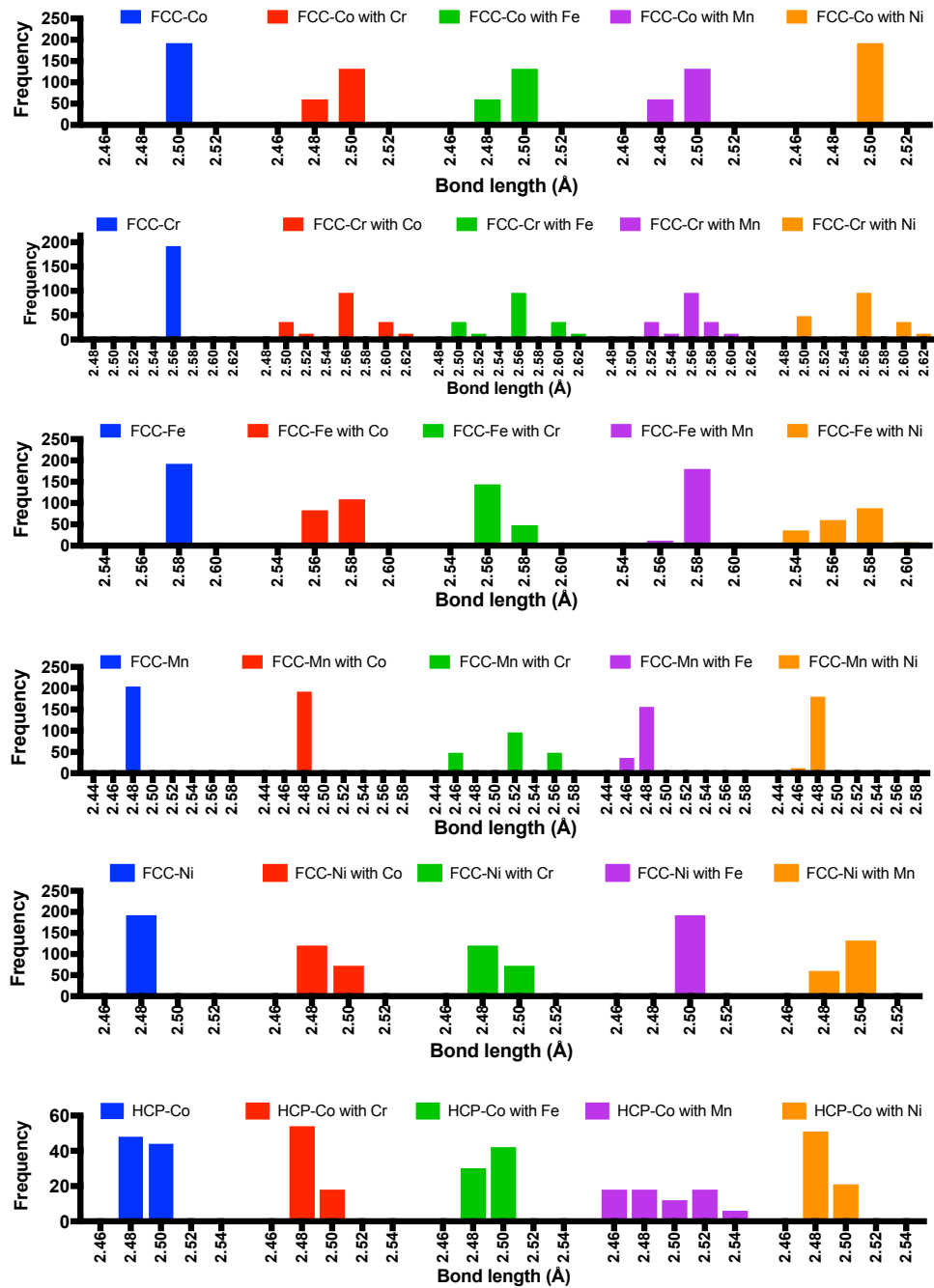


Figure 8.8: Frequency of different bond lengths in FCC and HCP (in the case of Co) matrix. Lower values of frequency in case of HCP-Co in comparison with FCC cases is due to the lower number of atoms in HCP-supercell studied here in comparison with FCC supercell.

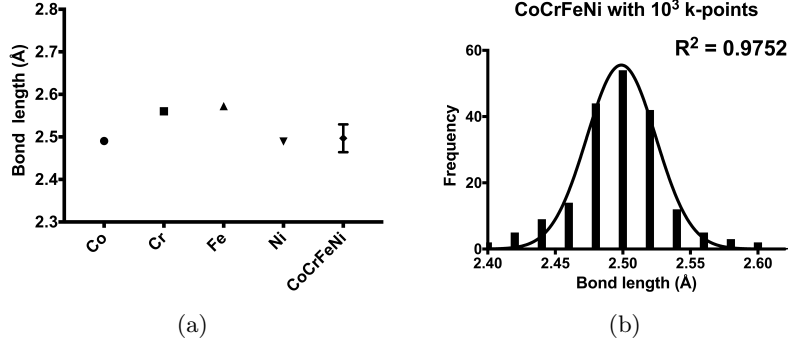


Figure 8.9: Bond length values for the CoCrFeNi with reference to bond-length values of the FCC forms of Co, Cr, Fe and Ni.

The increase in the yield strength due to SRO is understood in terms of the additional stress required for a dislocation to move through a slip plane, which is due to the presence of an interface between the ordered and disordered region [199]. The occurrence of SRO and its effect on the mechanical properties of Ni-20% Cr alloy has been reported, where an increase in the yield strength and fluctuations in the stress-strain curve in the temperature regime of 400-600°C or the Portevin-Le Chatelier (PLC) effect is exhibited, due to movement of dislocations through Cr-clusters [200, 201]. The existence of SRO was predicted in HEAs using DFT and Monte-Carlo simulations, where a greater number of Ni-Cr and Cr-Co pairs in comparison to Cr-Cr pairs in ternary CoCrNi and quaternary CoCrFeNi HEA was predicted [202] and has been experimentally verified with Extended X-ray Fine Structure (EXAFS) studies for the ternary system [196]. The PLC type serration behaviour has been reported for the CoFeNi alloy in a temperature-range of 400-500 °C, while for CoCrFeNi and CoCrFeMnNi HEA, it is observed in a temperature regime of 300-600 °C. Now, the influence of the SRO in HEA can be crucial for both low and high temperature deformation [62, 203, 204].

In view of the above, we have generated the 2X2X2 supercell with FCC matrix

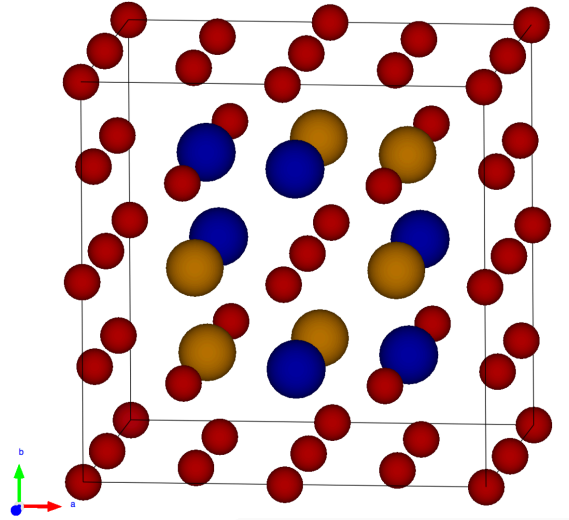


Figure 8.10: Schematic figure of the 2X2X2 supercell with SRO. In this figure red blue and golden spheres represents Co, Cr and Fe atoms, respectively. The atomic radius of atoms represented here not to scale the relative atomic-size difference between atoms.

and alloying elements in the first nearest-neighbour (1NN) to study the influence of alloying elements on the interatomic separation variation. So, we generated a FCC-Co matrix, with three distinct cases of alloying in the 1NN. In the first case, 6 Cr and 6 Fe atoms surround Co in the centre of the supercell (schematically shown in Fig. 8.10). In the second case, for the FCC-Co supercell, 6 atoms each of Cr and Ni atoms are introduced in 1NN and in last case, 6 Fe and 6 Ni atoms were introduced in 1NN. We have similarly carried out calculations for FCC-Fe and FCC-Ni. Note that the aim of this set of calculations is to see how the interatomic separations vary, if the identity of the alloying elements that are ordered in the lattice is varied. These calculations were carried out with a 6X6X6 k -points grid.

Figure 8.11 shows the bond-length variation for Co, Fe and Ni matrices in the FCC lattice with different types of atoms introduced in 1NN positions. It can be seen that,

when 6 of each of Cr and Fe is added in the 1NN of FCC-Co matrices, the bond length range is 2.44-2.54 Å with a mean value of 2.50 Å with standard deviation of 0.02 Å. With the addition of 6 Cr and 6 Ni in the 1NN, the bond length range decreases and lies in the range of 2.46-2.52 Å, with a mean value of 2.49 Å with standard deviation of 0.011 Å. Addition of 6 Fe and 6 Ni to the 1NN leads to a slight increase in the bond length range, i.e., 2.46-2.54 Å with a mean value of 2.50 Å and a standard deviation of 0.018 Å. In the case of a FCC-Fe matrix, addition of 6 Co and 6 Cr in the 1NN leads to the bond length to be in range of 2.43-2.57 Å along with certain bonds having lengths in the range 2.61-2.63 Å. The mean value of the bond length was found to be 2.50 Å with a standard deviation of 0.033 Å. The bond length ranges from 2.44-2.64 Å in the case of 4 Co, 4 Cr and 4 Ni in the 1NN of FCC-Fe with a mean value of 2.52 Å and a standard deviation of 0.038 Å. With only 6 each of Cr and Ni in FCC-Fe, the bond-length is in range of 2.46-2.62 Å, with mean value of 2.53 Å and a standard deviation of 0.04 Å. The maximum standard deviation of bond-length can be seen in the case of addition of 6 Cr and 6 Ni in the 1NN of the FCC-Fe matrix with a value of 0.041 Å with a mean bond length of 2.528 Å. The bond length range is 2.44-2.60 Å. In the case of the FCC-Ni matrix, the presence of 4 Co, 4 Cr, and 4 Fe in the 1NN lead to bond length variation of 2.46-2.56 Å with a mean value of 2.51 Å and a standard deviation of 0.016 Å. With only 6 Co and 6 Fe in the 1NN in the same matrix, the bond length has a mean value of 2.502 Å with a standard deviation of 0.017 Å, while the bond length range is 2.46-2.54 Å, which is slightly less than the earlier case. So, it can be deduced from the above that the bond distortion due to SRO is dependent upon the chemical identity of the elements getting ordered in the lattice.

The influence of magnetism on distortion has been studied, where the individual magnetic nature of elements plays a crucial role in bond distortion characteristics [205,

206]. Also, in the case of CoCrNi, the competing ferromagnetic nature of Co and Ni and the antiferromagnetic nature of Cr leads to variation in properties, particularly with variation of Cr [194]. Figure 8.12 shows the magnetic moment of various elements, when they are added to a FCC-matrix of other elements and corresponding changes in magnetic moment at first (1NN) and second (2NN) nearest-neighbour positions. The magnetic moment of impurities in the FCC lattice has been shown for reference as well.

In the case of a FCC-Co matrix, Cr and Mn tend to align in an anti-ferromagnetic manner with respect to Co atoms with magnetic moments of $-2.94 \mu\text{B}$ and $-3.53 \mu\text{B}$, respectively. Both Cr and Mn matrices have similar behaviour in terms of bringing down the magnetic moment values of the impurity close to zero. In an FCC-Fe matrix, Cr shows anti-ferromagnetic ordering with a magnetic moment of $-3.45 \mu\text{B}$. Additionally, the magnetic moment of Mn in other FCC-matrices shows a pattern in which there is increase in the magnetic moment, except in the case of Mn in the FCC-Cr matrix, where the magnetic moment of Mn is close to the zero value. Figure 8.12 also shows the different magnetic moments associated with Co, Cr, Fe, Mn and Ni atoms in the FCC-CoCrFeNi alloy calculation. It can be seen that Fe shows maximum variation in magnetic moment followed by Cr, while least variation is exhibited by Ni.

The influence of magnetism on the quantum mechanical stress or Hellman-Feynman (HF) force was studied by carrying out additional non-spin polarised calculations for Cr, Fe and Mn matrices, with the addition of Co, Cr, Fe, Mn and Ni impurities. Figure 8.13(a) shows the HF force for Cr, Fe and Mn in FCC-lattices. It can be seen that the HF force on Cr is independent of magnetism, while in the case of Mn, there is an increase in the HF force due to magnetism, while the opposite trend is exhibited by FCC-Fe. It implies that, the magnetism influences the stresses at the atomic level differently for different atomic species. From the impurity-in-matrix calculations, it is

evident that magnetism generally causes an increase in HF stresses on the impurity atom, 1NN and 2NN atoms, except in the cases of Ni in FCC-Cr, Mn in FCC-Cr and Mn in FCC-Fe (Fig. 8.13(b)). The HF stress on the Ni and 1NN Cr decrease in the presence of magnetism, while there is an increase in HF stress on 2NN Cr atoms. For Mn as an impurity in FCC-Cr, there is no change in HF stress for a Mn impurity and 2NN Cr atoms. For Mn in FCC-Fe, a decrease of HF stress takes place due to magnetism on 1NN FCC-Fe atoms, while Mn impurity and 2NN Fe atoms have no influence stresses due to magnetism. The influence of magnetism is unique to the identity of the elements involved.

As, has been mentioned above, there is the possibility of SRO in the system, which might lead to the anisotropic distortion in the system. But, such SRO might change the local shear modulus, which decides the pressure field around the dislocation. Senkov *et al.* proposed the linear framework for determination of the shear modulus [149], where the net shear modulus of an alloy can be obtained by linear addition of shear modulus values for the constituent atomic species. This linear variation of shear modulus was used in other work as well [109,148,207]. But, it should be noted that elastic properties of metallic species might not show clear linear variation with composition [208].

Hence, the take-away point from the above observations is that distortion in these substitutional systems is caused by the local magnetic interactions between atomic species and thus, caution should be exercised while calculating the elastic properties with a simple averaging procedure.

As, has been seen in Fig. 8.8, there are two cases: where there is distortion (Cr, Fe, Mn and Ni in FCC-Co) and where there is negligible distortion (Ni in FCC-Co). To study the link between magnetism and distortion, we have plotted the negative and positive magnetic moment associated with atoms using the XCrySDen code [209]. A

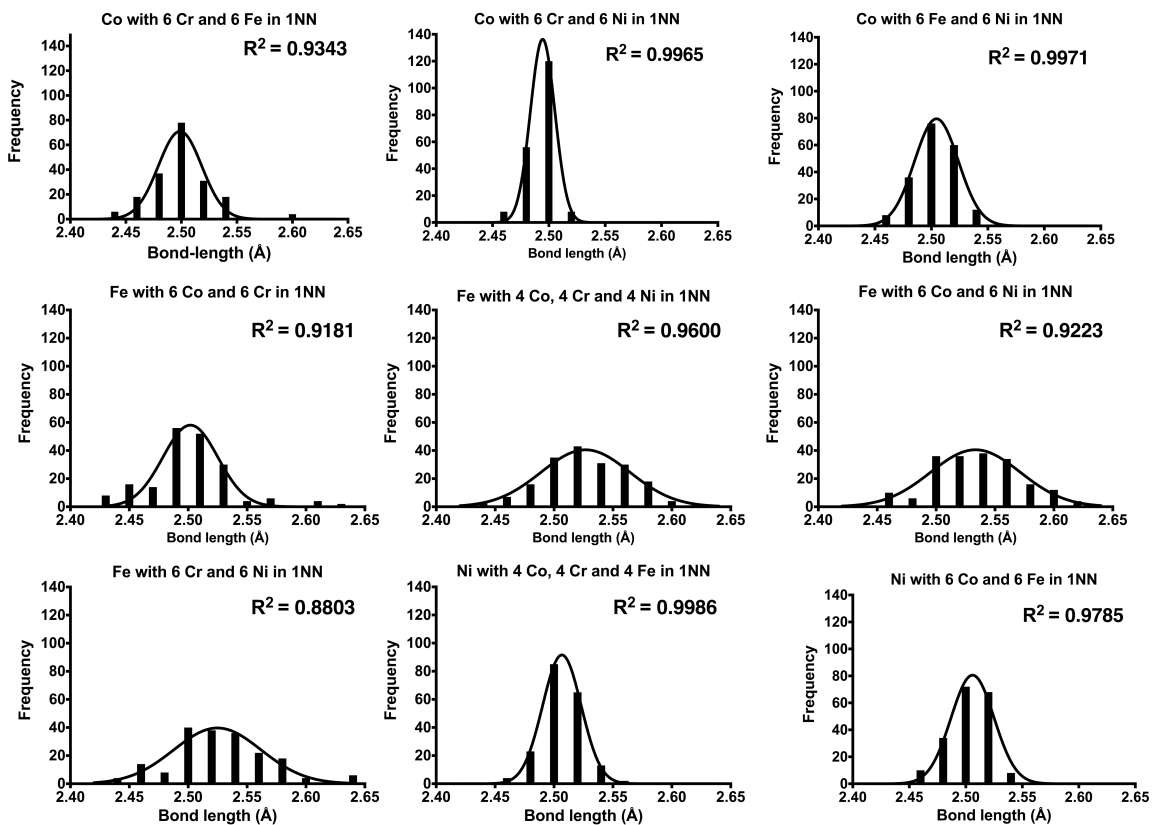


Figure 8.11: The frequency of different bond lengths for the FCC-matrix with different combination of atomic species in first nearest neighbour (1NN)

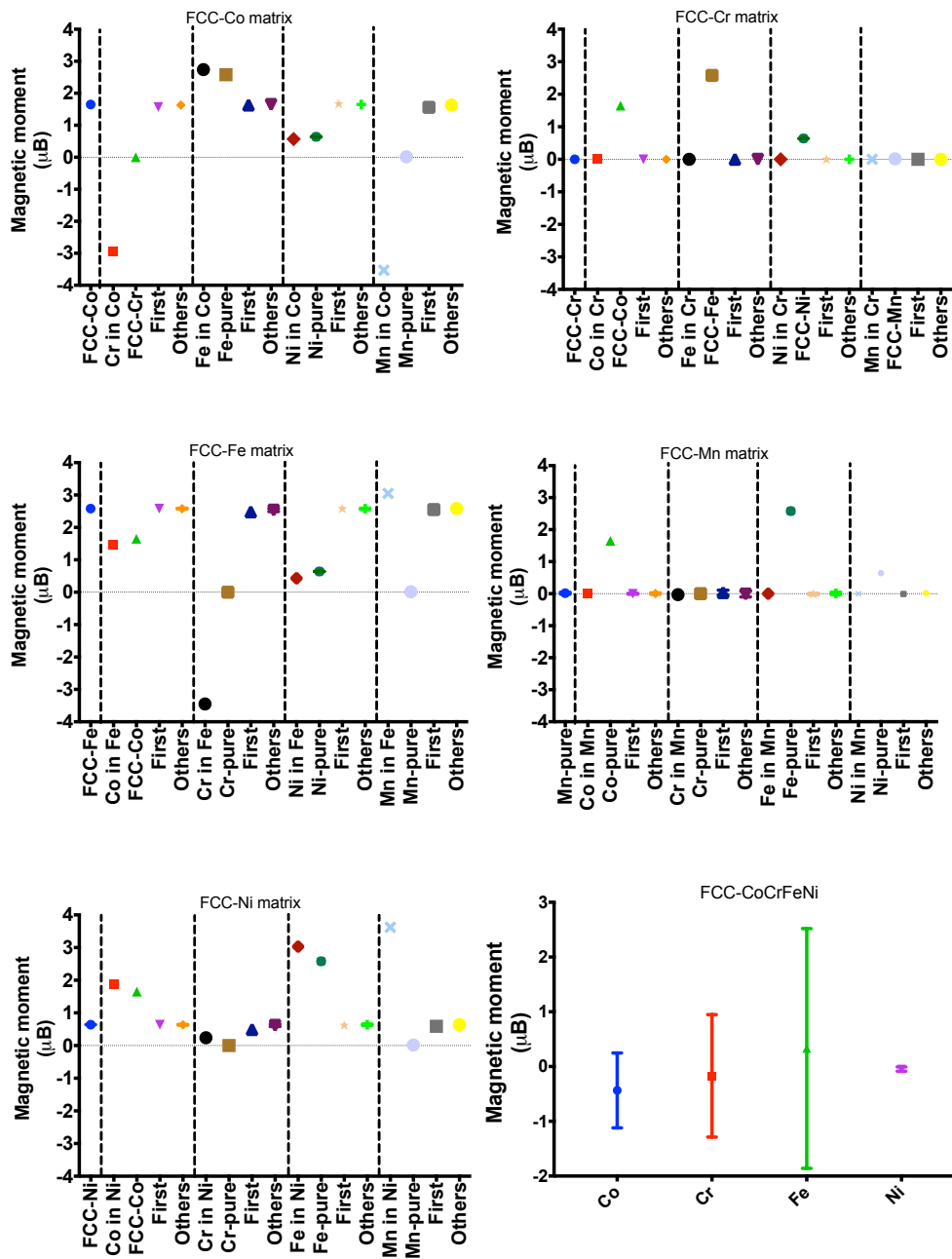
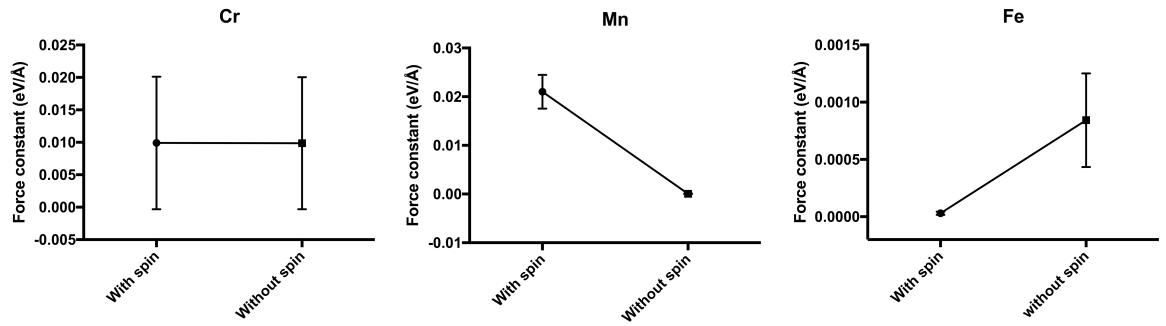
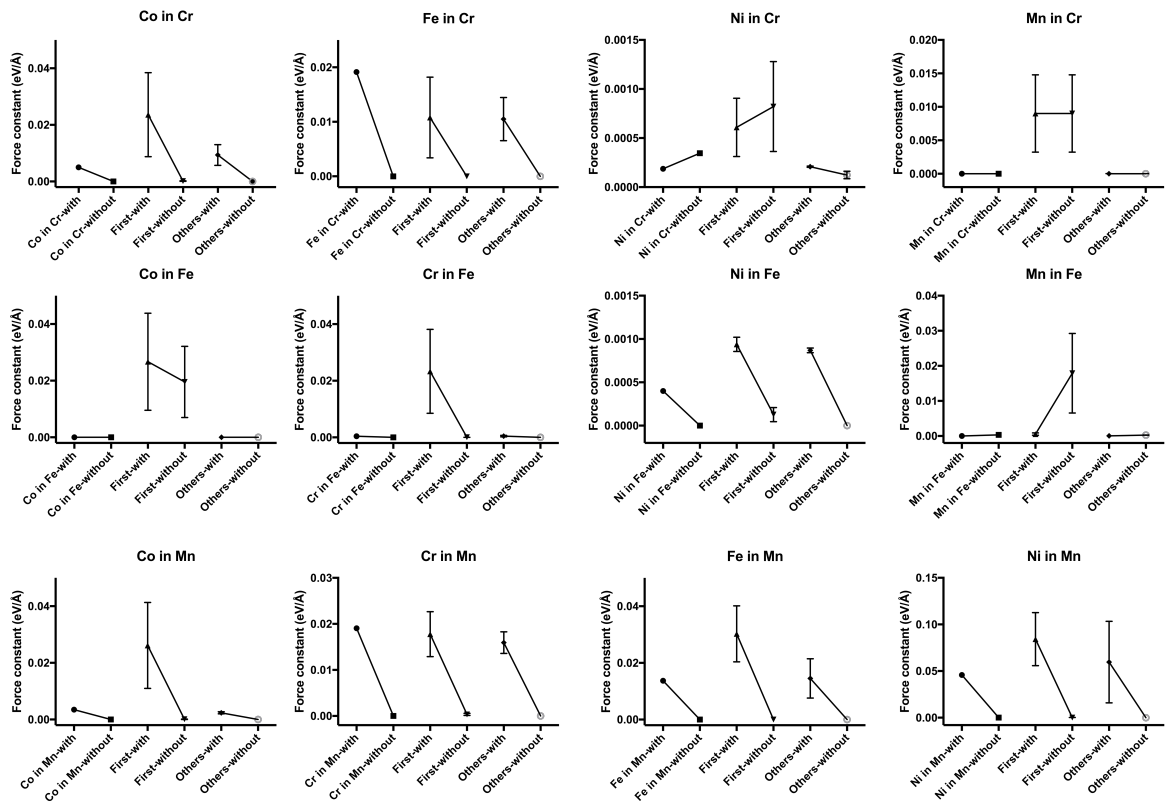


Figure 8.12: The magnetic moment variation for impurity-in-atom and FCC-CoCrFeNi calculation. Similar terminology as mentioned in Fig. 8.2 is employed here for labelling x-axis.



(a)



(b)

Figure 8.13: The influence of magnetism on the force constant at the impurity, first nearest neighbour (First) and second nearest-neighbour (Others) atoms. In this figure, we have compared the force constant on the impurity, first nearest-neighbour and second nearest neighbour atoms calculated with and without spin-polarised calculations.

code written by Mark Rutter [210] was used to convert the CASTEP binary file (.check file) into an .xsf file to be used for visualisation in the XCrySDen code. Figure 8.14 shows the magnetic moment distribution of Ni in a 2X2X2 supercell of FCC-Co. It can be seen that the magnetic moment on each atom is aligned in a parallel direction, as both Co and Ni are ferromagnetic. Note that, we observed negligible distortion in this case (Fig. 8.8). Figure 8.15(a) and 8.15(b) show the electrons with positive and negative spins respectively for the Co in the Cr system. It is evident that 1NN Cr has the same sign of spin, while 2NN Cr has opposite spin to that of the Co atom. Also, it can be seen that the spin on the 1NN and Co atom have an anisotropy associated with them (*i.e.*, non-spherical). Figure 8.16(a) and 8.16(b) show the positive and negative magnetic moment variation on Cr atoms due to the presence of an Fe atom in the centre of the supercell. It can be seen that the nearest neighbour Cr atom to the Fe impurity shows different magnetic moments, *i.e.*, Cr atoms have both positive and negative magnetic moments associated with them. Similar behaviour was exhibited when Mn and Ni were added to FCC-Cr, as shown in Fig. 8.17 and 8.18, respectively. It can be also said that the d-orbitals of Cr assume a complementary spin to the spin of other d-orbitals, as can be clearly seen for Mn in FCC-Cr. Cr has five electrons in d-orbitals ($[Ar]3d^54s^1$). So, by Hund's rule of maximum multiplicity, all of them should be aligned along the same direction, *i.e.*, they should have the same spin orientation. But, with the addition of an impurity in the Cr-matrix, it can be seen that certain d-orbitals exhibit an opposite sign of spin. In view of the above, it can be deduced that distortion due to the Cr arises from the change in the orientation of spin in d-orbitals of the Cr atom in the presence of other transition metals.

We have also plotted spin for FCC-CoCrFeNi, as can be seen in Fig. 8.19(a) and 8.19(b). The spin-ordering is evident in this case with certain spin orientations

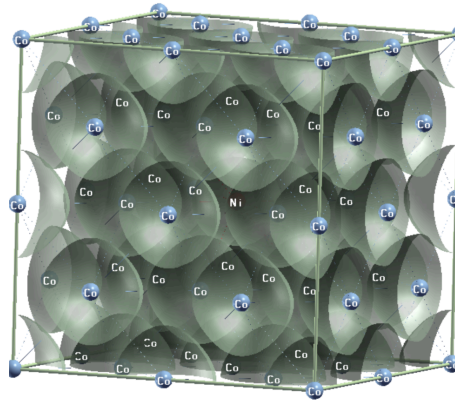


Figure 8.14: Magnetic moment distribution in a supercell containing Ni impurity in the FCC-Co matrix.

surrounding corresponding complementary spin orientations and in certain cases, spin anisotropy on particular atoms is also clear. We have seen that certain atoms have HF forces associated with them, possibly arising due to spin-inhomogeneity. We have also attempted to carry out spin-polarised geometry optimisation for 5X2X2 supercell of FCC-CoCrFeMnNi alloy with 80 atoms. The calculation did not converge within the specified tolerance limit for geometry optimisation. But, we have plotted positive and negative spin around atoms along with the HF force, as shown in Fig. 8.20 and 8.21, respectively. It can be deduced from these figures that there is spin ordering in the system, as we have seen for FCC-CoCrFeNi, with electrons with positive moment surrounding electrons with negative moment. We have shown a zoomed in perspective in Fig. 8.22(a) and 8.22(b). This observation is in line with recently reported spin-frustration reported for this alloy [211] and spin-mediated ordering in CoCrFeNi [212]. Note that, we did not observe HF forces of similar magnitude for impurity-in-matrix calculations implying that spin-inhomogeneity and spin-ordering may be one of the possible reasons for high quantum mechanical stress in HEAs.

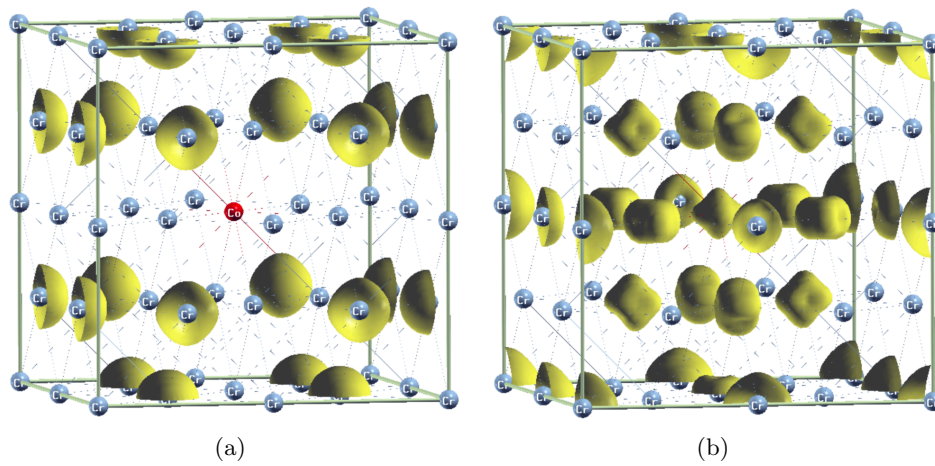


Figure 8.15: Distribution of positive and negative magnetic moment for Co in FCC-Cr matrix calculations.

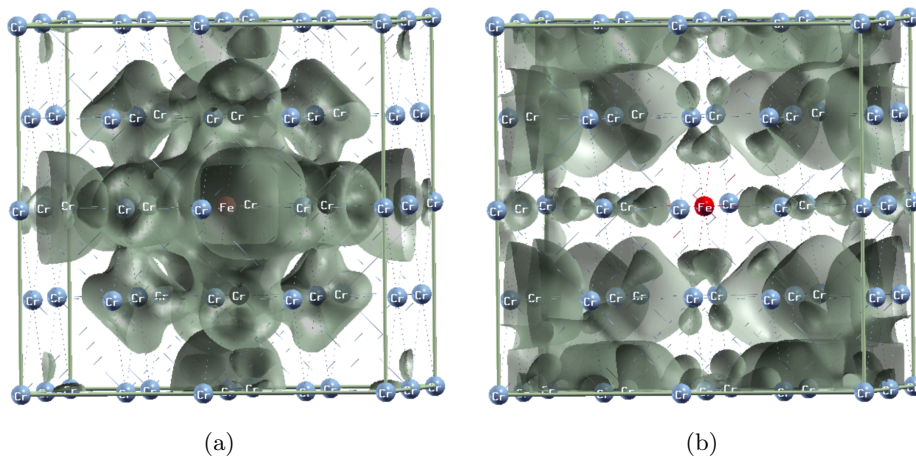


Figure 8.16: Distribution of positive and negative magnetic moment for Fe in FCC-Cr matrix calculations.

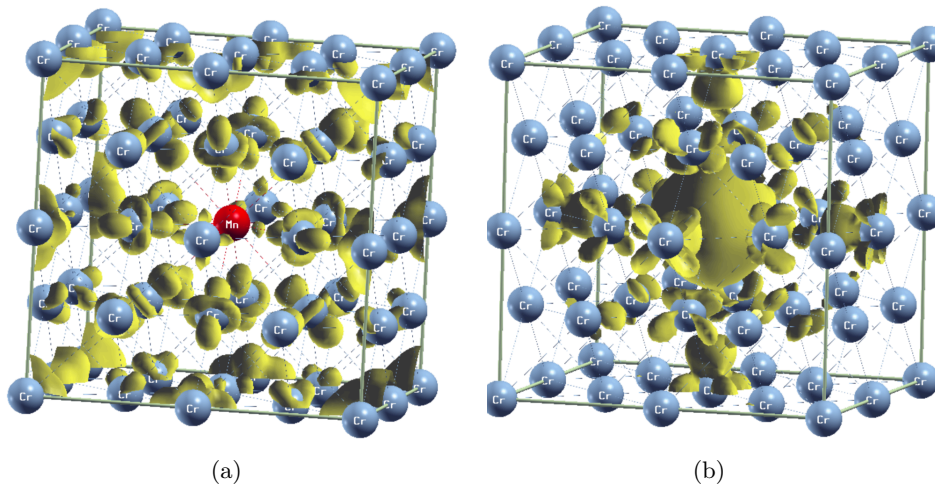


Figure 8.17: Distribution of positive and negative magnetic moment for Mn in FCC-Cr matrix calculations.

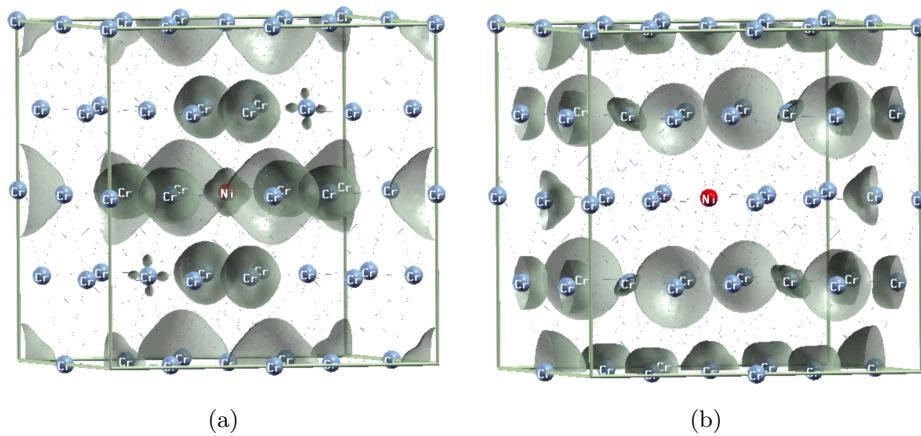


Figure 8.18: Distribution of positive and negative magnetic moment for Ni in FCC-Cr matrix calculations.

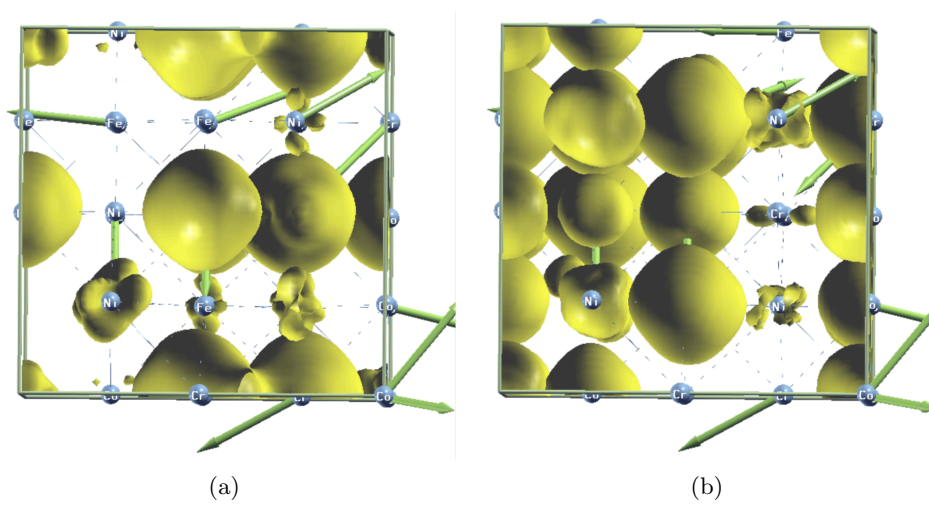


Figure 8.19: Figure showing (a) electrons with positive spin moment surrounding negative spins and (b) electrons with negative spin moment surrounding positive spins for FCC-CoCrFeNi.

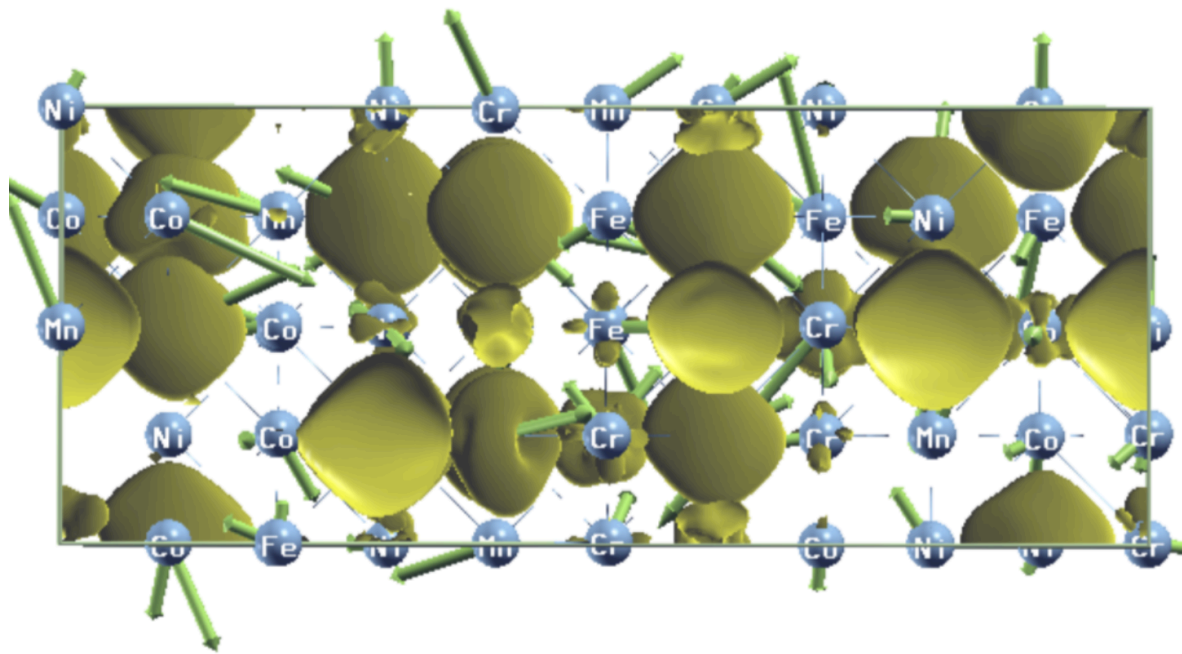


Figure 8.20: Distribution of electrons with positive moment in a 5X2X2 supercell of FCC-CoCrFeMnNi.

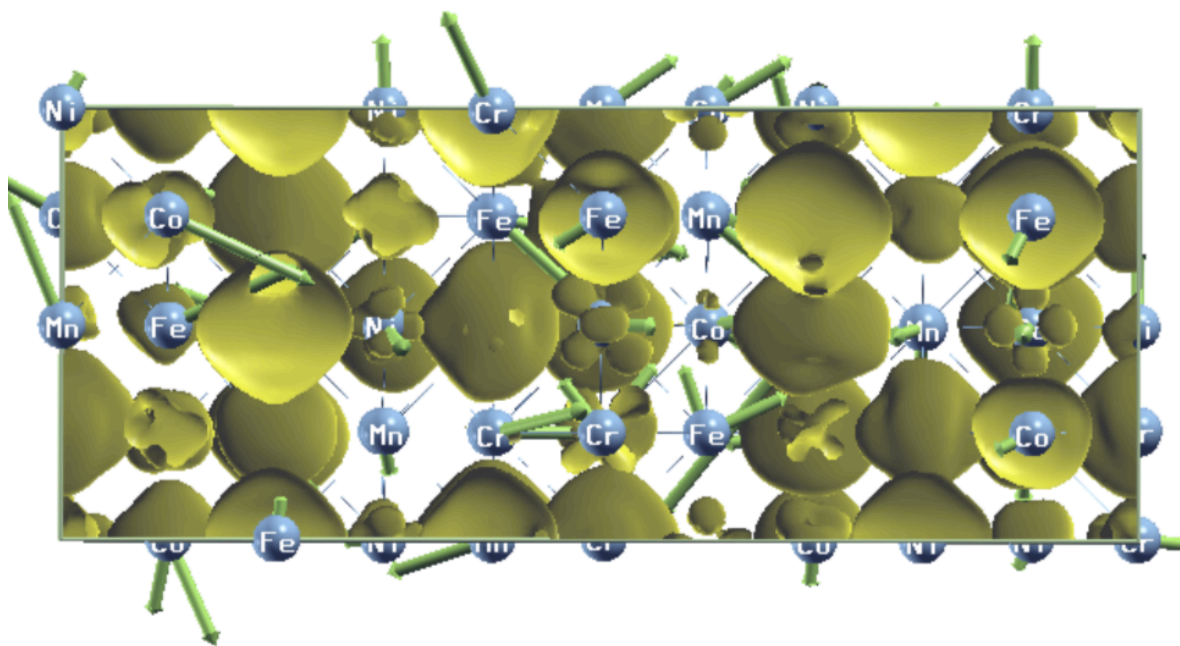


Figure 8.21: Distribution of electrons with negative moment in a 5X2X2 supercell of FCC-CoCrFeMnNi.

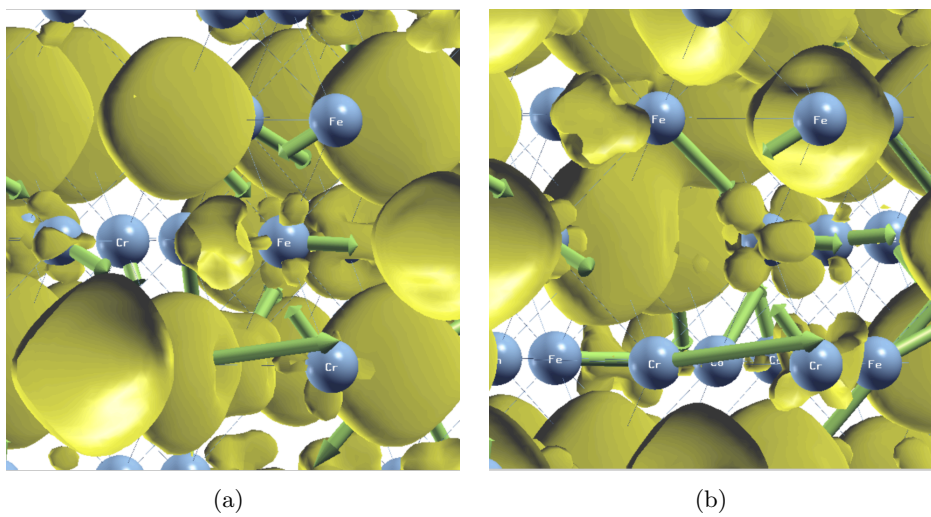


Figure 8.22: Figure showing (a) electrons with positive spin moment surrounding negative spins and (b) electrons with negative spin moment surrounding positive spins for FCC-CoCrFeMnNi.

8.4 Conclusions and future work

The present investigation aimed to develop a more fundamental understanding of the influence of a transition metal on another transition metal in terms of their interaction and effect on alloy formation. The local electronic redistribution due to a particular transition metal (i.e. impurity) in another transition metal (matrix) was studied and its implication for enthalpy calculations was discussed. Additionally, the effect of magnetism on the evolution of distortion in these systems was studied. The following conclusions can be drawn from this work:

1. The enthalpy of mixing for HEAs is routinely being calculated using Miedema's model, which was originally devised for binary alloys. The limitations of the Miedema's model stem from an inadequate description of the electronegativity parameter in this model.
2. Short range order in alloys can lead to significant bond distortion, which again depends upon the elements which exhibit such order.
3. Cr as an alloying element causes significant distortion in comparison to other transition metals (Co, Fe, Mn, and Ni) studied in this work. It has been demonstrated that such distortion may originate from different spin orientations in same d-orbitals of the Cr atom in the presence of other transition metals.
4. The quantum mechanical stress in multicomponent alloys may arise from spin ordering which leads to significant quantum-mechanical stress in the system.

Future work in this area should be directed along the following themes:

1. The electronegativity scale needs to be defined for each element, depending upon

its environment. An accurate scale could be used for enthalpy calculations to generate better alloy predictions.

2. Full-linearised Augmented Plane Wave (FLAPW) calculations could be carried out to study the influence of pseudopotentials on charge redistribution.
3. The spin ordering could be studied for a range of alloys, which are known to exhibit exotic mechanical properties to develop understanding of the influence of spin-spin interactions on emergent mechanical properties of engineering alloys.
4. The influence of the impurity on the magnetic state of the matrix need to be studied by increasing size of the supercell to study the long-ranged nature of spin effects.

* * * * *

Chapter 9

Concluding remarks

The present investigation has aimed to look into issue of phase stability in high-entropy alloys and oxides, evolution of the distortion in such multicomponent systems and the origin of attractive mechanical properties of certain high-entropy alloys. The following conclusions can be drawn from this work:

1. A procedure based on the hybrid genetic algorithm-molecular dynamics was developed for sampling positional-disordered materials. It has been shown that configurational entropy is simply not dependent upon the number of elements constituting the system, but it is dependent upon the identity of elements forming these systems. It has additionally been shown that the configurational entropy influences the phase selection in high-entropy alloys (though such a mechanism needs to be probed much rigorously in the future work). It has been shown for multicomponent oxides that as the number of types of cations in the system increases, the bond length values progresses towards a constant value.
2. The influence of alloying elements on the evolution of lattice friction in multi-

component alloys was studied using a Monte Carlo approach. It was shown that the energy range arising due to dislocation-solute interaction is a much more fundamental parameter for screening alloys which might exhibit exotic mechanical properties. This energy range can be a fundamental parameter for describing lattice friction of the alloy, independent of whether strong or weak dislocation pinning might be taking place. It should be noted that in certain cases where dislocation core-solute interactions are complicated in nature, the energetic contributions due to such complications need to be accounted.

3. The DFT studies on charge redistribution due to interaction among elements have demonstrated that electronegativity parameter being employed in Miedema's model can lead to erroneous prediction for multicomponent high-entropy alloys.
4. Spin-polarised DFT studies of transition metal alloys have shown that distortion in substitutional transition metal alloys possibly arises due to interactions of electrons with complimentary spins. It has been shown that in the presence of transition metals like Co, Fe, Mn and Ni, certain d-electrons of Cr show opposite orientation with respect to the spin orientation of other d-electrons. This observation provides an explanation of the strengthening capability of Cr. Additionally, the spin-polarised DFT studies of the concentrated alloys have shown that there is a tendency for spin-ordering in systems with multiple component with different magnetic ground-states.

In the end, it is emphasised that there is the need to develop a hierarchical computational approach for studying structure-property correlations of multicomponent systems. In such an approach parameters correlating the structure and properties need to be clearly segregated in terms of their influence. In the next stage, parameters with

lesser influence on the structure and property of interest can be studied using computationally cheap or even empirical approaches, while the critical parameters should be studied using sophisticated computational approaches to develop a holistic representation of structure-property correlation, which may be helpful in designing new materials.

* * * * *

Bibliography

- [1] B. Gludovatz, A. Hohenwarter, D. Catoor, E. H. Chang, E. P. George, and R. O. Ritchie. A fracture-resistant high-entropy alloy for cryogenic applications. *Science*, 345(6201):1153–1158, 2014.
- [2] Z. Li, K. G. Pradeep, Y. Deng, D. Raabe, and C. C. Tasan. Metastable high-entropy dual-phase alloys overcome the strength–ductility trade-off. *Nature*, 534(7606):227–230, 2016.
- [3] Y. I Zhao, D. H. Lee, M. Y. Seok, J. A. Lee, M. P. Phaniraj, J. Y. Suh, H. Y. Ha, J. Y. Kim, U. Ramamurty, and J. Jang. Resistance of CoCrFeMnNi high-entropy alloy to gaseous hydrogen embrittlement. *Scripta Materialia*, 135:54–58, 2017.
- [4] H. Luo, Z. Li, and D. Raabe. Hydrogen enhances strength and ductility of an equiatomic high-entropy alloy. *Scientific Reports*, 7(1):9892, 2017.
- [5] K. E. Nygren, K. M. Bertsch, S. Wang, H. Bei, A. Nagao, and I. M. Robertson. Hydrogen embrittlement in compositionally complex FeNiCoCrMn fcc solid solution alloy. *Current Opinion in Solid State and Materials Science*, 2017.
- [6] F. Granberg, K. Nordlund, M. W. Ullah, K. Jin, C. Lu, H. Bei, L. M. Wang, F. Djurabekova, W. J. Weber, and Y. Zhang. Mechanism of radiation damage

- reduction in equiatomic multicomponent single phase alloys. *Physical Review Letters*, 116(13):135504, 2016.
- [7] O. A. Waseem and H. J. Ryu. Powder metallurgy processing of a $W_xTaTiVCr$ high-entropy alloy and its derivative alloys for fusion material applications. *Scientific Reports*, 7:1926, 2017.
- [8] D. D. Belyea, M. S. Lucas, E. Michel, J. Horwath, and C. W. Miller. Tunable magnetocaloric effect in transition metal alloys. *Scientific Reports*, 5:15755, 2015.
- [9] P. Koželj, S. Vrtnik, A. Jelen, S. Jazbec, Z. Jagličić, S. Maiti, M. Feuerbacher, W. Steurer, and J. Dolinšek. Discovery of a superconducting high-entropy alloy. *Physical Review Letters*, 113(10):107001, 2014.
- [10] C. M. Rost, E. Sachet, T. Borman, A. Moballeggh, E. C. Dickey, D. Hou, J. L. Jones, S. Curtarolo, and J. P. Maria. Entropy-stabilized oxides. *Nature communications*, 6:8485, 2015.
- [11] K. Yalamanchili, F. Wang, I. C. Schramm, J. M. Andersson, M. P. Johansson Jöesaar, F. Tasnádi, F. Mücklich, N. Ghafoor, and M. Odén. Exploring the high entropy alloy concept in $(AlTiVNbCr)N$. *Thin Solid Films*, 636:346–352, 2017.
- [12] A. G. de la Odra, M. A. Avilés, Y. Torres, E. Chicardi, and F. J. Gotor. A new family of cermets: Chemically complex but microstructurally simple. *International Journal of Refractory Metals and Hard Materials*, 63:17–25, 2017.
- [13] Y. Lu, Z. Tang, B. Wen, G. Wang, S. Wu, T. Wang, Y. Zhang, Z. Chen, Z. Cao, and T. Li. A promising new class of plasticine: Metallic plasticine. *Journal of Materials Science & Technology*, 34:344–348, 2017.

- [14] D. R. Gaskell. *Introduction to the Thermodynamics of Materials*. Taylor&Francis, New York, 3rd edition, 1995.
- [15] M. Glazer and J. Wark. *Statistical mechanics: a survival guide*. Oxford University Press, 1st edition, 2001.
- [16] N. L. Allan, G. D. Barrera, R. M. Fracchia, M. Y. Lavrentiev, M. B. Taylor, I. T. Todorov, and J. A. Purton. Free energy of solid solutions and phase diagrams via quasiharmonic lattice dynamics. *Physical Review B*, 63(9):094203, 2001.
- [17] C. L. Freeman. *Simulation of Solid Solutions and Interfaces*. PhD thesis, University of Bristol, 2005.
- [18] H. C. Andersen. Molecular dynamics simulations at constant pressure and/or temperature. *The Journal of Chemical Physics*, 72(4):2384–2393, 1980.
- [19] W. G Hoover. Canonical dynamics: equilibrium phase-space distributions. *Physical Review A*, 31(3):1695, 1985.
- [20] S. Nosé. A molecular dynamics method for simulations in the canonical ensemble. *Molecular Physics*, 52(2):255–268, 1984.
- [21] S. Nosé. A unified formulation of the constant temperature molecular dynamics methods. *The Journal of Chemical Physics*, 81(1):511–519, 1984.
- [22] P. Hohenberg and W. Kohn. Inhomogeneous electron gas. *Physical Review*, 136:B864–B871, Nov 1964.
- [23] W. Kohn and L. J. Sham. Self-consistent equations including exchange and correlation effects. *Physical Review*, 140:A1133–A1138, Nov 1965.

- [24] H. J. Monkhorst and J. D. Pack. Special points for brillouin-zone integrations. *Physical Review B*, 13:5188–5192, Jun 1976.
- [25] C. L. Fu and K. M. Ho. First-principles calculation of the equilibrium ground-state properties of transition metals: Applications to Nb and Mo. *Physical Review B*, 28:5480–5486, Nov 1983.
- [26] M. Methfessel and A. T. Paxton. High-precision sampling for brillouin-zone integration in metals. *Physical Review B*, 40:3616–3621, Aug 1989.
- [27] N. Marzari, D. Vanderbilt, A. De Vita, and M. C. Payne. Thermal contraction and disordering of the Al(110) surface. *Physical Review Letters*, 82:3296–3299, Apr 1999.
- [28] D. Sholl and J. A. Steckel. *Density functional theory: a practical introduction*. John Wiley & Sons, 2011.
- [29] B. Cantor, I.T. H. Chang, P. Knight, and A. J. B. Vincent. Microstructural development in equiatomic multicomponent alloys. *Materials Science and Engineering: A*, 375:213–218, 2004.
- [30] Y. Zhang, T. T. Zuo, Z. Tang, M. C. Gao, K. A. Dahmen, P. K. Liaw, and Z. P. Lu. Microstructures and properties of high-entropy alloys. *Progress in Materials Science*, 61:1–93, 2014.
- [31] A. Takeuchi, K. Amiya, T. Wada, K. Yubuta, and W. Zhang. High-entropy alloys with a hexagonal close-packed structure designed by equi-atomic alloy strategy and binary phase diagrams. *Journal of Materials*, 66(10):1984–1992, 2014.

- [32] L. Lilensten, J. P. Couzinié, L. Perrière, J. Bourgon, N. Emery, and I. Guillot. New structure in refractory high-entropy alloys. *Materials Letters*, 132:123–125, 2014.
- [33] J. W. Yeh, S. K. Chen, S. J. Lin, J. Y. Gan, T. S. Chin, T. T. Shun, C. H. Tsau, and S. Y. Chang. Nanostructured high-entropy alloys with multiple principal elements: novel alloy design concepts and outcomes. *Advanced Engineering Materials*, 6(5):299–303, 2004.
- [34] H. P. Chou, Y. S. Chang, S. K. Chen, and J. W. Yeh. Microstructure, thermo-physical and electrical properties in $\text{Al}_x\text{CoCrFeNi}$ ($0 \leq x \leq 2$) high-entropy alloys. *Materials Science and Engineering: B*, 163(3):184–189, 2009.
- [35] G. Y. Ke, S. K. Chen, T. Hsu, and J. W. Yeh. FCC and BCC equivalents in as-cast solid solutions of $\text{Al}_x\text{Co}_y\text{Cr}_z\text{Cu}_{0.5}\text{Fe}_v\text{Ni}_w$ high-entropy alloys. volume 31, pages 669–683, 2006.
- [36] U. Mizutani. *Hume-Rothery rules for structurally complex alloy phases*. CRC Press, 2016.
- [37] S. Guo, C. Ng, J. Lu, and C. T. Liu. Effect of valence electron concentration on stability of fcc or bcc phase in high entropy alloys. *Journal of Applied Physics*, 109(10):103505, 2011.
- [38] S. Guo. Phase selection rules for cast high entropy alloys: an overview. *Materials Science and Technology*, 31(10):1223–1230, 2015.

- [39] S. Singh, N. Wanderka, B. S. Murty, U. Glatzel, and J. Banhart. Decomposition in multi-component alcohrofeni high-entropy alloy. *Acta Materialia*, 59(1):182–190, 2011.
- [40] F. Tian, L. K. Varga, N. Chen, L. Delczeg, and L. Vitos. Ab initio investigation of high-entropy alloys of 3 d elements. *Physical Review B*, 87(7):075144, 2013.
- [41] A. J. Zaddach, C. Niu, C. C. Koch, and D. L. Irving. Mechanical properties and stacking fault energies of NiFeCrCoMn high-entropy alloy. *Journal of Materials*, 65(12):1780–1789, 2013.
- [42] M. S. Daw, S. M. Foiles, and M. I. Baskes. The embedded-atom method: a review of theory and applications. *Materials Science Reports*, 9(7-8):251–310, 1993.
- [43] V. Heine, I. J. Robertson, M. C. Payne, J. N. Murrell, J. C. Phillips, and D. Weaire. Many-atom interactions in solids. *Philosophical Transactions of the Royal Society of London A: Mathematical, Physical and Engineering Sciences*, 334(1635):393–405, 1991.
- [44] A. R. Leach. *Molecular modelling: principles and applications*. Pearson Education, 2001.
- [45] M. W. Finnis and J. E. Sinclair. A simple empirical n-body potential for transition metals. *Philosophical Magazine A*, 50(1):45–55, 1984.
- [46] A. P. Sutton and J. Chen. Long-range Finnis–Sinclair potentials. *Philosophical Magazine Letters*, 61(3):139–146, 1990.
- [47] M. S. Daw and M. I. Baskes. Semiempirical, quantum mechanical calculation of hydrogen embrittlement in metals. *Physical Review Letters*, 50(17):1285, 1983.

- [48] R. A. Johnson. Alloy models with the embedded-atom method. *Physical Review B*, 39:12554–12559, Jun 1989.
- [49] X. W. Zhou, H. N. G. Wadley, R. A. Johnson, D. J. Larson, N. Tabat, A. Cerezo, A. K. Petford-Long, G. D. W. Smith, P. H. Clifton, R. L. Martens, and T. F. Kelly. Atomic scale structure of sputtered metal multilayers. *Acta Materialia*, 49(19):4005–4015, 2001.
- [50] W. Smith and T. R. Forester. DL_POLY_2. 0: A general-purpose parallel molecular dynamics simulation package. *Journal of Molecular Graphics*, 14(3):136–141, 1996.
- [51] M. P. Allen and D. J. Tildesley. *Computer simulation of liquids*. Oxford university press, 2nd edition, 2017.
- [52] J. D. Gale. GULP: A computer program for the symmetry-adapted simulation of solids. *Journal of the Chemical Society, Faraday Transactions*, 93(4):629–637, 1997.
- [53] A. Cunliffe, C. L. Freeman, and I. Todd. An electronic structure approach to properties prediction in high entropy solid solutions. *Private communication*.
- [54] Z. Lin, R. A. Johnson, and L. V. Zhigilei. Computational study of the generation of crystal defects in a BCC metal target irradiated by short laser pulses. *Physical Review B*, 77(21):214108, 2008.
- [55] Md Meraj and S. Pal. Deformation of $\text{Ni}_{20}\text{W}_{20}\text{Cu}_{20}\text{Fe}_{20}\text{Mo}_{20}$ high entropy alloy for tensile followed by compressive and compressive followed by tensile loading: A

molecular dynamics simulation based study. In *IOP Conference Series: Materials Science and Engineering*, volume 115, page 012019. IOP Publishing, 2016.

- [56] T. Brink, L. Koch, and K. Albe. Structural origins of the boson peak in metals: From high-entropy alloys to metallic glasses. *Physical Review B*, 94(22):224203, 2016.
- [57] L. Koch, F. Granberg, T. Brink, D. Utt, K. Albe, F. Djurabekova, and K. Nordlund. Local segregation versus irradiation effects in high-entropy alloys: Steady-state conditions in a driven system. *Journal of Applied Physics*, 122(10):105106, 2017.
- [58] L. Xie, P. Brault, A. L. Thomann, and J. M. Bauchire. AlCoCrCuFeNi high entropy alloy cluster growth and annealing on silicon: A classical molecular dynamics simulation study. *Applied Surface Science*, 285:810–816, 2013.
- [59] S. W. Kao, J. W. Yeh, and T. S. Chin. Rapidly solidified structure of alloys with up to eight equal-molar elements—a simulation by molecular dynamics. *Journal of Physics: Condensed Matter*, 20(14):145214, 2008.
- [60] Debyer code: <https://code.google.com/p/debyer/>. *Date accessed: 06-05-2015*.
- [61] G. Anand, R. Goodall, and C. L. Freeman. Role of configurational entropy in body-centred cubic or face-centred cubic phase formation in high entropy alloys. *Scripta Materialia*, 124:90–94, 2016.
- [62] F. Otto, Y. Yang, H. Bei, and E. P. George. Relative effects of enthalpy and entropy on the phase stability of equiatomic high-entropy alloys. *Acta Materialia*, 61(7):2628–2638, 2013.

- [63] R. Grau-Crespo and U. V. Waghmare. Simulation of crystals with chemical disorder at lattice sites. *Molecular Modeling for the Design of Novel Performance Chemicals and Materials*, page 303, 2012.
- [64] D. A. Porter and K. E. Easterling. *Phase transformations in metals and alloys*. Chapman & Hall, London, 1992.
- [65] John H Holland. Genetic algorithms. *Scientific American*, 267(1):66–73, 1992.
- [66] C. Barrón, S. Gómez, D. Romero, and A. Saavedra. A genetic algorithm for lennard-jones atomic clusters. *Applied Mathematics Letters*, 12(7):85–90, 1999.
- [67] J. M. C. Marques and F. B. Pereira. An evolutionary algorithm for global minimum search of binary atomic clusters. *Chemical Physics Letters*, 485(1-3):211–216, 2010.
- [68] J. Zhao, R. Shi, L. Sai, X. Huang, and Y. Su. Comprehensive genetic algorithm for ab initio global optimisation of clusters. *Molecular Simulation*, 42(10):809–819, 2016.
- [69] N. Dugan and S. Erkoç. Genetic algorithms in application to the geometry optimization of nanoparticles. *Algorithms*, 2(1):410–428, 2009.
- [70] G. Trimarchi, P. Graf, and A. Zunger. Exploring the configurational space of binary alloys: Different sampling for different cell shapes. *Physical Review B*, 74(1):014204, 2006.
- [71] https://en.wikipedia.org/wiki/Metropolis-Hastings_algorithm.
- [72] R. Christian and G. Casella. *Monte Carlo Statistical Methods*. Springer, 2004.

- [73] A. Sharma, P. Singh, D. D. Johnson, P. K. Liaw, and G. Balasubramanian. Atomistic clustering-ordering and high-strain deformation of an $\text{Al}_{0.1}\text{CrCoFeNi}$ high-entropy alloy. *Scientific Reports*, 6:31028, 2016.
- [74] A. Sharma, S. A. Deshmukh, P. K. Liaw, and G. Balasubramanian. Crystallization kinetics in $\text{Al}_x\text{CrCoFeNi}$ ($0 \leq x \leq 40$) high-entropy alloys. *Scripta Materialia*, 141:54–57, 2017.
- [75] A. Sharma, R. Singh, P. K. Liaw, and G. Balasubramanian. Cuckoo searching optimal composition of multicomponent alloys by molecular simulations. *Scripta Materialia*, 130:292–296, 2017.
- [76] W. M. Choi, Y. Kim, D. Seol, and B. J. Lee. Modified embedded-atom method interatomic potentials for the Co-Cr, Co-Fe, Co-Mn, Cr-Mn and Mn-Ni binary systems. *Computational Materials Science*, 130:121–129, 2017.
- [77] C. Wu, B. J. Lee, and X. Su. Modified embedded-atom interatomic potential for Fe-Ni, Cr-Ni and Fe-Cr-Ni systems. *Calphad*, 57:98–106, 2017.
- [78] P. Wang, Y. Wu, J. Liu, and H. Wang. Impacts of atomic scale lattice distortion on dislocation activity in high-entropy alloys. *Extreme Mechanics Letters*, 17:38–42, 2017.
- [79] G. Bonny, N. Castin, and D. Terentyev. Interatomic potential for studying ageing under irradiation in stainless steels: the FeNiCr model alloy. *Modelling and Simulation in Materials Science and Engineering*, 21(8):085004, 2013.

- [80] Y. Mishin, M. J. Mehl, D. A. Papaconstantopoulos, A. F. Voter, and J. D. Kress. Structural stability and lattice defects in copper: Ab initio, tight-binding, and embedded-atom calculations. *Physical Review B*, 63(22):224106, 2001.
- [81] J. M. Winey, A. Kubota, and Y. M. Gupta. Thermodynamic approach to determine accurate potentials for molecular dynamics simulations: thermoelastic response of aluminum. *Modelling and Simulation in Materials Science and Engineering*, 18(2):029801, 2010.
- [82] J. Li, Q. H. Fang, B. Liu, Y. W. Liu, and Y. Liu. Mechanical behaviors of alcrfecuni high-entropy alloys under uniaxial tension via molecular dynamics simulation. *RSC Advances*, 6(80):76409–76419, 2016.
- [83] T. L. Underwood and G. J. Ackland. monteswitch: A package for evaluating solid–solid free energy differences via lattice-switch Monte Carlo. *Computer Physics Communications*, 215:204–222, 2017.
- [84] K. Luo, M. R. Roberts, N. Guerrini, N. Tapia-Ruiz, R. Hao, F. Massel, D. M. Pickup, S. Ramos, Y. S. Liu, J. Guo, A. V. Chadwick, L. C. Duda, and P. G. Bruce. Anion redox chemistry in the cobalt free 3d transition metal oxide intercalation electrode $\text{Li}[\text{Li}_{0.2}\text{Ni}_{0.2}\text{Mn}_{0.6}]\text{O}_2$. *Journal American Chemical Society*, 138(35):11211–11218, 2016.
- [85] Z. Lu, H. Zhang, W. Lei, D. C. Sinclair, and I. M. Reaney. High-figure-of-merit thermoelectric la-doped a-site-deficient SrTiO_3 ceramics. *Chemistry of Materials*, 28(3):925–935, 2016.
- [86] D. B. Miracle and O. N. Senkov. A critical review of high entropy alloys and related concepts. *Acta Materialia*, 122:448–511, 2017.

- [87] A. Moballeggh, C. M. Rost, J. P. Maria, and E. C. Dickey. Chemical homogeneity in entropy-stabilized complex metal oxides. *Microscopy and Microanalysis*, 21(S3):1349–1350, 2015.
- [88] R. Djenadic, A. Sarkar, O. Clemens, C. Loho, M. Botros, V. S. K. Chakravadhanula, C. Kübel, S. S. Bhattacharya, A. S. Gandhi, and H. Hahn. Multicomponent equiatomic rare earth oxides. *Materials Research Letters*, 5(2):102–109, 2017.
- [89] S. Jiang, T. Hu, J. Gild, N. Zhou, J. Nie, M. Qin, T. Harrington, K. Vecchio, and J. Luo. A new class of high-entropy perovskite oxides. *Scripta Materialia*, 142:116–120, 2018.
- [90] D. Berardan, A. K. Meena, S. Franger, C. Herrero, and N. Dragoe. Controlled Jahn-Teller distortion in (MgCoNiCuZn)O-based high entropy oxides. *Journal of Alloys and Compounds*, 704:693–700, 2017.
- [91] Z. Rak, C. M. Rost, M. Lim, P. Sarker, C. Toher, S. Curtarolo, J. P. Maria, and D. W. Brenner. Charge compensation and electrostatic transferability in three entropy-stabilized oxides: Results from density functional theory calculations. *Journal of Applied Physics*, 120(9):095105, 2016.
- [92] C. M. Rost, Z. Rak, D. W. Brenner, and J. P. Maria. Local structure of the $\text{Mg}_x\text{Ni}_x\text{Co}_x\text{Cu}_x\text{Zn}_x\text{O}$ ($x=0.2$) entropy-stabilized oxide: An EXAFS study. *Journal of the American Ceramic Society*, 100(6):2732–2738, 2017.
- [93] X. Sang, E. D. Grimley, C. Niu, D. L. Irving, and J. M. LeBeau. Direct observation of charge mediated lattice distortions in complex oxide solid solutions. *Applied Physics Letters*, 106(6):061913, 2015.

- [94] D. Bérardan, S. Franger, D. Dragoë, A. K. Meena, and N. Dragoë. Colossal dielectric constant in high entropy oxides. *Physica Status Solidi (RRL)-Rapid Research Letters*, 10(4):328–333, 2016.
- [95] D. Bérardan, S. Franger, A. K. Meena, and N. Dragoë. Room temperature lithium superionic conductivity in high entropy oxides. *Journal of Materials Chemistry A*, 4(24):9536–9541, 2016.
- [96] B. Raveau. Transition metal oxides: Promising functional materials. *Journal of the European Ceramic Society*, 25(12):1965–1969, 2005.
- [97] J. D. Gale and A. L. Rohl. The general utility lattice program (GULP). *Molecular Simulation*, 29(5):291–341, 2003.
- [98] C. R. A. Catlow and A. M. Stoneham. Ionicity in solids. *Journal of Physics C: Solid State Physics*, 16(22):4321–4338, 1983.
- [99] G. V. Lewis and C. R. A. Catlow. Potential models for ionic oxides. *Journal of Physics C: Solid State Physics*, 18(6):1149, 1985.
- [100] M. S. Islam and L. J. Winch. Defect chemistry and oxygen diffusion in the $\text{HgBa}_2\text{Ca}_2\text{Cu}_3\text{O}_{8+\delta}$ superconductor: A computer simulation study. *Physical Review B*, 52(14):10510, 1995.
- [101] G. Anand, A. P. Wynn, C. M. Handley, and C. L. Freeman. Phase stability and distortion in high-entropy oxides. *Acta Materialia*, 146:119–125, 2018.
- [102] J. W. Yeh. Physical metallurgy of high-entropy alloys. *Journal of Material-Springer*, 67(10):2254–2261, 2015.

- [103] S.Q. Xia, M.C. Gao, and Y. Zhang. Abnormal temperature dependence of impact toughness in $\text{Al}_x\text{CoCrFeNi}$ system high entropy alloys. *Materials Chemistry and Physics*, 210:213–221, 2018.
- [104] D. Li, C. Li, T. Feng, Y. Zhang, G. Sha, J. J. Lewandowski, P. K. Liaw, and Y. Zhang. High-entropy $\text{Al}_{0.3}\text{CoCrFeNi}$ alloy fibers with high tensile strength and ductility at ambient and cryogenic temperatures. *Acta Materialia*, 123:285–294, 2017.
- [105] K. V. S. Thurston, B. Gludovatz, A. Hohenwarter, G. Laplanche, E. P. George, and R. O. Ritchie. Effect of temperature on the fatigue-crack growth behavior of the high-entropy alloy CrMnFeCoNi . *Intermetallics*, 88:65–72, 2017.
- [106] Y. H. Jo, S. Jung, W. M. Choi, S. S. Sohn, H. S. Kim, B. J. Lee, N. J. Kim, and S. Lee. Cryogenic strength improvement by utilizing room-temperature deformation twinning in a partially recrystallized VCrMnFeCoNi high-entropy alloy. *Nature Communications*, 8:15719, 2017.
- [107] G. Laplanche, A. Kostka, O. M. Horst, G. Eggeler, and E. P. George. Microstructure evolution and critical stress for twinning in the CrMnFeCoNi high-entropy alloy. *Acta Materialia*, 118:152–163, 2016.
- [108] G. Laplanche, A. Kostka, C. Reinhart, J. Hunfeld, G. Eggeler, and E. P. George. Reasons for the superior mechanical properties of medium-entropy CrCoNi compared to high-entropy CrMnFeCoNi . *Acta Materialia*, 128:292–303, 2017.
- [109] I. Toda-Caraballo and P. E. J. Rivera-Díaz-del Castillo. Modelling solid solution hardening in high entropy alloys. *Acta Materialia*, 85:14–23, 2015.

- [110] C. Varvenne, A. Luque, and W. A. Curtin. Theory of strengthening in fcc high entropy alloys. *Acta Materialia*, 118:164–176, 2016.
- [111] I. Toda-Caraballo. A general formulation for solid solution hardening effect in multicomponent alloys. *Scripta Materialia*, 127:113–117, 2017.
- [112] T. Tsuru and D. C. Chrzan. Effect of solute atoms on dislocation motion in Mg: An electronic structure perspective. *Scientific Reports*, 5:8793, 2015.
- [113] R. Bullough and R. C. Newman. The kinetics of migration of point defects to dislocations. *Reports on Progress in Physics*, 33(1):101, 1970.
- [114] R. L. Fleischer. Solution hardening. *Acta Metallurgica*, 9(11):996–1000, 1961.
- [115] R. L. Fleischer. Substitutional solution hardening. *Acta Metallurgica*, 11(3):203–209, 1963.
- [116] R. Labusch. A statistical theory of solid solution hardening. *Physica Status Solidi (b)*, 41(2):659–669, 1970.
- [117] C. Varvenne, G. P. M. Leyson, M. Ghazisaeidi, and W. A. Curtin. Solute strengthening in random alloys. *Acta Materialia*, 124:660–683, 2017.
- [118] L. Ventelon, B. Lüthi, E. Clouet, L. Proville, B. Legrand, D. Rodney, and F. Willaime. Dislocation core reconstruction induced by carbon segregation in bcc iron. *Physical Review B*, 91:220102, Jun 2015.
- [119] A. Argon. *Strengthening mechanisms in crystal plasticity*. Number 4. Oxford University Press on Demand, 2008.

- [120] S. Patinet and L. Proville. Depinning transition for a screw dislocation in a model solid solution. *Physical Review B*, 78(10):104109, 2008.
- [121] T. Mohri and K. Watanabe. Studies on the statistical problems of the solid solution hardening. *Memoirs of the Faculty of Engineering, Hokkaido University*, 15(1):19–28, 1979.
- [122] T. Mohri and T. Suzuki. Solid solution hardening by impurities. *Materials Engineering-New York*, 15:259–259, 1999.
- [123] P. Kratochvíl and E. Neradová. Solid solution hardening in some copper base alloys. *Czechoslovak Journal of Physics B*, 21(12):1273–1278, 1971.
- [124] T. H. Wille, W. Gieseke, and C. H. Schwink. Quantitative analysis of solution hardening in selected copper alloys. *Acta Metallurgica*, 35(11):2679–2693, 1987.
- [125] J. Zander, R. Sandström, and L. Vitos. Modelling mechanical properties for non-hardenable aluminium alloys. *Computational Materials Science*, 41(1):86–95, 2007.
- [126] J. Zander and R. Sandström. One parameter model for strength properties of hardenable aluminium alloys. *Materials & Design*, 29(8):1540–1548, 2008.
- [127] Z. Wu, Y. Gao, and H. Bei. Thermal activation mechanisms and labusch-type strengthening analysis for a family of high-entropy and equiatomic solid-solution alloys. *Acta Materialia*, 120:108–119, 2016.
- [128] G. Paul M. Leyson, W. A. Curtin, L. G. Hector Jr, and C. F. Woodward. Quantitative prediction of solute strengthening in aluminium alloys. *Nature Materials*, 9(9):750–755, 2010.

- [129] B. L. Gyorffy. Coherent-potential approximation for a nonoverlapping-muffin-tin-potential model of random substitutional alloys. *Physical Review B*, 5(6):2382, 1972.
- [130] J. M. Schoen. Augmented-plane-wave virtual-crystal approximation. *Physical Review*, 184:858–863, Aug 1969.
- [131] G. P. M. Leyson, L. G. Hector, and W. A. Curtin. Solute strengthening from first principles and application to aluminum alloys. *Acta Materialia*, 60(9):3873–3884, 2012.
- [132] C. Varvenne and W. A. Curtin. Strengthening of high entropy alloys by dilute solute additions: CoCrFeNiAl_x and CoCrFeNiMnAl_x alloys. *Scripta Materialia*, 138:92–95, 2017.
- [133] C. Varvenne and W. A. Curtin. Predicting yield strengths of noble metal high entropy alloys. *Scripta Materialia*, 142:92–95, 2018.
- [134] J. P. Hirth. Dislocations. In R. W. Cahn and P. Haasen, editors, *Physical Metallurgy Vol. III*, chapter 20, pages 1831–1875. Elsevier Science BV, Amsterdam, The Netherlands, 1996.
- [135] J. N. Wang. Prediction of peierls stresses for different crystals. *Materials Science and Engineering: A*, 206(2):259–269, 1996.
- [136] J. L. Bassani, K. Ito, and V. Vitek. Complex macroscopic plastic flow arising from non-planar dislocation core structures. *Materials Science and Engineering: A*, 319:97–101, 2001.

- [137] V. V. Vitek. Core structure of screw dislocations in body-centred cubic metals: relation to symmetry and interatomic bonding. *Philosophical Magazine*, 84(3-5):415–428, 2004.
- [138] Z. Wu, H. Bei, G. M. Pharr, and E. P. George. Temperature dependence of the mechanical properties of equiatomic solid solution alloys with face-centered cubic crystal structures. *Acta Materialia*, 81:428–441, 2014.
- [139] J. P. Hirth and J. Lothe. *Theory of dislocations*. John Wiley & Sons, New York, 1982.
- [140] I. H. Katzarov and A. T. Paxton. Is the pinning of ordinary dislocations in γ -tial intrinsic or extrinsic in nature? a combined atomistic and kinetic Monte Carlo approach. *Acta Materialia*, 59(3):1281–1290, 2011.
- [141] L. Patriarca, A. Ojha, H. Sehitoglu, and Y. I. Chumlyakov. Slip nucleation in single crystal FeNiCoCrMn high entropy alloy. *Scripta Materialia*, 112:54–57, 2016.
- [142] W. Abuzaid and H. Sehitoglu. Critical resolved shear stress for slip and twin nucleation in single crystalline FeNiCoCrMn high entropy alloy. *Materials Characterization*, 129:288–299, 2017.
- [143] Z. Wu, H. Bei, F. Otto, G. M. Pharr, and E. P. George. Recovery, recrystallization, grain growth and phase stability of a family of fcc-structured multi-component equiatomic solid solution alloys. *Intermetallics*, 46:131–140, 2014.
- [144] Y. Y. Zhao and T. G. Nieh. Correlation between lattice distortion and friction stress in Ni-based equiatomic alloys. *Intermetallics*, 86:45–50, 2017.

- [145] S. Yoshida, T. Bhattacharjee, Y. Bai, and N. Tsuji. Friction stress and hall-petch relationship in CoCrNi equi-atomic medium entropy alloy processed by severe plastic deformation and subsequent annealing. *Scripta Materialia*, 134:33–36, 2017.
- [146] H. S. Oh, D. Ma, G. P. Leyson, B. Grabowski, E. S. Park, F. Körmann, and D. Raabe. Lattice distortions in the FeCoNiCrMn high entropy alloy studied by theory and experiment. *Entropy*, 18(9):321, 2016.
- [147] H. M. Ledbetter and R. P. Reed. Elastic properties of metals and alloys, i. iron, nickel, and iron-nickel alloys. *Journal of Physical and Chemical Reference Data*, 2(3):531–618, 1973.
- [148] I. Toda-Caraballo, E. I. Galindo-Nava, and P. E. J. Rivera-Díaz-del Castillo. Unravelling the materials genome: symmetry relationships in alloy properties. *Journal of Alloys and Compounds*, 566:217–228, 2013.
- [149] O. N. Senkov, J. M. Scott, S. V. Senkova, D. B. Miracle, and C. F. Woodward. Microstructure and room temperature properties of a high-entropy TaNbHfZrTi alloy. *Journal of Alloys and Compounds*, 509(20):6043–6048, 2011.
- [150] R. Tarumi, Y. Kawasaki, Y. Tabe, H. Ogi, M. Hirao, and T. Kagayama. Magnetic phase transition and elastic properties of α -Mn at low temperature. *Japanese Journal of Applied Physics*, 45(5S):4497, 2006.
- [151] P. Soven. Coherent-potential model of substitutional disordered alloys. *Physical Review*, 156(3):809, 1967.

- [152] D. W. Taylor. Vibrational properties of imperfect crystals with large defect concentrations. *Physical Review*, 156:1017–1029, Apr 1967.
- [153] J. Korringa. On the calculation of the energy of a bloch wave in a metal. *Physica*, 13(6-7):392–400, 1947.
- [154] W. Kohn and N. Rostoker. Solution of the schrödinger equation in periodic lattices with an application to metallic lithium. *Physical Review*, 94(5):1111, 1954.
- [155] F. Tian, Y. Wang, D. L. Irving, and L. Vitos. Applications of coherent potential approximation to HEAs. In *High-Entropy Alloys*, pages 299–332. Springer, 2016.
- [156] M. Ogura, T. Fukushima, R. Zeller, and P. H. Dederichs. Structure of the high-entropy alloy $\text{Al}_x\text{CrFeCoNi}$: fcc versus bcc. *Journal of Alloys and Compounds*, 715:454–459, 2017.
- [157] Y. Zhang, G. M. Stocks, K. Jin, C. Lu, H. Bei, B. C. Sales, L. Wang, L. K. Béland, R. E. Stoller, G. D. Samolyuk, M. Caro, A. Caro, and W. J. Weber. Influence of chemical disorder on energy dissipation and defect evolution in concentrated solid solution alloys. *Nature communications*, 6:8736, 2015.
- [158] P. Singh, A. V. Smirnov, and D. D. Johnson. Atomic short-range order and incipient long-range order in high-entropy alloys. *Physical Review B*, 91(22):224204, 2015.
- [159] P. Singh, A. Sharma, A. V. Smirnov, M. S. Diallo, P. Ray, G. Balasubramanian, and D. D. Johnson. Discovery and design of high-strength refractory multi-principal element alloys. *arXiv preprint arXiv:1710.06983*, 2017.

- [160] K. Jasiewicz, B. Wiendlocha, P. Korbeń, S. Kaprzyk, and J. Tobola. Superconductivity of $\text{Ta}_{34}\text{Nb}_{33}\text{Hf}_8\text{Zr}_{14}\text{Ti}_{11}$ high entropy alloy from first principles calculations. *Physica Status Solidi (RRL)-Rapid Research Letters*, 10(5):415–419, 2016.
- [161] F. Tian, L. K. Varga, N. Chen, J. Shen, and L. Vitos. Ab initio design of elastically isotropic TiZrNbMoV_x high-entropy alloys. *Journal of Alloys and Compounds*, 599:19–25, 2014.
- [162] F. Tian, L. K. Varga, N. Chen, L. Delczeg, and L. Vitos. Ab initio investigation of high-entropy alloys of 3d elements. *Physical Review B*, 87:075144, Feb 2013.
- [163] K. Tarafder, S. Ghosh, B. Sanyal, O. Eriksson, A. Mookerjee, and A. Chakrabarti. Electronic and magnetic properties of disordered Fe–Cr alloys using different electronic structure methods. *Journal of Physics: Condensed Matter*, 20(44):445201, 2008.
- [164] L. Vitos, I. A. Abrikosov, and B. Johansson. Anisotropic lattice distortions in random alloys from first-principles theory. *Physical Review Letters*, 87(15):156401, 2001.
- [165] D. A. Rowlands, J. B. Staunton, and B. L. Györffy. Korringa-Kohn-Rostoker nonlocal coherent-potential approximation. *Physical Review B*, 67:115109, Mar 2003.
- [166] D. A. Rowlands, A. Ernst, B. L. Györffy, and J. B. Staunton. Density functional theory for disordered alloys with short-range order: Systematic inclusion of charge-correlation effects. *Physical Review B*, 73:165122, Apr 2006.

- [167] D. A. Rowlands. Short-range correlations in disordered systems: nonlocal coherent-potential approximation. *Reports on Progress in Physics*, 72(8):086501, 2009.
- [168] A. Marmodoro, A. Ernst, S. Ostanin, L. Sandratskii, P. E. Trevisanutto, N. N. Lathiotakis, and J. B. Staunton. Short-range ordering effects on the electronic bloch spectral function of real materials in the nonlocal coherent-potential approximation. *Physical Review B*, 94:224205, Dec 2016.
- [169] A. Zunger, S. H. Wei, L. G. Ferreira, and James E. Bernard. Special quasirandom structures. *Physical Review Letters*, 65:353–356, Jul 1990.
- [170] F. Körmann, Y. Ikeda, B. Grabowski, and M. H. F. Sluiter. Phonon broadening in high entropy alloys. *npj Computational Materials*, 3(1):36, 2017.
- [171] N. L. Okamoto, K. Yuge, K. Tanaka, H. Inui, and E. P. George. Atomic displacement in the crmnfeconi high-entropy alloy—a scaling factor to predict solid solution strengthening. *AIP Advances*, 6(12):125008, 2016.
- [172] M. C. Gao, C. Niu, C. Jiang, and D. L. Irving. Applications of special quasirandom structures to high-entropy alloys. In *High-Entropy Alloys*, pages 333–368. Springer, 2016.
- [173] L. Bellaiche and D. Vanderbilt. Virtual crystal approximation revisited: Application to dielectric and piezoelectric properties of perovskites. *Physical Review B*, 61:7877–7882, Mar 2000.

- [174] S. J. Clark, M. D. Segall, C. J. Pickard, P. J. Hasnip, M. I. J. Probert, K. Refson, and M. C. Payne. First principles methods using CASTEP. *Zeitschrift für Kristallographie-Crystalline Materials*, 220(5/6):567–570, 2005.
- [175] D. Vanderbilt. Soft self-consistent pseudopotentials in a generalized eigenvalue formalism. *Physical Review B*, 41:7892–7895, Apr 1990.
- [176] D. R. Hamann, M. Schlüter, and C. Chiang. Norm-conserving pseudopotentials. *Physical Review Letters*, 43:1494–1497, Nov 1979.
- [177] J. P. Perdew, K. Burke, and M. Ernzerhof. Generalized gradient approximation made simple. *Physical Review Letters*, 77:3865–3868, Oct 1996.
- [178] A. R. Miedema, P. F. De Chatel, and F. R. De Boer. Cohesion in alloys—fundamentals of a semi-empirical model. *Physica B+ C*, 100(1):1–28, 1980.
- [179] J. A. Alonso and N. H. March. *Electrons in metals and alloys*. Academic Press, 2012.
- [180] S. Guo and C. T. Liu. Phase stability in high entropy alloys: formation of solid-solution phase or amorphous phase. *Progress in Natural Science: Materials International*, 21(6):433–446, 2011.
- [181] S. Guo, Q. Hu, C. Ng, and C. T. Liu. More than entropy in high-entropy alloys: Forming solid solutions or amorphous phase. *Intermetallics*, 41:96–103, 2013.
- [182] X. Yang and Y. Zhang. Prediction of high-entropy stabilized solid-solution in multi-component alloys. *Materials Chemistry and Physics*, 132(2):233–238, 2012.

- [183] D. J. M. King, S. C. Middleburgh, A. G. McGregor, and M. B. Cortie. Predicting the formation and stability of single phase high-entropy alloys. *Acta Materialia*, 104:172–179, 2016.
- [184] M. H. Tsai, J. H. Li, A. C. Fan, and P. H. Tsai. Incorrect predictions of simple solid solution high entropy alloys: Cause and possible solution. *Scripta Materialia*, 127:6–9, 2017.
- [185] L. A. Dominguez, R. Goodall, and I. Todd. Prediction and validation of quaternary high entropy alloys using statistical approaches. *Materials Science and Technology*, 31(10):1201–1206, 2015.
- [186] Z. Leong, I. Todd, and R. Goodall. Structural dependency of some multiple principal component alloys with the Thomas-Fermi-Dirac electron density. *Scripta Materialia*, 146:95–99, 2018.
- [187] R. S. Mulliken. Electronic population analysis on LCAO–MO molecular wave functions. I. *The Journal of Chemical Physics*, 23(10):1833–1840, 1955.
- [188] C. Fonseca Guerra, J. W. Handgraaf, E. J. Baerends, and F. M. Bickelhaupt. Voronoi deformation density (VDD) charges: Assessment of the Mulliken, Bader, Hirshfeld, Weinhold, and VDD methods for charge analysis. *Journal of Computational Chemistry*, 25(2):189–210, 2004.
- [189] M. D. Segall, R. Shah, C. J. Pickard, and M. C. Payne. Population analysis of plane-wave electronic structure calculations of bulk materials. *Physical Review B*, 54:16317–16320, Dec 1996.

- [190] R. F. W. Bader. Atoms in molecules. *Accounts of Chemical Research*, 18(1):9–15, 1985.
- [191] G. Henkelmann. <http://theory.cm.utexas.edu/henkelman/code/bader/>. Date accessed: 10-10-2017.
- [192] W. Tang, E. Sanville, and G. Henkelman. A grid-based bader analysis algorithm without lattice bias. *Journal of Physics: Condensed Matter*, 21(8):084204, 2009.
- [193] K. Jin, B. C. Sales, G. M. Stocks, G. D. Samolyuk, M. Daene, W. J. Weber, and H. Zhang, Y. and Bei. Tailoring the physical properties of Ni-based single-phase equiatomic alloys by modifying the chemical complexity. *Scientific Reports*, 6:20159, 2016.
- [194] B. C. Sales, K. Jin, H. Bei, G. M. Stocks, G. D. Samolyuk, A. F. May, and M. A. McGuire. Quantum critical behavior in a concentrated ternary solid solution. *Scientific Reports*, 6:26179, 2016.
- [195] S. Liu and Y. Wei. The gaussian distribution of lattice size and atomic level heterogeneity in high entropy alloys. *Extreme Mechanics Letters*, 11:84 – 88, 2017.
- [196] F. X. Zhang, S. Zhao, K. Jin, H. Xue, G. Velisa, H. Bei, R. Huang, J. Y. P. Ko, D. C. Pagan, J. C. Neufeind, W. J. Weber, and Y. Zhang. Local structure and short-range order in a NiCoCr solid solution alloy. *Physical Review Letters*, 118:205501, May 2017.
- [197] M. S. Lucas, G. B. Wilks, L. Mauger, J. A. Munoz, O. N. Senkov, E. Michel, J. Horwath, S. L. Semiatin, Matthew B. Stone, M. B. Stone, D. L. Abernathy, and

- E. Karapetrova. Absence of long-range chemical ordering in equimolar FeCoCrNi. *Applied Physics Letters*, 100(25):251907, 2012.
- [198] J. B. Cohen and M. E. Fine. Some aspects of short-range order. *Journal de Physique et Le Radium*, 23(10):749–762, 1962.
- [199] J. C. Fisher. On the strength of solid solution alloys. *Acta Metallurgica*, 2(1):9–10, 1954.
- [200] N. R. Dudova, R. O. Kaibyshev, and V. A. Valitov. Short-range ordering and the abnormal mechanical properties of a Ni-20% Cr alloy. *The Physics of Metals and Metallography*, 108(6):625–633, 2009.
- [201] N. R. Dudova, V. A. Valitov, and R. O. Kaibyshev. Short-range order and mechanical properties of nichrome. In *Doklady Physics*, volume 54, pages 77–79. Springer, 2009.
- [202] A. Tamm, A. Aabloo., M. Klintonberg, M. Stocks, and A. Caro. Atomic-scale properties of Ni-based FCC ternary, and quaternary alloys. *Acta Materialia*, 99:307–312, 2015.
- [203] J. Antonaglia, X. Xie, Z. Tang, C. W. Tsai, J. W. Qiao, Y. Zhang, M. O. Laktionova, E. D. Tabachnikova, J. W. Yeh, O. N. Senkov, M. C. Gao, J. T. Uhl, P. K. Liaw, and K. A. Dahmen. Temperature effects on deformation and serration behavior of high-entropy alloys (HEAs). *Journal of Materials*, 66(10):2002–2008, 2014.

- [204] M. Komarasamy, K. Alagarsamy, and R. S. Mishra. Serration behavior and negative strain rate sensitivity of $\text{Al}_{0.1}\text{CoCrFeNi}$ high entropy alloy. *Intermetallics*, 84:20–24, 2017.
- [205] C. Liu, M. Asato, N. Fujima, and T. Hoshino. Full-potential KKR calculations for Lattice Distortion around Impurities in Al-based dilute alloys, based on the generalized-gradient approximation. *Physics Procedia*, 75:1088–1095, 2015.
- [206] C. Liu, M. Asato, N. Fujima, and T. Hoshino. Full-potential KKR calculations for Lattice Distortion around Impurities in Al-based dilute alloys, based on the generalized-gradient approximation. *Transactions of the Materials Research Society of Japan*, 40(2):159–164, 2015.
- [207] H. M. Ledbetter and R. P. Reed. Elastic Properties of Metals and Alloys, I. Iron, Nickel, and Iron-Nickel Alloys. *Journal of Physical and Chemical Reference Data*, 2(3):531–618, 1973.
- [208] E. H. F. Date and K. W. Andrews. Anisotropic and composition effects in the elastic properties of polycrystalline metals. *Journal of Physics D: Applied Physics*, 2(10):1373, 1969.
- [209] A. Kokalj. Computer graphics and graphical user interfaces as tools in simulations of matter at the atomic scale. *Computational Materials Science*, 28(2):155–168, 2003.
- [210] M. J. Rutter. <http://src.tcm.phy.cam.ac.uk/viewvc/mjr/check2xsf/>. Date accessed: 21-11-2017.

- [211] O. Schneeweiss, M. Friák, M. Dudová, D. Holec, M. Šob, D. Kriegner, V. Holý, P. Beran, E. P. George, J. Neugebauer, and A. Dlouhý. Magnetic properties of the CrMnFeCoNi high-entropy alloy. *Physical Review B*, 96:014437, Jul 2017.
- [212] C. Niu, A. J. Zaddach, A. A. Oni, X. Sang, J. W. Hurt III, J. M. LeBeau, C. C. Koch, and D. L. Irving. Spin-driven ordering of Cr in the equiatomic high entropy alloy NiFeCrCo. *Applied Physics Letters*, 106(16):161906, 2015.

* * * * *